A Study of Aging in Male Cortical Bone Using Nanoindentation

A Dissertation Presented for the
Doctor of Philosophy
Degree
The University of Tennessee, Knoxville

Robert Christopher Singleton
August 2020

Copyright © 2020
By Robert Christopher Singleton
All rights reserved.

DEDICATION

This work is dedicated to my parents, who have always supported and encouraged me.

ACKNOWLEDGEMENTS

A number of people have had a positive impact on me and this work over the course of my graduate school career. I owe a thank you to all of you:

First and foremost, my advisor Dr. George Pharr. Thank you for your guidance.

Colleagues at Vanderbilt University:
Dr. Jeffry Nyman, PI of the Vanderbilt portion of this project. Thank you for your guidance as well, and for instruction on bone mechanics.
Dr. Mathilde Granke and Dr. Sasidhar Uppuganti, who are responsible for the non-nanoindentation data used in this study. Thank you for your hard work. My work would not be possible without yours.

Committee members: Dr. Warren Oliver, Dr. Timothy Truster, and Dr. Claudia Rawn. Thank you. Also, Dr. Roberto Benson for serving on my proposal defense committee.

Fellow research group members, especially Dr. Brittnee Mound and Dr. Ryan Ginder. You made graduate school more enjoyable. Also, thank you to Dr. Erik Herbert, Dr. Kurt Johanns, and Dr. S. P. Pardhasaradhi. I learned a lot from you in the first couple of years of graduate school.

Financial support for this work was provided by the National Science Foundation under grant number 1069165.

ABSTRACT

The incidence of bone fracture increases with age, due to both declining bone quantity and quality. Towards the goal of an improved understanding of the causes of the age-related decline in the fracture toughness of male cortical bone, nanoindentation experiments were performed on femoral diaphysis specimens from men aged 21-98 years and tibiae from male Fischer F344 rats aged 6, 12, and 24 months (n = 6-11 per age group). Bone is an anisotropic viscoelastic material with a complex hierarchical structure, in which water plays a critical mechanical role by conferring ductility. Because aged bone has been found to have less matrix-bound water and dry bone is less viscoelastic, the nanoindentation method used was designed to be sensitive to changes in viscoelasticity. In both experiments, the specimens were tested dry in air and immersed in phosphate buffered saline solution. In the human femur experiment, longitudinal (n = 26) and transverse (n = 25) specimens were tested. The results for the human femur and rat tibia experiments were similar: indentation stiffness (storage modulus) and hardness were found to increase with age, while viscoelasticity (loss modulus) was unchanged. Further analyses used fracture, compositional (mineralization, bound water, crosslinking concentrations), and structural (porosity, osteonal area fraction) data collected by collaborators. The increases in indentation stiffness and hardness with age were best explained by increased mineralization with age. In both experiments, indentation stiffness and hardness were negatively correlated with the fracture toughness parameters, which is consistent with a tradeoff between material strength and toughness. In keeping with the complex structure of bone, the fracture toughness of the human femur specimens was best predicted by a combination of indentation, compositional, and structural terms. In conclusion, this study found increased stiffness and hardness with age in male cortical bone, a change which contributed to decreased fracture toughness. On the other hand, viscoelasticity was unchanged with age and was not associated with fracture toughness.

TABLE OF CONTENTS

Chapter 1 Introduction 1
Chapter 2 Experimental Details 10
2.1 Study Design 11
2.2 Indentation Experimental Design 16
2.3 Indentation Theory and Equations 20
2.4 Indentation Method 33
2.5 Hydration System 42
2.6 Specimen Preparation 44
2.7 Nanoindentation Experimental Procedure 45
2.8 Fracture, Compositional, and Structural Data 47
2.9 Indentation-qBEI Site-matching 54
2.10 Indent-level to Specimen-level Values 57
2.11 Statistics 59
2.12 Indent Exclusion 61
2.13 Specimen Exclusion and Number of Specimens 62
2.14 Correlations Amongst Indentation Parameters 65
Chapter 3 Results 68
3.1 Indentation Data: Wet vs. Dry 69
3.2 Indentation Data: Longitudinal vs. Transverse 69
3.3 Indentation Data: Osteonal vs Interstitial 79
3.4 Indentation Data: Periosteal vs. Mid-cortex 79
3.5 Indentation Data: Changes with Age 79
3.6 Regression Models of Indentation Data 90
3.7 Correlations Between Indentation and Compositional Data 91
3.8 Correlations Between Fracture Data and Compositional and Structural Data ... 103
3.9 Correlations Between Indentation and Fracture Data 110
3.10 Regression Models of Fracture 120
3.11 Changes in Fracture with Age 120

3.12 Changes in Compositional and Structural Data with Age 124
3.13 Correlations Amongst Compositional and Structural Data 133
Chapter 4 Discussion 141
4.1 Factors Which Affect Bone Indentation Data 142
4.2 Effect of Bone Composition on Mechanical Properties 160
4.3 Dependence of Bone Fracture on Composition, Structure, and Indentation Data 163
4.4 Compositional and Structural Changes with Age 171
Chapter 5 Conclusions 176
5.1 Primary Conclusions 177
5.2 Closing Remarks 180
5.3 Proposed Future Work 181
References 182
Appendix 198
A.1 Defined Indent Exclusion Criteria 199
Vita 201

LIST OF TABLES

Table 1: Summary of human femur fracture, compositional, and structural parameter data 13
Table 2: Summary of rat bone fracture, compositional, and structural parameter data . 15
Table 3: Number of human femur experiment data points 64
Table 4: Number of rat bone experiment data points 66
Table 5: Correlations amongst indentation parameters. Sorted by decreasing correlation strength. 66
Table 6: Comparison of human femur Wet and Dry indentation data 70
Table 7: Comparison of rat tibia Wet and Dry indentation data 74
Table 8: Comparison of Longitudinal and Transverse indentation data for the human femur specimens 78
Table 9: Comparison of human femur Osteonal and Interstitial indentation data 80
Table 10: Comparison of rat tibia Periosteal and Mid-cortex indentation data 82
Table 11: Comparison of human femur indentation data between Young and Aged age groups and indentation data correlations with age 83
Table 12: Change in Wet condition human femur indentation data over the full donor age range, evaluated from IRLS fit 88
Table 13: Comparison of rat tibia indentation data by age group 89
Table 14: Correlations between human femur indentation and compositional data 92
Table 15: Human femur site-matched indentation – qBEI Ca wt.% correlation data 97
Table 16: Correlations between rat tibia Mid-cortex indentation data and rat bone compositional data 100
Table 17: Correlations between human femur fracture parameters and compositional and structural data 104
Table 18: Correlations between rat fracture parameters and compositional and structural data 109
Table 19: Correlations between human femur indentation and fracture data 114

Table 20: Correlations between rat fracture parameters and Mid-cortex indentation data 119
Table 21: Regression models of human femur fracture data..... 122
Table 22: Comparison of human femur fracture data between Young and Aged age groups and fracture data correlations with Age..... 123
Table 23: Comparison of rat fracture data between age groups 126
Table 24: Comparison of human femur compositional and structural data between Young and Aged age groups and correlations with age..... 128
Table 25: Comparison of rat compositional and structural data between age groups. 132
Table 26: Correlations amongst the human femur compositional and structural data. 137
Table 27: Correlations amongst the rat compositional and structural data..... 137
Table 28: Bone nanoindentation E and H data from studies with both wet and dry tests 143
Table 29: Bone viscoelastic loss factor data from studies with both wet and dry tests 144
Table 30: Cortical bone nanoindentation anisotropy data from this and other studies 146
Table 31: Transverse section osteonal and interstitial nanoindentation data from studies with multiple human donors 148
Table 32: Experimental details for nanoindentation studies of aging in human cortical bone..... 151
Table 33: Experimental details for nanoindentation studies of aging in human trabecular bone..... 156

LIST OF FIGURES

Figure 1: Schematic of the complex hierarchical structure of bone, with an emphasis on the presence of water. [8]..... 3
Figure 2: Examples of Osteonal and Interstitial indents for human femur Longitudinal (top) and Transverse (bottom) specimens. 18
Figure 3: Screenshot from the indent site selection GUI showing the selected locations for 4 Osteonal indents (encircled triangles) in a Transverse specimen. The 30 μm radius circles were used to ensure adequate interindent and indent-pore spacing.19
Figure 4: Example of Mid-cortex and Periosteal indent locations in a 24 month old rat tibia specimen. The Periosteal region increases in size with age and is easily distinguished by its lamellar appearance. 21
Figure 5: Images of a rat tibia specimen from each age group, with approximate indentation regions of interest represented by the red boxes. Note the increase in periosteal lamellae with age. 22
Figure 6: Screenshot from the indent site selection GUI, showing the selected locations of 20 Periosteal indents in one of the 6 month old rat tibia specimens. The 20 μm radius circles were used to ensure adequate interindent and indent-periosteal surface spacing. 23
Figure 7: Screenshot from the indent site selection GUI, showing the selected locations (green triangles) of 20 Mid-cortex indents in one of the 12 month old rat tibia specimens. Mid-cortex indents were most often arranged as rectangular arrays, with large surface features avoided by manual relocation of problematic indents. Note the extra indent in the first row, which was moved from the second row, to avoid a surface feature..... 24
Figure 8: Schematic of indentation load (P) vs. displacement (h) plot for a viscoelastic material. Displacement is shown to increase during the hold at peak load, due to creep. Contact depth (h_c) is less than displacement, by an amount which depends

upon the contact stiffness (S). S can be calculated from harmonic P and h data (CSM technique), or from the initial slope of the unloading curve. 26
Figure 9: Schematic of harmonic loading (blue) and the resultant phase-delayed displacement (orange) of a viscoelastic material. Note that the phase angle (δ) is the amount of lag between the load and displacement waveforms. 28
Figure 10: Spring and dashpot damped harmonic oscillator model of indenter-sample contact. The instrument and the sample each contribute to the total measured stiffness and damping. The sample (blue elements with s subscripts) and instrument (orange elements with i subscripts) are in parallel, and each consists of a spring with stiffness K in parallel with a dashpot with damping coefficient C. 31
Figure 11: Example of indentation Load vs. Time during the period of contact with the sample. First, load was increased until the displacement target was reached. The small increase in load after the initial loading segment is due the start of harmonic loading. After the harmonic displacement target was reached, load was held constant for 2 minutes, for the primary data acquisition period. The small load drop at the end of the hold segment is due to the end of harmonic loading. Load was then increased to the previous maximum, held 5 s, and finally unloaded in 1 s. 36
Figure 12: Example of indentation Displacement vs. Time, plotted from contact with the sample surface to the end of the test. Note the period of negative displacement at the end of the test. After each indent, the indenter was backed off of the sample 1 μm and oscillated in free space, in order to characterize and correct for the instrument's contribution to the measured data. 37
Figure 13: Example indentation Load vs Displacement plot. In this human femur indent, the end-of-loading displacement target was 1 μm. Viscoelastic creep is seen as the change in displacement after loading. The second, smaller increase in load is due to the start of harmonic loading. 38
Figure 14: Example indentation Displacement vs. Time plot for the period between loading and unloading. The increase in displacement is predominately due to viscoelastic creep, with a small contribution from harmonic displacement. The

creep rate progressively decreases throughout the 2 minute hold period, and is small during the primary data acquisition period, the last minute of the hold segment. The small load decrease towards the end is due to the end of harmonic loading. 39
Figure 15: Example indentation Harmonic displacement vs Time plot for the period of harmonic loading, when in contact with the specimen. First, the harmonic load was increased until the harmonic displacement target (4 μm) was reached. Harmonic load was then held constant for the duration of the 2 minute hold. 40
Figure 16: Hydration system: (A) Experimental setup prior to hydration (B) Voltage divider circuit used to regulate PBS solution level to ensure the sample stayed immersed (C) Sample holder schematic (D) Syringe pump 43
Figure 17: The notched human femur SENB specimens were subjected to 3-point bending fracture until failure (A). A progressive, displacement-controlled load-unload-dwell protocol was used (B). J and K values were calculated for each unloading segment (C). K_{init} was calculated as the equivalent K value at the intersection of a 0.2 mm offset line with a fit to the J-Δa data, J-integral as the value of J at failure, and K_{grow} as the slope of K vs. $\Delta a^{1/2}$ (D). [54] 48
Figure 18: The notched, whole rat femora were loaded monotonically in 3-point bending until failure. A region of stable crack propagation preceded unstable crack growth. The angles shown (upper left image) are for the angles of the initial crack and the onset of unstable crack growth, respectively. [56]..... 50
Figure 19: Osteon area fraction (OstAr) was calculated from a subregion of each qBEI image (A). Voids were programmatically separated from the bone matrix, and the bone matrix was then manually segmented between osteonal (grey) and interstitial (white) regions (B). [55]..... 55
Figure 20: Example screenshot from the last step in the indentation-qBEI site-matching process. At right is an indentation site selection GUI image, and at left is the same location in the qBEI image. The 4 green dots in the qBEI image were manually adjusted to coincide with the indent locations in the indentation site-selection

image. Also, note how the osteonal regions tend to be slightly darker than the interstitial regions in the qBEI image, indicating a lower level of mineralization. 56
Figure 21: Composite indentation microscope image for a Transverse specimen (Right) and corresponding qBEI image (Left). Indent locations are indicated by the green circles. Indent qBEI Ca wt.% values were calculated by averaging the pixel values within each of the 10 μm radius circles. 58
Figure 22: Boxplot of human femur E′ data grouped by Condition, Section, and Age. Significant age group differences are indicated by the comparison lines located above the boxes. Wet – Dry and Longitudinal – Transverse comparison lines are not shown, since in each instance Dry > Wet and Transverse > Longitudinal. 71
Figure 23: Boxplot of human femur E″ data grouped by Condition, Section, and Age. Wet – Dry and Longitudinal – Transverse comparison lines are not shown, since in each instance Wet > Dry and Transverse > Longitudinal. No significant differences were seen when comparing between age groups. 72
Figure 24: Boxplot of human femur H data grouped by Condition, Section, and Age. Significant age group differences are indicated by the comparison lines located above the boxes. Wet – Dry and Longitudinal – Transverse comparison lines are not shown, since in each instance Dry > Wet and Transverse > Longitudinal. 73
Figure 25: Boxplot of rat tibia E′ data grouped by Condition, Location, and Age. Significant differences between Periosteal and Mid-cortex data are indicated by comparison lines located above the boxes. Significant age group differences are indicated by the comparison lines below the boxes. Wet – Dry comparison lines are not shown, since in each instance Dry > Wet..... 75
Figure 26: Boxplot of rat tibia E″ data grouped by Condition, Location, and Age. Significant differences between Periosteal and Mid-cortex data are indicated by comparison lines located below the boxes. Wet – Dry comparison lines are not shown, since in each instance Wet > Dry. No age group differences were significant. 76

Figure 27: Boxplot of rat tibia H data grouped by Condition, Location, and Age. Significant differences between Periosteal and Mid-cortex data are indicated by comparison lines located above the boxes. Significant age group differences are indicated by the comparison lines below the boxes. Wet – Dry comparison lines are not shown, since in each instance Dry > Wet..... 77
Figure 28: Boxplots of human femur Osteonal and Interstitial H data. Significant Osteonal – Interstitial differences are shown by comparison lines above the boxes. 81
Figure 29: Scatterplots of human femur E′ vs. Age data. Significant correlations are indicated by best fit lines. 85
Figure 30: Scatterplots of human femur E″ vs. Age data. Significant correlations are indicated by best fit lines. 86
Figure 31: Scatterplots of human femur H vs. Age data. Significant (solid line) and nearly significant (dashed line) correlations are indicated by best fit lines. 87
Figure 32: Scatterplots of human femur E′ vs. TMD data. Significant (solid lines) and nearly significant (dashed line) correlations are indicated by best fit lines. 93
Figure 33: Scatterplots of human femur E′ vs. BoundWater data. Significant (solid line) and nearly significant (dashed line) correlations are indicated by best fit lines. 94
Figure 34: Scatterplots of human femur E′ vs Pentosidine data. Significant (solid line) and nearly significant (dashed line) correlations are indicated by best fit lines. 96
Figure 35: Boxplots of the specimen r_s values between the human femur site-matched indentation and qBEI Ca wt.% data. The p-values shown above the boxes indicate a significant correlation between the indentation and qBEI Ca wt.% data..... 98
Figure 36: Boxplot of Interstitial/Osteonal qBEI Ca wt.% ratios for the human femur Transverse specimens. As indicated by the p-value above the box, Interstitial mineralization was seen to be greater than Osteonal mineralization. 99
Figure 37: Scatterplots of rat E′ vs. TMD data. Significant correlations are indicated by best fit lines. 101

Figure 38: Scatterplots of rat E′ vs. BoundWater data. Significant correlations are indicated by best fit lines. 101
Figure 39: Scatterplots of rat E′ vs. Pentosidine data. Significant correlations are indicated by best fit lines. 102
Figure 40: Scatterplots of human femur fracture parameters vs. Porosity (left) and PoreWater (right). Significant correlations are indicated by best fit lines. 105
Figure 41: Scatterplots of human femur fracture parameters vs. BoundWater. Significant correlations are indicated by best fit lines. 106
Figure 42: Scatterplots of human femur fracture parameters vs. TMD. Significant correlations are indicated by best fit lines. 107
Figure 43: Scatterplots of human femur fracture parameters vs. OstAr. Significant correlations are indicated by best fit lines. 108
Figure 44: Scatterplots of rat fracture parameters vs. Porosity (top) and PoreWater (bottom). Significant correlations are indicated by best fit lines. 111
Figure 45: Scatterplots of rat fracture parameters vs. BoundWater. Significant correlations are indicated by best fit lines. 112
Figure 46: Scatterplots of rat fracture parameters vs. TMD. Significant correlations are indicated by best fit lines. 112
Figure 47: Scatterplots of rat fracture parameters vs. Pentosidine. Significant correlations are indicated by best fit lines. 113
Figure 48: Scatterplots of human femur K_{init} vs. E′ data. Significant correlations are indicated by best fit lines. 115
Figure 49: Scatterplots of human femur J-integral vs. E′ data. Significant correlations are indicated by best fit lines. 116
Figure 50: Scatterplot of human femur J-integral vs. H data. Significant correlations are indicated by best fit lines. 117
Figure 51: Scatterplots of human femur K_{grow} vs. E′ data. Significant correlations are indicated by best fit lines. 118

Figure 52: Scatterplots of rat K_c vs. E′. Significant correlations are indicated by best fit lines. 121
Figure 53: Scatterplots of rat CrackingToughness vs. E′. Significant correlations are indicated by best fit lines. 121
Figure 54: Scatterplots of human femur fracture data vs. Age. Significant correlations are indicated by best fit lines. 125
Figure 55: Boxplot of rat K_c data by age group. Significant differences between age groups are indicated by comparison lines above the boxes. 127
Figure 56: Boxplot of rat CrackingToughness data by age group. Significant differences between age groups are indicated by comparison lines above the boxes. 127
Figure 57: Scatterplots of human femur Porosity (top) and PoreWater (bottom) data vs. age. Neither parameter was significantly correlated with age. 129
Figure 58: Scatterplot of human femur BoundWater data vs. Age. As indicated by the best fit line, BoundWater and Age were negatively correlated. 130
Figure 59: Scatterplot of human femur TMD data vs. Age. As indicated by the best fit line, TMD and Age were positively correlated. 130
Figure 60: Scatterplot of human femur Pentosidine data vs. Age. As indicated by the best fit line, PE and age were positively correlated. 131
Figure 61: Scatterplot of human femur OstAr data vs. Age. As indicated by the best fit line, OstAr and Age were negatively correlated. 131
Figure 62: Boxplots of rat Porosity (top) and PoreWater (bottom) data by age group. Significant differences between age groups are indicated by comparison lines above the boxes. 134
Figure 63: Boxplot of rat BoundWater data by age group. Significant differences between age groups are indicated by comparison lines above the boxes. 135
Figure 64: Boxplot of rat TMD data by age group. Significant differences between age groups are indicated by comparison lines above the boxes. 135
Figure 65: Boxplots of rat Pentosidine data by age group. Significant differences between age groups are indicated by comparison lines above the boxes. 136

Figure 66: Scatterplots of PoreWater vs. Porosity for human (top) and rat (bottom) specimens. PoreWater and Porosity were positively correlated for both sets of specimens. 138
Figure 67: Scatterplots of BoundWater vs. Porosity for human (top) and rat (bottom) specimens. BoundWater and Porosity were negatively correlated for both sets of specimens. 139
Figure 68: Scatterplots of BoundWater vs. TMD for human (top) and rat (bottom) specimens. BoundWater and TMD were negatively correlated for both sets of specimens. 140

CHAPTER 1
INTRODUCTION

The incidence of bone fracture increases with age and is a problem with significant societal costs [1-4]. For example, about 30% of people with a hip fracture will die in the following year [4]. Although fragility fractures are commonly associated with elderly women, men suffer as well. The hip fracture incidence in men is approximately that of a women who is 5 years younger [1], and men are responsible for approximately 1 out of every 4 hip fracture cases in the United States [4]. Traditionally, the increase in fracture incidence among the elderly was attributed to declining bone mass. The criterion used to diagnose osteoporosis, areal bone mineral density (BMD) by dual-energy X-ray absorptiometry, is primarily a measure of bone mass. However, the probability of a fracture increases with age independently of BMD [1-3]. For the same BMD, an 80 year old woman has a hip fracture probability that is 3 to 6 times greater than that of a 50 year old woman [2]. Thus, with age there is a decline in both bone *quantity* and *quality*, where quality refers to the fracture resistance of a given quantity of bone. In a large observational study, only 21% of the male non-vertebral fractures occurred in osteoporotic men, which demonstrates the shortcomings in using BMD as a predictor of fracture risk [1]. The motivation of this study is the expectation that an improved understanding of the mechanisms behind the age-related decline in bone quality will inform better diagnostic and treatment options.

Bone is a composite material with hierarchical levels of organization from the molecular to the macroscale, as illustrated in Figure 1. It has 3 primary components, which are an inorganic mineral phase, an organic phase, and water. By weight, these constituents are in the approximate proportion of 65:25:10, respectively, for mature human bone [5]. On a volumetric basis the typical range is 33-43% mineral phase, 32-44% organic phase, and 15-25% water [6]. The organic phase is predominantly type I collagen. The collagen molecules have a triple-helix structure with a diameter of 1.5 nm and a length of 300 nm. The mineral phase consists of carbonated hydroxyapatite ($Ca_5(PO_4)_3OH$) platelets, with dimensions of ~2 x 20 x 50 nm. Having a thickness of only 2-3 nm allows the platelets to be flaw-insensitive despite being composed of a normally brittle material [7]. The next level up in the structural hierarchy are the

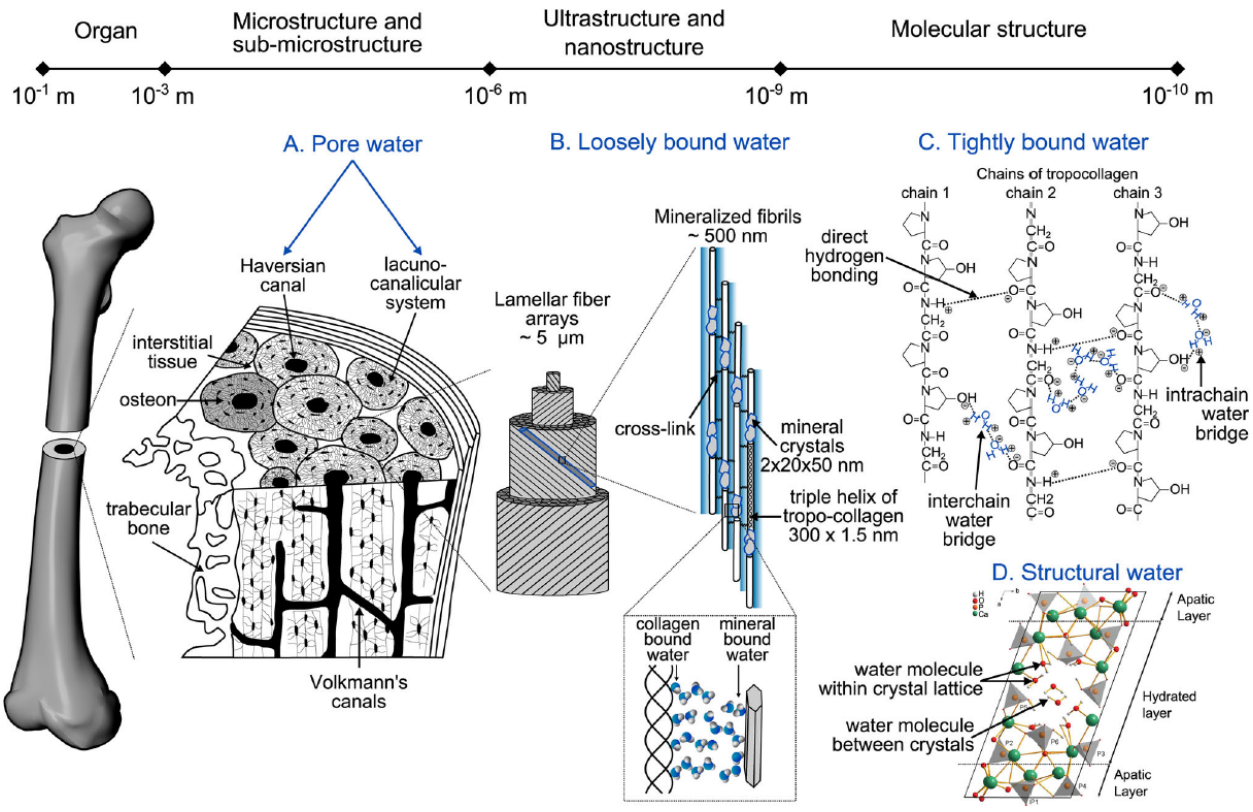


Figure 1: Schematic of the complex hierarchical structure of bone, with an emphasis on the presence of water. [8]

mineralized collagen fibrils, which are ~5-10 μm in length and ~100 nm in diameter. The tropocollagen molecules self-assemble such that they are all parallel, with an offset of 67 nm between neighboring molecules and a 35 nm gap between molecules in the axial direction. The structure is stabilized by covalent crosslinks between adjacent collagen molecules. After creation of the collagen scaffold, the mineral platelets nucleate in the gaps and share the same alignment as the collagen molecules.

At the next hierarchical scale, the mineralized collagen fibrils form larger fibers. Arrays of the mineralized collagen fibers can be organized in a variety of patterns, leading to the diversity seen in bone structure and function [9]. In mature human bone, layers of fibers are stacked together to form lamellae ~5 μm thick. The fibers are held together by thin, partially calcified layers of proteoglycans and other non-collagenous proteins. In cortical bone, the dense mineralized tissue surrounding the medullary canal of long bones, osteons are formed from groups of concentric hollow cylinder-shaped lamellae, with a cement line demarking the outer boundary. Osteons have a diameter of ~200-300 μm and also feature a central vascular channel (Haversian canal) with a diameter of ~50-90 μm [10]. The osteonal lamellae have a rotated plywood-type structure, such that the fibers rotate around the osteonal axis but adjacent lamellae have a different direction of rotation [11]. The ends of long bones and the vertebral bodies of the spine are filled with a less dense form of bone known as trabecular (or cancellous) bone. The sponge-like architecture of trabecular bone is comprised of individual rod- or plate-shaped trabeculae, with thicknesses of ~100-300 μm.

The fracture resistance of cortical bone is especially important because 80% of fractures are non-vertebral and occur at sites which are predominantly cortical [12]. Because of its greater surface area, trabecular bone loss begins earlier than cortical bone loss. For men, around 42% of total lifetime trabecular bone loss occurs before 50 years of age, compared to 15% for cortical bone [13]. Thus, the increase in fracture incidence in the elderly occurs after substantial trabecular bone loss has already occurred and is at a time when bone loss is predominantly cortical. The importance of cortical bone at a common fracture site, the femoral neck, has been demonstrated in a

study in which complete removal of all trabecular bone only resulted in a failure load decrease of 7% [14]. A decline in cortical bone quality can therefore substantially reduce whole-bone fracture resistance.

With a Young's modulus of ~109-114 GPa, the mineral platelets are responsible for the stiffness of bone [9]. Collagen, along with water, is responsible for bone's ductility and toughness. Collagen also confers viscoelasticity to bone. The mechanical role of collagen can be seen clearly in treatments which affect the organic phase but not the mineral phase. Ionizing radiation [15], thermal denaturation [16], and ashing [17] reduce the toughness of bone, primarily by decreasing strain at failure. In vivo, the mechanics of the collagen phase depend upon the concentration and type of the collagen crosslinks.

The mechanical role of water should not be underestimated. Refer to Figure 1 for a schematic of the presence of water throughout the structural hierarchy. A portion of the water within bone resides not in the matrix itself but in pores, such as Haversian canals. Within the bone matrix, water can be found bound to the collagen and mineral surfaces, as well as between them and trapped within the mineral and collagen phases themselves [8]. Water acts as a plasticizer for collagen because water – collagen hydrogen bonding prevents direct collagen – collagen bonding. Additionally, dehydration reduces the distance between the tropocollagen molecules and the mineral platelets [18]. Dry bone has lower toughness than wet bone due to decreased failure strain, while the stiffness and ultimate strength are increased [17, 19, 20]. When bone is dry, the strain fraction in the mineral phase is increased due to the lower collagen ductility. Dehydration in anhydrous solvents with lower hydrogen bonding capacities than water, such as ethanol, approximates the behavior of dry bone [21-23]. Finally, wet bone was greater viscoelastic energy dissipation than dry bone [24, 25].

Bone is an anisotropic material such that each bone is adapted to be strongest in the typical direction of loading. For long bones such as the femur, the osteons and mineralized collagen fibers are preferentially oriented in the axial direction. A transversely propagating crack must break the fibers, while a longitudinal crack needs

only to pull them apart. Bone fracture toughness is substantially higher in the transverse direction (“breaking”) than in the longitudinal direction (“splitting”) [26-29]. Additionally, in the transverse direction there are numerous interfaces which can impede a growing crack, such as between lamellae [30, 31] and the osteonal boundary (cement line) [32]. Osteons in particular are effective at forcing crack deflection. Crack deflection reduces the crack driving force and results in greater energy dissipation through a larger fracture surface.

Due to its complex structure, the fracture mechanics of bone are also complex, with relevant toughening mechanisms at all levels of the structural hierarchy [10, 33]. Note that bone fracture is a strain-controlled process [29]. At the smaller length scales (<1 μm), plastic deformation acts to blunt the crack tip and dissipate energy. These intrinsic energy dissipation mechanisms include stretching of the tropocollagen molecules, fibrillar sliding of the tropocollagen molecules within a mineralized collagen fibril, and fibrillar sliding of the mineralized collagen fibrils themselves. Toughening mechanisms at larger length scales act primarily behind the crack tip to reduce the crack driving force. These extrinsic toughening mechanisms include microcracking, crack deflection, and crack bridging by uncracked ligaments or intact fibrils. A change at any length scale can impact fracture toughness. For example, a change in the degree of mineralization can alter the plasticity of the bone matrix, while at a higher length scale, the crack path will depend on the distribution of the osteons.

Bone fractures in an increasingly brittle fashion with age, characterized by reduced strain at failure [19, 34, 35] and straighter crack paths [31, 36, 37]. A number of compositional and structural properties have been linked to declining bone quality with age, such as increased porosity [38], increased mineralization [39], in vivo microdamage accumulation [32], increased advanced glycation end-products (AGEs) [40], increased osteonal density [41], and decreased bound water content [42], among others. Given the number of concurrent changes with age at varying length scales, it is a challenge to determine the relative contribution of a given property change on fracture

toughness. Whole-bone fracture resistance is further complicated by factors separate from bone quality such as total bone mass and its distribution.

Human bones are constantly undergoing remodeling, where older, often damaged tissue is removed and replaced with new bone. The rate of bone turnover varies anatomically but is largely a function of surface area. Trabecular bone has approximately 20 times the surface area of cortical bone, and each year approximately 25% of trabecular bone is replaced, compared with 2-3% for cortical bone [6]. Remodeling is accomplished by the basic multicellular unit (BMU), wherein osteoclasts resorb bone, which is then replaced by unmineralized osteoid deposited by the trailing osteoblasts. After several months the end product of a BMU is an osteon in cortical bone or a bone packet in trabecular bone. Orchestrating the coupled actions of osteoclasts and osteoblasts are the osteocytes, terminally differentiated osteoblasts embedded throughout the mineralized matrix in lacunae and connected to one another via transverse processes passing through canaliculi.

As a consequence of remodeling, tissue age varies from one location to the next. Because mineralization is a function of tissue age, mineralization varies spatially as well. The distribution of local matrix mineralization values is described by the bone mineralization density distribution (BMDD). The time course of matrix mineralization proceeds in two stages. First is primary mineralization, where for several weeks the degree of mineralization increases rapidly to around 60% of the value of mature bone. Next is secondary mineralization, during which the degree of mineralization increases over the course of months to years but at a decreasing rate until reaching a physiological upper limit [43-45]. Thus, a bone's BMDD depends on the rate of turnover. An increase in the rate of turnover will result in a shifting of the BMDD towards lower mineralization values, while decreasing the rate of turnover will shift the BMDD towards higher mineralization values [45, 46]. For example, the BMDD of transiliac biopsies from women with postmenopausal osteoporosis is shifted towards lower mineralization values [47]. Postmenopausal osteoporosis is primarily caused by elevated turnover as result of a decline in estrogen levels [48]. Bisphosphonate treatment, which reduces

bone turnover, is seen to result in increased mineralization [49, 50], while parathyroid hormone treatment, which causes increased bone formation, results in decreased mineralization [51]. Note that it can take several years for a new steady-state BMDD to be established after a change in the rate of turnover. Mineralization heterogeneity, as measured by the width of the BMDD, is also a function of the turnover rate.

Nanoindentation is a useful technique in bone mechanics investigations because it is capable of measuring the mechanical properties of small volumes of material, independent of porosity (surface voids such as Haversian canals, lacunae, etc. can be avoided). This study was designed to identify mechanical property changes with age in adult male cortical bone at the tissue level. Similar indentation and compositional studies have found substantial variation between individuals and indicated that changes with age, if any, were likely to be modest. Therefore, specimens from a relatively large number of donors (n = 30), over a wide age range (21-98 years) were used. Because bone matrix properties vary within a given bone and between tissue types, it is necessary to sample a number of different regions in order to accurately characterize a given specimen. In this study, each specimen contained 64 indents, split between 8 osteonal and 8 interstitial locations. Given the anisotropy of bone and the importance of water to bone's mechanical properties, longitudinally and transversely sectioned specimens were tested in both wet and dry conditions. Since declining bound water has been associated with the age-related decline in bone quality, and since matrix hydration affects bone viscoelasticity, the nanoindentation method used was designed to be sensitive to possible changes in viscoelasticity with age. In addition to the nanoindentation data, this study also includes fracture, compositional, and structural data. These data enable several questions to be addressed: If the nanoindentation data change with age, were any compositional changes responsible? Are the indentation and fracture data correlated? What combination of parameters best predicted the fracture data? A similar, complementary experiment was performed in a rat model of aging. Together these experiments test the hypothesis that the age-related decline in the fracture toughness of male cortical bone is at least partially attributable to changing

mechanical properties of the bone matrix itself and that such a change is measurable via nanoindentation.

CHAPTER 2
EXPERIMENTAL DETAILS

2.1 Study Design

2.1.1 Overview

This study consisted of indentation, fracture, compositional, and structural data for human and rat bones. Each experiment was designed to identify changes with age. The primary questions addressed in this study were:

1) What factors affected the indentation data?
2) Were there changes with age?
3) What factors were associated with decreased fracture toughness? Could any of the observed changes with age be a contributor?

The indentation method used was designed to be sensitive to viscoelasticity. The primary indentation parameters reported in this study are storage modulus (E′), loss modulus (E″), and hardness (H). To study the effect of hydration, indentation experiments were conducted with the bone specimens tested dry in air (Dry condition) and immersed in phosphate buffered saline (PBS) solution (Wet condition). Because bone mechanical properties vary spatially, each indentation test consisted of a large number of indents, spread between a number of regions of interest.

2.1.2 Human Femur Experiments

The human femur cortical bone samples were from 30 male donors, aged 21-98 years. Thus, these samples covered nearly 8 decades of adult male aging. There were 2 cortical femur specimens for each donor, with one specimen being longitudinally sectioned and the other transversely sectioned, relative to the long axis of the femur. Nanoindentation measurements were performed on each bone specimen in both the Wet and Dry hydration conditions. In each indentation experiment, indents were split between osteonal and interstitial locations. Therefore, the 4 variables in the human femur indentation data were:

1) Condition (Wet vs. Dry)

2) Section (Longitudinal vs. Transverse)
3) Age (21-98 years)
4) Location (Osteonal vs. Interstitial)

Table 1 provides a summary of the human femur fracture, compositional, and structural parameters. For fracture testing, single edge notched bend (SENB) specimens were tested in 3-point bending. The fracture parameters in this experiment were K_{init} (critical stress intensity at crack initiation), J-integral (J-integral value at failure), and K_{grow} (change in critical stress intensity per change in crack length). The structural parameters were Porosity (cortical porosity volume percentage), PoreWater (pore water volume fraction), and OstAr (osteonal area fraction). Porosity and PoreWater are both measures of the volume of voids within the cortical bone specimens, while OstAr is a measure of the proportion of the cross-sectional area occupied by osteonal bone. Porosity was measured by micro-computed tomography (μCT), PoreWater by ^{1}H nuclear magnetic resonance (^{1}H NMR) spectroscopy, and OstAr by quantitative backscattered electron imaging (qBEI). The compositional parameters in the human femur experiment were TMD (tissue mineral density), BoundWater (bound water volume fraction), PE (pentosidine crosslinking concentration), and qBEI Ca wt.%. TMD and qBEI Ca wt.% are measures of the degree of bone mineralization. BoundWater quantifies the amount of water within the bone matrix, as opposed to the water within voids, which is measured by PoreWater.

Along with correlations with age, changes with age were assessed by splitting the donors into two age groups: Young (age ≤ 60 years, n = 14) and Aged (age > 60 years, n = 16). Sixty years was chosen as the age cutoff for two reasons. First, this age cutoff gives nearly equal group sizes. Second, bone turnover in adult men progressively decreases to a minimum at around 60 years of age [52]. For all donors, the mean age ± standard deviation was 63.5 ± 23.7 years. For the Young and Aged groups, these values were 42.1 ± 14.5 years and 82.1 ± 10.5 years, respectively.

Table 1: Summary of human femur fracture, compositional, and structural parameter data

Name	Description	Measurement Technique
K_{init}	Critical stress intensity at crack initiation	SENB 3-point bending
J-integral	J-integral value at failure	”
K_{grow}	Critical stress intensity for crack growth	”
Porosity	Cortical porosity	μCT
TMD	Tissue mineral density	”
PoreWater	Pore water volume fraction	^{1}H NMR
BoundWater	Bound water volume fraction	”
PE	Pentosidine crosslinking concentration	HPLC
OstAr	Osteonal area fraction	qBEI
qBEI Ca wt.%	Degree of mineralization	”

SENB = single edge notched bend
μCT = micro-computed tomography
^{1}H NMR = ^{1}H nuclear magnetic resonance spectroscopy
HPLC = high-performance liquid chromatography
qBEI = quantitative backscattered electron imaging

2.1.3 Rat Bone Experiments

The rat bone samples were collected from 36 male Fischer F344 rats split evenly between 6 month, 12 month, and 24 month age groups. For rats, this age range spans young adulthood to old age. The life expectancy of male Fischer F344 rats is ~29 months [53]. Indentation experiments were performed on tibial specimens, with the direction of indentation being parallel to the long axis of the bones. Like in the human femur experiment, specimens were indented in both the Wet and Dry hydration conditions. The indents were divided between locations in the mid-cortex and the periosteal lamellae. Thus, the 3 indentation variables in the rat experiment were:

1) Condition (Wet vs. Dry)
2) Age (6, 12, and 24 months)
3) Location (Mid-cortex vs. Periosteal)

Table 2 provides a description of the fracture, composition, and structural data in the rat experiments. For fracture testing, 3-point bending of notched whole femora was used. The fracture parameters were K_c and CrackingToughness. K_c is the stress intensity at max load for the initial notch and CrackingToughness is the work of fracture, adjusted for cross-sectional area and excluding the notch. The structural parameters were Porosity and PoreWater. The compositional parameters were TMD, BoundWater, and PE.

2.1.4 Division of Labor and Previously Published Works

This study was a joint project between researchers at the University of Tennessee and Vanderbilt University. All nanoindentation work was performed by the author at the University of Tennessee. Specimen preparation and the collection of fracture, compositional, and structural data were done by the collaborators at Vanderbilt. Detailed explanations of the experimental methods employed in the collection of the Vanderbilt data have been published previously [54-56]. Refer to these works for a more complete description of the Vanderbilt data experimental techniques than is included herein. Specifically, see Granke et. al for complete information

Table 2: Summary of rat bone fracture, compositional, and structural parameter data

Name	Description	Measurement Technique
K_c	Critical stress intensity of initial notch	3-point bending
CrackingToughness	Span-adjusted work of fracture	”
Porosity	Cortical porosity	μCT
TMD	Tissue mineral density	”
PoreWater	Pore water volume fraction	^{1}H NMR
BoundWater	Bound water volume fraction	”
PE	Pentosidine crosslinking concentration	HPLC

μCT = micro-computed tomography
^{1}H NMR = ^{1}H nuclear magnetic resonance spectroscopy
HPLC = high-performance liquid chromatography
qBEI = quantitative backscattered electron imaging
Fracture and ^{1}H NMR used notched left femur
μCT used un-notched right femur
HPLC used right radius

regarding the human femur data [54, 55], and refer to Uppuganti et. al for further details regarding the rat data [56].

2.2 Indentation Experimental Design

2.2.1 Equipment

Nanoindentation experiments were conducted using a NanoIndenter XP instrument (Agilent Technologies, Oak Ridge, TN) with a Berkovich diamond tip (Micro Star Technologies, Huntsville, TX). The Berkovich tip is a 3-sided pyramidal indenter with a centerline-face angle of 65.3°. The tip area function was periodically calibrated using a fused silica reference material. A custom indentation method was used, the description of which can be found in the Indentation Method section. A hydration system was designed in order to test the bone samples in a fully hydrated state, the details of which are described in the Hydration System section. A MATLAB GUI was developed for indentation site selection, with desired indent locations selected individually by mouse click. Adequate spacing between indents and between indents and pores was ensured by a circular region drawn around each selected indent location. For areas free of surface features needing to be avoided, indents could also be placed as a rectangular array.

2.2.2 Human Femur

Sixty individual bone specimens comprised the human femur dataset: 1 Longitudinal section and 1 Transverse section each from 30 donors. Each of the 60 specimens was subjected to nanoindentation in the Wet and Dry hydration conditions, for a total of 120 individual nanoindentation tests. Note that the final dataset was smaller than this, as detailed in Specimen Exclusion. Specifically, 26 Longitudinal and 25 Transverse specimens constituted the final dataset (Wet and Dry for each). Each human femur indentation experiment contained 64 total indents. The 64 indents were divided between 8 regions of interest, with each region being an osteonal area and a nearby interstitial area. Each osteonal and interstitial region contained 4 indents. Figure

2 gives examples of Osteonal and Interstitial indent placements. In Transverse sections, osteons were identified by circumferential lamellae around a central Haversian canal. All non-Osteonal regions were considered Interstitial, which includes old, remodeled osteon fragments. The Osteonal – Interstitial distinction was less clear-cut for the Longitudinal sections. Again, the defining feature of an osteon was lamellae around a central Haversian canal. In this case, the Haversian canal has the shape of an elongated ellipse. Interstitial regions were non-adjacent to Haversian canals and had a less distinctly lamellar structure than the osteonal regions.

The end-of-loading displacement target for the human femur indents was 1 μm. Note that due to viscoelastic creep during the hold segment, the maximum displacement was often ~100-200 nm greater than this. The indent target depth of 1 μm was selected to be relatively large yet ensure that osteonal and interstitial indents probed only their respective regions, without influence from the surrounding regions or pores. Larger indents are preferable because: (a) the effect of surface roughness is minimized, (b) the corrections for instrument dynamics are smaller relative to the measured values, and (c) it allows an increased harmonic amplitude (improved signal-to-noise ratio for dynamic measurements). The minimum spacing between indents was 30 μm (i.e. 30x the end-of-loading displacement target). Indents were also kept at least this distance from pores. Thus, Osteonal indents were generally located equidistant from the Haversian canal and the cement line. Figure 3 is a screenshot from the indent site selection GUI, showing Osteonal indent location selection.

2.2.3 Rat Tibia

The rat tibia dataset was comprised of 36 specimens: 12 specimens each from 6, 12, and 24 month old age groups. Each specimen was tested via nanoindentation in both the Wet and Dry hydration conditions, for a total of 72 planned indentation tests. Note that the final dataset used was smaller than this, as described in the Specimen Exclusion section. Specifically, there were 24 Wet and 31 Dry indentation experiments included in the final dataset. Each rat tibia indentation experiment contained 80 indents, split evenly between Mid-cortex and Periosteal regions. The 40 indents in each region

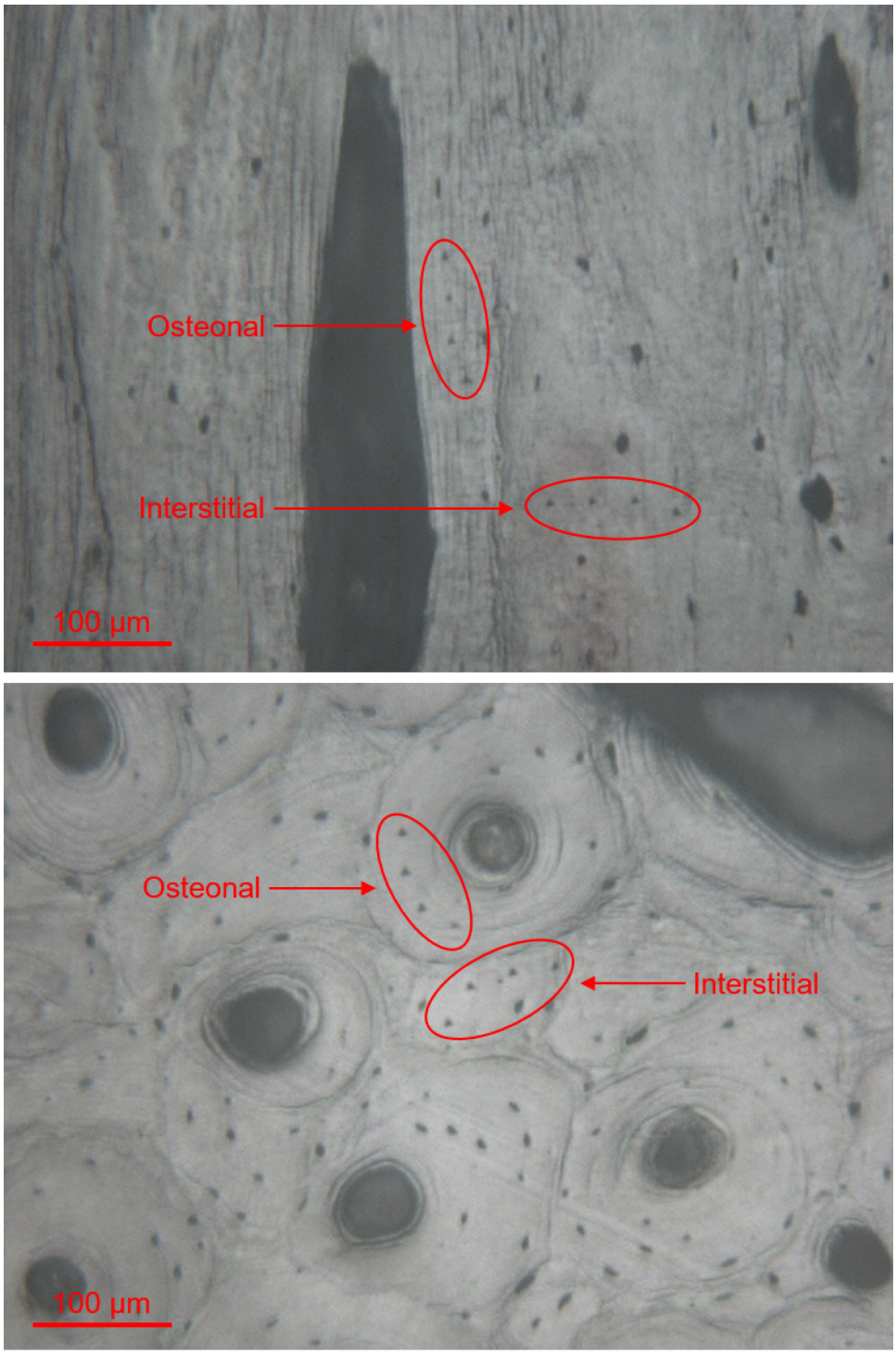


Figure 2: Examples of Osteonal and Interstitial indents for human femur Longitudinal (top) and Transverse (bottom) specimens.

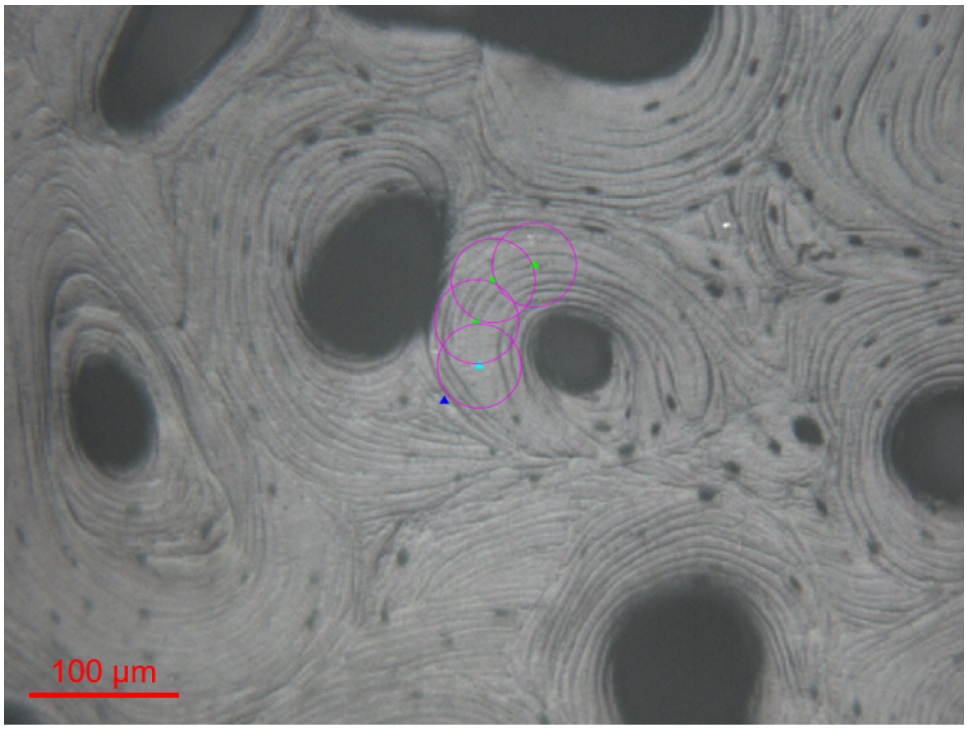


Figure 3: Screenshot from the indent site selection GUI showing the selected locations for 4 Osteonal indents (encircled triangles) in a Transverse specimen. The 30 µm radius circles were used to ensure adequate interindent and indent-pore spacing.

were comprised of 2 arrays of 20 indents each. Indents were located in the anterior quadrant of the tibiae cross sections. See Figure 4 for an example of Mid-cortex and Periosteal indent locations. In this figure, the indents can be faintly seen in 4 rectangular arrays of 20 indents apiece.

See Figure 5 for a picture of a representative rat tibia specimen from each age group. The region of interest in the nanoindentation experiments is indicated by the red boxes. Note the increase in size of the periosteal lamellae region with increasing age. The end-of-loading displacement target for the rat tibia indents was 500 nm, and the minimum indent spacing was 20 μm (40x the end-of-loading displacement). The indent depth was limited by the thickness of the periosteal lamellae region in the youngest age group. See Figure 6 for an example of Periosteal indent site selection for a 6 month specimen. In this specimen, the Periosteal region is only wide enough to permit indents single-file. As the Periosteal region increases in thickness with age, rectangular indent arrays could be employed, as was seen in Figure 4 for a 24 months specimen. The Mid-cortex region contained numerous small surface features which could not be entirely avoided. However, indents with questionable data were later excluded, as described in the Indent Exclusion section. Larger surface features were avoided, though. See Figure 7 for a GUI screenshot of an array of 20 Mid-cortex indents. Note the small features distributed throughout the Mid-cortex region. Also, note that one indent from the array has been manually removed from the second row and added to the first row, in order to avoid an apparent surface void.

2.3 Indentation Theory and Equations

2.3.1 Quasi-static Indentation

Nanoindentation uses an indenter tip of known geometry and load-displacement data to measure mechanical properties of small volumes of material. Most commonly, Young’s modulus (E) and hardness (H) are measured using the Oliver-Pharr method [57]. During indentation both the indenter and the indented material deform elastically,

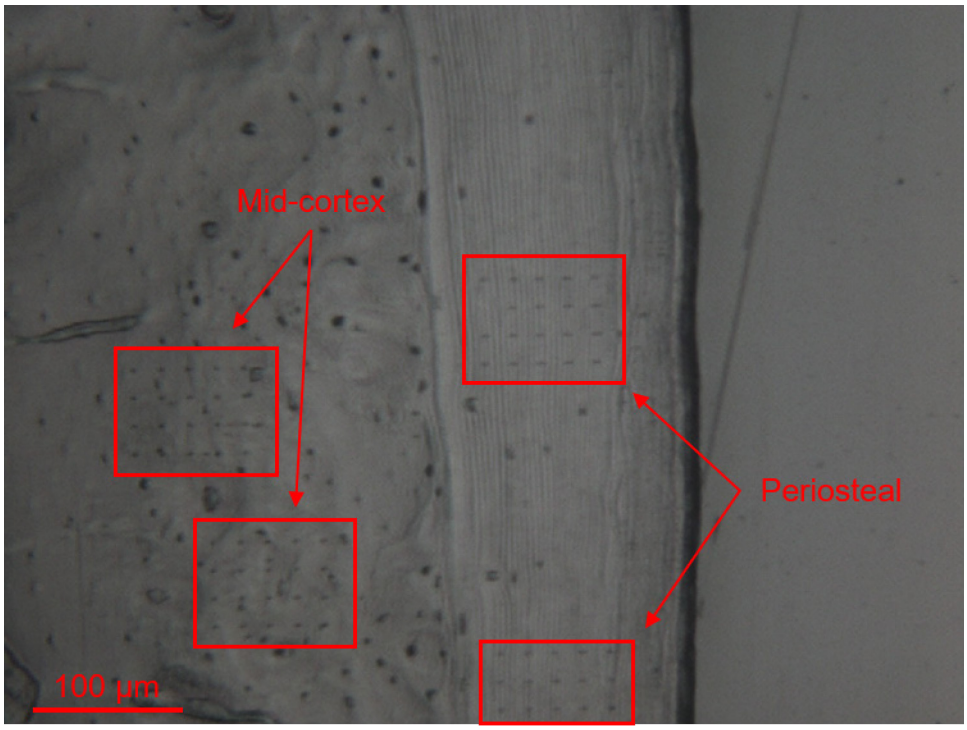


Figure 4: Example of Mid-cortex and Periosteal indent locations in a 24 month old rat tibia specimen. The Periosteal region increases in size with age and is easily distinguished by its lamellar appearance.

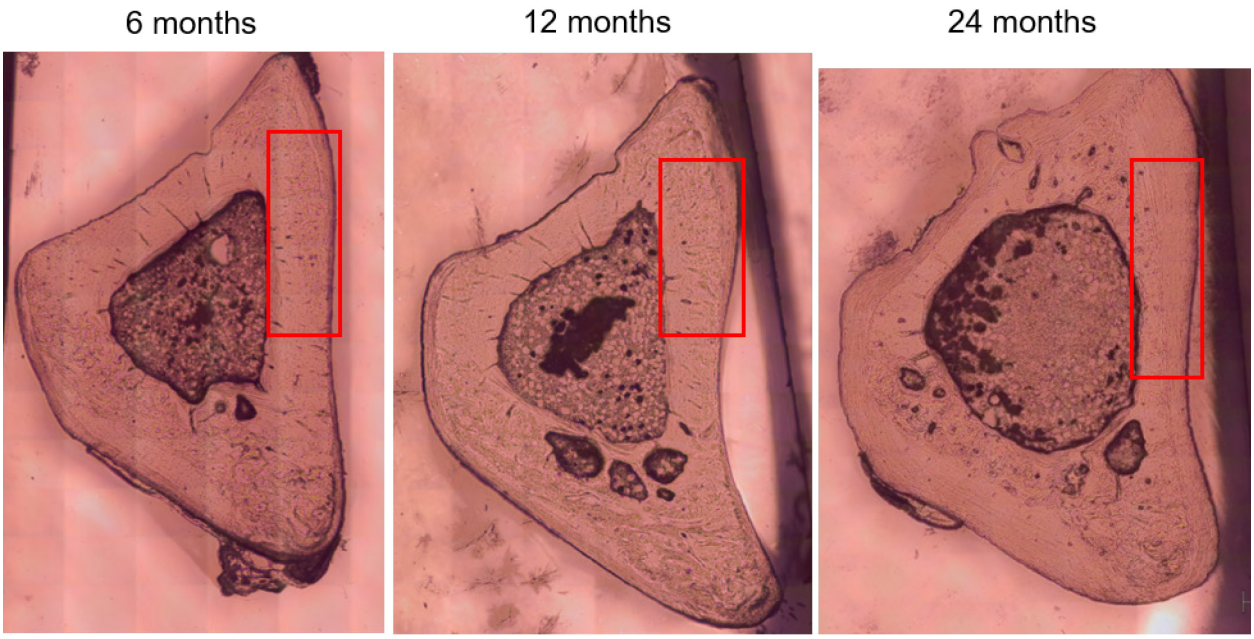


Figure 5: Images of a rat tibia specimen from each age group, with approximate indentation regions of interest represented by the red boxes. Note the increase in periosteal lamellae with age.

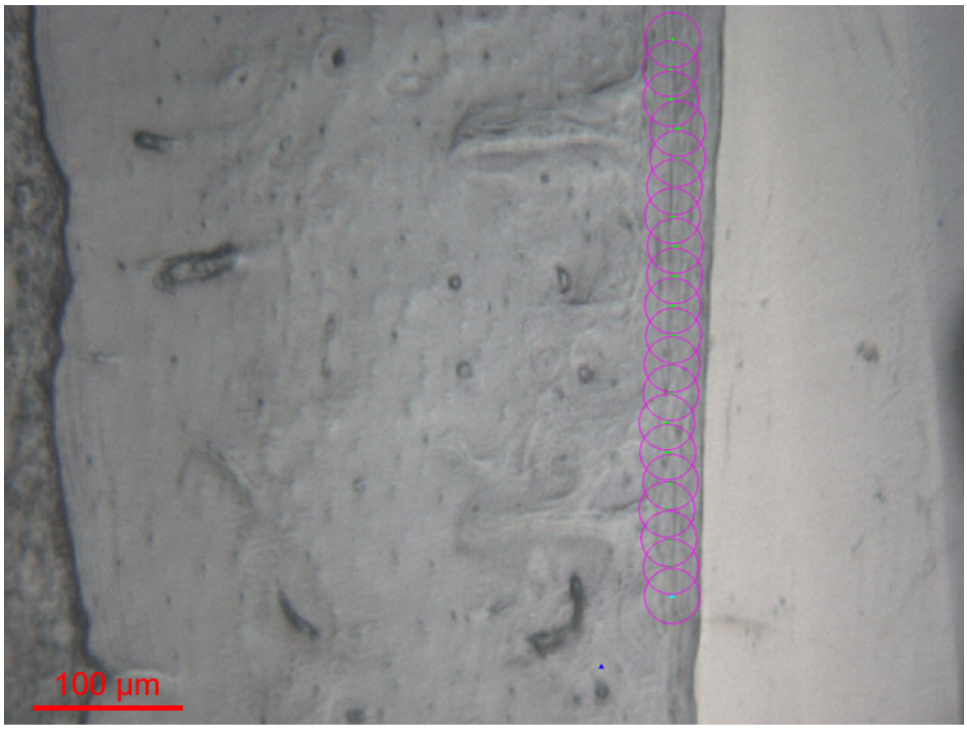


Figure 6: Screenshot from the indent site selection GUI, showing the selected locations of 20 Periosteal indents in one of the 6 month old rat tibia specimens. The 20 µm radius circles were used to ensure adequate interindent and indent-periosteal surface spacing.

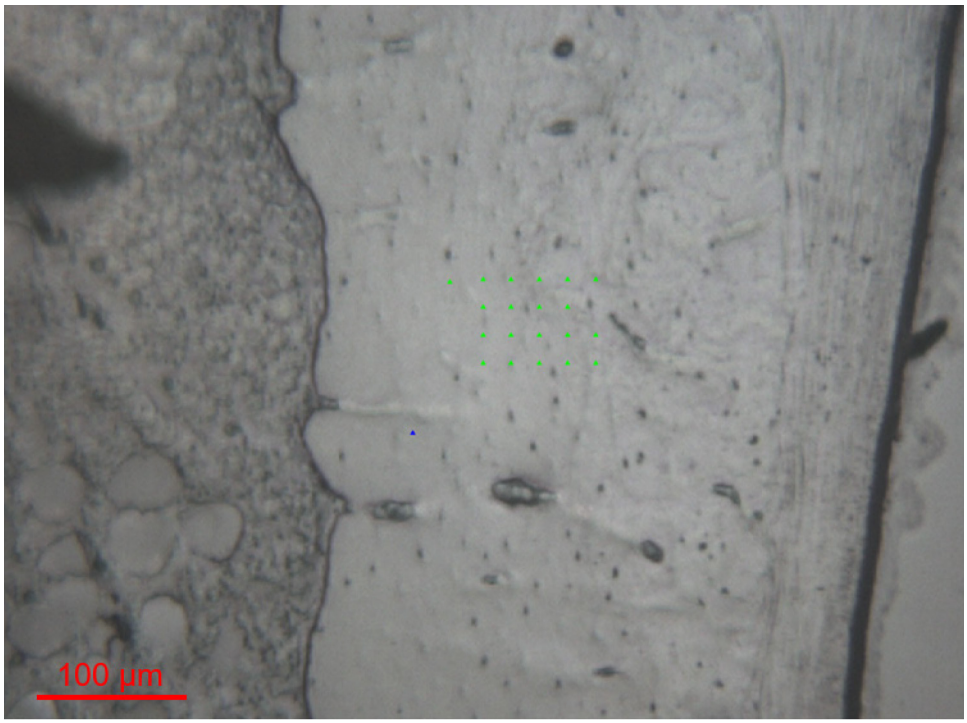


Figure 7: Screenshot from the indent site selection GUI, showing the selected locations (green triangles) of 20 Mid-cortex indents in one of the 12 month old rat tibia specimens. Mid-cortex indents were most often arranged as rectangular arrays, with large surface features avoided by manual relocation of problematic indents. Note the extra indent in the first row, which was moved from the second row, to avoid a surface feature.

and the effective elastic modulus of the system is known as the reduced modulus (E_R). Reduced modulus, measured contact stiffness (S), and indenter projected contact area (A_c) are related by

$$E_R = \frac{\sqrt{\pi}}{2\beta}\frac{S}{\sqrt{A_c}} \tag{1}$$

where β is a constant which depends upon indenter geometry. Once E_R has been calculated using Equation 1, E can be calculated by

$$\frac{1}{E_R} = \frac{1-\nu^2}{E} + \frac{1-\nu_i^2}{E_i} \tag{2}$$

where E_i and ν_i are Young's modulus and Poisson's ratio, respectively, of the indenter tip. Finally, ν is the Poisson's ratio of the indented material, which is often assumed. Measured contact stiffness, S, can be calculated from the initial portion of the unloading curve as dP/dh, for load on sample P and displacement into surface h. A_c is a function of indenter contact depth (h_c), which can be calculated from the shape of the indenter tip, but in practice the tip area function is generally determined by indenting a reference material. Contact depth, h_c, is less than the total displacement of the indenter tip for materials which exhibit sink-in, due to elastic displacement of the material's surface:

$$h_c = h - \varepsilon\frac{P}{S} \tag{3}$$

In Equation 3, ε is a constant based on indenter geometry. Hardness is calculated as the ratio of maximum load (P_{max}) to A_c at that peak load.

$$H = \frac{P_{max}}{A_c} \tag{4}$$

See Figure 8 for a schematic load vs. displacement plot for the indentation of a viscoelastic material.

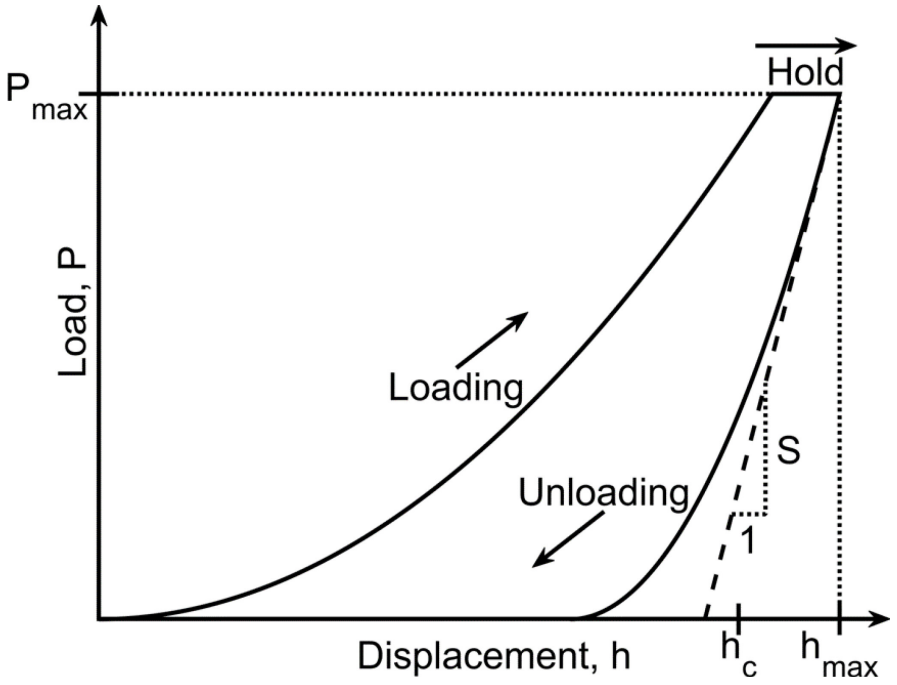


Figure 8: Schematic of indentation load (P) vs. displacement (h) plot for a viscoelastic material. Displacement is shown to increase during the hold at peak load, due to creep. Contact depth (h_c) is less than displacement, by an amount which depends upon the contact stiffness (S). S can be calculated from harmonic P and h data (CSM technique), or from the initial slope of the unloading curve.

2.3.2 Viscoelasticity

Viscoelastic materials exhibit both elastic and viscous mechanical properties. When subjected to deformation, part of the input energy is stored elastically and part is dissipated as heat. Viscoelastic materials demonstrate time-dependent behavior such as creep and stress relaxation. When a linear viscoelastic material is subjected to a harmonic stress, the resulting strain is also harmonic but is delayed relative to the input stress:

$$\sigma = \sigma_o \sin(\omega t) \tag{5}$$

$$\varepsilon = \varepsilon_0 \sin(\omega t + \delta) \tag{6}$$

were σ is stress, σ_0 is stress amplitude, ε is strain, ε_0 is strain amplitude, ω is angular frequency, t is time, and δ is the amount of phase lag between input stress and resulting strain. See Figure 9 for a schematic illustration of the relation between harmonic load and displacement in a viscoelastic material. The stress-strain relationship of the viscoelastic material under harmonic loading can be described by the complex modulus (E*):

$$E^* = E' + iE'' \tag{7}$$

where $i = \sqrt{-1}$ and

$$E' = \frac{\sigma_o}{\varepsilon_0}\cos(\delta) \tag{8}$$

$$E'' = \frac{\sigma_o}{\varepsilon_0}\sin(\delta) \tag{9}$$

E′ and E″ are known as the storage modulus and loss modulus, respectively. E′ is in-phase with the input stress and describes the elastic behavior of the material, while E″ is 90° out-of-phase and describes its viscous behavior.

2.3.3 Dynamic Indentation

E′ and E″ of a viscoelastic material can be measured by nanoindentation through the use of the continuous stiffness measurement (CSM) technique. In CSM a small

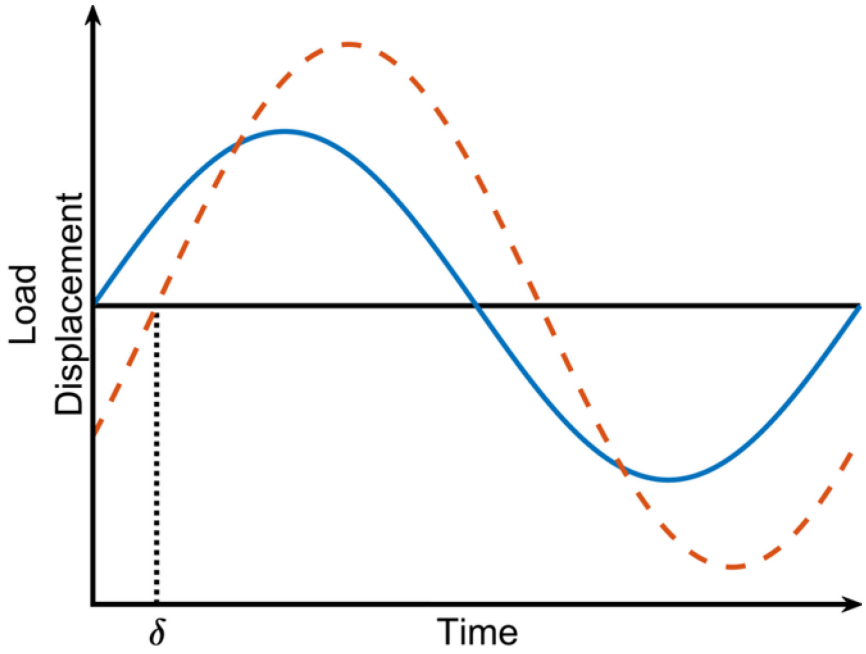


Figure 9: Schematic of harmonic loading (blue) and the resultant phase-delayed displacement (orange) of a viscoelastic material. Note that the phase angle (δ) is the amount of lag between the load and displacement waveforms.

harmonic load is superimposed on the much larger load required to drive the indenter into the sample. Contact stiffness can be continuously measured as the ratio of harmonic load amplitude to harmonic displacement amplitude. In practice, a lock-in amplifier is used to measure S and δ. Like in Equation 7, S can be split into in-phase elastic (K_s) and out-of-phase viscous (ωC_s) components:

$$S^* = K_s + i\omega C_s \tag{10}$$

Through elastic-viscoelastic correspondence and Equation 1, E_R^* and S^* are related by

$$E_R^* = \frac{\sqrt{\pi}}{2\beta}\frac{S^*}{\sqrt{A_c}} \tag{11}$$

Using Equations 7 and 10 and separating the real (elastic) and imaginary (viscous) terms we have

$$E_R' = \frac{\sqrt{\pi}}{2\beta}\frac{K_s}{\sqrt{A_c}} \tag{12}$$

$$E_R'' = \frac{\sqrt{\pi}}{2\beta}\frac{\omega C_s}{\sqrt{A_c}} \tag{13}$$

where E_R' and E_R'' are reduced storage modulus and reduced loss modulus, respectively. Again, these reduced moduli represent the combined behavior of the indenter tip and sample together. How can just the properties of the sample be determined? The elastic solution is given by Equation 2, so

$$\frac{1}{E_R'} = \frac{1-\nu^2}{E'} + \frac{1-\nu_i^2}{E_i'} \tag{14}$$

The diamond indenter tip is not viscoelastic, so omitting the term in Equation 2 for the indenter tip gives:

$$\frac{1}{E_R''} = \frac{1-\nu^2}{E''} \tag{15}$$

Solving Equations 14 and 15 for E′ and E″ and using $E_i^{'}$ = E_i since the tip is not viscoelastic gives:

$$E' = (1-\nu^2)\left(\frac{1}{E_R'} - \frac{1-\nu_i^2}{E_i}\right)^{-1} \tag{16}$$

$$E'' = (1-\nu^2)E_R'' \tag{17}$$

Additionally, the material viscoelastic phase angle can be calculated by

$$\delta = \tan^{-1}\left(\frac{E''}{E'}\right) \tag{18}$$

2.3.4 Correction for Instrument Dynamics

To accurately measure E′ and E″, it is necessary to correct for the dynamics of the instrument itself. The harmonic motion of the instrument can be modeled as a damped harmonic oscillator. The equation of motion of a damped harmonic oscillator is

$$mh'' + Ch' + Kh = F\,cos(\omega t) \tag{19}$$

where m is the oscillator mass, h is displacement, C is the damping coefficient, K is the stiffness coefficient, F is the driving force with angular frequency ω, and t is time. The particular solution of this equation of motion is:

$$h(t) = \frac{F}{S}\cos(\omega t - \delta) \tag{20}$$

where harmonic stiffness, S, and phase delay, δ, are given by:

$$S = \sqrt{(K - m\omega^2)^2 + C^2\omega^2} \tag{21}$$

$$\delta = \text{atan2}(C\omega, K - m\omega^2) \tag{22}$$

with atan2 being the 4-quadrant inverse tangent function.

Figure 10 is a spring and dashpot mechanical model of the indenter-sample system. The sample is modeled by a spring of stiffness K_s in parallel with a dashpot with damping coefficient C_s. The instrument is similarly described by a spring of stiffness K_i

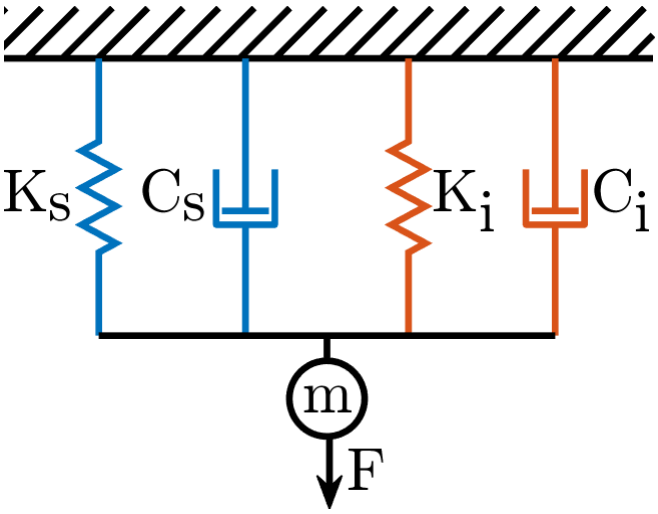


Figure 10: Spring and dashpot damped harmonic oscillator model of indenter-sample contact. The instrument and the sample each contribute to the total measured stiffness and damping. The sample (blue elements with s subscripts) and instrument (orange elements with i subscripts) are in parallel, and each consists of a spring with stiffness K in parallel with a dashpot with damping coefficient C.

in parallel with a dashpot with damping coefficient C_i. Because the sample and instrument elements are also in parallel,

$$K_m = K_i + K_s \tag{23}$$

$$C_m = C_i + C_s \tag{24}$$

where K_m and C_m are the stiffness and damping coefficients of the combined indenter-sample system. Using

$$S\cos(\delta) = K - m\omega^2 \tag{25}$$

$$S\sin(\delta) = \omega C \tag{26}$$

it is possible to the solve for K_s and ωC_s as

$$K_s = S_m\cos(\delta_m) - S_i\cos(\delta_i) \tag{27}$$

$$\omega C_s = S_m\sin(\delta_m) - S_i\sin(\delta_i) \tag{28}$$

where S_m and δ_m are the measured harmonic stiffness and phase angle with the indenter in contact with the sample. S_i and δ_i are the same values, except when the indenter is not in contact with the sample.

Thus, if we want to calculate K_s and ωC_s for use in Equations 12 and 13 to calculate $E_R^{'}$ and $E_R^{''}$, we can use two measurements of S and δ:

1) Indenter oscillating in contact with the sample → S_m and δ_m
2) Indenter oscillating in free space → S_i and δ_i

Note that it is not necessary to know the mass m in the dynamical model of the system in order to use Equations 27 and 28.

2.3.5 Summary of Calculations

In summary, the steps to calculate E′, E″, and H were:

1) Measure P, h, S_m, δ_m, S_i, and δ_i
2) Calculate K_s and ωC_s from Equations 27 and 28
3) Calculate h_c from Equation 3 (using K_s in the place of S)

4) Calculate A_c from a previously measured tip area function ($A_c = f(h_c)$)
5) Calculate $E_R^{'}$ and $E_R^{''}$ from Equations 12 and 13
6) Calculate E′, E″, and H from Equations 14, 15, and 4

Input values for the Berkovich diamond tip were:

- $\varepsilon = 0.75$
- $\beta = 1.034$
- $E_i^{'} = 1143$ GPa
- $\nu_i = 0.3$

The Poisson's ratio of bone used was $\nu = 0.3$.

2.4 Indentation Method

The first stage of this study was the development of an indentation method which could accurately measure the viscoelasticity of bone and its potential change with age. The method was required to work equally well in the Wet and Dry hydration conditions. Important features of the method were:

1) *Instrument characterization and correction for each indent*: As discussed in the Correction for Instrument Dynamics section, E′ and E″ cannot be accurately determined without an accurate characterization of the instrument's dynamics (S_i and δ_i). This was accomplished by lifting the indenter from the surface of the sample after each indent and oscillating it in free space. The instrument's dynamics vary with position within the indenter's range of travel and could potentially change with time over the course of months of experiments. Additionally, it was unknown to what extent the instrument's dynamics would be sensitive to immersion in PBS in the Wet tests. For these reasons, it was decided that the most accurate method would be to measure S_i and δ_i for each indent, near the surface of each sample.
2) *A relatively long hold period at peak load* (2 minutes): Indents in bone, as with other viscoelastic materials, demonstrate indenter creep. After loading, this creep

can be rapid and then decreases progressively over time. There are a couple of advantages to a longer hold time. First, the data are more consistent during the more steady-state situation of minimal creep. Second, noise in the data can be averaged out over longer data acquisition times.

3) *Increased harmonic amplitude* (4 nm): The larger the amplitude, the better the signal-to-noise ratio of S and δ from the lock-in amplifier. However, the lock-in amplifier works by assuming that harmonic load and harmonic displacement are perfect sine waves, as depicted in Figure 9. This is true only if S is constant, which is a good approximation for small harmonic amplitudes. However, as harmonic amplitude increases, the assumption of constant S begins to break down and the accuracy of the S and δ measurements decreases. The default harmonic amplitude of the NanoIndenter XP is 2 nm. The large indent depths and long hold times used in this study allowed the harmonic amplitude to be increased without sacrificing measurement accuracy.
4) *Quick unload segment* (1 s): Viscoelastic creep occurring during unloading can lead to an overestimation of unload stiffness. In cases where creep outpaces the unloading rate, the measured unload stiffness can even be negative. The primary results in this study were derived from the hold segment at peak load, using the CSM technique. The unloading data were used for comparative purposes. In this indentation method, creep during unloading was avoided by the long hold period, which allowed creep to die down, and by a rapid unloading rate.
5) *No thermal drift correction*: In nanoindentation, volumetric changes due to thermal expansion or contraction within the sample or the instrument itself can lead to errors in measured displacements. Some indentation methods attempt to correct for thermal drift by employing a hold segment after partially unloading the indenter. Any displacement changes during this hold segment are assumed to be due to thermal drift. This is not a good assumption with viscoelastic materials, because viscoelastic materials demonstrate time-dependent behavior. Many viscoelastic materials partially recover after the indenter is retracted, i.e., the

indentation impression gets smaller. For example, the Dry indents in this study were usually clearly visible while the Wet indents were often not, as the more viscoelastic Wet indents recovered to a greater degree than the Dry indents. Thermal drift correction would be especially problematic for viscoelastic creep studies.

The steps in the developed indentation method were:

1) Approach the surface.
2) Load until the displacement target is reached. Loading was exponential, at a $\dot{P}/P$ rate of 0.5 s^{-1}, where $\dot{P}$ is the loading rate and P is the load on sample. A constant $\dot{P}/P$ results in a constant indentation strain rate when the hardness does not vary with depth.
3) Turn CSM on (i.e. begin indenter oscillation) with a harmonic displacement target of 4 nm and an oscillation frequency of 45 Hz.
4) Switch CSM to load control when the 4 nm harmonic displacement target was reached.
5) Hold 2 minutes. This is the primary data acquisition segment.
6) Turn CSM off (i.e. stop indenter oscillation).
7) Hold 5 seconds.
8) Increase load to the previous maximum to compensate for CSM being turned off.
9) Hold 5 seconds.
10) Unload the indenter tip from the sample in ≈1 second.
11) Back the indenter tip off 1 μm from the surface of the sample.
12) Turn CSM on with a 115 μN harmonic load and a frequency of 45 Hz.
13) Hold 15 seconds. This is the instrument dynamics characterization segment.

Figures 11-15 illustrate important features of the indentation method. Figure 11 is an example plot of Load vs. Time, for the period of contact with the sample. Figure 12 is a sample Displacement vs. Time plot, shown from first contact with the sample surface to the end of the test. The period of negative displacement is when the indenter was

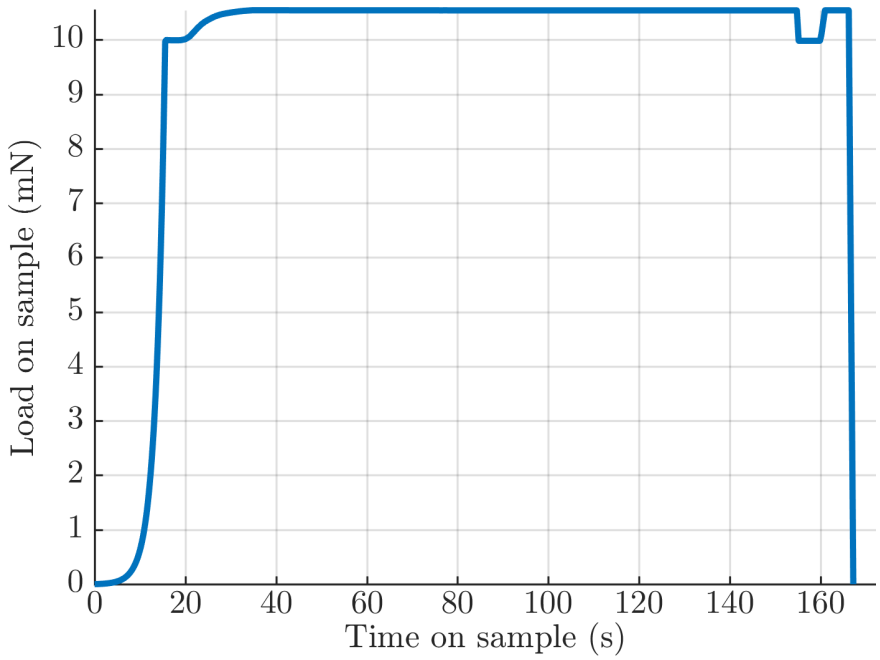


Figure 11: Example of indentation Load vs. Time during the period of contact with the sample. First, load was increased until the displacement target was reached. The small increase in load after the initial loading segment is due the start of harmonic loading. After the harmonic displacement target was reached, load was held constant for 2 minutes, for the primary data acquisition period. The small load drop at the end of the hold segment is due to the end of harmonic loading. Load was then increased to the previous maximum, held 5 s, and finally unloaded in 1 s.

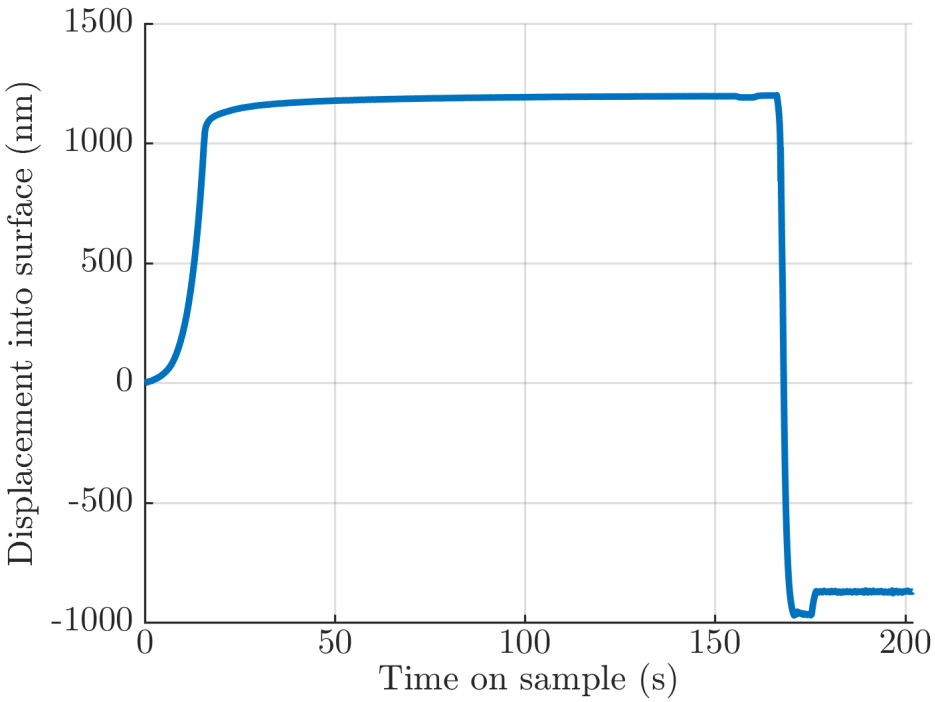


Figure 12: Example of indentation Displacement vs. Time, plotted from contact with the sample surface to the end of the test. Note the period of negative displacement at the end of the test. After each indent, the indenter was backed off of the sample 1 μm and oscillated in free space, in order to characterize and correct for the instrument's contribution to the measured data.

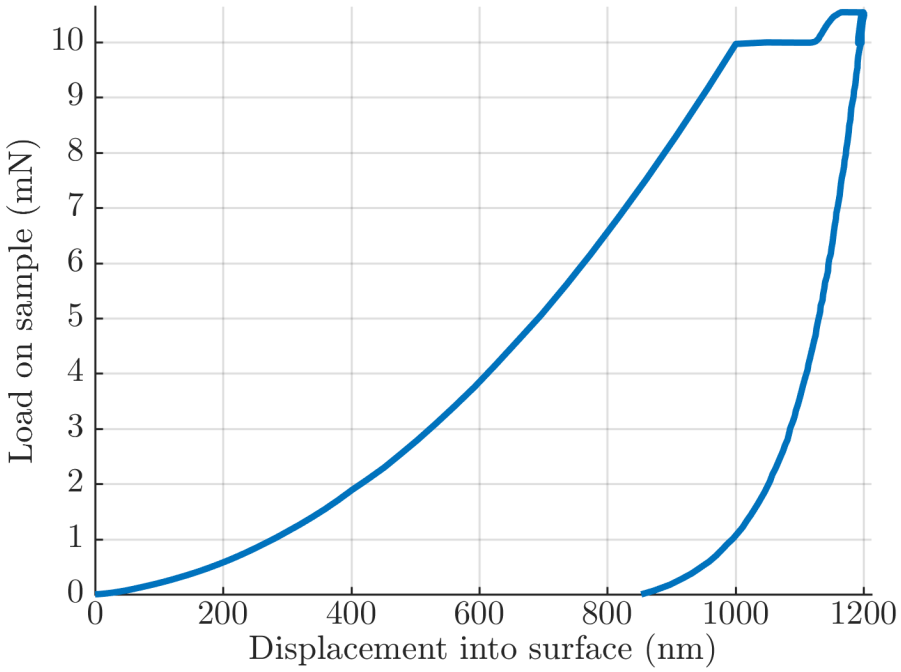


Figure 13: Example indentation Load vs Displacement plot. In this human femur indent, the end-of-loading displacement target was 1 μm. Viscoelastic creep is seen as the change in displacement after loading. The second, smaller increase in load is due to the start of harmonic loading.

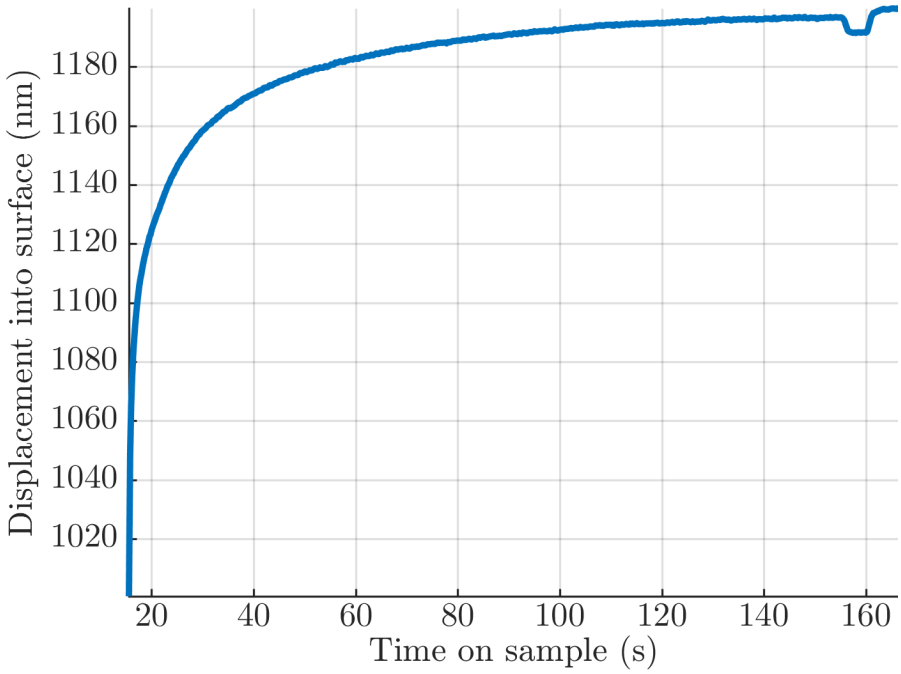


Figure 14: Example indentation Displacement vs. Time plot for the period between loading and unloading. The increase in displacement is predominately due to viscoelastic creep, with a small contribution from harmonic displacement. The creep rate progressively decreases throughout the 2 minute hold period, and is small during the primary data acquisition period, the last minute of the hold segment. The small load decrease towards the end is due to the end of harmonic loading.

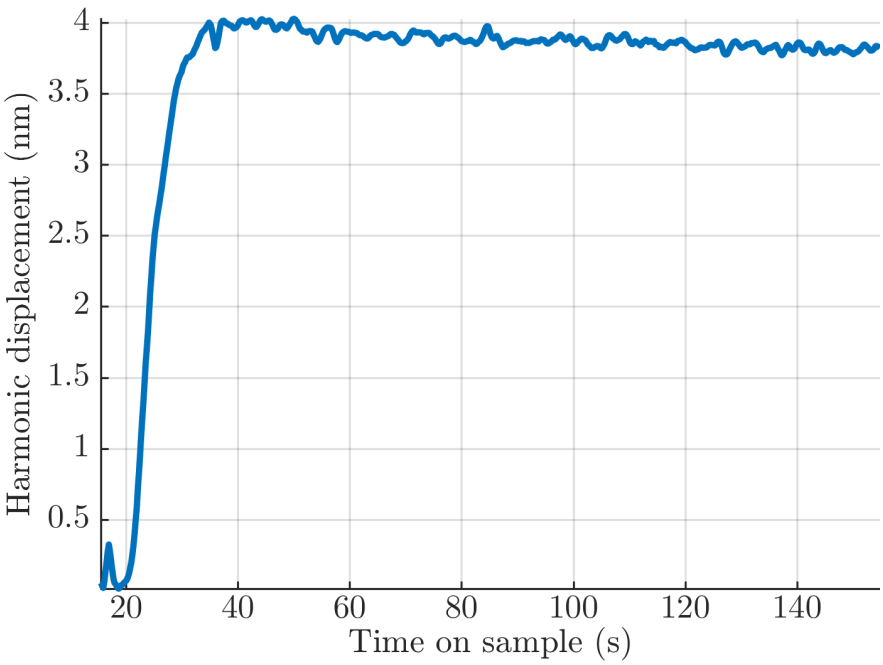


Figure 15: Example indentation Harmonic displacement vs Time plot for the period of harmonic loading, when in contact with the specimen. First, the harmonic load was increased until the harmonic displacement target (4 μm) was reached. Harmonic load was then held constant for the duration of the 2 minute hold.

retracted and oscillated in free space in order to measure S_i and δ_i. Figure 13 is a plot of Load vs. Displacement, during indenter contact with the sample. Figure 14 is a plot of Displacement vs. Time but only from the end of loading to the start of unloading. Lastly, Figure 15 is an example plot of Harmonic Displacement vs. Time, shown during the time CSM is on during the hold at peak load. The oscillation frequency used in this study (45 Hz) was selected for experimental, not physiological reasons, as it was not clear what the most physiologically relevant oscillation frequency would be regarding bone fracture.

As seen in Figure 14, indenter creep into the sample was large immediately after loading was terminated and progressively decreased throughout the 2 minute hold segment. However, not all of the displacement change seen in Figure 14 was due to creep; some was due to turning on CSM in step 4 and the resulting increase in harmonic displacement (from 0 to 4 nm, as seen in Figure 15). Viscoelastic creep can also be seen in Figure 13 (refer to Figure 8 for a schematic P-h plot). The increasing load from turning on the CSM is responsible for the smaller second increase in load seen in Figure 13. It can also be seen on the Load – Time plot, Figure 11. The short, temporary load drop prior to unloading seen in Figure 11 is described by indentation method steps 6-9. Prior to unloading the indenter oscillation was stopped, meaning that load on sample decreased. Load was then increased back to P_{max}, so that the unloading segment occurred at P_{max} and h_{max}.

As discussed in the Correction for Instrument Dynamics section, calculation of E′ and E″ requires harmonic stiffness and phase angle values for when the indenter is in free space (S_i, δ_i). These values were calculated by averaging the data from the last 5 seconds of the 15 second free-space oscillation step (#13). The indentation parameters (E′, E″, H, etc.) were calculated continuously during the 2 minute hold segment (step #5). The final values were taken as the averages over the last minute of the hold period. By averaging the data over a relatively long time interval, variability due to noise in the data was minimized.

2.5 Hydration System

To generate physiologically accurate mechanical data, bone specimens must be tested in a hydrated state. For the Wet condition nanoindentation experiments, the bone specimens were fully immersed in 0.01 M phosphate buffered saline solution (PBS, Sigma-Aldrich P3813, Saint Louis, MO). PBS solution was used for the hydrated tests, as opposed to plain water, in order to prevent mineral dissolution from the surface of the bone specimens. The components of the hydration system can be seen in Figure 16. The sample holder consisted of an inner sample puck surrounded by an outer hollow cylinder. Both components were stainless steel. The sample puck could slide vertically within the outer cylinder, which enabled the sample surface to be set a fixed distance from the top surface of the outer cylinder (1.3 mm). A polyurethane O-ring housed in grooves around the perimeter of the inner sample puck kept the PBS solution from leaking through the gap between the puck and the outer cylinder.

In order for the sample to remain immersed through the duration of an experiment, it was necessary to compensate for evaporative liquid loss. This was done by a syringe pump with liquid-level feedback. The syringe pump was homemade and powered by an Arduino microcontroller, which was connected to the indenter computer. The liquid level was measured using two probes and a voltage divider circuit, the schematics of which are shown in Figure 16. When the liquid level was lower than desired, the two probes were isolated and the measured voltage would be 5 V. However, when the liquid level was sufficient, the probes were electrically connected by the PBS solution and the measured voltage would be minimal. The liquid-level voltage was measured after the completion of each indent. Thus, the syringe pump was not active while an indent was in progress. The syringe pump was connected to the specimen holder via a small hole in the cylindrical outer ring (refer to Figure 16). The syringe tip was passed through a tapered round plug, which was then inserted into the hole. Thus, liquid was added to the sample well in a bottom-up fashion.

As mentioned earlier, the surface of the bone specimens was set to be 1.3 mm below the outer cylinder ring top surface. This value was limited by the total range of

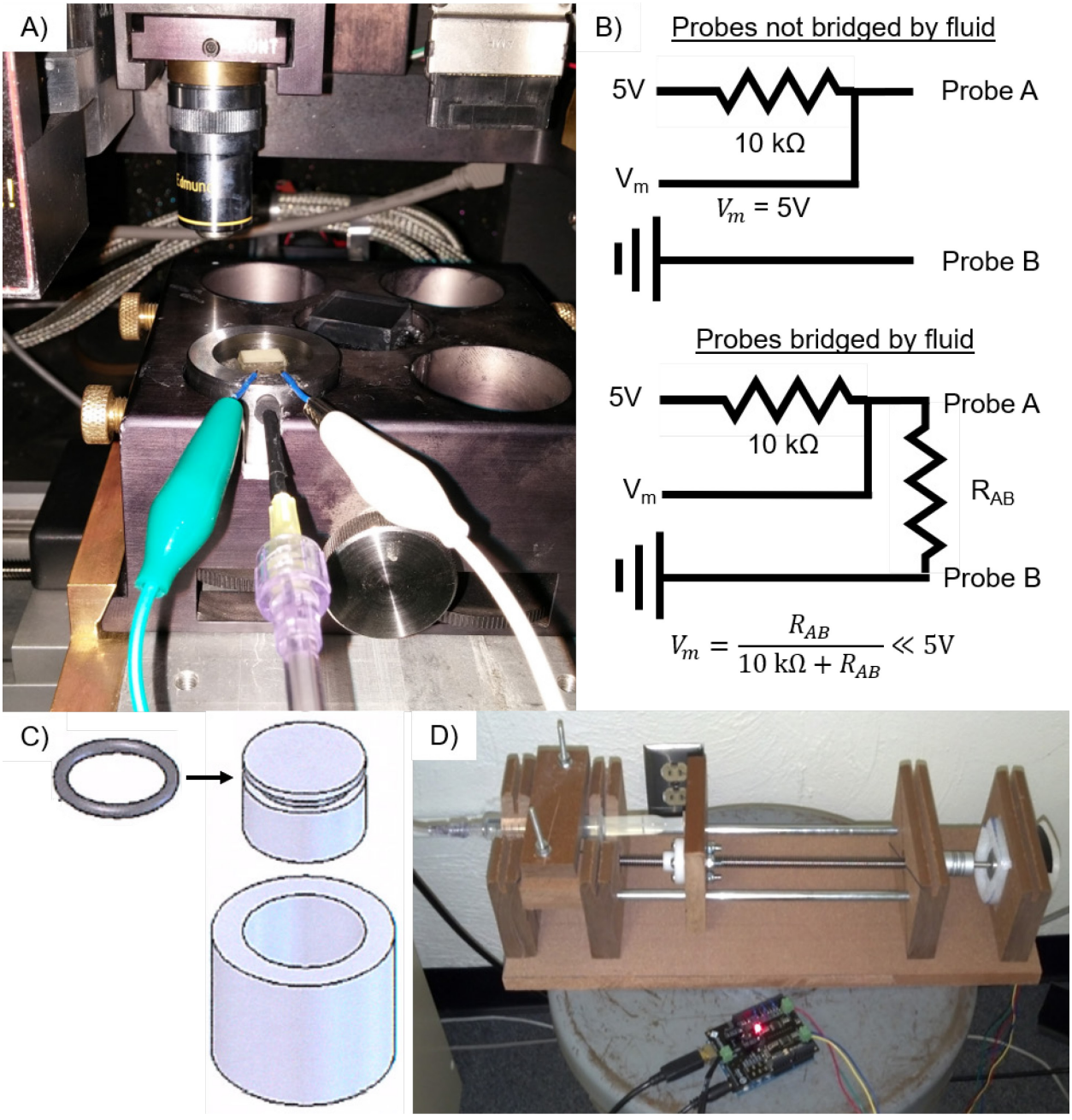


Figure 16: Hydration system: (A) Experimental setup prior to hydration (B) Voltage divider circuit used to regulate PBS solution level to ensure the sample stayed immersed (C) Sample holder schematic (D) Syringe pump

travel of the instrument (~2 mm). This 1.3 mm distance was set using the NanoIndenter XP's microscope. First, the outer ring was locked in place at the desired height, using a fixed-height reference sample (seen in the middle specimen holder in Figure 16). Next, the microscope focal point was lowered 1.3 mm and the inner sample puck's height was raised until the sample surface was in focus. Also, note that the specimen immersion depth was typically greater than 1.3 mm, as surface tension caused the PBS solution to dome-up slightly towards the center of the specimen holder.

2.6 Specimen Preparation

2.6.1 Human Femur

The human femur specimens were obtained from the Musculoskeletal Transplant Foundation (Edison, NJ), the Vanderbilt Donor Program (Nashville, TN), and the National Disease Research Interchange (Philadelphia, PA). Cortical SENB specimens (approximate size 25 x 5 x 2.5 mm^3) were cut from the lateral quadrant of the femoral mid-shaft. The SENB specimens were notched with a low-speed saw and then further sharpened with a razorblade lubricated with 1 μm diamond solution. Prior to fracture testing, the notched region of the specimens was imaged by μCT. After fracture testing, the specimens used for nanoindentation, ^{1}H NMR spectroscopy, HPLC, and qBEI were cut from the SENB specimen. The Transverse set of nanoindentation specimens was created by cutting ~3 mm thick cross-sections from the SENB specimens, away from the region of fracture. Comparably-sized Longitudinal nanoindentation specimens were created by sectioning along the long axis of the SENB specimens. Note that the qBEI and nanoindentation Transverse specimens were the same, with qBEI being performed first. The ^{1}H NMR specimens were created by cutting ~5 mm thick cross-sections. Lastly, a smaller segment (~2 x 2 x 2.5 mm^3) was cut for HPLC analysis.

The indentation surfaces were prepared by first grinding with successive grits (800, 1200, and 4000) of silicon carbide papers (EXAKT SiC grinding paper, EXAKT Technologies, Oklahoma City, OK). Next, the surface was polished by hand using a

synthetic cloth (South Bay Technology, Torrance, CA) and 0.05 μm aluminum oxide suspension (MasterPrep, Buehler, Lake Bluff, IL). Specimens were stored frozen in PBS-soaked gauze. For more information, these human femur sample preparation details are also reported in [54, 55].

2.6.2 Rat Bones

The male Fischer F344 rats used in this study were obtained from the National Institute on Aging. After being euthanized at either 6, 12, or 24 months of age, the following bones were collected from each rat: both femora, right radius, and left tibia. The left femur was notched and used for fracture and ^{1}H NMR, the un-notched right femur for μCT, the right radius for HPLC, and the left tibia for nanoindentation. The left femur was notched mid-shaft, on the posterior side. This was done using a low-speed circular saw with a thin diamond-embedded blade. The notch was then further sharpened with a razor blade lubricated with a 1 μm polycrystalline diamond solution. The nanoindentation specimens were made by transversely sectioning a segment from the left tibia mid-shaft. This segment was then dehydrated in ethanol and subsequently embedded in PMMA. Refer to Nyman et al. for a full description of the embedding procedure used [58]. These specimens were polished in a similar manner as described for the human femur specimens: successive grits of SiC paper, followed by polishing with 0.05 μm alumina suspension. The rat bone sample preparation procedures were also published previously [56].

2.7 Nanoindentation Experimental Procedure

2.7.1 Human Femur

The human femur indentation experimental procedure involved the following steps:

1) Remove the specimen from the freezer.
2) Mount the specimen on the sample puck using cyanoacrylate adhesive.

3) Gently clean the sample surface and indentation tip with a methanol-moistened wipe (Kimwipe, Kimberly-Clark Professional).
4) Adjust specimen height (and outer cylinder height if a Wet test, as described in the Hydration System section).
5) Select and image the indent locations.
6) If a Wet test, then turn on the syringe pump and hydrate the sample.
7) Begin the indentation experiment after a 2 hour delay.
8) After the test, image the indent locations again. If a Wet test, then remove the PBS solution and clean the sample surface first.
9) Return the specimen to the freezer.

The 2 hour delay (step #7) served two purposes. First, it allowed the specimens to become fully hydrated in the Wet experiments. Second, it allowed the system to reach thermal equilibrium. As discussed in the Indentation Method section, thermal contraction/expansion can result in measured displacement errors. Comparisons of before and after images confirmed that the indents were placed accurately. However, note that after images were missing in some cases. Additionally, note that the residual Dry indentations were larger and more distinct than the Wet ones, presumably due to greater viscoelastic recovery in the Wet case.

2.7.2 Rat Tibia

The rat tibia indentation procedure was similar to that of the human femur experiments, with one important difference: a 24 hour rehydration step was added. Unlike the human femur specimens, the rat tibia specimens were dehydrated in ethanol and embedded in PMMA. A preliminary test on one of the rat tibia specimens revealed that the 2 hour delay used with the human femur specimens was insufficient. Specifically, E′ and H were seen to decrease with time for ~10 hours. Hydration of dried bone specimens is known to cause volumetric expansion, and PMMA can also swell due to water absorption. This volumetric change could be seen in the displacement data during the peak-load hold segment. As a viscoelastic material, displacement is expected

to increase during this hold segment, due to creep. However, for the first ~3 hours of the test, displacement was seen to decrease during the hold segment, presumably due to volumetric expansion of the specimen. While a rehydration time > 10 hours would have been sufficient, the 24 rehydration time was chosen for experimental convenience; it was easiest to set up an experiment at the same time each day. It was verified that there was no evidence of a change in the rat tibia indentation data with time (Wilcoxon signed rank test on the distribution of Mid-cortex indent – indent index correlation values). Note that since the rat tibia specimens were not stored frozen, the indentation procedure omitted steps 1 and 9. Finally, note that the Wet indents were generally not visible in the indenter microscope. The Dry indents were visible, albeit quite small (see Figure 4).

2.8 Fracture, Compositional, and Structural Data

The procedures for the measurements described in this section have been published previously, in greater detail there are described here. Information regarding the human femur fracture, μCT, ^{1}H NMR spectroscopy, and HPLC are given in Granke et al. (2015) [54], while the qBEI details are given in Granke et al. (2016) [55]. For information regarding the rat bone measurements refer to Uppuganti et al. [56].

2.8.1 Fracture – Human Femur

The SENB cortical femur specimens (~25 x 5 x 2.5 mm^3) were subjected to 3-point bending load-to-failure testing, according to ASTM Standard 1820 guidelines. Crack propagation was in the transverse direction, i.e., normal to the osteonal direction. The fracture protocol was displacement-controlled and consisted of repeated load-unload-dwell segments until failure. An example Force vs. Load-line displacement plot can be seen as Figure 17, part B. A J-integral value (J) was calculated for each unloading segment. Thus, J was calculated as a function of crack extension (Δa). The fracture parameters K_{init}, J-integral, and K_{grow} were then calculated from the J vs. Δa

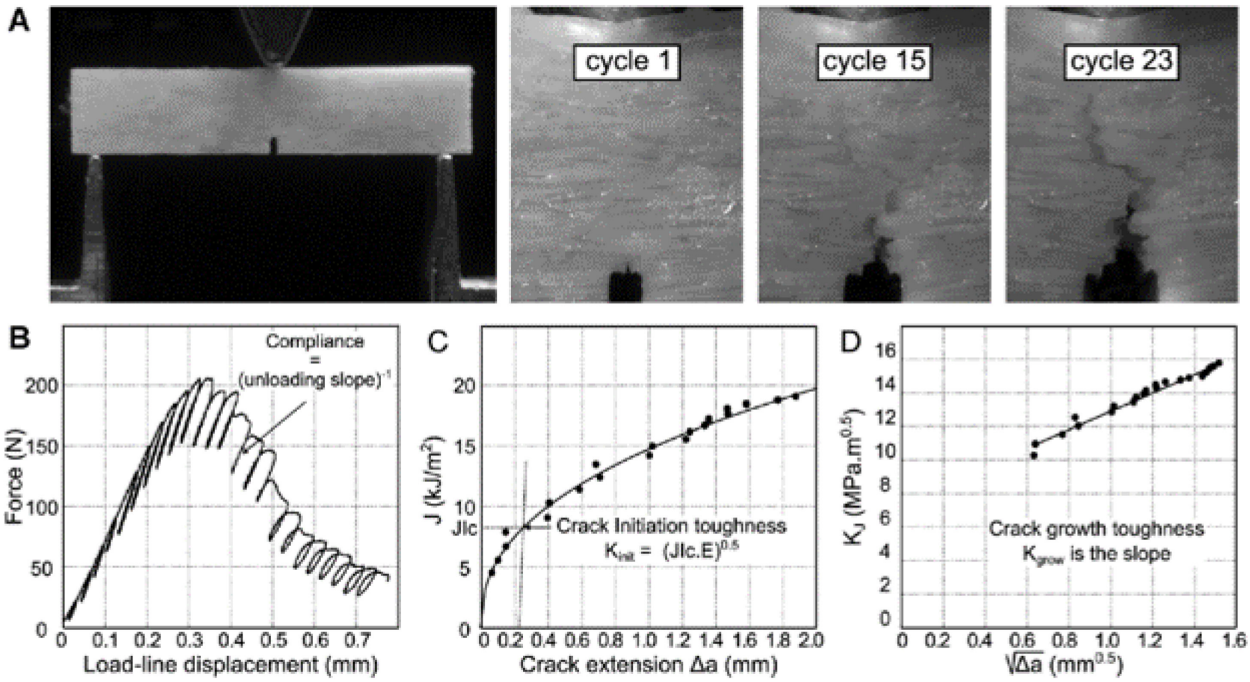


Figure 17: The notched human femur SENB specimens were subjected to 3-point bending fracture until failure (A). A progressive, displacement-controlled load-unload-dwell protocol was used (B). J and K values were calculated for each unloading segment (C). K_{init} was calculated as the equivalent K value at the intersection of a 0.2 mm offset line with a fit to the J-Δa data, J-integral as the value of J at failure, and K_{grow} as the slope of K vs. $\Delta a^{1/2}$ (D). [54]

data. J-integral was simply the value of J at failure. Next, the J values were converted into the stress intensity factor at the crack tip (K_J) from the K-J equivalence equation:

$$K_J = \sqrt{J\left(\frac{E}{1-\nu^2}\right)} \tag{29}$$

where E is Young's modulus, calculated from the initial loading stiffness, and ν is Poisson's ratio (0.3). K_{init} was calculated from Equation 29 for J = J_{Ic}, where J_{Ic} was the point of intersection between a curve fit to the J vs. Δa data and a 0.2 mm offset line. K_{grow} was calculated as the slope of K_J vs $\sqrt{\Delta a}$. Note that K_{grow} could not be calculated for specimens which fractured in a brittle fashion (4 specimens). The calculation of K_{init} and K_{grow} are illustrated in Figure 17 parts C and D, respectively. Thus, K_{init} is a measure of stress intensity at the onset of cracking, and K_{grow} describes the rise in stress intensity with stable crack propagation. Note that in order to observe more cycles before failure, a smaller initial crack than recommended by ASTM E1820 was used. Due to this smaller initial crack, the fracture parameter values reported in this study tend to be higher than are reported in the literature for human cortical bone.

2.8.2 Fracture – Rat Femur

The notched rat femora were monotonically loaded in a 3-point bending configuration until failure. The critical stress intensity at the initial notch (Kc) was calculated from the equations found in Ritchie et al. [59]. These equations are based on the solution for a circumferential through-wall crack in a cylindrical pipe:

$$K_I = F_b \sigma_b \sqrt{\pi R_m \Theta} \tag{30}$$

where F_b is a geometry factor, σ_b is the applied bending stress, R_m is the mean radius of the bone, and Θ is the half-crack angle. During testing, there was a period of stable crack growth preceding unstable crack growth at failure. See Figure 18 for images from the rat femur fracture testing. The angles shown are for the initial notch and point of

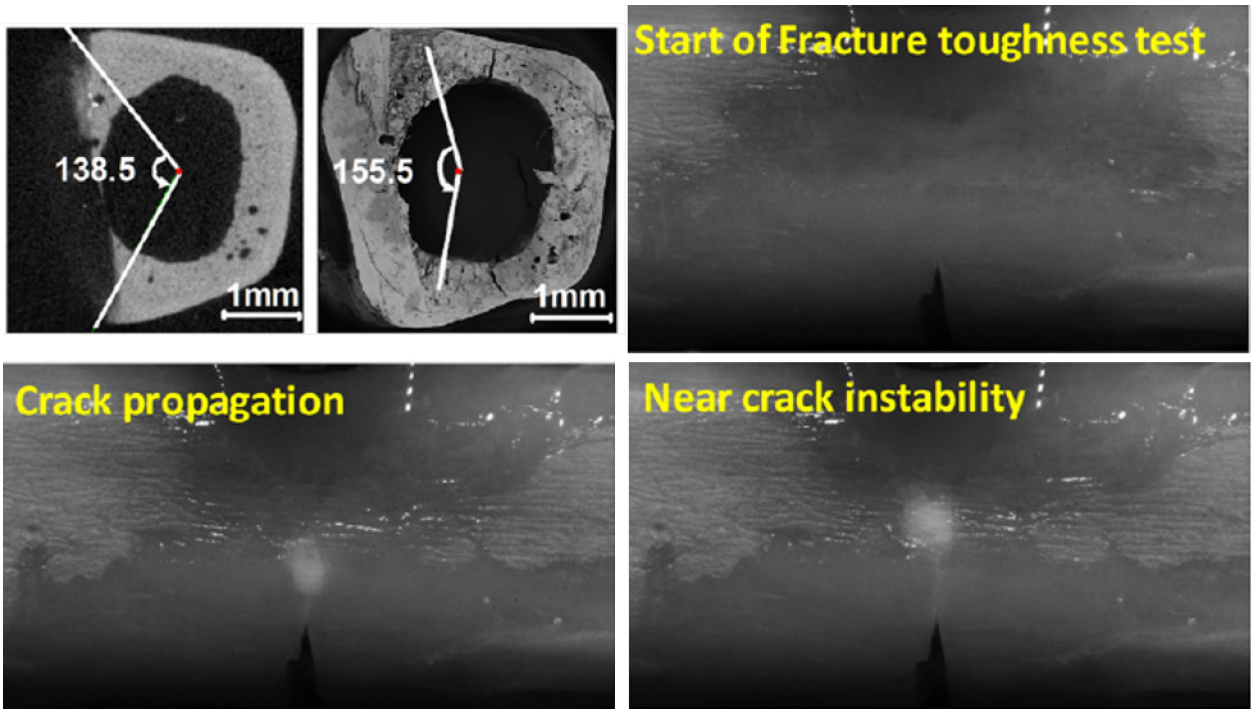


Figure 18: The notched, whole rat femora were loaded monotonically in 3-point bending until failure. A region of stable crack propagation preceded unstable crack growth. The angles shown (upper left image) are for the angles of the initial crack and the onset of unstable crack growth, respectively. [56]

cracking instability, respectively from left to right. Also calculated for the fracture tests was CrackingToughness:

$$CrackingToughness = \frac{3W_f}{Ct.Ar * Span} \quad (31)$$

where W_f is work-to-fracture (area under force vs. displacement curve), Ct.Ar is the cortical cross-sectional area, and Span is the 3-point bending apparatus span length (16 mm). Thus, CrackingToughness has units of energy per volume. Dividing W_f by volume (Ct.Ar*Span), rather than cross-sectional area (Ct.Ar), was done to facilitate comparisons with fracture tests performed on the rat radii (presented in Uppuganti et al. but not here) [56]. Dimensional measurements such as Ct.Ar, moment of inertia, R_m, notch angle, etc., were derived from μCT measurements.

2.8.3 μCT

The SENB human femur specimens were imaged by μCT (mCT50, Scanco Medical AG, Brüttisellen, Switzerland) prior to fracture testing. The scanned region was 1.3 mm wide, centered on the notch, and the voxel size was 5 μm. The volume imaged in front of the notch was used to calculate tissue mineral density (TMD) and intracortical porosity (Porosity). Attenuation coefficients were converted into volumetric mineral density using a calibration phantom of hydroxyapatite (HA) and the manufacturer's beam hardening correction. Voxels with a volumetric bone mineral density greater than 660 mgHa/cm^3 were assigned to the matrix, and TMD was calculated as the average mineral density of the matrix voxels. Porosity was calculated as the fraction of voxels with a density less than 600 mgHa/cm^3. Also, note that the original crack size used in the fracture calculations was measured from the μCT scans.

In the rat bone experiment, μCT scans (same instrument) were performed on the un-notched right femora. The region scanned was a 4 mm long segment of the femur mid-shaft, and the voxel size was 10 μm. The TMD and Porosity calculations were the same as above. Voxels with a mineral density greater than 900.5 mgHa/cm^3 were

assigned to the matrix, while a lower threshold of 794 mgHa/cm^3 was used for the calculation of Porosity.

2.8.4 ^{1}H NMR Spectroscopy

Water in bone can be located in pores or inside the bone matrix itself, where it interacts with the collagen molecules through hydrogen bonding. It is possible to differentiate between pore water and bound water, based on transverse relaxation time constant (T_2), as measured by ^{1}H NMR. The specimens, along with a reference volume of water, were inserted into a low proton, loop-gap style radiofrequency coil (RF) and placed in a 4.7 T horizontal-bore magnet (Varian Medical Systems, Santa Clara, CA). Upon 90°/180° RF pulses (human femur specimens: ~5/10 μs, rat femur specimens: ~9/18 μs), Carr-Purcell-Meiboom-Gill measurements with 10,000 echoes were collected at 100 μs spacing. The echo magnitudes were fitted with multiple exponential decay functions, to yield the T_2 spectrum. For the human femur specimens, the water types were distinguished by the following T_2 reaction times: 150 μs to 1 ms (bound water), 1 ms to 600 ms (pore water), and 600 ms to 10 s (reference). The volumes of bound and pore water were calculated as the ratio of their respective integrated T_2 spectrum areas to that of the known reference volume. Finally, these bound water and pore water volumes were divided by the specimen volume to calculate BoundWater and PoreWater volume fractions, respectively. For the rat femur the threshold T_2 time between pore water and reference water was 1 ms, and the T_2 time ranges used were otherwise the same. Also, note that BoundWater and PoreWater have volume fraction units (%) for the human femur specimens, while for the rat femur specimens they are in units of mol/L.

2.8.5 HPLC

Pentosidine crosslinking concentration (PE) was determined by HPLC for samples taken from the human femur SENB specimens. First, the specimens were demineralized in 20% EDTA and then hydrolyzed in 6N HCL. The acid was then removed using a vacuum concentrator (Savant SPD131DDA SpeedVac with cold trap,

ThermoScientific, Rockford, IL). The hydrolysate was suspended in ultrapure water, divided evenly, and dried in a vacuum concentrator. Half of the specimen was used to measure pentosidine concentration, while the other half was used to measure collagen concentration via hydroxyproline assay.

For the pentosidine assay, the residue was resuspended in a solution containing an internal standard (pyridoxine). The solution was filtered, diluted with buffer (0.5% (vol/vol) heptafluorobutyric acid (HFBA) in 10% acetonitrile), and injected into the HPLC system (Beckman-Coulter System 126, Brea, CA) using a silica-based column (Waters Spherisorb ODS2). Varying concentrations of pentosidine served as standards. The detector was a Waters fluorescence detector, and the excitation/emission wavenumbers were 328/378 nm. For the hydroxyproline assay, an internal standard of α-amino-butyric acid (α-ABA) was used. The amino acids and standard were derivatized with phenyl isothiocyanate (PITC) and resuspended in a buffer (5% acetonitrile in 5 mM disodium phosphate), along with varying concentrations of hydroxyproline and proline. For the hydroxyproline assay, a Waters Pico-Tag column was used, with a UV detector. Conversion from hydroxyproline concentration to collagen concentration was done using the fact that hydroxyproline comprises 14% of type I collagen. HPLC measurements of the rat radius samples were performed using the same equipment, in a similar manner.

2.8.6 qBEI

Before qBEI the Transverse human femur specimens were dried for several days in a vacuum desiccator at room temperature. The bone specimens were imaged alongside aluminum and carbon standards (EMS, Hatfield, PA) using a Quanta FEG 250 ESEM (FEI Company, Hillsboro, OR) instrument equipped with a low-voltage, high-contrast backscattered electron detector. Image resolution was 1.2 μm per pixel. Image greyscale values were converted to calcium weight percentage values using the method described by Roschger et al., which assumes a linear relationship between atomic number Z, greyscale value, and calcium weight percent [60]. After adjusting image

contrast and brightness such that the carbon and aluminum greyscale values (GS) are 25 and 225, respectively, Ca wt.% is calculated by

$$\text{Ca wt.}\% = 0.1733 * GS - 4.3326 \quad (32)$$

Osteon area fraction (OstAr) was also calculated from the qBEI images. First, pixels were assigned to either bone matrix or porosity, with the threshold greyscale value determined using Otsu's method. Next, a contrast-enhanced subregion (1.5 mm x 1.5 mm) was manually segmented into osteonal and interstitial regions. OstAr was then calculated as the fraction of osteonal-segmented pixels in the subregion. See Figure 19 for an example of osteonal-interstitial segmentation for one of the qBEI subregions.

2.9 Indentation-qBEI Site-matching

The indentation-qBEI correlations were calculated using site-matched indent-level data. For each of the human femur Transverse specimens, the indentation locations on the corresponding qBEI image were determined by the following procedure (implemented with MATLAB):

1) Create a composite image from all of the individual indentation microscope images.
2) Identify two of the same locations on the qBEI and composite indentation images.
3) Scale and rotate the indentation location data to match the scale and orientation of the qBEI data, using the 2 coincident points from step 2. At this point the indent locations are approximate.
4) For each 4-indent array, manually refine the indentation locations by comparing the site selection GUI screenshot with the corresponding approximate location on the qBEI image. A screenshot from this step can be seen as Figure 20.

At each site-matched location, the Ca wt.% value was calculated as the mean value of all of the pixels within a 10 μm radius. The qBEI images had a resolution of ~0.83 pixels/μm, so this circular region consisted of 213 pixels. Site-matched locations

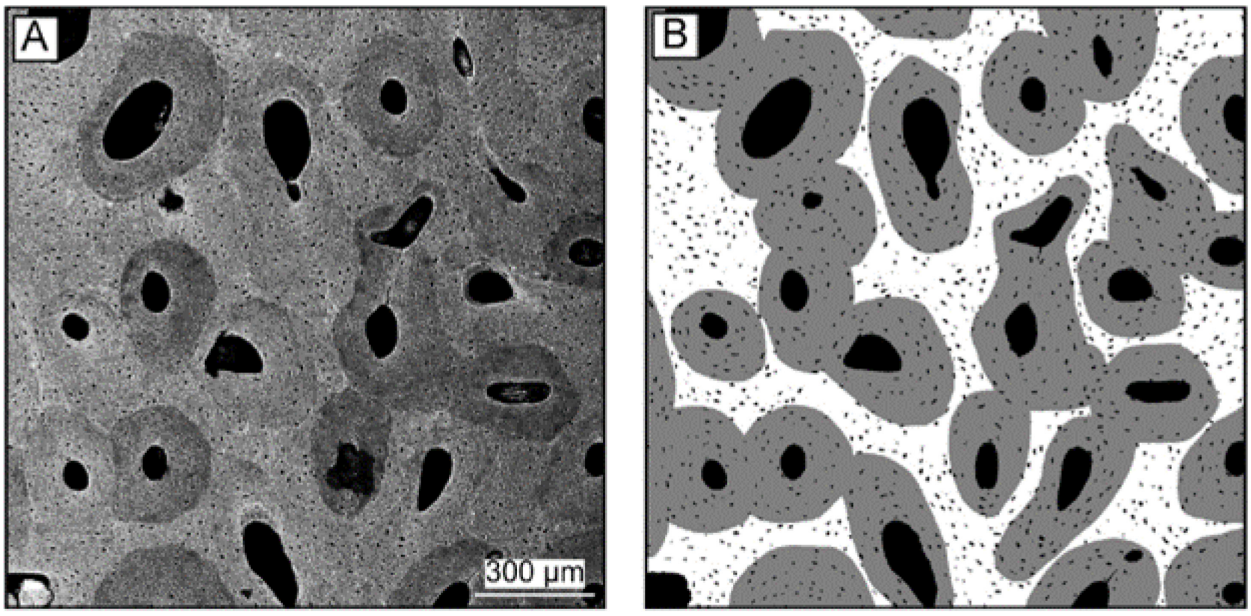


Figure 19: Osteon area fraction (OstAr) was calculated from a subregion of each qBEI image (A). Voids were programmatically separated from the bone matrix, and the bone matrix was then manually segmented between osteonal (grey) and interstitial (white) regions (B). [55]

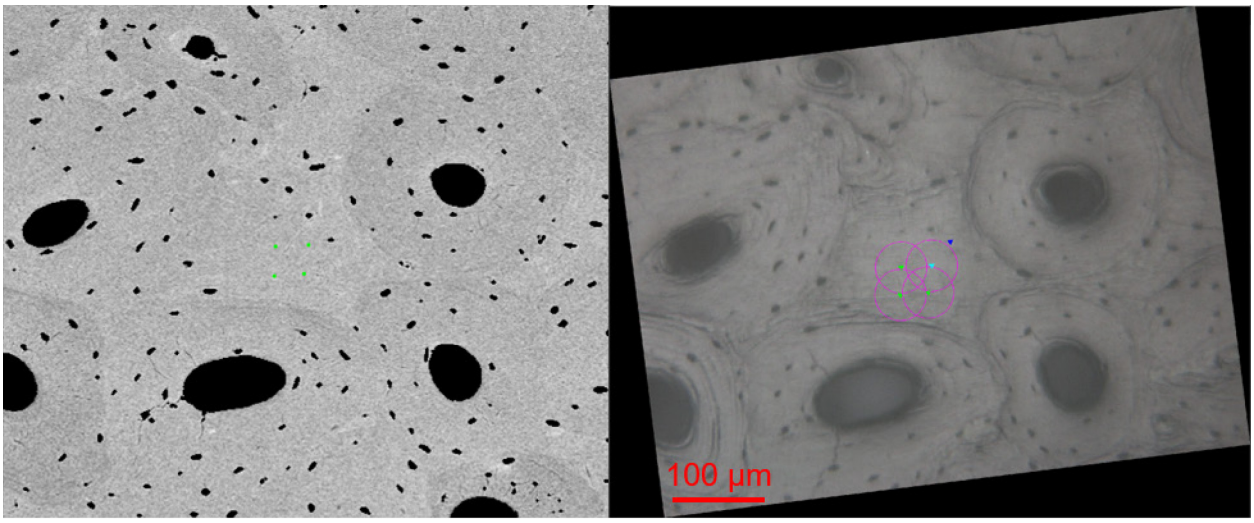


Figure 20: Example screenshot from the last step in the indentation-qBEI site-matching process. At right is an indentation site selection GUI image, and at left is the same location in the qBEI image. The 4 green dots in the qBEI image were manually adjusted to coincide with the indent locations in the indentation site-selection image. Also, note how the osteonal regions tend to be slightly darker than the interstitial regions in the qBEI image, indicating a lower level of mineralization.

containing a void pixel were excluded. However, the spatial precision of nanoindentation to avoid surface voids was such that few data points were excluded for this reason. Figure 21 shows the identified indent locations on a Transverse specimen's qBEI image and the corresponding composite indentation image. The green circles in the qBEI image are the same size (10 μm radius) as used to calculate the mean Ca wt.% at each indentation location.

2.10 Indent-level to Specimen-level Values

All of the other statistical calculations in this study were done with specimen-level data as inputs, meaning a single representative value for each specimen. For example, the human femur indentation experiments (Ex: Longitudinal section – Wet condition) consisted of 64 indents each. These data points must be reduced to a single, representative specimen-level data point. For example, suppose

$$\mathbf{H_{1,Longitudinal,Wet,Osteonal}} = [x_1, x_2, x_3 \cdots x_n] \tag{33}$$

represents all of the H values for donor #1, Longitudinal section, Wet condition, and Osteonal location, where n is the number of such indents. First, the representative specimen-level representative Osteonal and Interstitial values were calculated as the mean of all osteonal and interstitial values, respectively:

$$\mathrm{H}_{1,\mathrm{Longitudinal,Wet,Osteonal}} = \mathrm{mean}\left(\mathbf{H_{1,Longitudinal,Wet,Osteonal}}\right) \tag{34}$$

$$\mathrm{H}_{1,\mathrm{Longitudinal,Wet,Interstitial}} = \mathrm{mean}\left(\mathbf{H_{1,Longitudinal,Wet,Interstitial}}\right) \tag{35}$$

Second, for calculations in which Location (i.e. Osteonal or Interstitial) was not considered, the representative specimen-level value used was the average of the Osteonal and Interstitial specimen-level representative values:

$$\mathrm{H}_{1,\mathrm{Longitudinal,Wet}} = \frac{\mathrm{H}_{1,\mathrm{Longitudinal,Wet,Osteonal}} + \mathrm{H}_{1,\mathrm{Longitudinal,Wet,Interstitial}}}{2} \tag{36}$$

The average of the Osteonal and Interstitial representative values was used because there were often not an equal number of osteonal and interstitial indents.

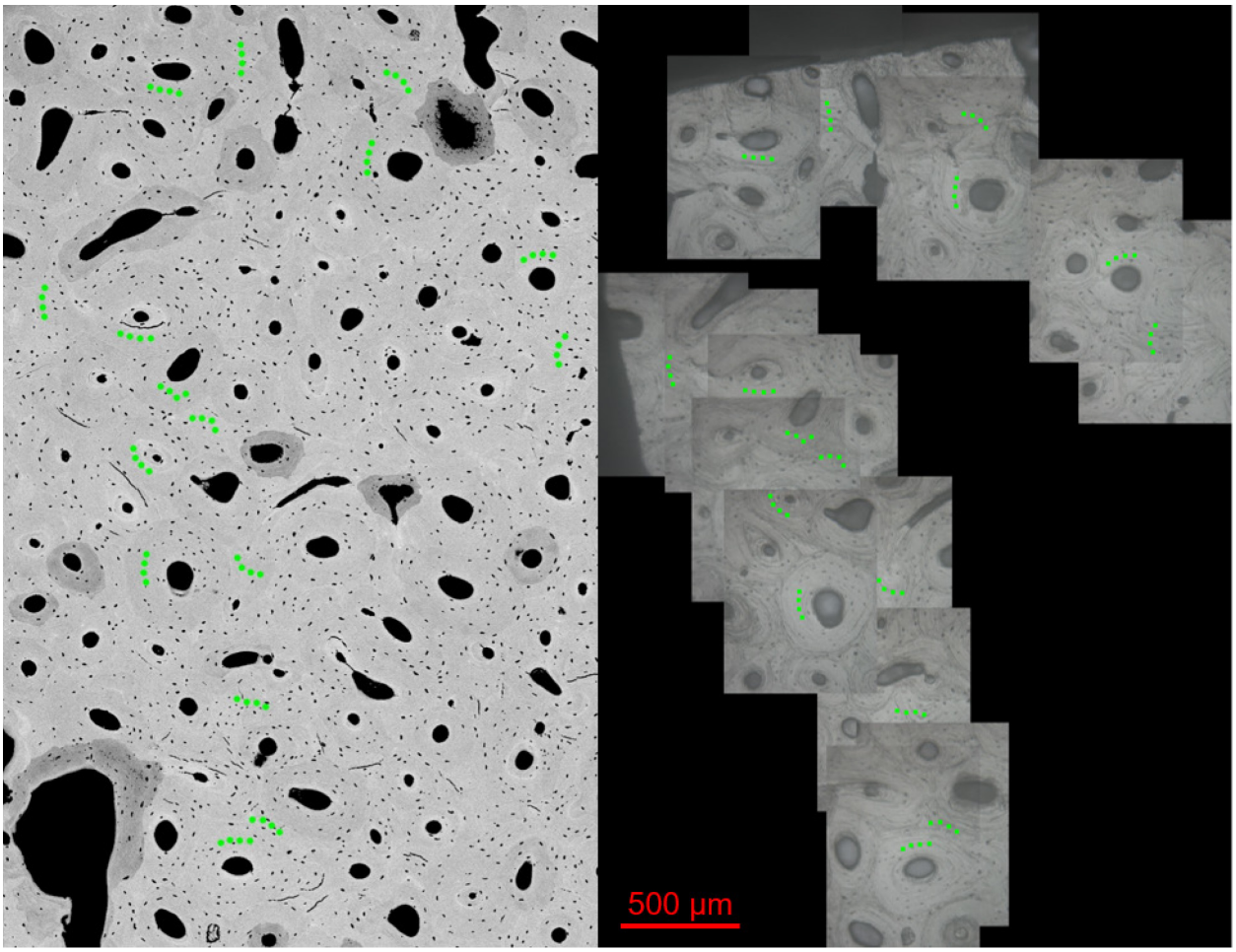


Figure 21: Composite indentation microscope image for a Transverse specimen (Right) and corresponding qBEI image (Left). Indent locations are indicated by the green circles. Indent qBEI Ca wt.% values were calculated by averaging the pixel values within each of the 10 µm radius circles.

For the rat tibia indentation tests, the calculations for the representative specimen-level Periosteal and Mid-cortex values were performed similarly. For example, for rat donor #1, Wet condition:

$$\mathrm{H}_{1,\mathrm{Wet,Periosteal}} = \mathrm{mean}\left(\mathbf{H}_{\mathbf{1,Wet,Periosteal}}\right) \quad (37)$$

$$\mathrm{H}_{1,\mathrm{Wet,Mid-cortex}} = \mathrm{mean}\left(\mathbf{H}_{\mathbf{1,Wet,Mid-cortex}}\right) \quad (38)$$

However, for calculations in which Location was not considered, the representative Mid-cortex value was used. The Mid-cortex value was used because the size of the Periosteal region is variable with age, while the size of the Mid-cortex region is more constant. The periosteal region of the youngest rats is small enough that macroscale mechanical properties will be determined predominately by the properties of the Mid-cortex region.

2.11 Statistics

2.11.1 Overview

All statistical hypothesis tests used were either nonparametric or robust. This was done because the data were not generally normally distributed and to reduce the influence of extreme values. A significance level of 0.05 was used for all statistical hypothesis tests. In tables, results which were nearly significant ($0.05 < p < 0.10$) are also reported with an asterisk. All hypothesis tests were double-sided.

Correlations were calculated as Spearman rank correlations (r_s). Correlation best-fit lines, as well as some linear regression models, were calculated via iteratively reweighted least squares (IRLS), using the Huber weight function and tuning constant of 1.345σ. The Wilcoxon rank sum test was used for comparisons between 2 unpaired groups: human femur Wet vs. Dry, Longitudinal vs. Transverse, and Young vs. Aged. The Wilcoxon signed rank test was used for comparisons of 2 paired groups: human femur Osteonal vs. Interstitial and rat tibia Periosteal vs. Mid-cortex. The Wilcoxon signed rank test was also used to test the distribution of site-matched indentation-qBEI correlations (null hypothesis: $\mathrm{median}(r_s) = 0$). Testing the rat data for changes with age

was done in two steps. First, the Kruskal-Wallis test was used to determine if there was a significant difference between age groups. If so, then Dunn's test was used to identify which pairs of age groups were significantly different. For Dunn's test, the p-values were adjusted using the Holm–Šidák adjustment for multiple comparisons, with a family-wise error rate (FWER) of 0.05. For boxplots the maximum whisker length was 1.5 times the interquartile range, and values outside of this range were plotted as outliers (red plus signs).

2.11.2 Indentation Regression Models

Linear regression models with the indentation parameters as the response variable and Condition, Section, Age, and Location as the predictor variables were created. The models were constructed using ordinary least squares (OLS) in a step-up fashion, starting with a constant model. The criterion for adding terms to the model was an F-test of the change in the sum of the squared error that results from adding the given term. The significance level for adding terms was 0.05. Age was offset by 21 years, the age of the youngest donor, so that the constant term would represent the indentation value for that age. Each regression model contained 204 data points (i.e., Donor–Section–Condition–Location combination).

2.11.3 Fracture Regression Models

Linear regression models were created to determine which combination of parameters best predicted the human femur fracture data. The predictor variables used were the indentation, compositional, and structural parameters which had significant correlations with the fracture parameter response variable. With this restricted set of predictor variables, each possible model with up to 4 terms was evaluated using OLS. The selected models were those with the highest Adjusted-R^2 value for each fracture parameter. The selected OLS models were also rerun with IRLS, since OLS models can be sensitive to influential data points. To avoid multicollinearity amongst the predictor variables, models with a variance inflation factor (VIF) greater than 5 were excluded (the VIFs in the selected models were ≤ 1.5). To enable a comparison of the relative

importance of each predictor variable despite differing units, the coefficients were standardized. Given a regression equation with unstandardized coefficients (α),

$$Y = \alpha_1 X_1 + \alpha_2 X_2 + \cdots + \alpha_k X_k \tag{39}$$

the standardized coefficients (β) were calculated by:

$$\beta_i = \frac{Std(X_i)}{Std(Y)} * \alpha_i \tag{40}$$

The magnitude of a standardized coefficient is an estimate of the change in the response variable (number of standard deviations) for a one standard deviation change in the associated predictor variable.

2.11.4 Outlier Exclusion

Statistical outliers were identified using a robust z-score (i.e. number of standard deviations from the sample mean) estimate:

$$\hat{z} = \frac{X_i - \text{median}(X)}{1.4826 * \text{MAD}(X)} \tag{41}$$

for data set X, where MAD is median absolute deviation:

$$\text{MAD} = \text{median}\big(X_i - \text{median}(X)\big) \tag{42}$$

See the Indent Exclusion section for details on how $\hat{z}$ was used to identify and exclude individual indents. Similarly, refer to the Specimen Exclusion section regarding the exclusion of one donor from the human femur experiment as a Porosity extreme outlier.

2.12 Indent Exclusion

Various experimental issues could cause spurious indentation data. Bad indentation data could be caused by software issues such as missing data index markers (Ex: end of loading, start of hold, etc.) or by experimental issues such as false surface finds or too short of an approach distance. The largest experimental issue was precipitation of salt from the PBS solution onto the indenter shaft, which could impair

indenter motion. Due to the large number of indents in this study (>10,000) and to avoid subjectivity, an automated procedure was developed to exclude questionable indentation data. Problematic data were identified by comparison with the behavior of an idealized indent in bone. For example, indenter creep into the sample during the hold segment is expected since bone is viscoelastic but a decrease in displacement during the hold would be unusual. Figures 11-15 are good examples of acceptable indentation data.

Automated indent exclusion functioned in two stages. First, each indent was checked for 13 different exclusion criteria. These defined exclusion criteria are detailed in Appendix A.1. Second, outliers among the remaining indents were removed to catch any questionable data that may have been missed in the first step. Outliers were identified by $|\hat{z}| > 2$, where $\hat{z}$ was a robust z-score estimate (see the Outlier Exclusion section for more information). This value was chosen as ≈95% of normally distributed data lies within 2 standard deviations of the mean. The parameters used for outlier exclusion were E', E'', H, and δ. For the human femur indentation data, outlier exclusion was done separately for each Condition – Section combination. Similarly, for the rat tibia indentation data, outlier exclusion was done separately for each Condition – Age Group combination.

2.13 Specimen Exclusion and Number of Specimens

2.13.1 Human Femur Experiment

The original human femur dataset consisted of specimens from 30 donors (1 Longitudinal section and 1 Transverse section). However, the final dataset was smaller than this because some specimens were excluded. First, one donor was excluded as an extreme Porosity outlier. The Porosity robust z-score estimate ($\hat{z}$, see Outlier Exclusion) for this donor was 21.4. No other donor had a Porosity $\hat{z}$ greater than 5.9. Thus, the bones from this donor were not representative of those from the other 29

donors and their inclusion could have skewed the results. For all of the other fracture, compositional, and structural parameters, no $\hat{z}$ value was greater than 5.1.

Next, for the indentation data, 3 Longitudinal and 4 Transverse specimens were excluded. The 3 Longitudinal section exclusions were due to experimental issues during Wet testing. For example, the surface of the specimen may not have remained submerged, or salt buildup could have interfered with the motion of the indenter. One of the excluded Transverse specimens was damaged and could not be tested. The other 3 Transverse specimens were excluded due to having a measured surface tilt greater than 4° in either the Wet or Dry experiments. Unlike the Longitudinal specimens, the Transverse specimens were tested with qBEI before the indentation experiments. The residual adhesive from mounting the Transverse experiments for qBEI testing was difficult to cleanly remove, given the small size of the specimens and the fact that the polished top surface could not be touched. Thus, some of the specimens were not mounted perfectly flat for indentation. Surface tilt leads to an underestimation of the actual projected contact area of the indenter and consequently an overestimation in E′, E″, and H. For somewhat blunt tips such as the Berkovich (centerline-to-face angle of 65.3°), this error can be appreciable even at relatively low surface tilt angles. Surface tilt was calculated by fitting a plane to the non-excluded indent surface displacements.

The number of data points in the human femur experiment is listed in Table 3. All calculations were done with the maximum amount of available data, rather than restricting the set of specimens to only those with no missing data. For example, the correlation between K_{init} and Age had 29 data points, while the correlation between E′ – Longitudinal – Wet and Age had 26 data points. Also, note that 4 specimens were missing K_{grow} data, so calculations involving K_{grow} had 4 fewer data points than calculations with K_{init} and J-integral. As can be seen in Table 3, when grouped by age, the Young and Aged groups had a roughly equal number of data points. Note that one of the excluded Longitudinal specimens was from the oldest donor. Consequently, the donor age range covered by the Longitudinal indentation data (21-97 years) was 1 year less than for the Transverse indentation data (21-98 years).

Table 3: Number of human femur experiment data points

	Fracture*, Composition, Structure	Indentation: Longitudinal	Indentation: Transverse
Young	14	13	12
Aged	15	13	13
Total	29	26	25

*K_{grow} data missing for 4 specimens
Young = Age $\leq$ 60 years
Aged = Age $>$ 60 years

2.13.2 Rat Bone Experiment

The original rat bone dataset consisted of bones from 36 donors, split evenly between the 3 age groups. As with the human femur experiment, the final dataset was smaller. The final number of data points in the rat bone experiment is shown in Table 4. Five specimens were excluded in the Dry test condition, due to being run with incorrect method inputs. These specimens were not tested in the Wet condition. An additional 7 specimens were excluded due to Wet testing experimental issues, leaving 24 specimens in the indentation Wet dataset. Also, note that fracture data was missing for 1 specimen from the 24 months age group.

2.14 Correlations Amongst Indentation Parameters

Four indentation parameters were considered for this study. These were the viscoelastic parameters storage modulus (E′), loss modulus (E″), and phase angle (δ), as well as indentation hardness (H). The correlations amongst these indentation parameters are shown in Table 5, with the rows sorted by decreasing correlation strength. The strongest correlation was between E′ and H, which were positively correlated for all experiments. For the human femur experiments, E′/H was in the range 31-39. Next, δ was correlated with the other 3 parameters. Because δ was correlated with each of the other parameters, it was removed from further consideration. Viscoelastic phase angle results can be inferred from the positive correlation with E′ and the negative correlation with E″. Thus, the 3 indentation parameters reported in this study were E′, E″, and H. E″ was most often not found to be significantly correlated with E′ or H.

Most commonly reported in nanoindentation experiments are Young's modulus (E) and H. For a purely elastic material E′ = E and E″ = 0. When E′ ≫ E″, then E′ ≈ E. For the human femur indentation data grouped by Section and Condition, the average E′/E″ values ranged from 23 for Longitudinal – Wet to 57 for Transverse – Dry. In this study, E′ values were generally 5-10% lower than E values. E results are not reported since these results can be inferred from those shown for E′. H results are reported,

Table 4: Number of rat bone experiment data points

	Fracture*, Composition, Structure	Indentation: Wet	Indentation: Dry
6 months	12	9	10
12 months	12	6	11
24 months	12	9	10
Total	36	24	31

*Fracture data missing for 1 specimen (24 months group)

Table 5: Correlations amongst indentation parameters. Sorted by decreasing correlation strength.

Indentation Parameters		Human Femur				Rat Tibia	
		Longitudinal		Transverse			
		Wet	Dry	Wet	Dry	Wet	Dry
E'	H	0.89	0.72	0.72	0.85	0.96	0.92
E'	δ	-0.91	-0.81	-0.78	-0.61	-0.96	-0.72
H	δ	-0.89	-0.47	-0.67	-0.69	-0.98	-0.78
E''	δ	0.70	0.43		0.65		0.46
E'	E''	-0.40		0.45			
E''	H	-0.54					

Data are Spearman rank correlation coefficients (r_s)
E′ = Storage modulus
E″ = Loss modulus
H = Hardness
δ = Viscoelastic phase angle

despite the strong correlation between E′ and H. This was done because these parameters have different physical interpretations, to enable a direct comparison with other nanoindentation of bone studies, and because their results sometimes differed. In cases where the results for E′ and H were similar, often only the figures for E′ will be shown, as to include those for H would be redundant.

CHAPTER 3
RESULTS

3.1 Indentation Data: Wet vs. Dry

3.1.1 Human Femur

Table 6 compares the Wet vs. Dry human femur indentation data. There is a significant Wet – Dry difference for each indentation parameter. Namely, for E′ and H Dry > Wet, while for E″ Wet > Dry. Boxplots of E′, E″, and H for each Section – Condition – Age Group combination can be seen as Figures 22-24. Note that the effect of hydration on the indentation data is sufficiently large to be readily apparent in these figures.

3.1.2 Rat Tibia

Table 7 contains the rat tibia indentation Wet vs. Dry comparative data. Like for the human femur data, there was a significant Wet – Dry difference in every instance. Again E′ and H were greater Dry than Wet, and E″ was greater Wet than Dry. Figures 25, 26, and 27 are boxplots of the rat tibia indentation data grouped by Condition, Location, and Age for E′, E″, and H, respectively. Note again that the difference between the Wet and the Dry indentation data can be seen clearly in Figures 25-27.

3.1.3 Comparison Between Human and Rat Results

Hydration had a similar effect on the human femur and rat tibia specimens. In both cases, hydration was seen to result in increased stiffness (E′) and hardness and decreased viscoelasticity (E″).

3.2 Indentation Data: Longitudinal vs. Transverse

Refer to Table 8 for the comparison between the human femur Longitudinal and Transverse indentation data. In each instance there was a significant Longitudinal – Transverse difference. Specifically, Transverse > Longitudinal for all 3 indentation parameters. These differences can be seen in Figures 22-24.

Table 6: Comparison of human femur Wet and Dry indentation data

Parameter	Section	Wet	Dry	p
E'	Longitudinal	14.1 (1.0)	17.1 (0.8)	<0.001
	Transverse	20.4 (1.6)	26.7 (1.5)	<0.001
E''	Longitudinal	0.61 (0.02)	0.40 (0.01)	<0.001
	Transverse	0.66 (0.03)	0.47 (0.03)	<0.001
H	Longitudinal	0.40 (0.04)	0.51 (0.03)	<0.001
	Transverse	0.54 (0.04)	0.87 (0.08)	<0.001

Data in Wet and Dry columns are Mean (SD)
p = Wilcoxon rank sum test p-value

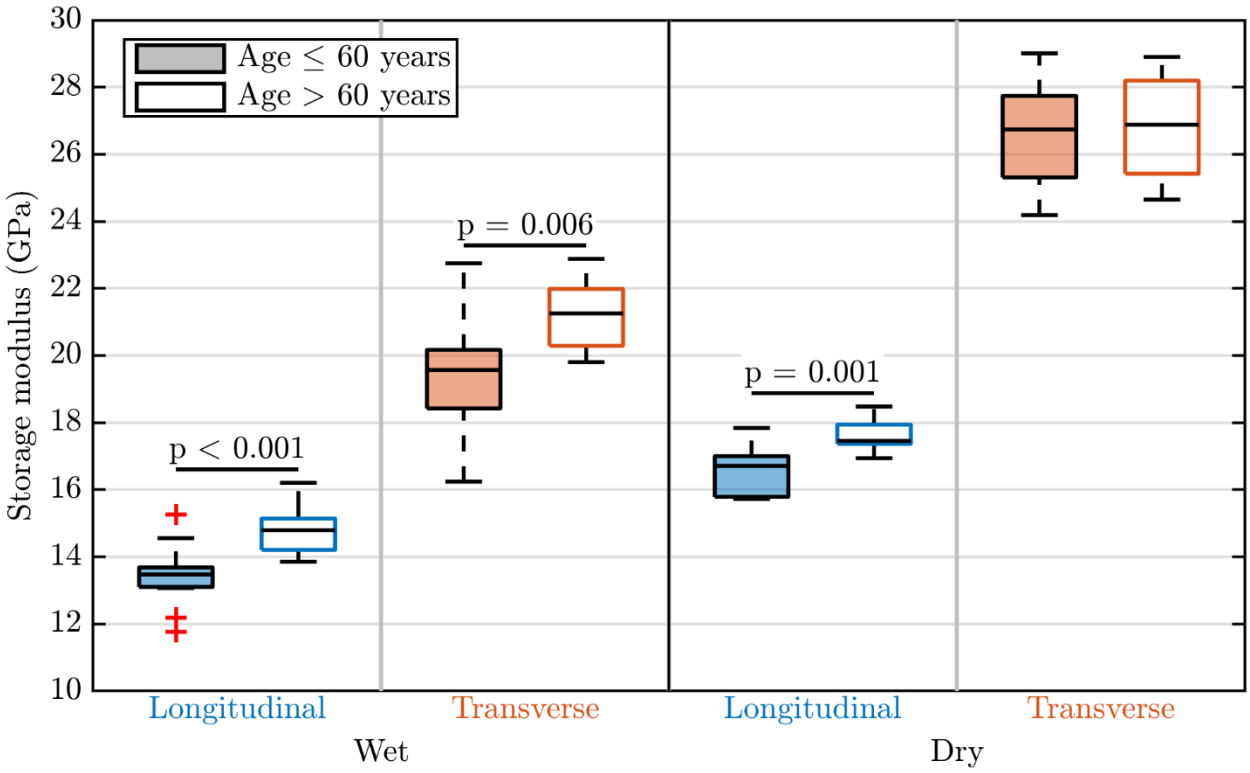


Figure 22: Boxplot of human femur E′ data grouped by Condition, Section, and Age. Significant age group differences are indicated by the comparison lines located above the boxes. Wet – Dry and Longitudinal – Transverse comparison lines are not shown, since in each instance Dry > Wet and Transverse > Longitudinal.

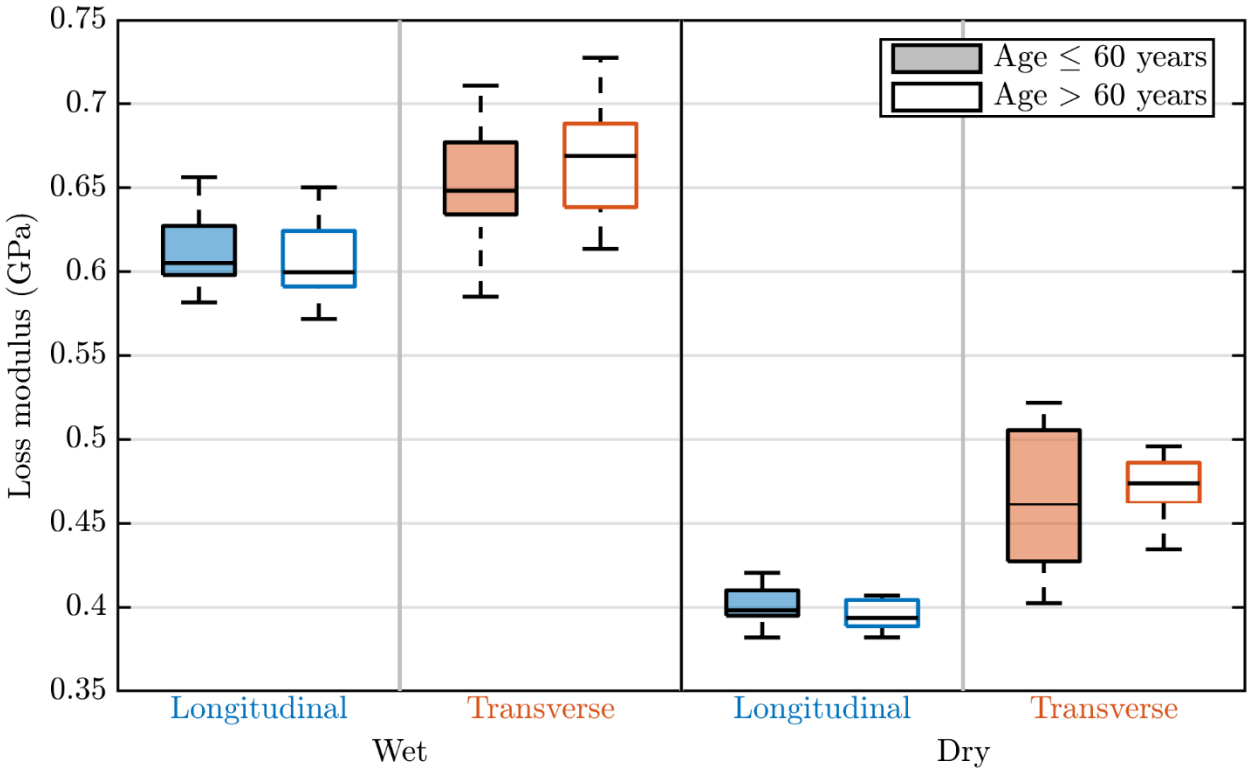


Figure 23: Boxplot of human femur E″ data grouped by Condition, Section, and Age. Wet – Dry and Longitudinal – Transverse comparison lines are not shown, since in each instance Wet > Dry and Transverse > Longitudinal. No significant differences were seen when comparing between age groups.

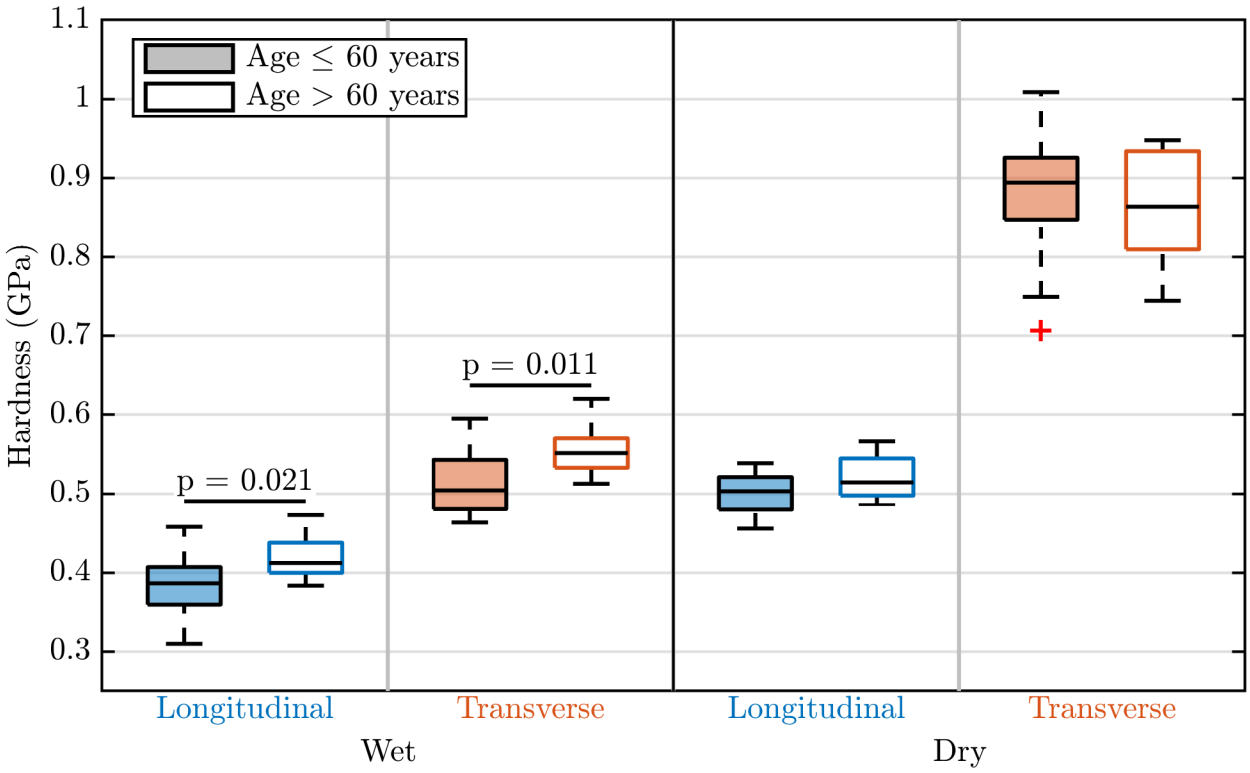


Figure 24: Boxplot of human femur H data grouped by Condition, Section, and Age. Significant age group differences are indicated by the comparison lines located above the boxes. Wet – Dry and Longitudinal – Transverse comparison lines are not shown, since in each instance Dry > Wet and Transverse > Longitudinal.

Table 7: Comparison of rat tibia Wet and Dry indentation data

Parameter	Age	Location	Wet	Dry	p
E'	6 months	Periosteal	12.8 (2.6)	27.4 (1.4)	<0.001
		Mid-cortex	18.3 (1.5)	31.3 (0.9)	<0.001
	12 months	Periosteal	16.2 (2.9)	28.7 (1.3)	<0.001
		Mid-cortex	22.7 (2.3)	33.1 (1.3)	<0.001
	24 months	Periosteal	16.4 (3.3)	29.8 (1.2)	<0.001
		Mid-cortex	23.4 (2.7)	33.9 (1.4)	<0.001
E''	6 months	Periosteal	0.78 (0.08)	0.43 (0.01)	<0.001
		Mid-cortex	0.88 (0.04)	0.43 (0.02)	<0.001
	12 months	Periosteal	0.83 (0.05)	0.43 (0.01)	<0.001
		Mid-cortex	0.92 (0.03)	0.44 (0.01)	<0.001
	24 months	Periosteal	0.84 (0.06)	0.44 (0.01)	<0.001
		Mid-cortex	0.87 (0.06)	0.44 (0.01)	<0.001
H	6 months	Periosteal	0.19 (0.05)	1.08 (0.08)	<0.001
		Mid-cortex	0.29 (0.05)	1.22 (0.05)	<0.001
	12 months	Periosteal	0.31 (0.08)	1.15 (0.05)	<0.001
		Mid-cortex	0.44 (0.12)	1.31 (0.06)	<0.001
	24 months	Periosteal	0.30 (0.10)	1.20 (0.07)	<0.001
		Mid-cortex	0.49 (0.12)	1.33 (0.07)	<0.001

Data in Wet and Dry columns are Mean (SD)
p = Wilcoxon rank sum test p-value

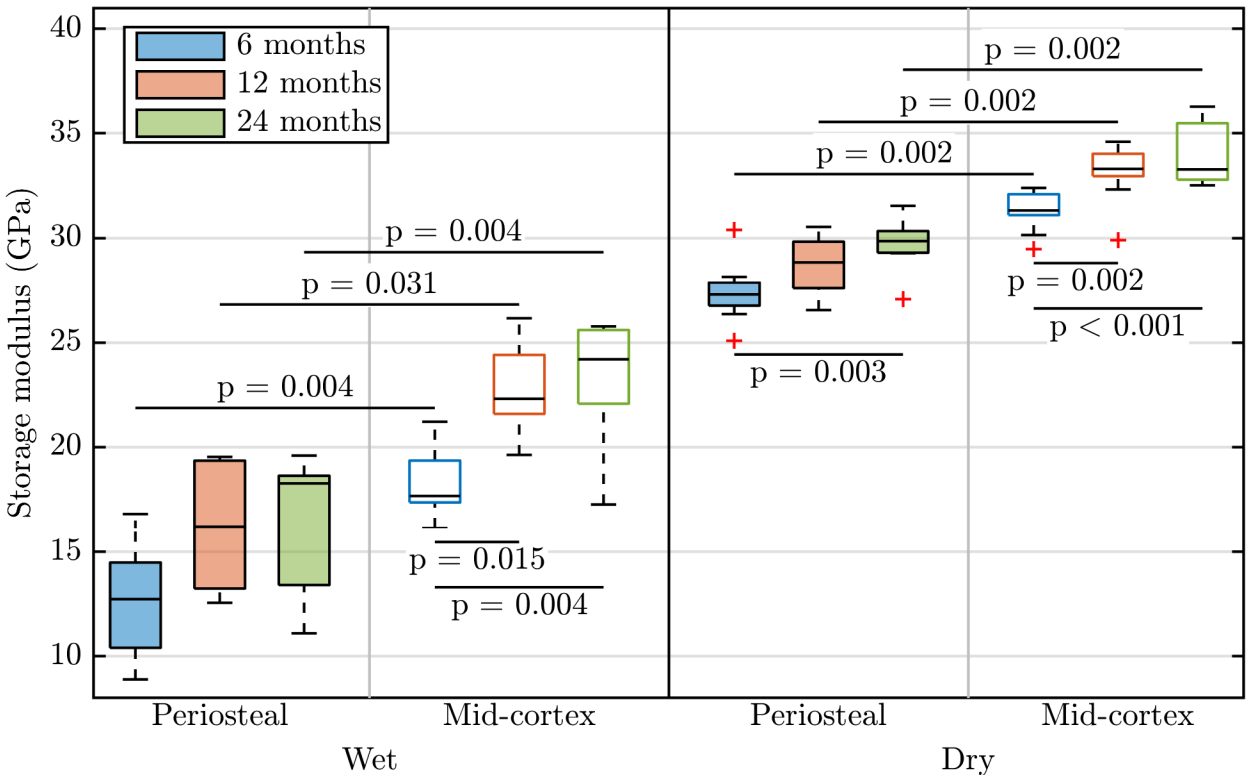


Figure 25: Boxplot of rat tibia E′ data grouped by Condition, Location, and Age. Significant differences between Periosteal and Mid-cortex data are indicated by comparison lines located above the boxes. Significant age group differences are indicated by the comparison lines below the boxes. Wet – Dry comparison lines are not shown, since in each instance Dry > Wet.

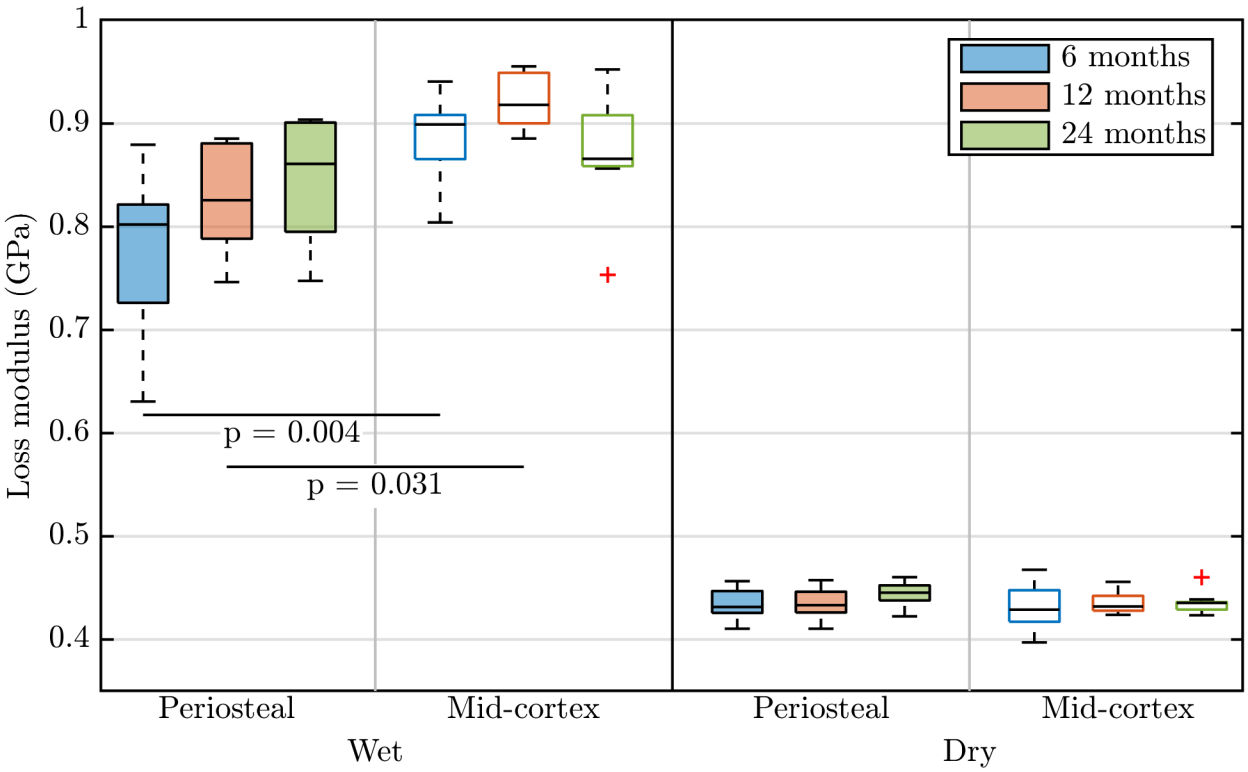


Figure 26: Boxplot of rat tibia E″ data grouped by Condition, Location, and Age. Significant differences between Periosteal and Mid-cortex data are indicated by comparison lines located below the boxes. Wet – Dry comparison lines are not shown, since in each instance Wet > Dry. No age group differences were significant.

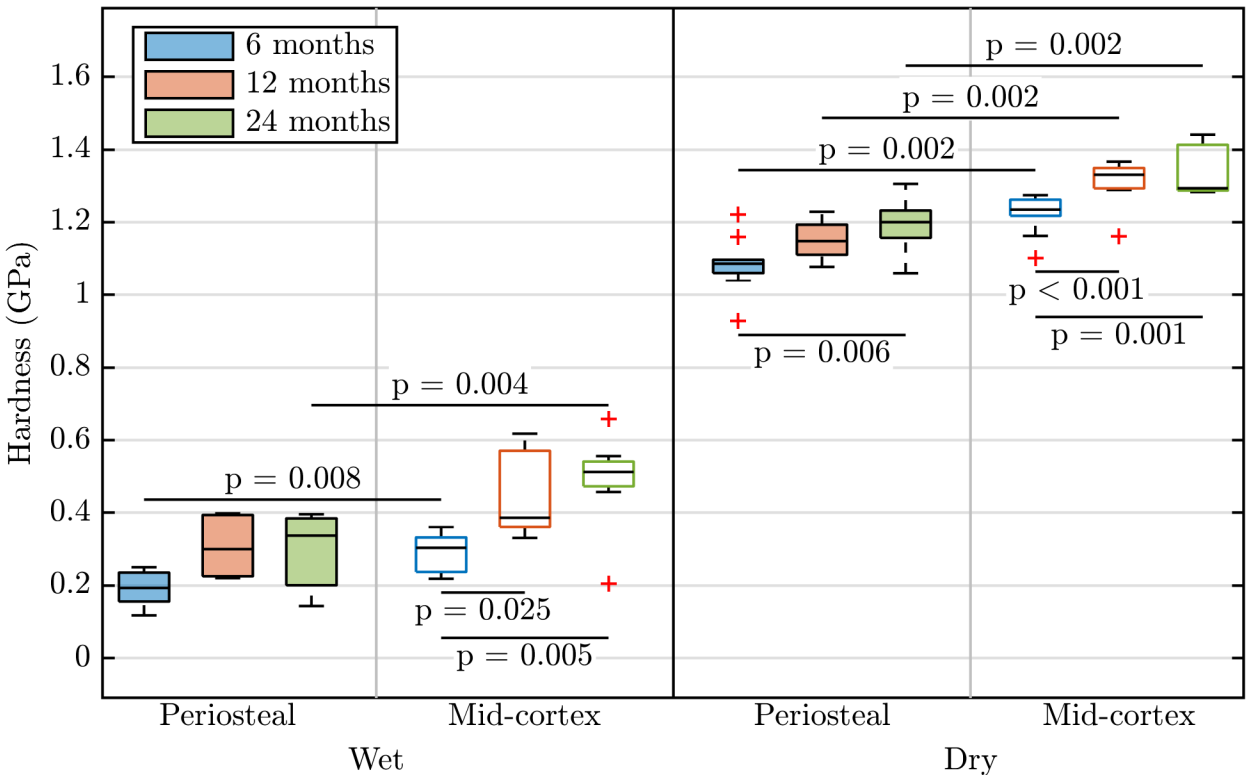


Figure 27: Boxplot of rat tibia H data grouped by Condition, Location, and Age. Significant differences between Periosteal and Mid-cortex data are indicated by comparison lines located above the boxes. Significant age group differences are indicated by the comparison lines below the boxes. Wet – Dry comparison lines are not shown, since in each instance Dry > Wet.

Table 8: Comparison of Longitudinal and Transverse indentation data for the human femur specimens

Parameter	Condition	Longitudinal	Transverse	p
E'	Wet	14.1 (1.0)	20.4 (1.6)	<0.001
	Dry	17.1 (0.8)	26.7 (1.5)	<0.001
E''	Wet	0.61 (0.02)	0.66 (0.03)	<0.001
	Dry	0.40 (0.01)	0.47 (0.03)	<0.001
H	Wet	0.40 (0.04)	0.54 (0.04)	<0.001
	Dry	0.51 (0.03)	0.87 (0.08)	<0.001

Data in Longitudinal and Transverse columns are Mean (SD)
p = Wilcoxon rank sum p-value

3.3 Indentation Data: Osteonal vs Interstitial

Table 9 compares the human femur Osteonal and Interstitial indentation data. Interstitial H was seen to be greater than Osteonal H. The only Section – Condition combination in which the Osteonal – Interstitial H difference was not statistically significant was Longitudinal – Dry, and in this instance the difference was nearly significant ($0.05 < p < 0.10$). The Osteonal and Interstitial H data are plotted as Figure 28. The trends for E′ and E″ were smaller and less consistent than for H. E′ and E″ each had 2 significant differences out of the 4 Section – Condition combinations tested, but the trends did not agree. The difference in Osteonal and Interstitial data for E′ and E″ was less than 4%, while for the statistically significant H differences, the differences were 5%, 8%, and 9%.

3.4 Indentation Data: Periosteal vs. Mid-cortex

Table 10 compares the rat tibia Periosteal and Mid-cortex indentation data. These data can be seen plotted in Figures 25-27. For E′ and H, in all cases Mid-cortex values were larger than Periosteal values. The only difference which was not statistically significant was H – 12 months – Dry, which was itself nearly significant. The Periosteal – Mid-cortex difference in E' and H values was greater in the Wet condition than the Dry condition (10-13% Dry and 29-39% Wet). For E″ there were two Age Group – Condition combinations with a statistically significant difference in Periosteal and Mid-cortex values; these were 6 months – Wet and 12 months – Wet, in which Mid-Cortex > Periosteal.

3.5 Indentation Data: Changes with Age

3.5.1 Human Femur

Table 11 deals with changes with age for the human femur indentation data. E′ was seen to increase with age. When grouped by age, Aged > Young for Longitudinal – Wet, Longitudinal – Dry, and for Transverse – Wet. However, there was no significant

Table 9: Comparison of human femur Osteonal and Interstitial indentation data

Parameter	Section	Condition	Osteonal	Interstitial	p
E'	Longitudinal	Wet	14.0 (1.4)	14.1 (1.0)	
		Dry	17.3 (0.9)	16.9 (0.8)	0.005
	Transverse	Wet	20.0 (1.9)	20.7 (1.8)	0.074*
		Dry	26.4 (1.6)	27.0 (1.6)	0.045
E''	Longitudinal	Wet	0.62 (0.03)	0.60 (0.03)	<0.001
		Dry	0.40 (0.01)	0.40 (0.01)	
	Transverse	Wet	0.66 (0.04)	0.66 (0.03)	
		Dry	0.46 (0.03)	0.47 (0.03)	<0.001
H	Longitudinal	Wet	0.38 (0.05)	0.42 (0.04)	0.002
		Dry	0.50 (0.03)	0.52 (0.03)	0.096*
	Transverse	Wet	0.51 (0.05)	0.56 (0.05)	<0.001
		Dry	0.84 (0.08)	0.89 (0.08)	<0.001

Data in Osteonal and Interstitial columns are Mean (SD)
p = Wilcoxon signed rank test p-value
* $0.05 < p < 0.10$

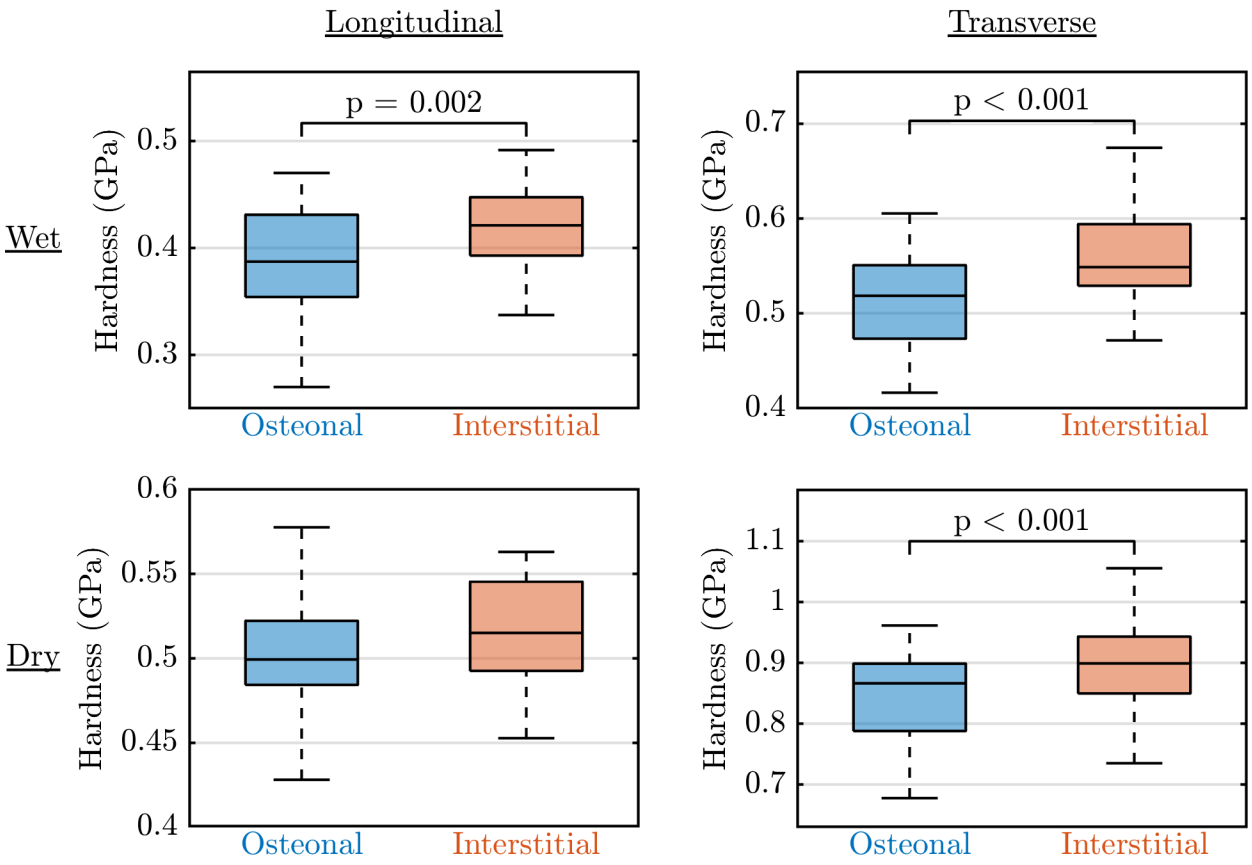


Figure 28: Boxplots of human femur Osteonal and Interstitial H data. Significant Osteonal – Interstitial differences are shown by comparison lines above the boxes.

Table 10: Comparison of rat tibia Periosteal and Mid-cortex indentation data

Parameter	Age	Condition	Periosteal	Mid-cortex	p
E'	6 months	Wet	12.8 (2.6)	18.3 (1.5)	0.004
		Dry	27.4 (1.4)	31.3 (0.9)	0.002
	12 months	Wet	16.2 (2.9)	22.7 (2.3)	0.031
		Dry	28.7 (1.3)	33.1 (1.3)	0.002
	24 months	Wet	16.4 (3.3)	23.4 (2.7)	0.004
		Dry	29.8 (1.2)	33.9 (1.4)	0.002
E''	6 months	Wet	0.78 (0.08)	0.88 (0.04)	0.004
		Dry	0.43 (0.01)	0.43 (0.02)	
	12 months	Wet	0.83 (0.05)	0.92 (0.03)	0.031
		Dry	0.43 (0.01)	0.44 (0.01)	
	24 months	Wet	0.84 (0.06)	0.87 (0.06)	
		Dry	0.44 (0.01)	0.44 (0.01)	0.064*
H	6 months	Wet	0.19 (0.05)	0.29 (0.05)	0.008
		Dry	1.08 (0.08)	1.22 (0.05)	0.002
	12 months	Wet	0.31 (0.08)	0.44 (0.12)	0.063*
		Dry	1.15 (0.05)	1.31 (0.06)	0.002
	24 months	Wet	0.30 (0.10)	0.49 (0.12)	0.004
		Dry	1.20 (0.07)	1.33 (0.07)	0.002

Data in Periosteal and Mid-cortex columns are Mean (SD)
p = Wilcoxon signed rank test p-value
* $0.05 < p < 0.10$

Table 11: Comparison of human femur indentation data between Young and Aged age groups and indentation data correlations with age

Parameter	Section	Condition	Young	Aged	p	r_s
E'	Longitudinal	Wet	13.4 (0.9)	14.7 (0.6)	<0.001	0.58
		Dry	16.6 (0.7)	17.6 (0.4)	0.001	0.59
	Transverse	Wet	19.5 (1.7)	21.2 (1.0)	0.006	0.61
		Dry	26.7 (1.5)	26.8 (1.5)		
E''	Longitudinal	Wet	0.61 (0.02)	0.61 (0.02)		
		Dry	0.40 (0.01)	0.40 (0.01)		
	Transverse	Wet	0.65 (0.03)	0.67 (0.03)		0.44
		Dry	0.46 (0.04)	0.47 (0.02)		
H	Longitudinal	Wet	0.38 (0.04)	0.42 (0.03)	0.021	0.34*
		Dry	0.50 (0.03)	0.52 (0.03)		
	Transverse	Wet	0.51 (0.04)	0.56 (0.03)	0.011	0.49
		Dry	0.88 (0.08)	0.86 (0.07)		

Data in Young and Aged columns are Mean (SD)
Young = Age ≤ 60 years
Aged = Age > 60 years
p = Wilcoxon rank sum test p-value
r_s = Spearman rank correlation coefficient
* $0.05 < p < 0.10$

Young – Aged difference in the Transverse – Dry case. The significant correlations with Age for E′ were the same as when grouped by age. Namely, all E′ were positively correlated with Age for each of the Section – Condition combinations, apart from Transverse – Wet. Figure 29 shows scatterplots of the E′ vs. Age data, with significant correlations indicated by best fit lines.

E″ was generally seen to be unchanged with age. In the case of Transverse – Wet, E″ was positively correlated with Age. However, none of the other Section – Condition combinations had significant E″ – Age correlations. Also, there were no statistically significant E″ differences between the two age groups. The scatterplots of E″ vs. Age data are shown in Figure 30.

The trends with age for H were similar to E′ but were not as strong. Aged > Young for Longitudinal – Wet and Transverse – Wet. The H – Age correlation was significant for Transverse – Wet but was only nearly significant for Longitudinal – Wet. Unlike for E′, H did not have a significant age-dependence for Longitudinal – Dry. The human femur H vs. Age scatterplots can be seen as Figure 31.

The magnitudes of the Wet condition indentation changes with age are given in Table 12, calculated from IRLS fits with Age as the predictor variable. For both the Longitudinal and Transverse sections, E′ was ~15% greater when evaluated at the oldest donor age (97 years for Longitudinal, 98 years for Transverse) than the youngest donor age (21 years). The magnitudes of these changes were 1.9 GPa for the Longitudinal specimens and 2.8 GPa for the Transverse specimens. Similarly, the equations for H increased by ~12.5% over these age ranges, with increases of 0.05 GPa and 0.06 GPa, respectively. As mentioned previously, E″ had fewer significant changes with age than did E′ and H, with only the Transverse – Wet correlation being significant. The magnitudes of the changes with age for E″ were both less than 8%.

3.5.2 Rat Tibia

The rat tibia indentation changes with age data are shown in Table 13. Significant differences between age groups were seen for E′ and H but not for E″. E′ and H were seen to increase with age for Periosteal – Dry, Mid-cortex – Wet, and Mid-cortex

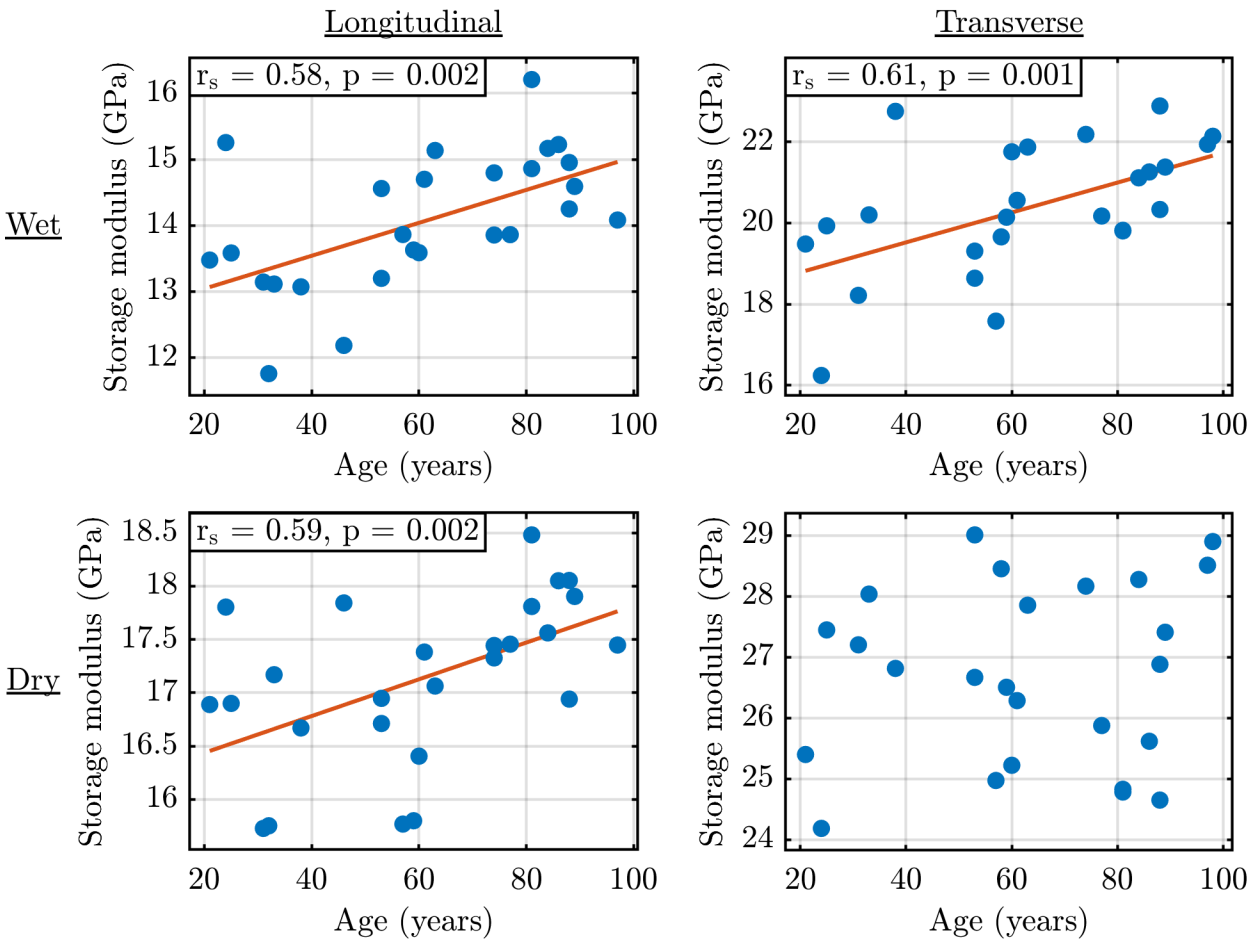


Figure 29: Scatterplots of human femur E′ vs. Age data. Significant correlations are indicated by best fit lines.

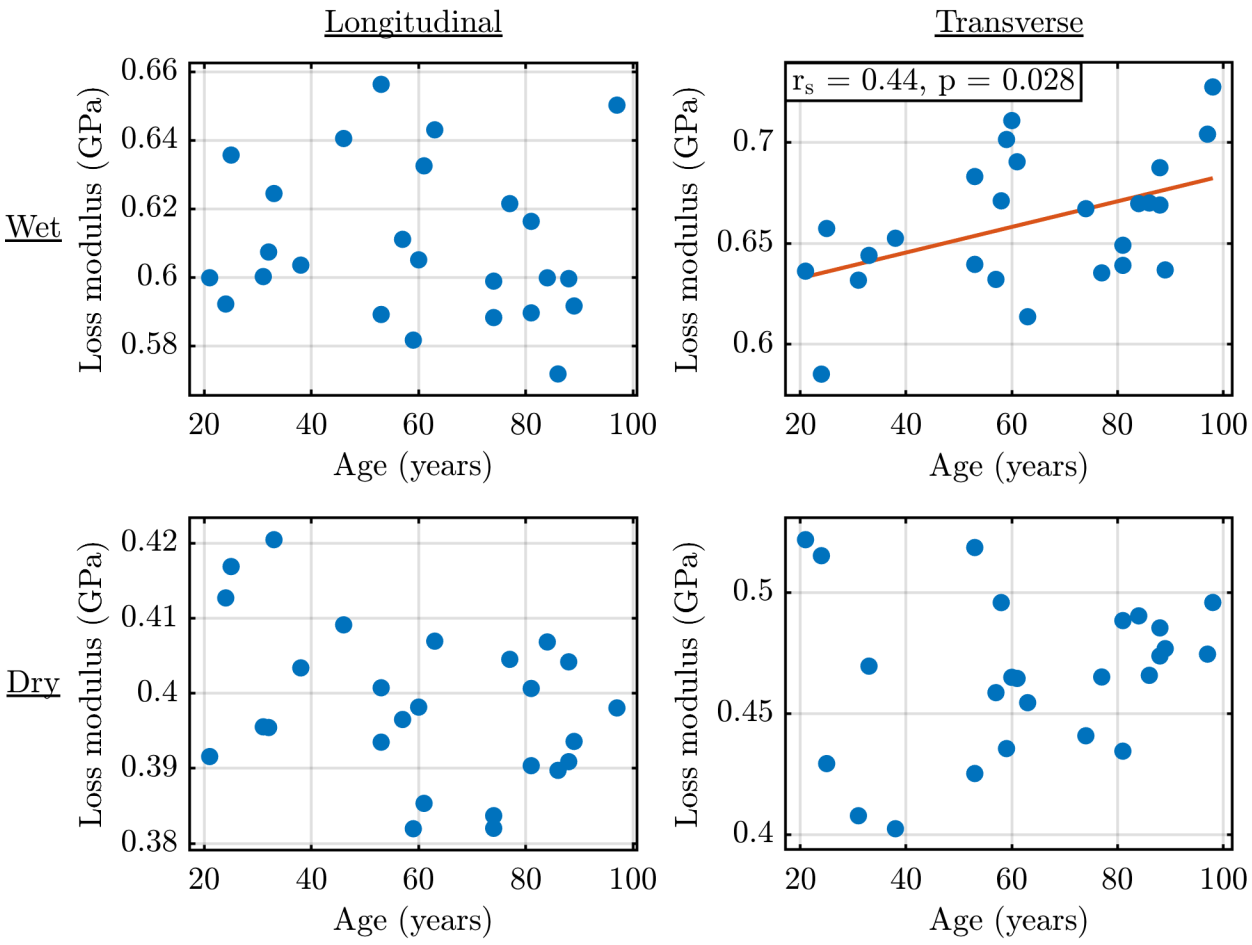


Figure 30: Scatterplots of human femur E″ vs. Age data. Significant correlations are indicated by best fit lines.

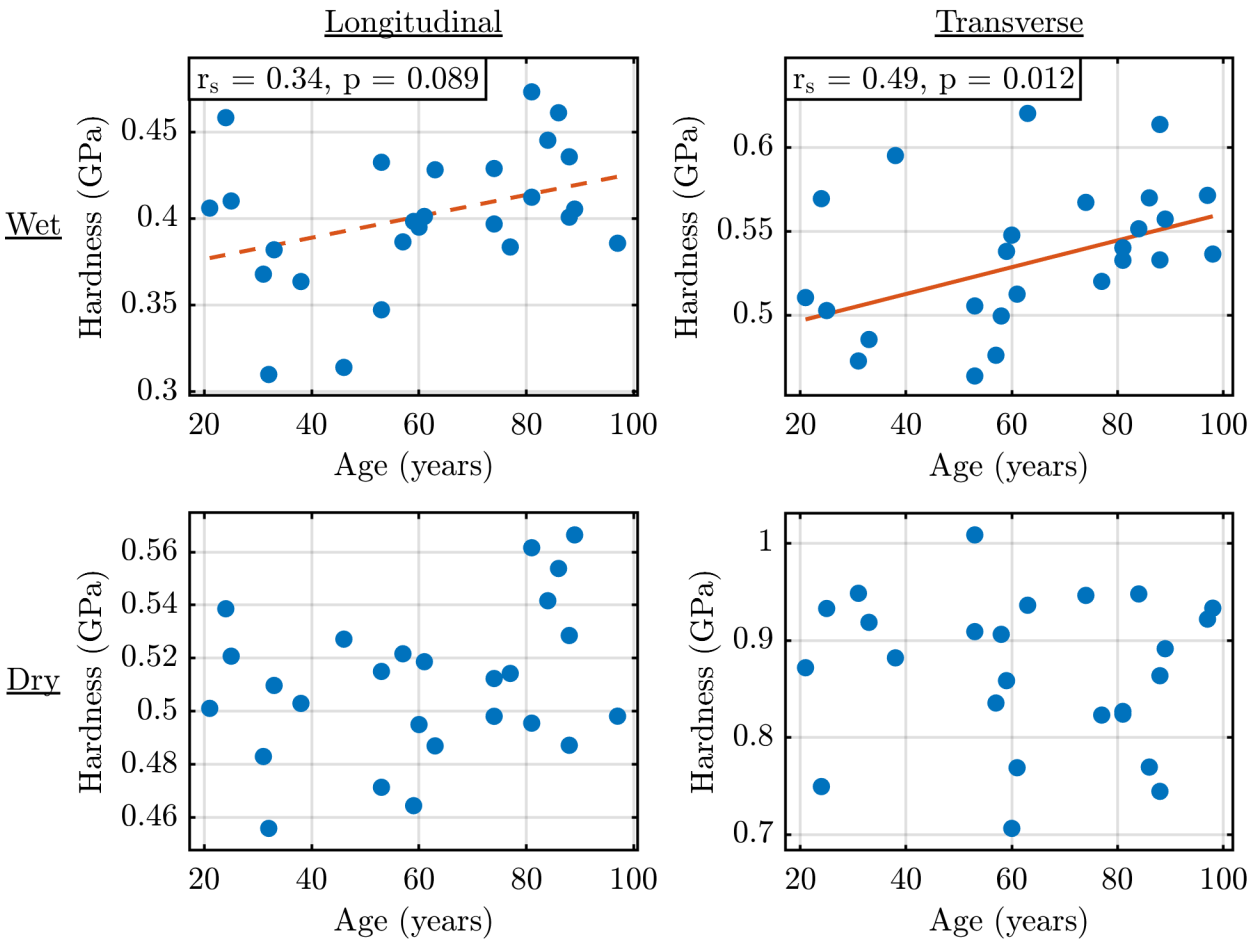


Figure 31: Scatterplots of human femur H vs. Age data. Significant (solid line) and nearly significant (dashed line) correlations are indicated by best fit lines.

Table 12: Change in Wet condition human femur indentation data over the full donor age range, evaluated from IRLS fit

Parameter	Section	Y(21)	Y(max)	Δ	Δ (%)
E'	Longitudinal	13.1	15.0	1.9	14.5
	Transverse	18.8	21.7	2.8	15.1
E"	Longitudinal	0.61	0.60	-0.01	-1.9
	Transverse	0.63	0.68	0.05	7.7
H	Longitudinal	0.38	0.42	0.05	12.5
	Transverse	0.50	0.56	0.06	12.4

Units are GPa, excepting Δ (%)
Y(21) = Fit evaluated at 21 years of age
Y(max) = Fit evaluated at 97 and 98 years for Longitudinal and Transverse, respectively
Δ = Y(max) – Y(21)

Table 13: Comparison of rat tibia indentation data by age group

Parameter	Location	Condition	Mean (SD)			p			
			6 months	12 months	24 months	KW	6 vs 12	12 vs 24	6 vs 24
E'	Periosteal	Wet	12.8 (2.6)	16.2 (2.9)	16.4 (3.3)	0.053*			
		Dry	27.4 (1.4)	28.7 (1.3)	29.8 (1.2)	0.004			0.003
	Mid-cortex	Wet	18.3 (1.5)	22.7 (2.3)	23.4 (2.7)	0.002	0.015		0.004
		Dry	31.3 (0.9)	33.1 (1.3)	33.9 (1.4)	<0.001	0.002		<0.001
E''	Periosteal	Wet	0.78 (0.08)	0.83 (0.05)	0.84 (0.06)				
		Dry	0.43 (0.01)	0.43 (0.01)	0.44 (0.01)				
	Mid-cortex	Wet	0.88 (0.04)	0.92 (0.03)	0.87 (0.06)	0.095*			
		Dry	0.43 (0.02)	0.44 (0.01)	0.44 (0.01)				
H	Periosteal	Wet	0.19 (0.05)	0.31 (0.08)	0.30 (0.10)	0.027	0.054*		
		Dry	1.08 (0.08)	1.15 (0.05)	1.20 (0.07)	0.009			0.006
	Mid-cortex	Wet	0.29 (0.05)	0.44 (0.12)	0.49 (0.12)	0.003	0.025		0.005
		Dry	1.22 (0.05)	1.31 (0.06)	1.33 (0.07)	<0.001	<0.001		0.001

KW = Kruskal-Wallis p-value
p = Dunn's test adjusted p-value for comparisons between age groups. Holm–Šidák adjustment with FWER = 0.05.
* $0.05 < p < 0.10$

– Dry. The difference between the 6 month and 24 month groups was the largest, followed by the 6 and 12 month groups. There were no significant differences between the 12 and 24 month old groups. Thus, E′ and H increased during skeletal maturation (6 vs. 12 month comparison) and slowed or plateaued thereafter (12 vs. 24 month comparison). The rat tibia indentation data for each Age Group – Condition – Location combination can be seen in Figures 25-27.

3.5.3 Comparison Between Human and Rat Results

Similar changes with age were seen in the human femur and rat tibia indentation data. In both experiments E′ and H increased with age, while E″ was largely unchanging with age. These changes with age occurred in both the Wet and Dry hydration test conditions.

3.6 Regression Models of Indentation Data

The linear regression models with the indentation parameters as the response variable and Condition, Section, Age, and Location as the predictor variables were:

$$E' = 12.9 + 6.2I_T + 3.8I_{Dry} + 3.3I_T I_{Dry} + 0.031(Age - 21) - 0.019I_{Dry}(Age - 21) \quad (43)$$

$$E'' = 0.61 - 0.21I_{Dry} + 0.05I_T - 0.02I_T I_{Dry} \quad (44)$$

$$H = 0.37 + 0.13I_T + 0.11I_{Dry} + 0.22I_T I_{Dry} + 0.04I_{Int} + 0.00035(Age - 21) \quad (45)$$

where the indicator variables are defined as:

$$I_T = \begin{cases} 0 & \text{Longitudinal} \\ 1 & \text{Transverse} \end{cases} \quad (46)$$

$$I_{Dry} = \begin{cases} 0 & \text{Wet} \\ 1 & \text{Dry} \end{cases} \quad (47)$$

$$I_{Int} = \begin{cases} 0 & \text{Osteonal} \\ 1 & \text{Interstitial} \end{cases} \quad (48)$$

E′, E″, and H are in GPa units, and Age is in years. Terms in the regression models are ordered left to right in the order in which they were added to the model. See the

Indentation Regression Models section (page 60) for more information about the models.

As would be expected, the terms in the final regression models are in agreement with the results of the statistical hypothesis tests presented in the preceding Wet vs. Dry, Longitudinal vs. Transverse, Osteonal vs. Interstitial, and Changes with Age sections. Namely,

$$\mathrm{E}' = f(\mathrm{Section}, \mathrm{Condition}, \mathrm{Age}) \quad (49)$$

$$\mathrm{E}'' = f(\mathrm{Section}, \mathrm{Condition}) \quad (50)$$

$$\mathrm{H} = f(\mathrm{Section}, \mathrm{Condition}, \mathrm{Age}, \mathrm{Location}) \quad (51)$$

For E′ and H, anisotropy had a larger effect in the model than did hydration, as the I_T term was added before the I_{Dry} term. For E″ the opposite was true, and the magnitude of the I_{Dry} term was approximately 4 times that of the I_T term. Indent location had a larger effect on H than did age, as the I_{Int} term was added to the model before the Age term. However, the opposite was true for E′, as E′ was a function of age but not location.

3.7 Correlations Between Indentation and Compositional Data

3.7.1 Human Femur

The correlations between the human femur indentation and compositional data are provided in Table 14. The strongest correlation was between E′ and TMD (tissue mineral density), in which a positive correlation was observed for Longitudinal – Wet, Longitudinal – Dry, and Transverse – Dry. Additionally, Transverse – Wet had a nearly significant positive correlation. E′ plotted against TMD is shown as Figure 32. Neither E″ nor H had any significant correlations with TMD. E′ was negatively correlated with BoundWater (bound water volume fraction) for Longitudinal – Dry, and the correlation for Longitudinal – Wet was nearly significant as well. Scatterplots of E′ vs. BoundWater can be seen in Figure 33. BoundWater was also negatively correlated with E″ in the case of Transverse – Dry, however, not for any of the other Section – Condition

Table 14: Correlations between human femur indentation and compositional data

	E'				E''				H			
	Longitudinal		Transverse		Longitudinal		Transverse		Longitudinal		Transverse	
	Wet	Dry	Wet	Dry	Wet	Dry	Wet	Dry	Wet	Dry	Wet	Dry
TMD	0.40	0.62	0.38*	0.40								
BoundWater	-0.38*	-0.40						-0.54				
PE			0.46	0.37*		-0.34*						

* 0.05 < p < 0.10
TMD = tissue mineral density
BoundWater = bound water volume fraction
PE = pentosidine crosslinking concentration

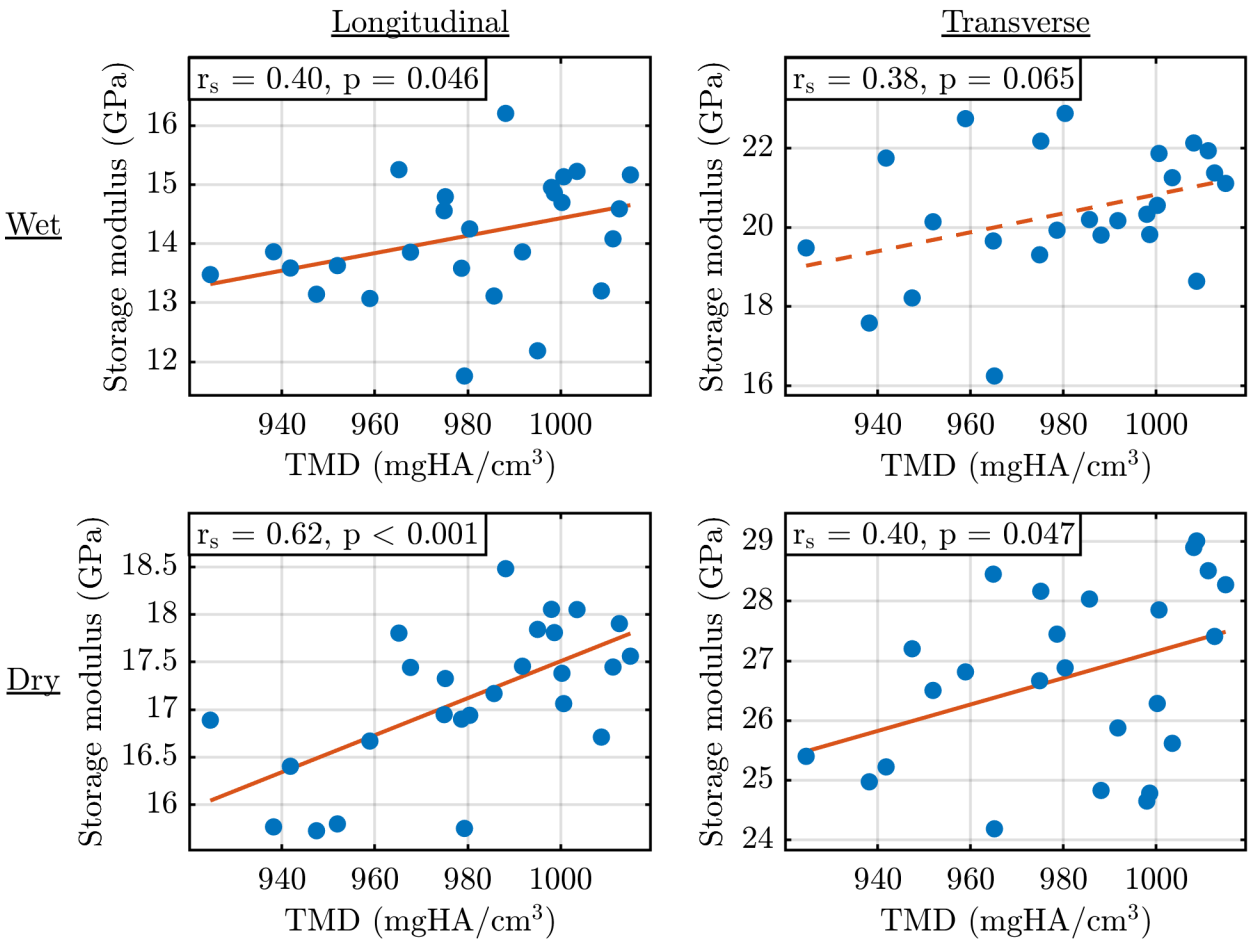


Figure 32: Scatterplots of human femur E′ vs. TMD data. Significant (solid lines) and nearly significant (dashed line) correlations are indicated by best fit lines.

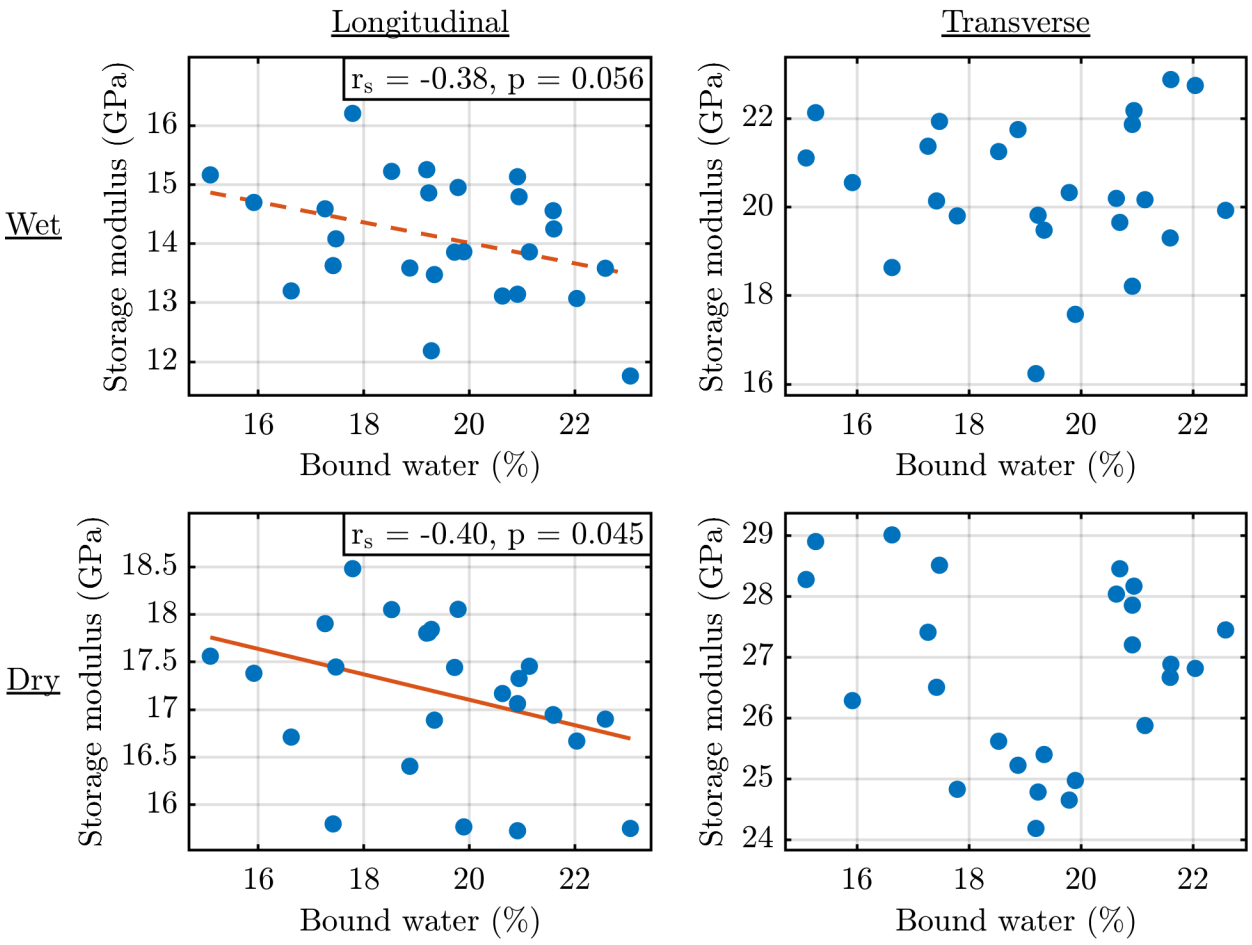


Figure 33: Scatterplots of human femur E′ vs. BoundWater data. Significant (solid line) and nearly significant (dashed line) correlations are indicated by best fit lines.

combinations. Finally, E′ was positively correlated with PE (pentosidine crosslinking concentration) for Transverse – Wet and nearly positively correlated for Transverse – Dry. Scatterplots of E′ against PE can be seen as Figure 34.

3.7.2 Site-matched Indentation – qBEI Correlations (Human Femur)

To directly assess the dependence of local mineralization on the indentation parameters, the locations of Transverse section indents were identified on the qBEI images, and for each specimen the correlation between the indentation data and the extracted local qBEI Ca wt.% was calculated. A summary of these correlations is shown in Table 15. E′ and H were positively correlated with qBEI Ca wt.%, with the mean correlation coefficients being in the range 0.23-0.31. The null hypothesis was not rejected for E″, and E″ was therefore not found to be correlated with qBEI Ca wt.%. Boxplots of the site-matched indentation – qBEI correlation data are shown in Figure 35. From this figure it is readily seen that the bulk of the correlation values (r_s) for E′ and H were positive, while those for E″ were centered around 0.

The positive correlations between E′ and H and qBEI Ca wt.%. were partly driven by the difference in mineralization between osteonal and interstitial areas. For each specimen, Interstitial Ca wt.% was greater than Osteonal Ca wt.%. A boxplot of the ratio of these qBEI mineralization values can be seen as Figure 36. The mean Interstitial/Osteonal Ca wt.% ratio was 1.03.

3.7.3 Rat

The correlations between the rat indentation and compositional data are shown in Table 16. There were two consistent correlations. First, E′ and H were positively correlated with TMD for both Wet and Dry conditions. Second, E′ and H were negatively correlated with BoundWater, again for both Wet and Dry conditions. Plots of E′ vs TMD and vs. BoundWater can be seen as Figures 37 and 38. PE was mostly uncorrelated with the indentation data. However, E′ was positively correlated with PE in the Wet condition. Scatterplots of E′ vs. PE can be seen as Figure 39.

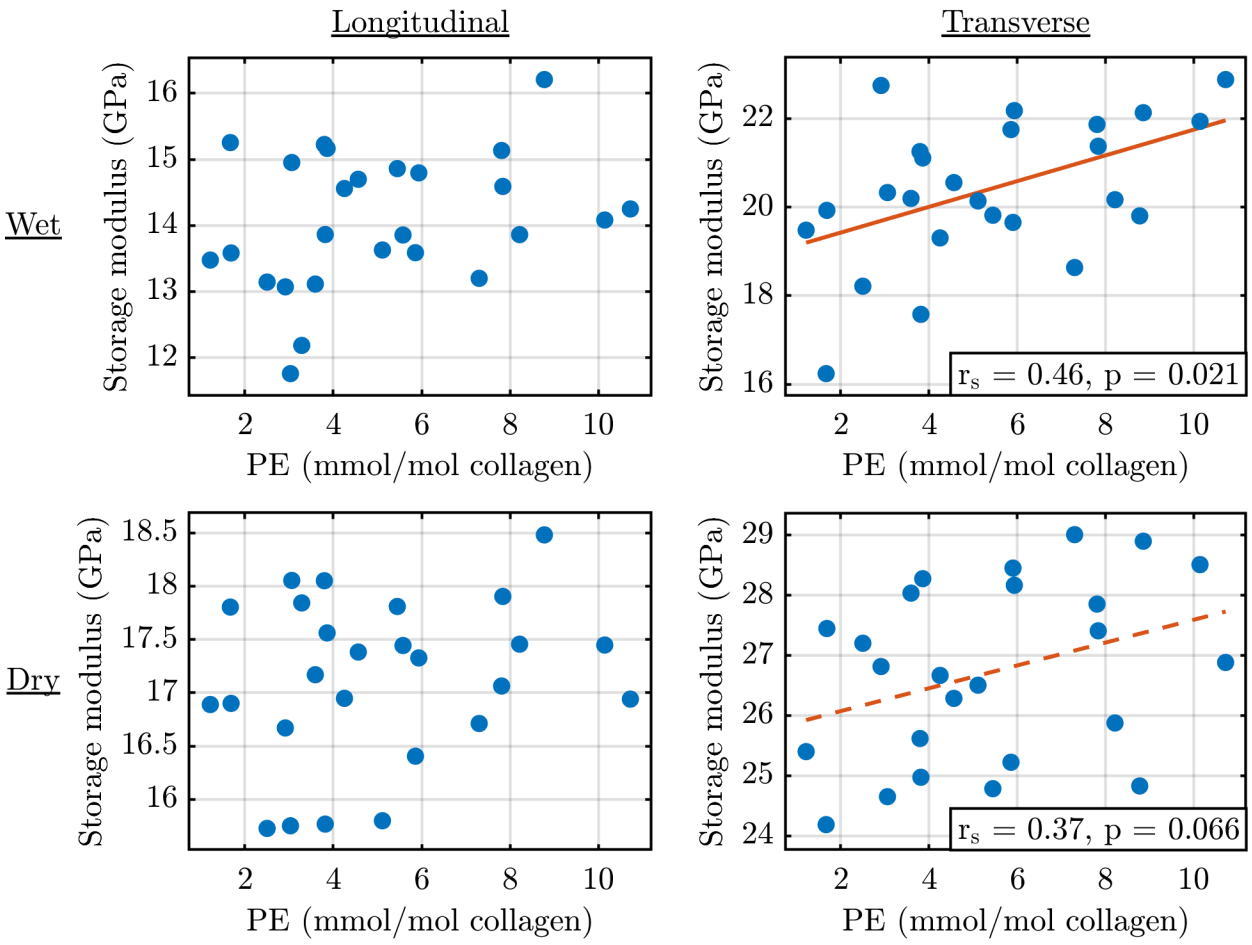


Figure 34: Scatterplots of human femur E′ vs Pentosidine data. Significant (solid line) and nearly significant (dashed line) correlations are indicated by best fit lines.

Table 15: Human femur site-matched indentation – qBEI Ca wt.% correlation data

Parameter	Condition	r_s	p
E'	Wet	0.23 (0.21)	<0.001
	Dry	0.23 (0.21)	<0.001
E"	Wet	-0.04 (0.25)	
	Dry	0.06 (0.19)	
H	Wet	0.28 (0.21)	<0.001
	Dry	0.31 (0.16)	<0.001

Data in r_s column are Mean (SD)
r_s = Spearman rank correlation coefficient
p = Wilcoxon signed rank test p-value

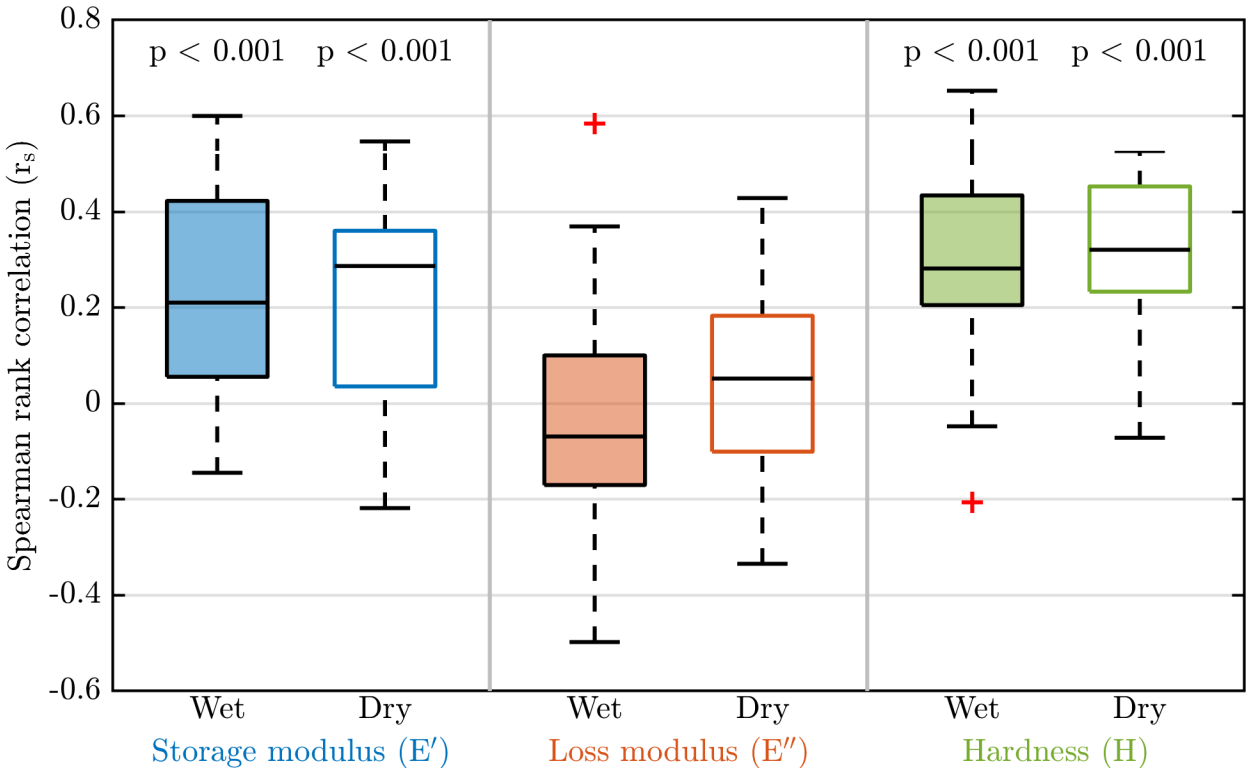


Figure 35: Boxplots of the specimen r_s values between the human femur site-matched indentation and qBEI Ca wt.% data. The p-values shown above the boxes indicate a significant correlation between the indentation and qBEI Ca wt.% data.

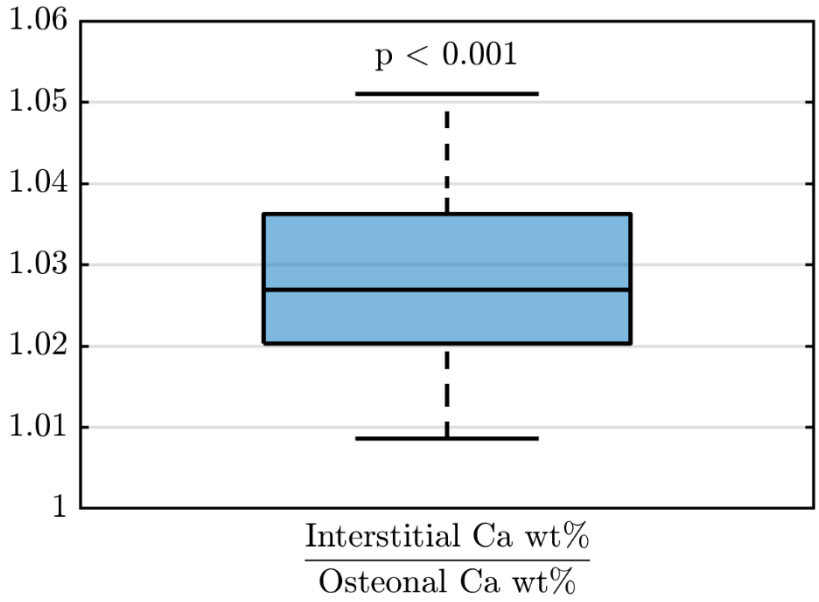


Figure 36: Boxplot of Interstitial/Osteonal qBEI Ca wt.% ratios for the human femur Transverse specimens. As indicated by the p-value above the box, Interstitial mineralization was seen to be greater than Osteonal mineralization.

Table 16: Correlations between rat tibia Mid-cortex indentation data and rat bone compositional data

	E'		E"		H	
	Wet	Dry	Wet	Dry	Wet	Dry
TMD	0.49	0.69			0.54	0.65
BoundWater	-0.67	-0.64			-0.69	-0.62
PE	0.41					

* 0.05 < p < 0.10

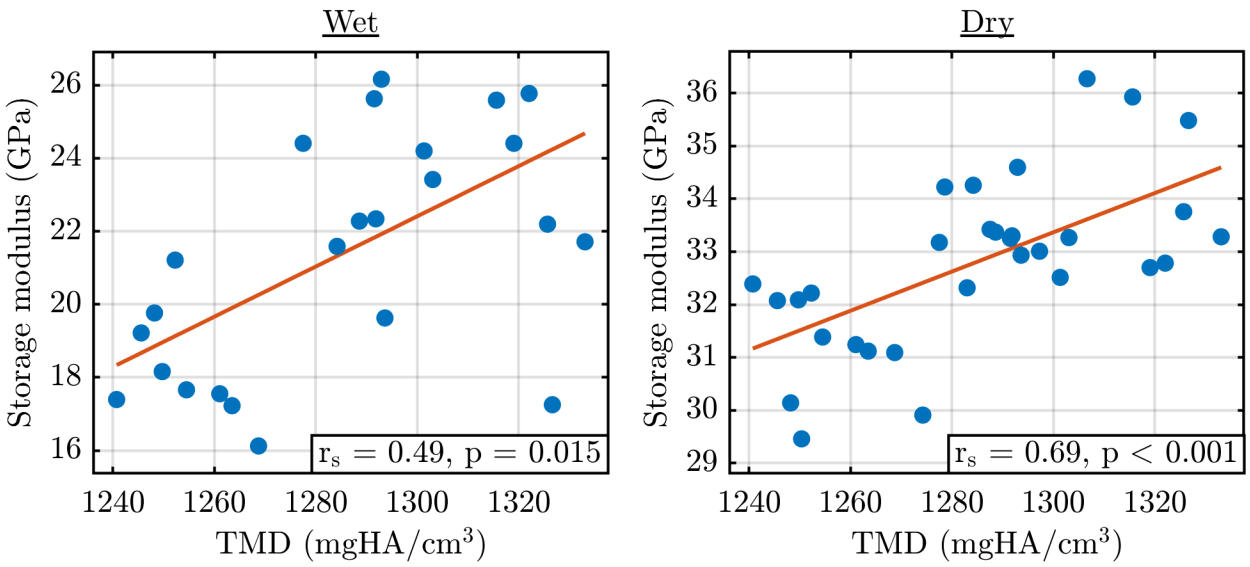


Figure 37: Scatterplots of rat E′ vs. TMD data. Significant correlations are indicated by best fit lines.

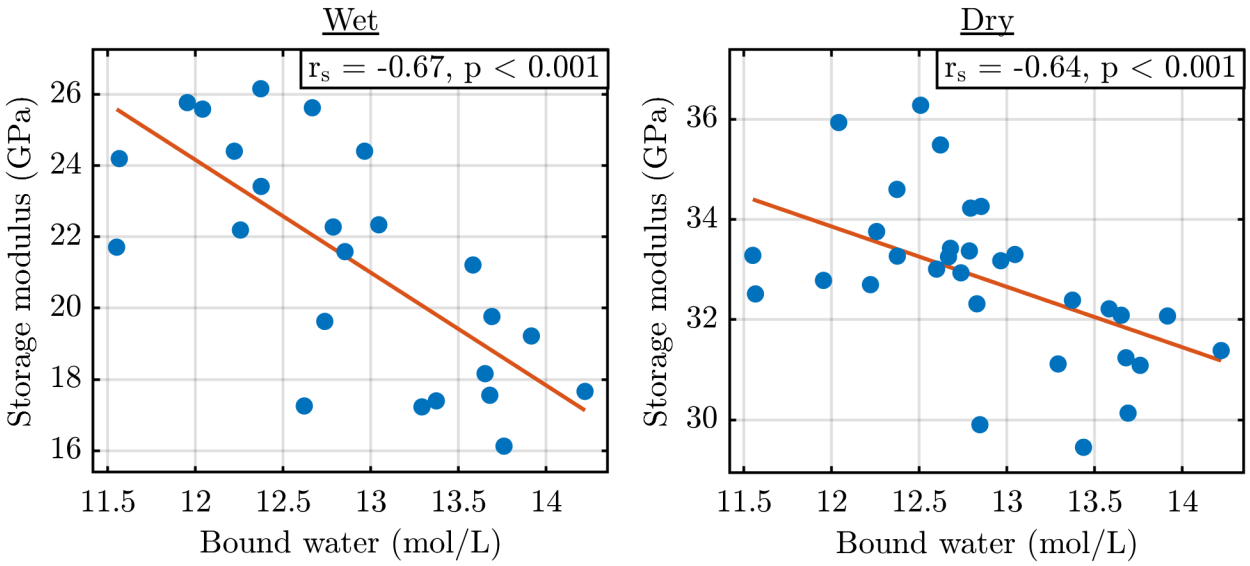


Figure 38: Scatterplots of rat E′ vs. BoundWater data. Significant correlations are indicated by best fit lines.

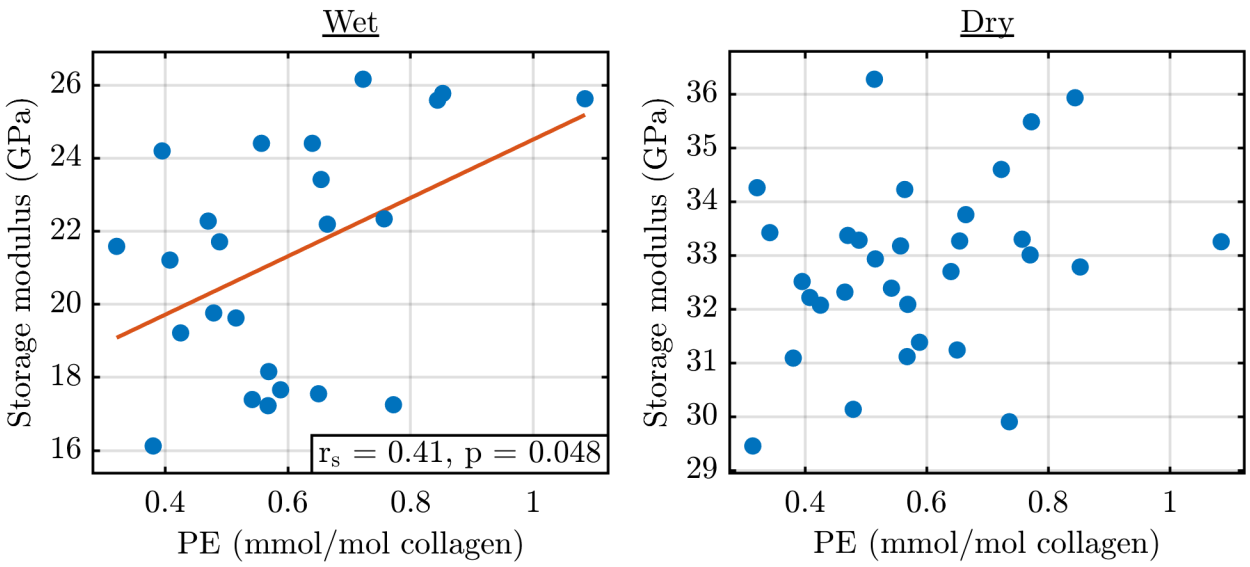


Figure 39: Scatterplots of rat E′ vs. Pentosidine data. Significant correlations are indicated by best fit lines.

3.7.4 Comparison Between Human and Rat Results

There was substantial similarity between the observed human and rat indentation – composition correlations. In both experiments, E′ was positively correlated with TMD and negatively correlated with BoundWater. E′ was also positively correlated with PE in both experiments; however, there were more instances of E′ and PE not being correlated than instances in which they were. The site-matched indentation-qBEI Ca wt.% correlations further support the idea that E′ and H increase with increased mineralization.

3.8 Correlations Between Fracture Data and Compositional and Structural Data

3.8.1 Human Femur

Correlations between the human femur fracture data and compositional and structural data are presented as Table 17. Out of the 6 composition and structure parameters, there were 5 significant correlations for K_{init}, 2 for J-integral, and none for K_{grow}. The terms associated with porosity (Porosity, PoreWater) were negatively correlated with K_{init}. See Figure 40 for scatterplots of the fracture parameters vs. Porosity and PoreWater. K_{init} was positively correlated with BoundWater. Also, TMD was negatively correlated with K_{init} and J-integral. Finally, OstAr (osteonal area fraction) was positively correlated with K_{init} and J-integral. Scatterplots of the K_{init}, J-integral, and K_{grow} vs. BoundWater, TMD, and OstAr are presented as Figures 41-43.

3.8.2 Rat

The correlations between the rat fracture parameters and the compositional and structural data can be found in Table 18. CrackingToughness had a significant correlation with each parameter, with the only positive correlation being with BoundWater. Thus, CrackingToughness was negatively correlated with porosity (Porosity, PoreWater), mineralization (TMD), and crosslinking (PE). There were three

Table 17: Correlations between human femur fracture parameters and compositional and structural data

	K_{init}	J-integral	K_{grow}
Porosity	-0.52		
PoreWater	-0.46		
BoundWater	0.61		
TMD	-0.53	-0.39	
OstAr	0.40	0.47	
PE			

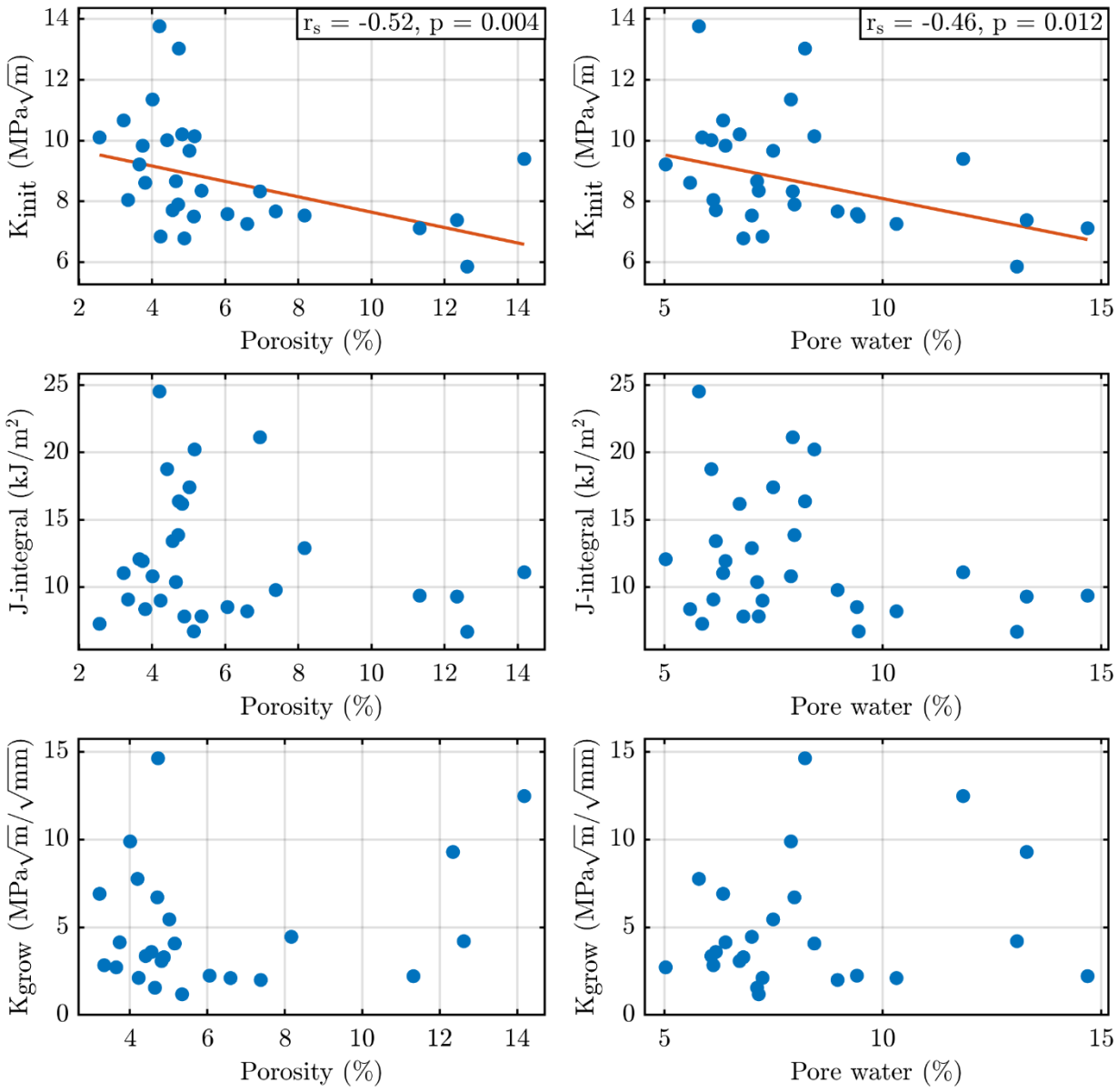


Figure 40: Scatterplots of human femur fracture parameters vs. Porosity (left) and PoreWater (right). Significant correlations are indicated by best fit lines.

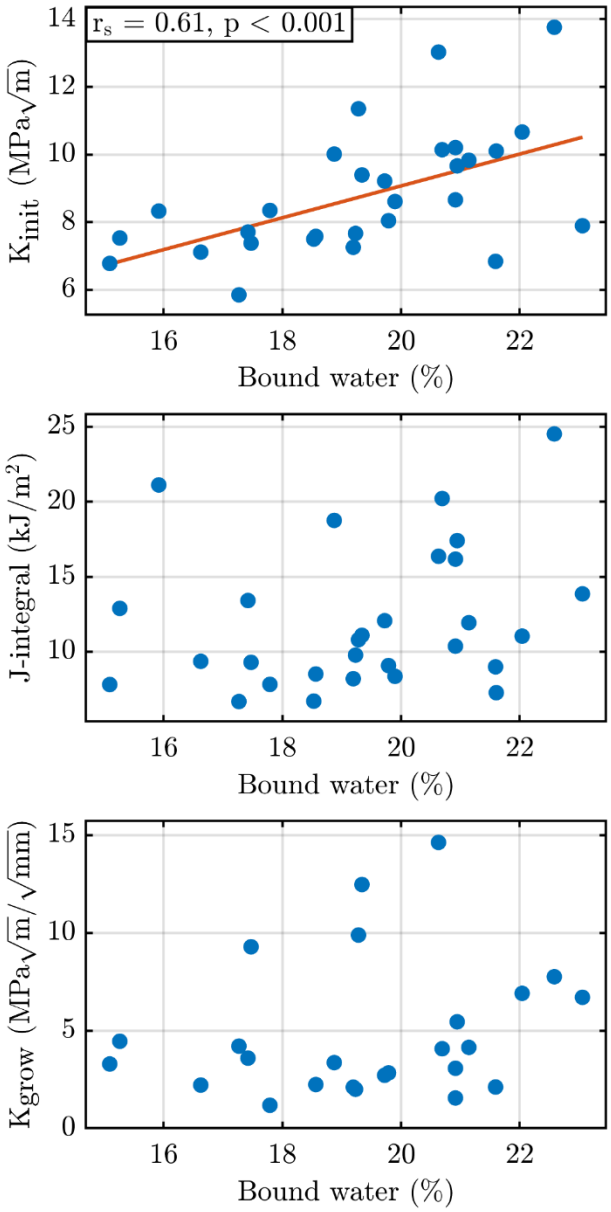


Figure 41: Scatterplots of human femur fracture parameters vs. BoundWater. Significant correlations are indicated by best fit lines.

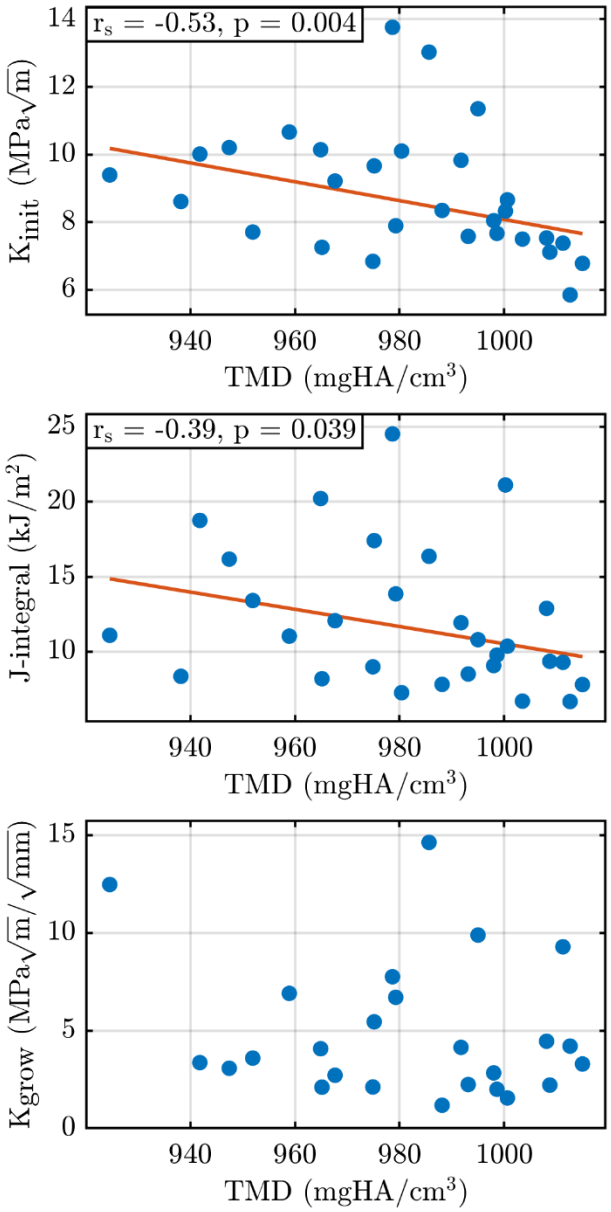


Figure 42: Scatterplots of human femur fracture parameters vs. TMD. Significant correlations are indicated by best fit lines.

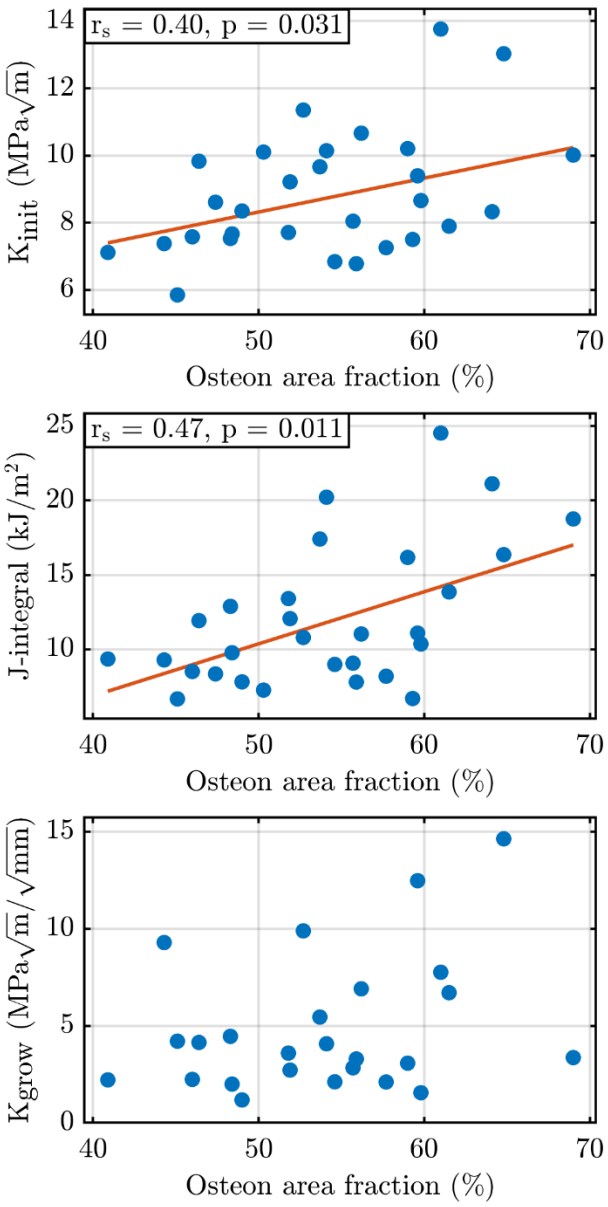


Figure 43: Scatterplots of human femur fracture parameters vs. OstAr. Significant correlations are indicated by best fit lines.

Table 18: Correlations between rat fracture parameters and compositional and structural data

	K_C	Cracking toughness
Porosity	0.48	-0.68
PoreWater		-0.51
BoundWater	-0.55	0.47
TMD	0.38	-0.58
PE		-0.45

significant correlations with K_c; namely Porosity, BoundWater, and TMD. The K_c correlations had the opposite signs as their corresponding CrackingToughness correlations. For example, TMD was positively correlated with K_c and negatively correlated with CrackingToughness. Scatterplots of the rat fracture data against the compositional and structural data can be seen in Figures 44-47.

3.8.3 Comparison Between Human and Rat Results

The correlations between the fracture data and compositional and structural data were similar for the human and rat experiments. K_{init} (human femur) and CrackingToughness (rat femur) were both positively correlated with BoundWater and negatively correlated with Porosity, PoreWater, and TMD.

3.9 Correlations Between Indentation and Fracture Data

3.9.1 Human Femur

The correlations between the human femur indentation and fracture data are shown in Table 19. There were no significant correlations for E″. The correlations between the fracture parameters and E′ and H were all negative. The only significant K_{init} correlations were with Longitudinal – Wet E′ and H. See Figure 48 for plots of K_{init} vs. E′. The fracture parameter with the most correlations was J-integral. Longitudinal – Wet and Longitudinal – Dry E′ and H were negatively correlated with J-integral. Transverse – Wet H was also negatively correlated with J-integral. Figures 49 and 50 are plots of J-integral vs. E′ and H, respectively. The significant K_{grow} correlations were the same as for K_{init} (i.e. Longitudinal – Wet E′ and H). Scatterplots of the K_{grow} vs. E′ data can be seen as Figure 51.

3.9.2 Rat

The correlations between the rat tibia Mid-cortex indentation and femur fracture data are given in Table 20. As with the human femur data, E″ had no significant correlations with fracture. K_c was positively correlated with E′ and H, while

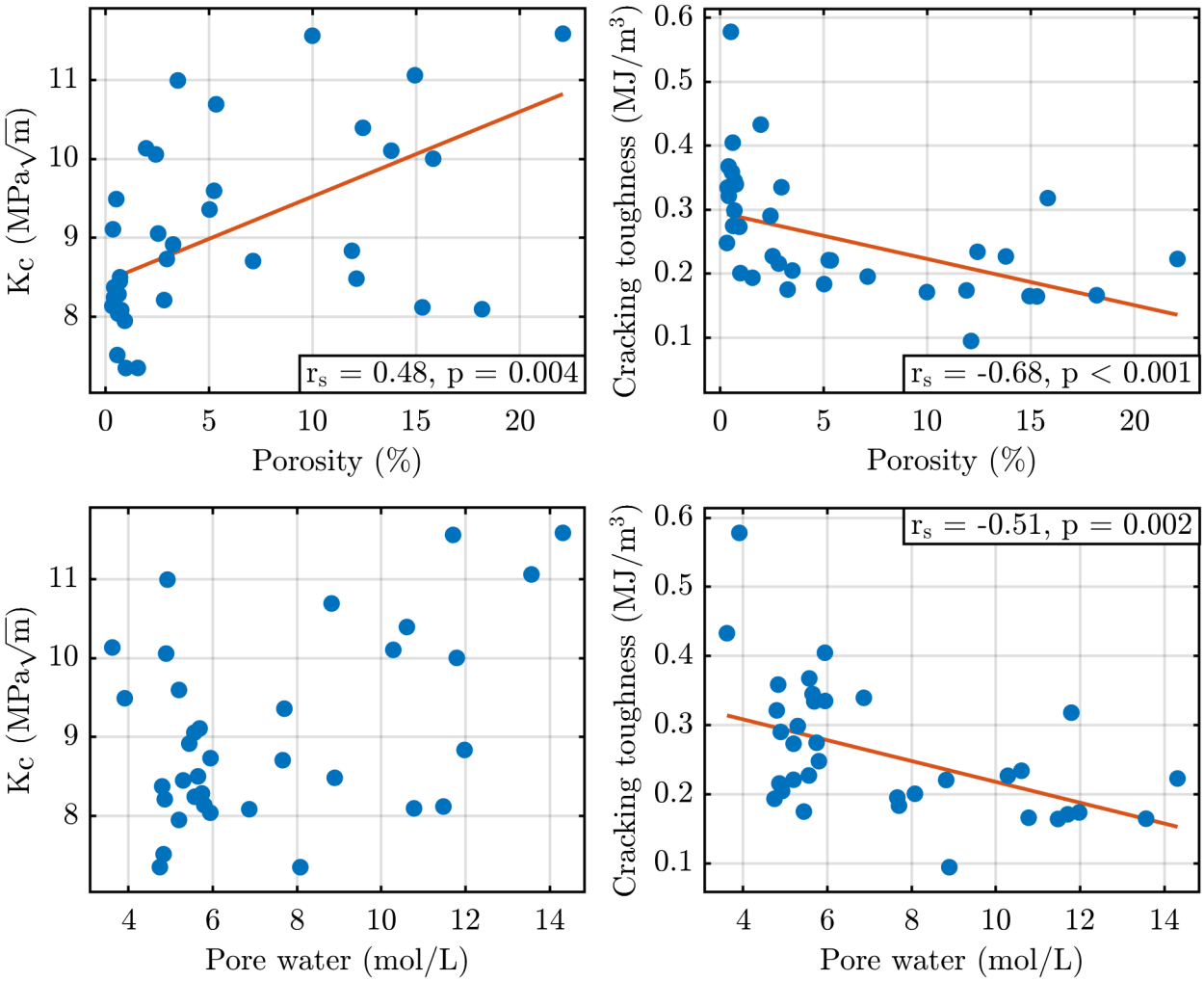


Figure 44: Scatterplots of rat fracture parameters vs. Porosity (top) and PoreWater (bottom). Significant correlations are indicated by best fit lines.

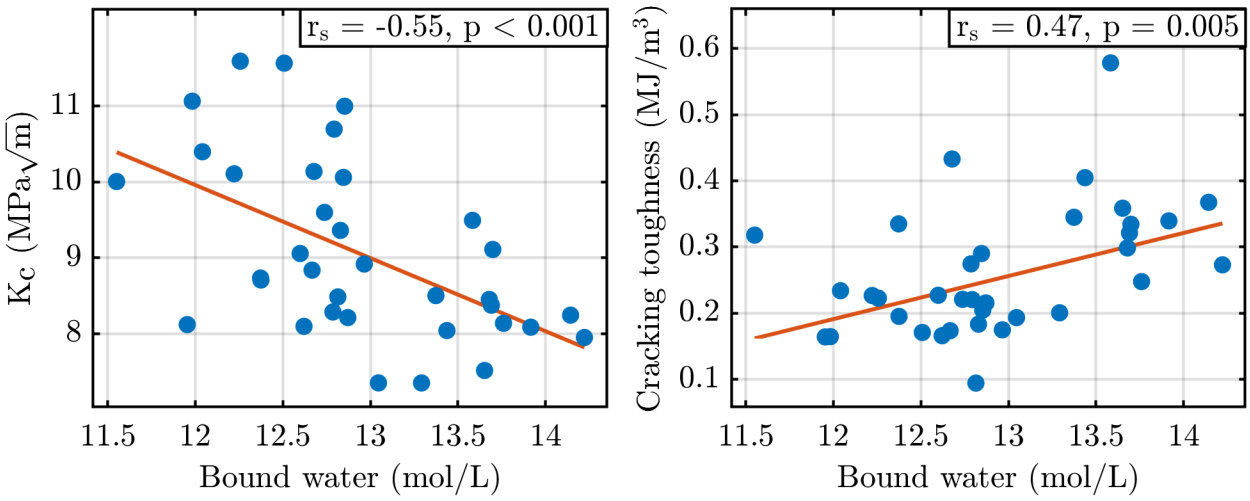


Figure 45: Scatterplots of rat fracture parameters vs. BoundWater. Significant correlations are indicated by best fit lines.

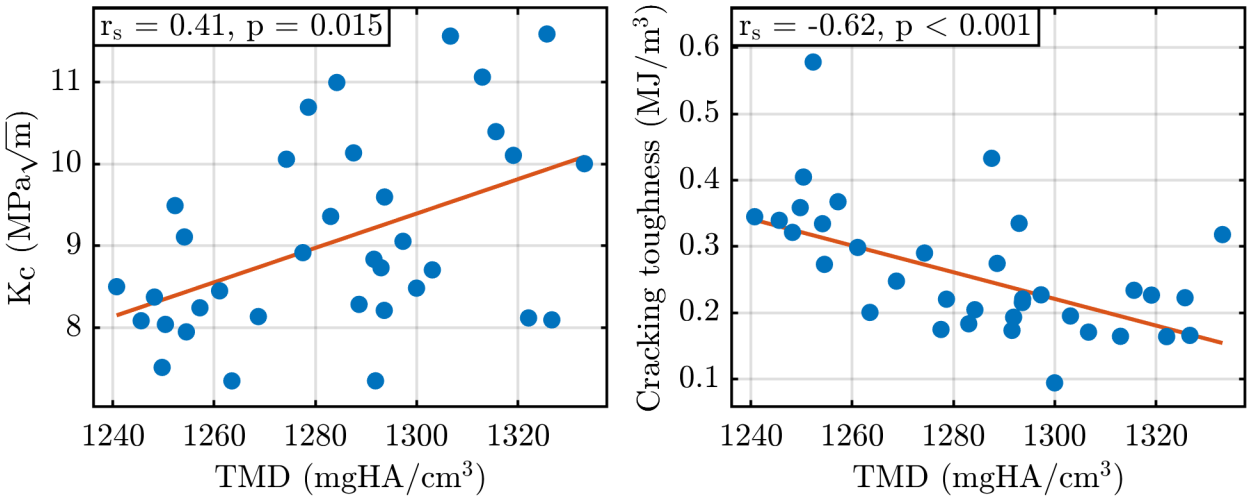


Figure 46: Scatterplots of rat fracture parameters vs. TMD. Significant correlations are indicated by best fit lines.

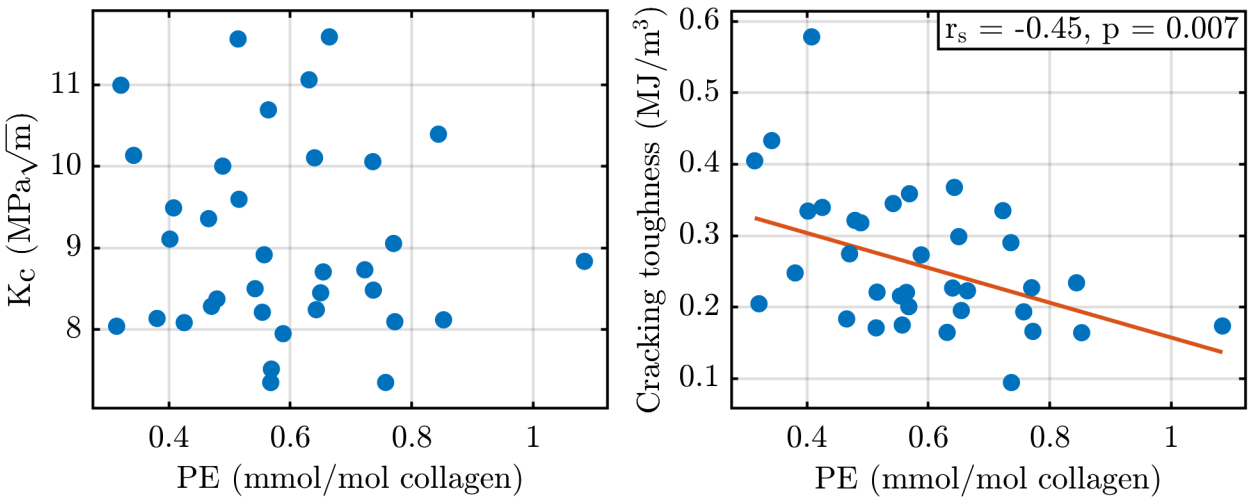


Figure 47: Scatterplots of rat fracture parameters vs. Pentosidine. Significant correlations are indicated by best fit lines.

Table 19: Correlations between human femur indentation and fracture data

	E'				E''				H			
	Longitudinal		Transverse		Longitudinal		Transverse		Longitudinal		Transverse	
	Wet	Dry	Wet	Dry	Wet	Dry	Wet	Dry	Wet	Dry	Wet	Dry
K_{init}	-0.53							-0.37*	-0.40			
J-integral	-0.56	-0.50			0.36*				-0.43	-0.49	-0.41	
K_{grow}	-0.66		0.41*	0.39*					-0.53			

* $0.05 < p < 0.10$

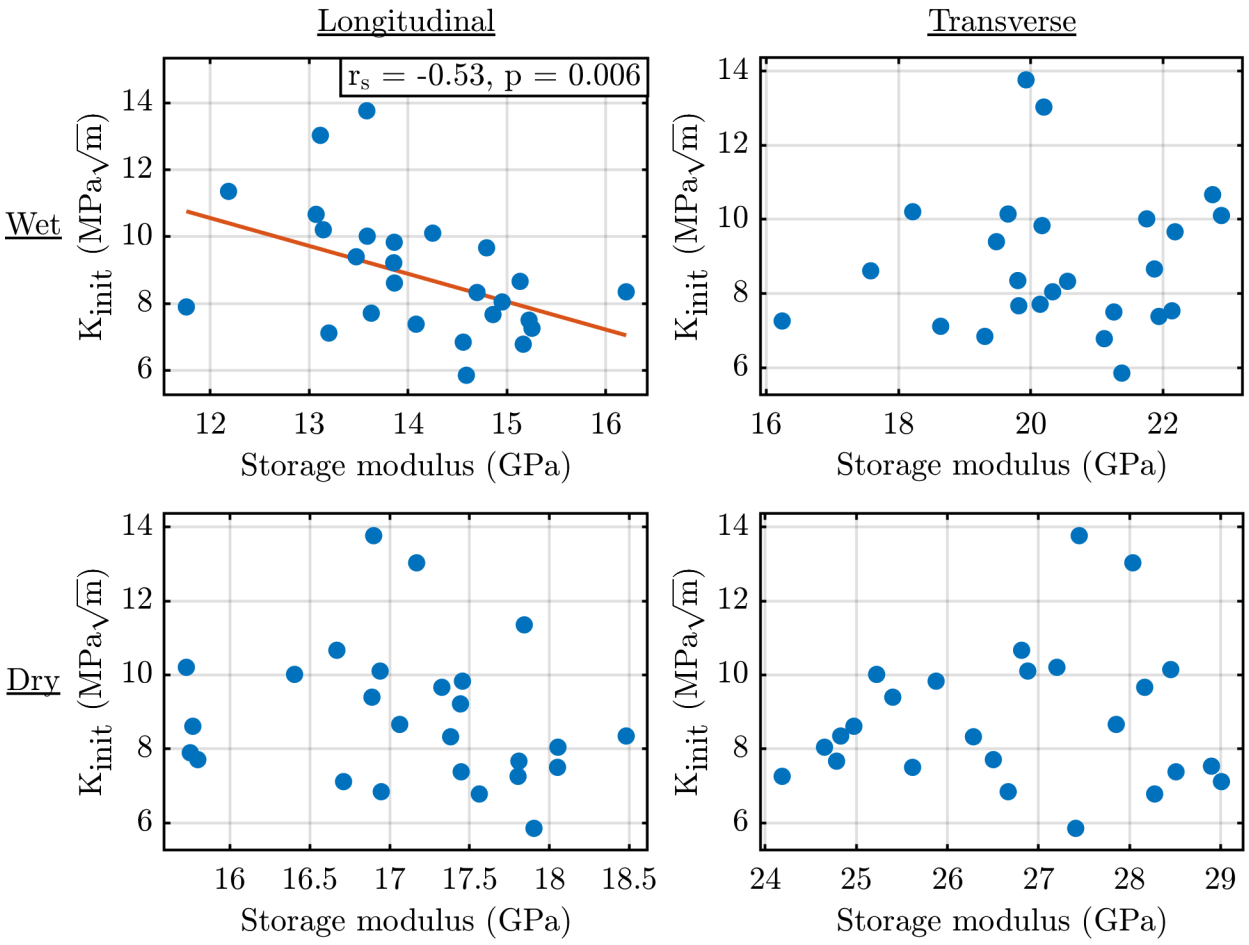


Figure 48: Scatterplots of human femur K_{init} vs. E′ data. Significant correlations are indicated by best fit lines.

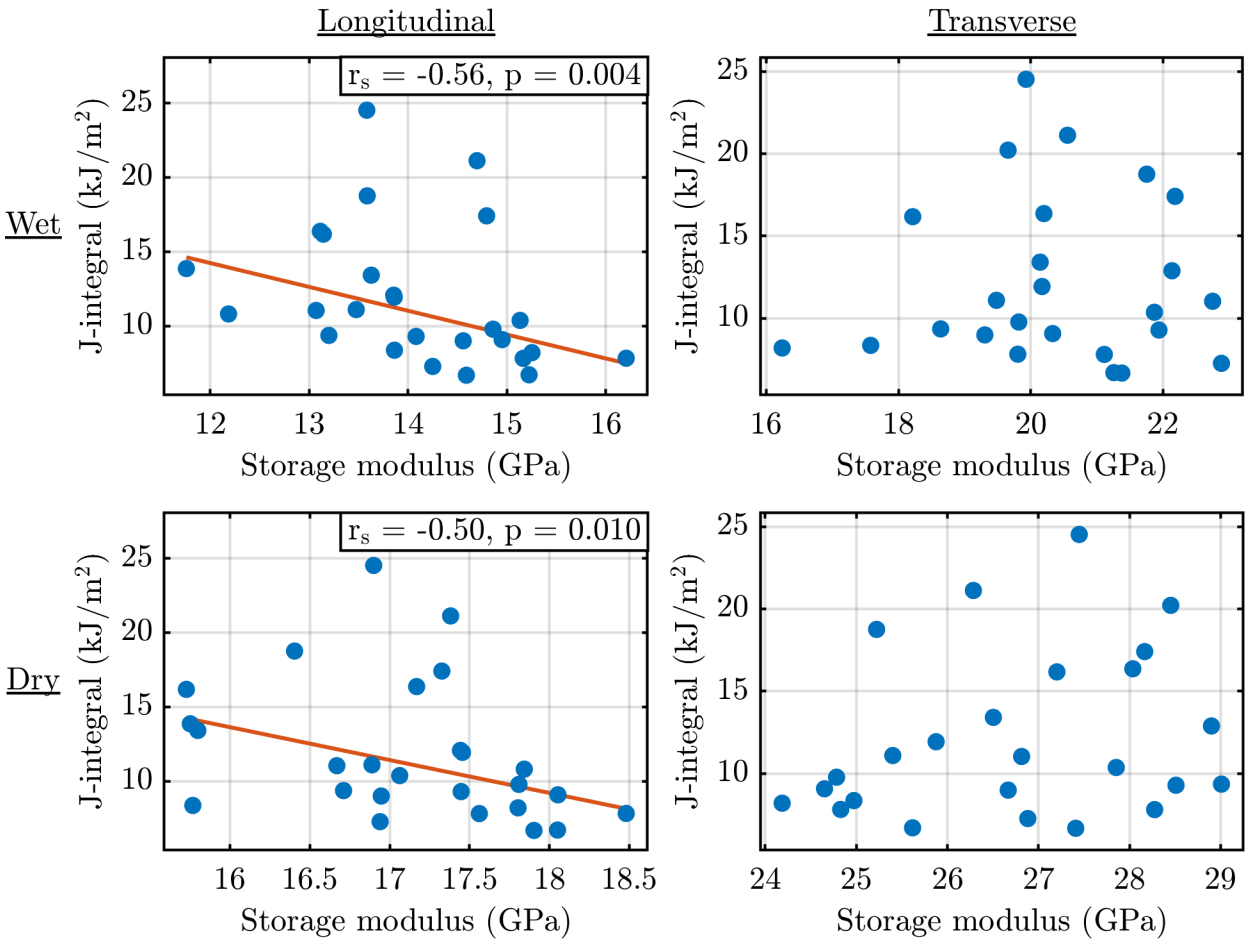


Figure 49: Scatterplots of human femur J-integral vs. E′ data. Significant correlations are indicated by best fit lines.

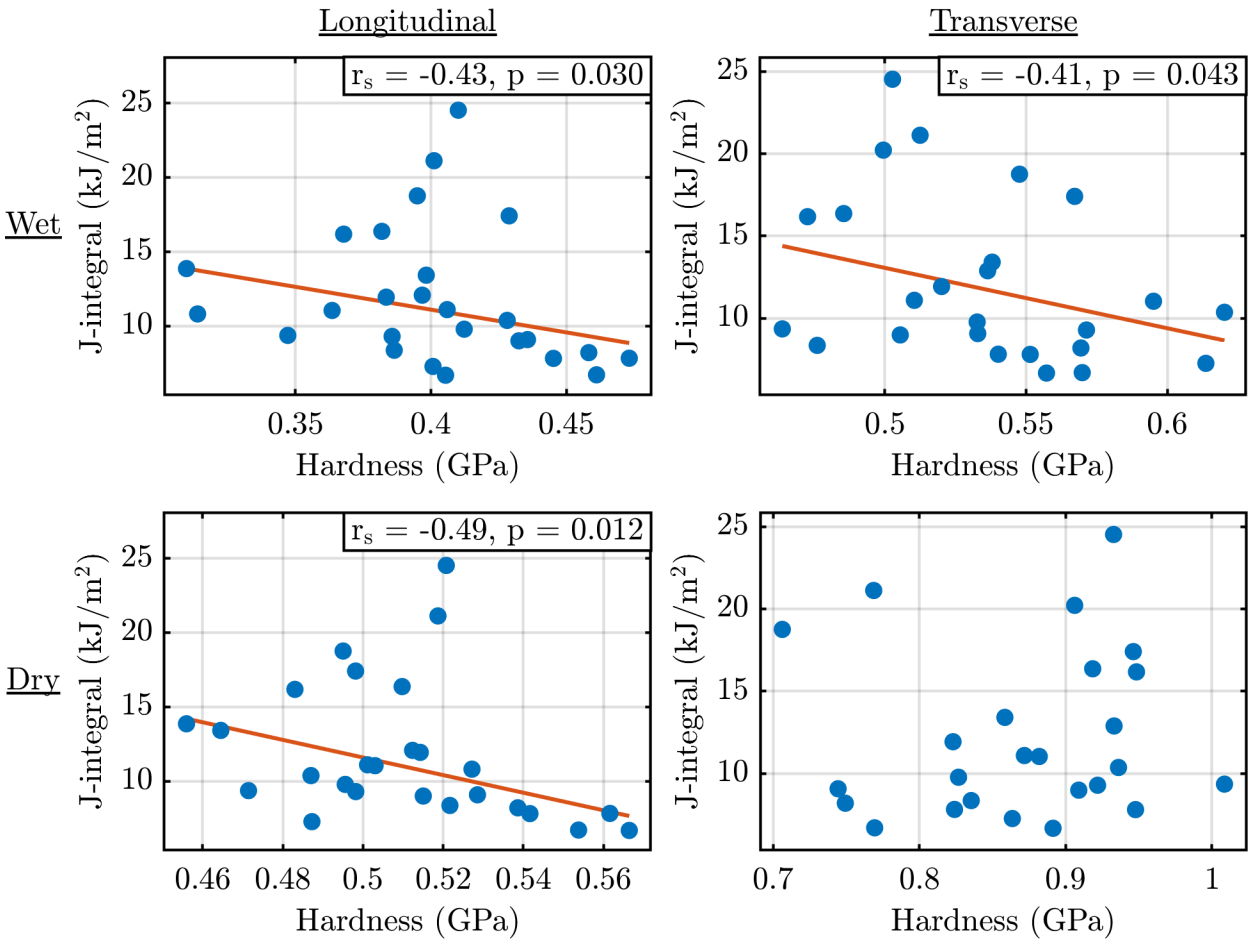


Figure 50: Scatterplot of human femur J-integral vs. H data. Significant correlations are indicated by best fit lines.

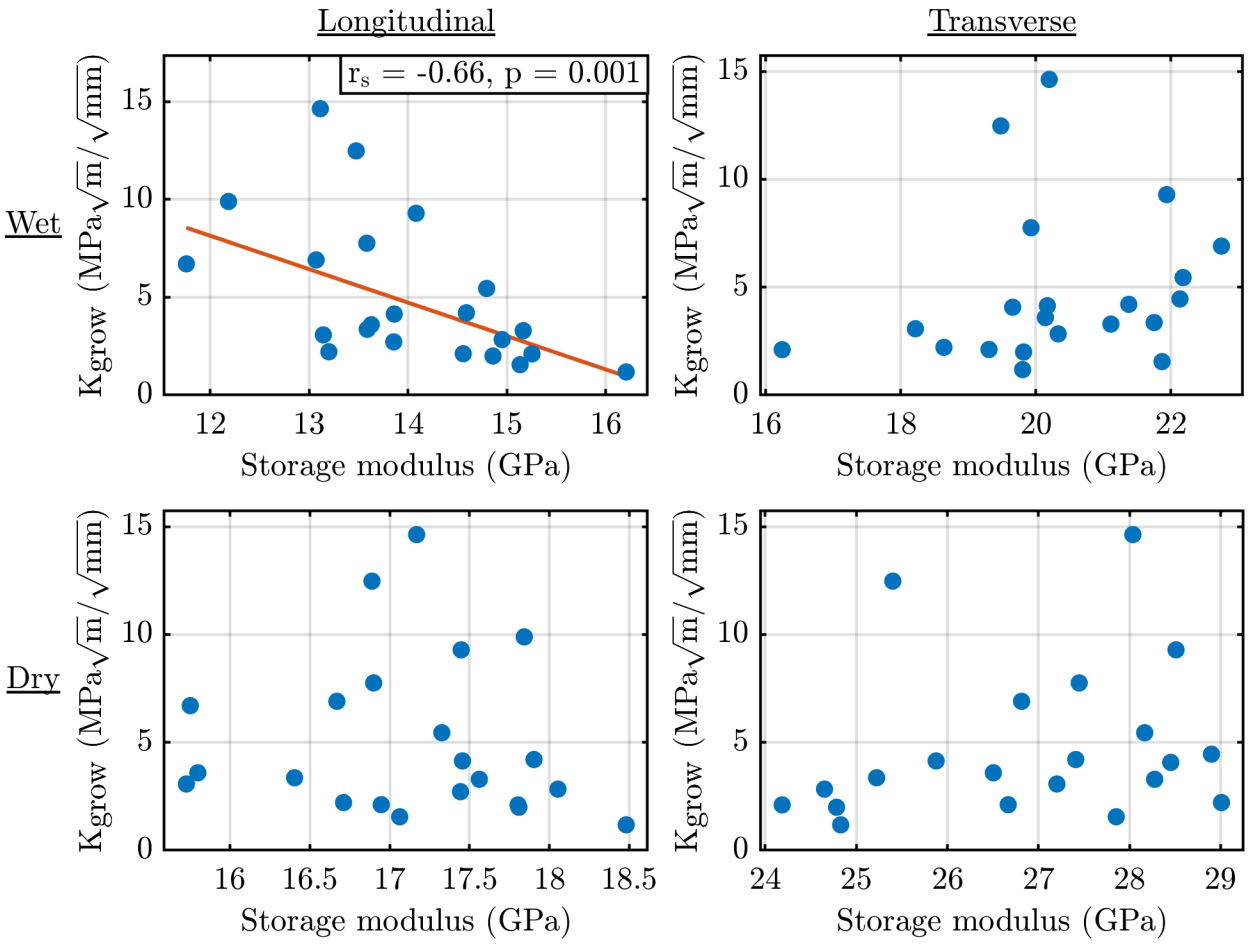


Figure 51: Scatterplots of human femur K_{grow} vs. E′ data. Significant correlations are indicated by best fit lines.

Table 20: Correlations between rat fracture parameters and Mid-cortex indentation data

	E'		E''		H	
	Wet	Dry	Wet	Dry	Wet	Dry
K_C	0.44	0.51			0.52	0.55
CrackingToughness		-0.39				-0.41

CrackingToughness was negatively correlated with Dry E′ and H. Refer to Figures 52 and 53 for scatterplots of K_c and CrackingToughness vs. E′.

3.9.3 Comparison of Human and Rat Results

In both sets of experiments there were no significant correlations between E″ and the fracture data. There were also negative correlations between fracture and E′ and H in both experiments. Specifically, E′ and H had negative correlations with K_{init}, J-integral, and K_{grow} (human femur) and CrackingToughness (rat femur).

3.10 Regression Models of Fracture

The linear regression models with the human femur fracture parameters as response variables and the indentation, compositional, and structural data as predictor variables are shown in Table 21. The most important takeaway from these models is their multi-factorial nature:

$$\mathrm{K_{init}} = f\left(\mathrm{E'_{L,Wet}}, \mathrm{BoundWater}, \mathrm{PoreWater}, \mathrm{OstAr}\right) \quad (52)$$

$$\mathrm{J\text{-}integral} = f(\mathrm{OstAr}, \mathrm{H_{L,Wet}}, \mathrm{H_{T,Wet}}) \quad (53)$$

$$\mathrm{K_{grow}} = f(\mathrm{E'_{L,Wet}}) \quad (54)$$

The K_{init} model was a function of indentation (Longitudinal – Wet E′), compositional (BoundWater), and structural (PoreWater, OstAr) terms. Likewise, the J-integral model was a function of indentation (Longitudinal – Wet H, Transverse – Wet H) and structural (OstAr) terms. However, K_{grow} was best fit by indentation data only.

3.11 Changes in Fracture with Age

3.11.1 Human Femur

Table 22 looks at changes in the human fracture parameters with age. K_{init} and J-integral were negatively correlated with Age, while K_{grow} was not. When grouped by age, the mean values of all 3 parameters were greater for Young than for Aged. The Young –

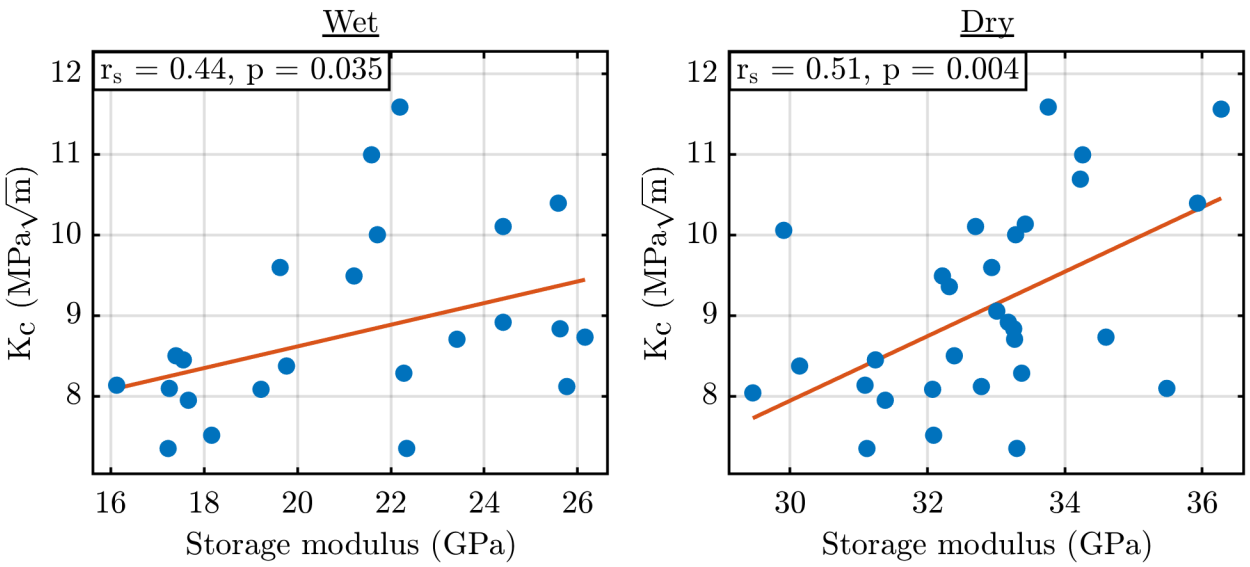


Figure 52: Scatterplots of rat K_c vs. E′. Significant correlations are indicated by best fit lines.

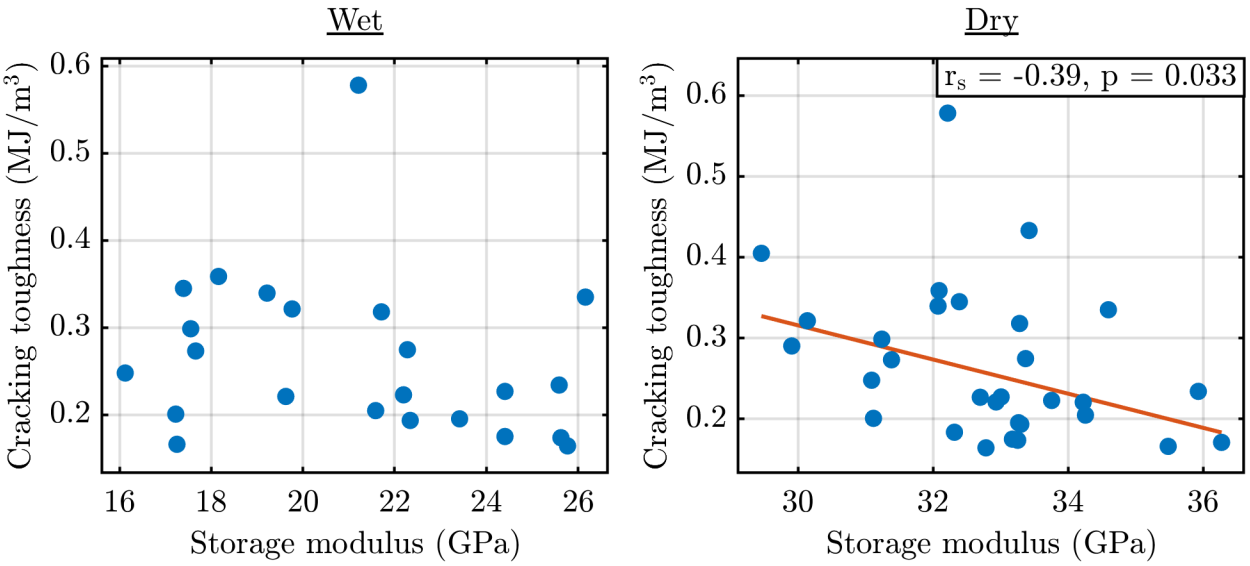


Figure 53: Scatterplots of rat CrackingToughness vs. E′. Significant correlations are indicated by best fit lines.

Table 21: Regression models of human femur fracture data

	Equation	Adj-R^2	n
K_{init}	$-0.32E'_{L,Wet} + 0.26BoundWater - 0.24PoreWater + 0.22OstAr$ $-0.43E'_{L,Wet} + 0.35BoundWater + 0.22OstAr - 0.18PoreWater$	0.39	26
J-integral	$0.65OstAr - 0.32H_{L,Wet} - 0.22H_{T,Wet}$ $0.59OstAr - 0.34H_{L,Wet} - 0.26H_{T,Wet}$	0.46	23
K_{grow}	$-0.56E'_{L,Wet}$ $-0.49E'_{L,Wet}$	0.28	22

The upper equation for each parameter is the OLS model with the highest Adj-R^2 value
The lower equation is the IRLS model with the same terms as in the upper OLS model
n = number of data points

Table 22: Comparison of human femur fracture data between Young and Aged age groups and fracture data correlations with Age

	Units	Young	Aged	p	r_s
K_{init}	$MPa\sqrt{m}$	9.57 (2.16)	8.17 (1.18)	0.077*	-0.44
J-integral	kJ/m^2	13.65 (4.97)	10.58 (4.07)	0.058*	-0.44
K_{grow}	$MPa\sqrt{m}/\sqrt{mm}$	6.07 (4.14)	3.61 (2.20)		

Data in Young and Aged columns are Mean (SD)
Young = Age ≤ 60 years
Aged = Age > 60 years
p = Wilcoxon rank sum test p-value
r_s = Spearman rank correlation coefficient
* $0.05 < p < 0.10$

Aged differences did not reach statistical significance but were nearly significant for K_{init} and J-integral. Refer to Figure 54 for the plots of the human femur fracture data vs. Age.

3.11.2 Rat Femur

See Table 23 for a comparison of rat femur fracture data between age groups. K_c increased with age, while CrackingToughness was seen to decrease with age. In both cases the significant differences between age groups were 6 vs. 12 months and 6 vs. 24 months, with the 6-24 month difference being the larger. See Figures 55 and 56 for boxplots of K_c and CrackingToughness by age group.

3.11.3 Comparison Between Human and Rat Results

In both experiments, the energy required to propagate a crack decreased with age. For the human femur specimens, K_{init} and J-integral were negatively correlated with Age, while for the rat femora, CrackingToughness decreased with age.

3.12 Changes in Compositional and Structural Data with Age

3.12.1 Human Femur

Refer to Table 24 for a comparison of the human femur compositional and structural data between the Young and Aged groups and for correlations with Age. Porosity and PoreWater were unchanged with age. BoundWater and OstAr were negatively correlated with Age, and their age group comparisons were nearly significant. TMD and PE were positively correlated with Age and had Aged > Young. See Figures 57-61 for plots of the human femur compositional and structural data against Age.

3.12.2 Rat Femur and Radius

The compositional and structural age group comparison data for the rat experiments are in Table 25. Each parameter was found to change with age. Porosity, PoreWater, TMD, and PE each increased with age, while BoundWater decreased with age. In most cases the biggest inter-age group difference was 6-24 months, although

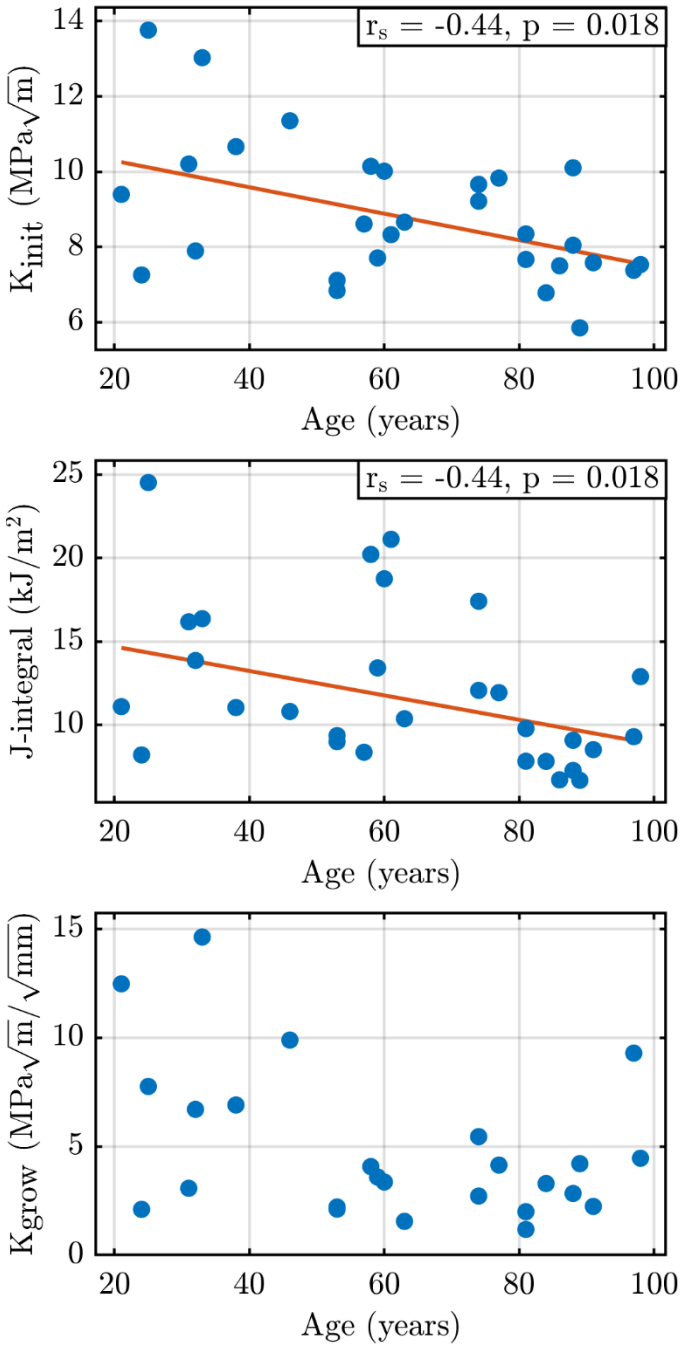


Figure 54: Scatterplots of human femur fracture data vs. Age. Significant correlations are indicated by best fit lines.

Table 23: Comparison of rat fracture data between age groups

Parameter	Units	Mean (SD)			p			
		6 months	12 months	24 months	KW	6 vs 12	12 vs 24	6 vs 24
K_c	$MPa/\sqrt{m}$	8.27 (0.60)	9.28 (1.08)	9.72 (1.34)	0.008	0.030		0.013
CrackingToughness	MJ/m^3	0.34 (0.09)	0.25 (0.07)	0.19 (0.06)	<0.001	0.041	0.097*	<0.001

KW = Kruskal-Wallis p-value
p = Dunn's test adjusted p-value for comparisons between age groups. Holm–Šidák adjustment with FWER = 0.05.
* $0.05 < p < 0.10$

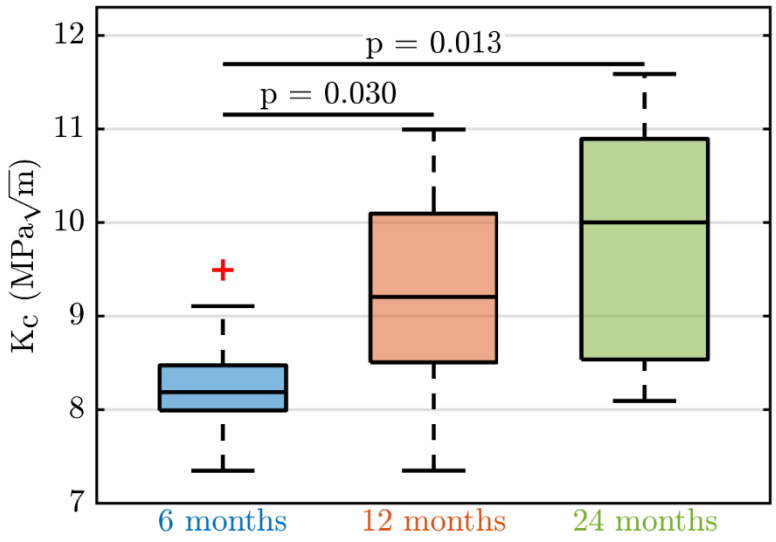


Figure 55: Boxplot of rat K_c data by age group. Significant differences between age groups are indicated by comparison lines above the boxes.

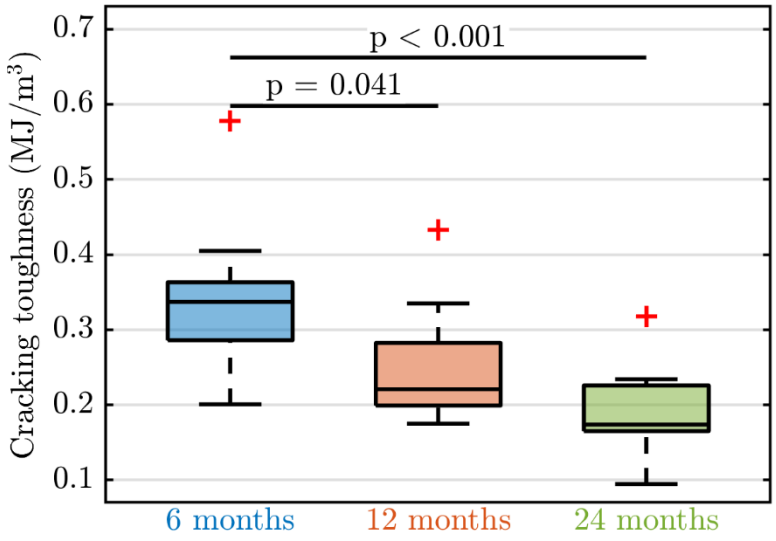


Figure 56: Boxplot of rat CrackingToughness data by age group. Significant differences between age groups are indicated by comparison lines above the boxes.

Table 24: Comparison of human femur compositional and structural data between Young and Aged age groups and correlations with age.

	Units	Young	Aged	p	r_s
Porosity	%	5.7 (3.1)	6.1 (3.0)		
PoreWater	%	8.1 (2.6)	8.1 (2.4)		
BoundWater	%	20.2 (1.9)	18.6 (2.1)	0.085*	-0.45
TMD	$mgHA/cm^3$	965 (23)	996 (14)	<0.001	0.64
PE	mmol/mol collagen	3.7 (1.8)	6.7 (2.4)	<0.001	0.75
OstAr	%	56.4 (7.1)	51.9 (6.0)	0.064*	-0.55

Data in Young and Aged columns are Mean (SD)
Young = Age ≤ 60 years
Aged = Age > 60 years
p = Wilcoxon rank sum test p-value
r_s = Spearman rank correlation coefficient

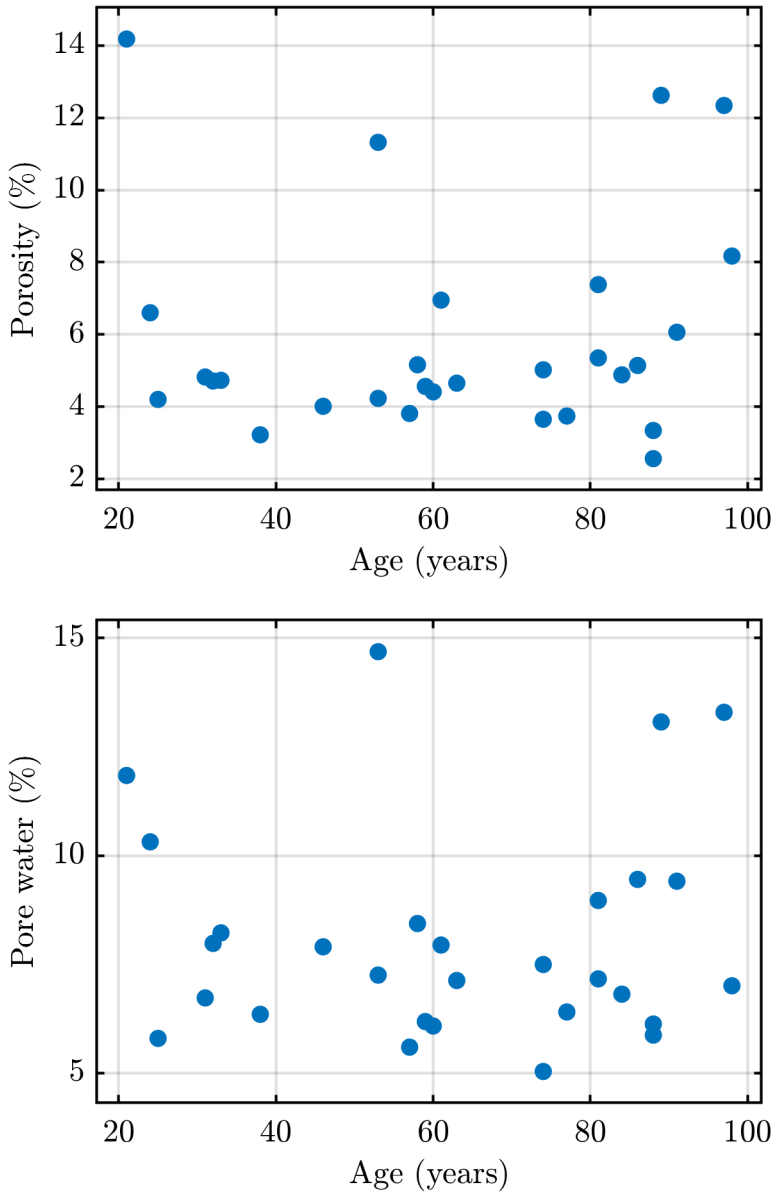


Figure 57: Scatterplots of human femur Porosity (top) and PoreWater (bottom) data vs. age. Neither parameter was significantly correlated with age.

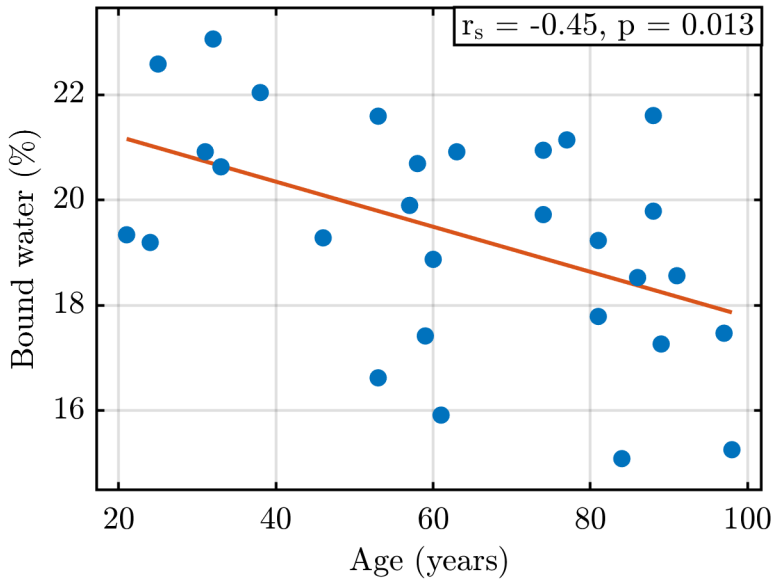


Figure 58: Scatterplot of human femur BoundWater data vs. Age. As indicated by the best fit line, BoundWater and Age were negatively correlated.

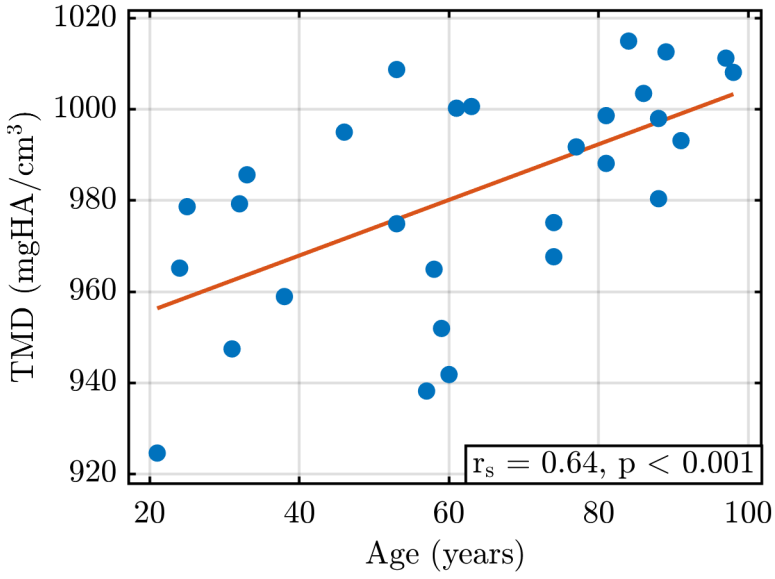


Figure 59: Scatterplot of human femur TMD data vs. Age. As indicated by the best fit line, TMD and Age were positively correlated.

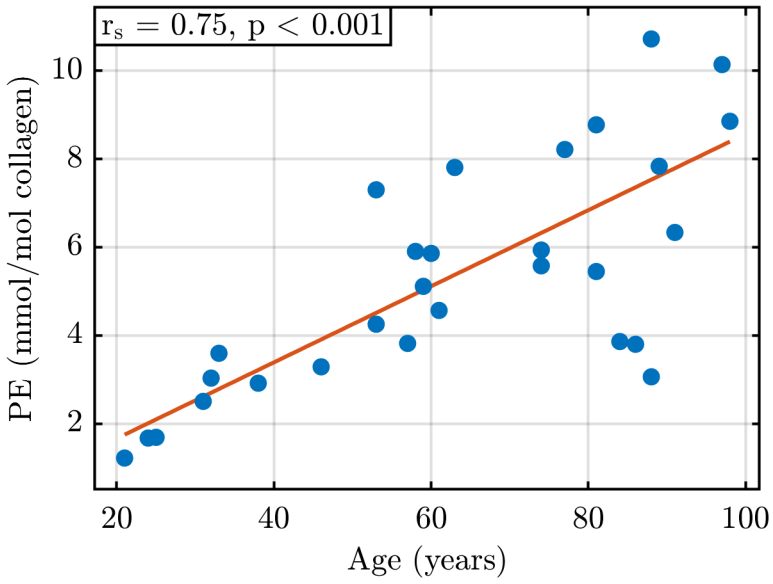


Figure 60: Scatterplot of human femur Pentosidine data vs. Age. As indicated by the best fit line, PE and age were positively correlated.

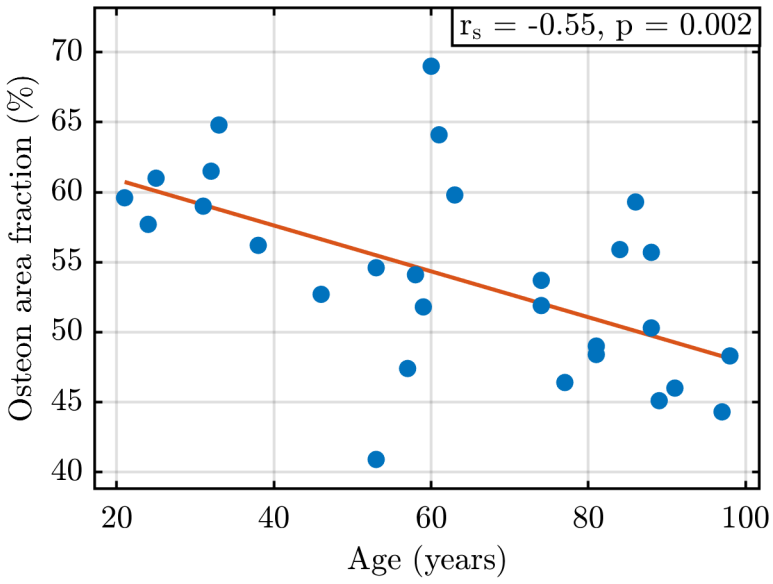


Figure 61: Scatterplot of human femur OstAr data vs. Age. As indicated by the best fit line, OstAr and Age were negatively correlated.

Table 25: Comparison of rat compositional and structural data between age groups

Parameter	Units	Mean (SD)			p			
		6 months	12 months	24 months	KW	6 vs 12	12 vs 24	6 vs 24
Porosity	%	0.6 (0.2)	3.1 (1.5)	14.0 (3.8)	<0.001	0.009	0.008	<0.001
PoreWater	mol/L	5.6 (1.1)	5.6 (1.4)	11.2 (1.8)	<0.001		<0.001	<0.001
BoundWater	mol/L	13.7 (0.3)	12.8 (0.2)	12.2 (0.4)	<0.001	0.005	0.020	<0.001
TMD	$mgHA/cm^3$	1254 (8)	1287 (7)	1313 (13)	<0.001	0.008	0.009	<0.001
PE	mmol/mol collagen	0.50 (0.11)	0.56 (0.15)	0.69 (0.19)	0.030			0.026

KW = Kruskal-Wallis p-value

p = Dunn's test adjusted p-value for comparisons between age groups. Holm–Šidák adjustment with FWER = 0.05.

many of the 6-12 and 12-24 month differences were also significant. For the boxplots of these data grouped by age, refer to Figures 62-65.

3.12.3 Comparison Between Human and Rat Results

There were several commonalities between the human and rat results in this section. In both experiments, TMD increased, BoundWater decreased, and PE increased with age. An important difference between the two experiments was that Porosity and PoreWater increased with age for the rat femur specimens but not for the human femur specimens.

3.13 Correlations Amongst Compositional and Structural Data

The correlations amongst the compositional and structural data are shown in Tables 26 and 27 for the human and rat experiments, respectively. There were a number of noteworthy shared correlations between the experiments. Firstly, Porosity and PoreWater were positively correlated. See Figure 66 for scatterplots of PoreWater vs. Porosity for both experiments. Secondly, BoundWater was negatively correlated with both Porosity and TMD. Plots of BoundWater vs. Porosity and TMD can be seen in Figures 67 and 68, respectively.

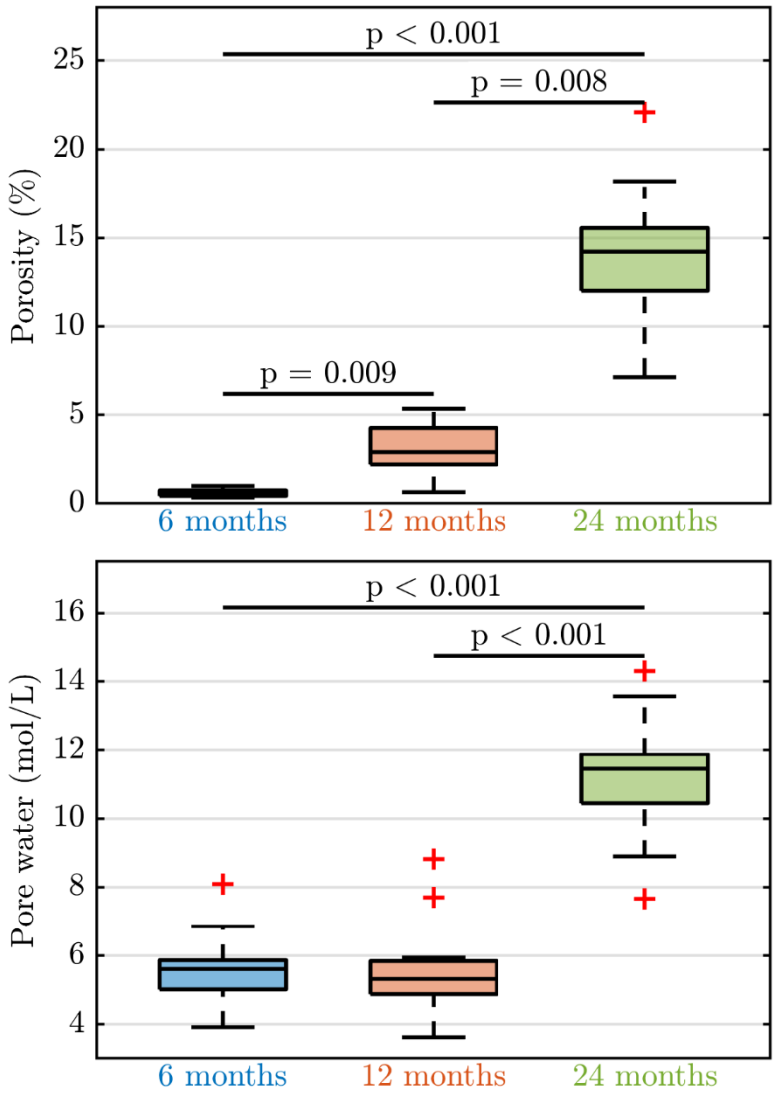


Figure 62: Boxplots of rat Porosity (top) and PoreWater (bottom) data by age group. Significant differences between age groups are indicated by comparison lines above the boxes.

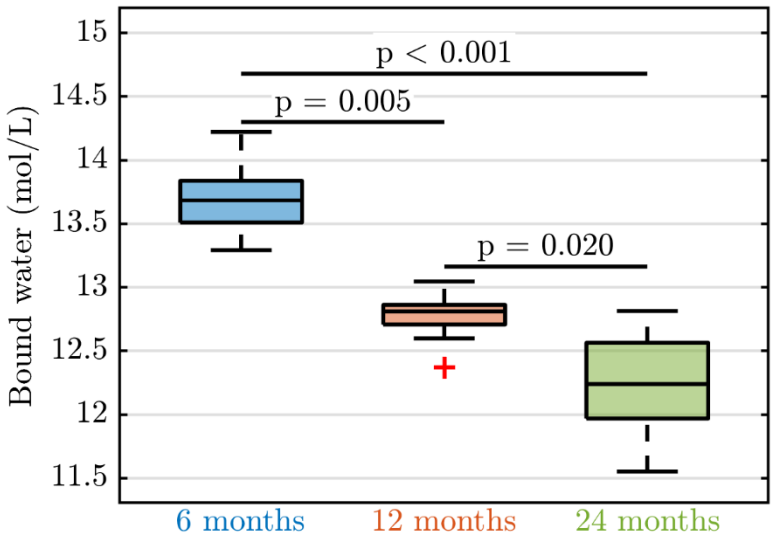


Figure 63: Boxplot of rat BoundWater data by age group. Significant differences between age groups are indicated by comparison lines above the boxes.

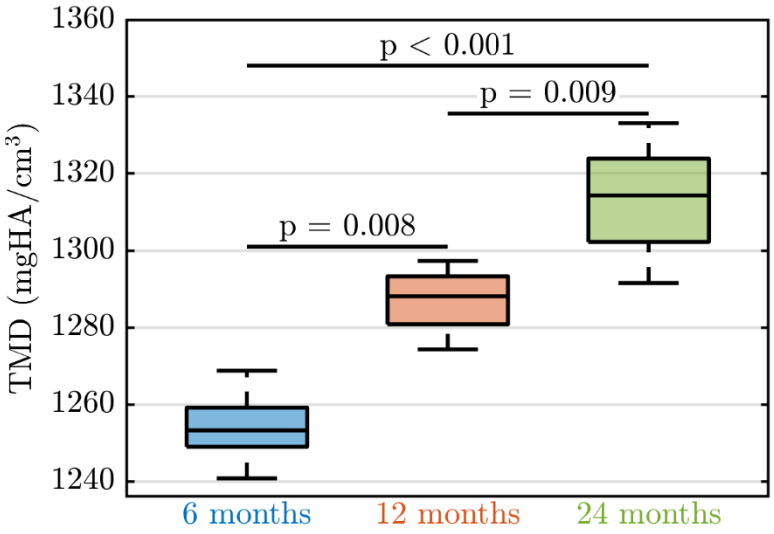


Figure 64: Boxplot of rat TMD data by age group. Significant differences between age groups are indicated by comparison lines above the boxes.

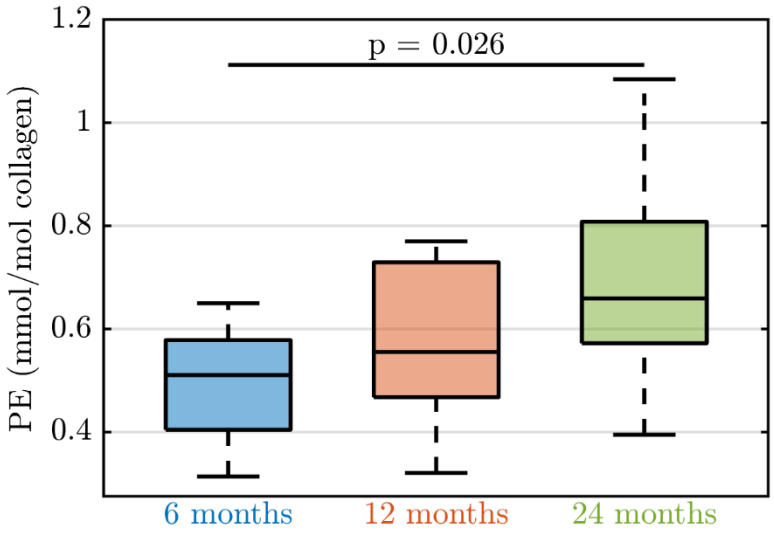


Figure 65: Boxplots of rat Pentosidine data by age group. Significant differences between age groups are indicated by comparison lines above the boxes.

Table 26: Correlations amongst the human femur compositional and structural data

	Porosity	Pore Water	Bound Water	TMD	PE
PoreWater	0.82				
BoundWater	-0.63	-0.37			
TMD	0.37	0.40	-0.51		
PE	x	x	x	0.46	
OstAr	x	x	0.32*	-0.33*	-0.63

Note: The area above and to the right of the main diagonal is empty
x = no correlation
* $0.05 < p < 0.10$

Table 27: Correlations amongst the rat compositional and structural data

	Porosity	Pore Water	Bound Water	TMD
PoreWater	0.71			
BoundWater	-0.87	-0.64		
TMD	0.75	0.55	-0.74	
PE	0.43	0.29*	-0.34	0.32*

Note: The area above and to the right of the main diagonal is empty
* $0.05 < p < 0.10$

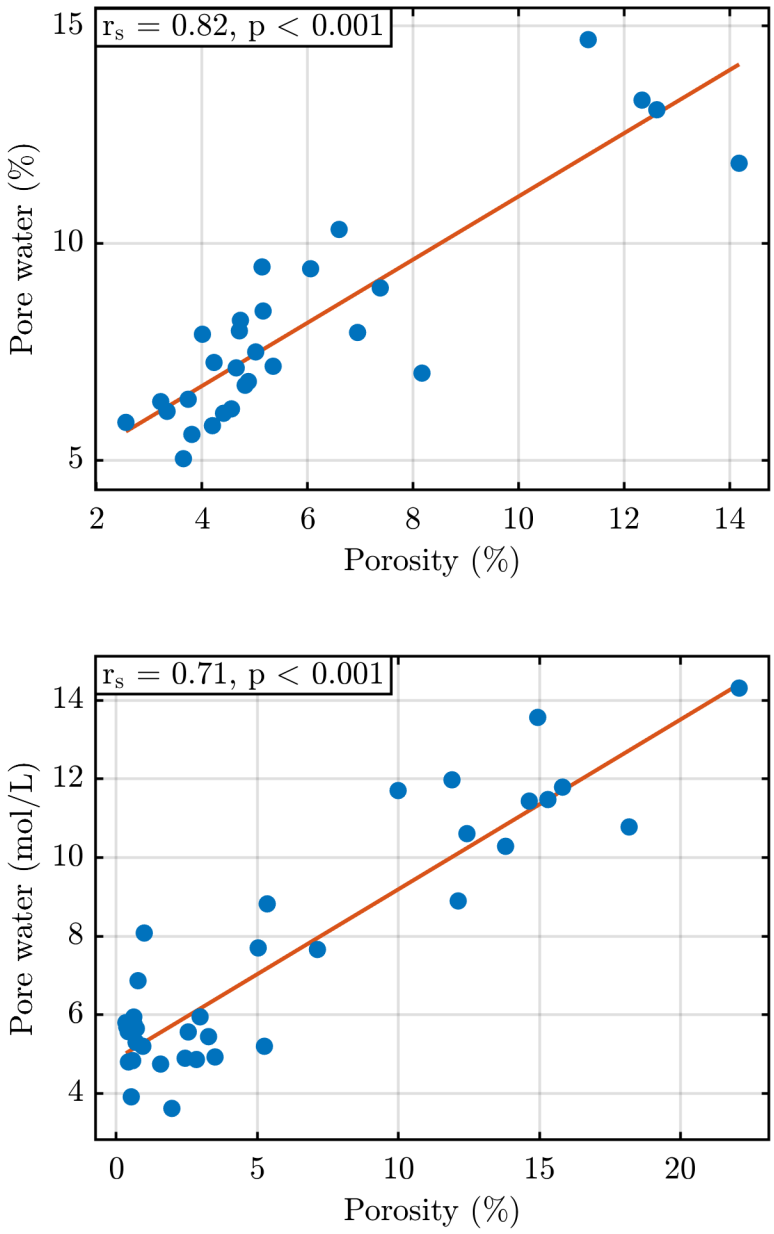


Figure 66: Scatterplots of PoreWater vs. Porosity for human (top) and rat (bottom) specimens. PoreWater and Porosity were positively correlated for both sets of specimens.

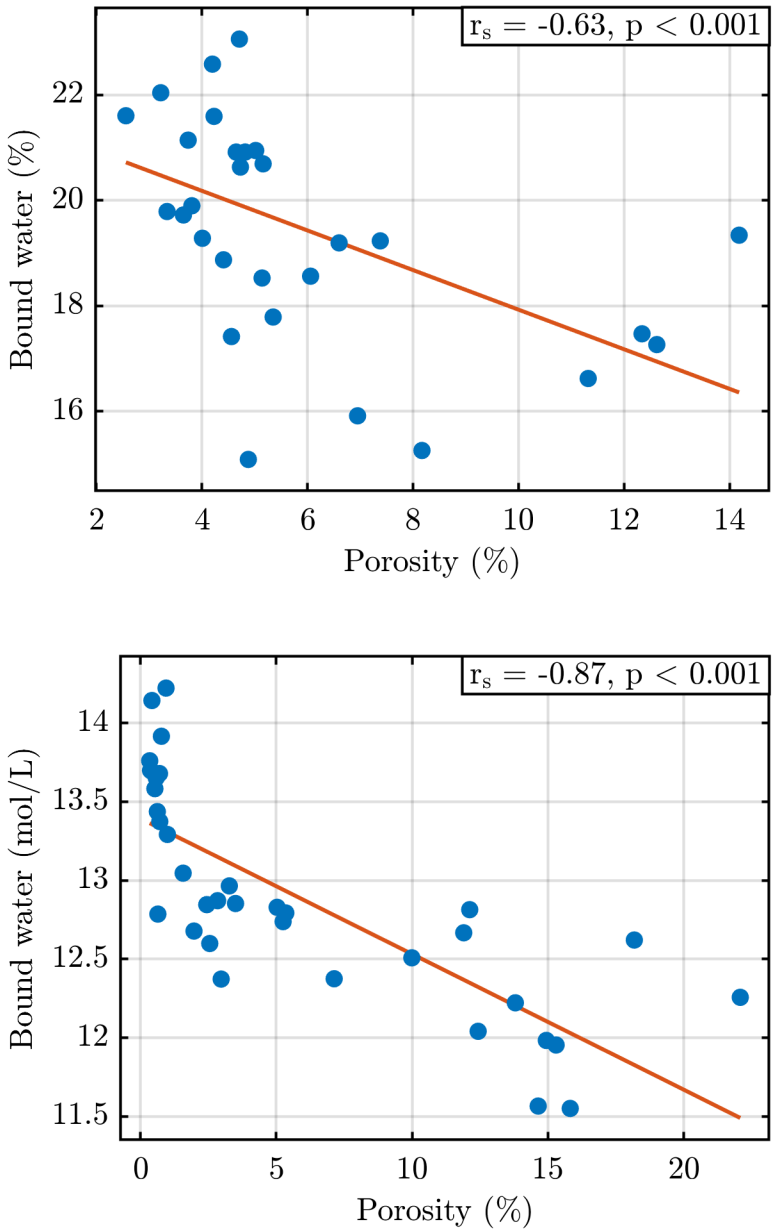


Figure 67: Scatterplots of BoundWater vs. Porosity for human (top) and rat (bottom) specimens. BoundWater and Porosity were negatively correlated for both sets of specimens.

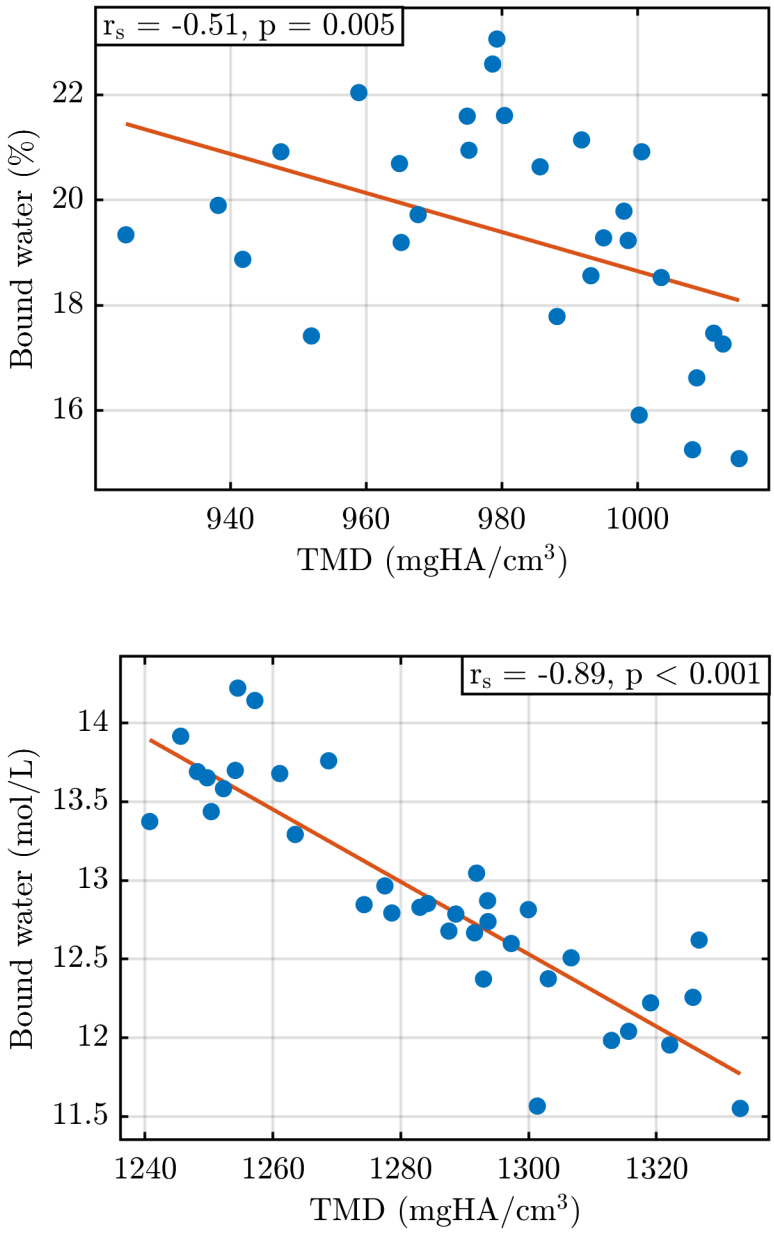


Figure 68: Scatterplots of BoundWater vs. TMD for human (top) and rat (bottom) specimens. BoundWater and TMD were negatively correlated for both sets of specimens.

CHAPTER 4
DISCUSSION

4.1 Factors Which Affect Bone Indentation Data

4.1.1 Hydration

As described in the Indentation Data: Wet vs. Dry section, the Wet indents had lower stiffness and hardness than the Dry indents, which is in agreement with other published data. Nine studies were identified with both wet and dry bone quasi-static nanoindentation data. The E and H data from these studies are shown in Table 28. These data represent a range of species, bones, donor ages, indentation directions, and experimental methods. In all cases the Wet values were lower than the Dry values. Only one study was on human cortical bone [61], the results of which were similar to those in this study. The study by Wolfram et al. on human vertebral trabeculae is by far the largest of those shown in Table 28, as it used specimens from 104 donors, while the others included 4 or fewer [62]. The remaining studies were all on animals. Interestingly, hydration status seems to have a greater effect on H than on E, as in this and the other studies, the E Wet/Dry ratio was greater than or equal to the H Wet/Dry ratio. On average, for the studies with both E and H data, E was 30% less when tested wet, while H was 41% lower. Also, note that the effect of hydration on the Longitudinal and Transverse specimens in this study should not be compared, as the Transverse specimens were dehydrated in a vacuum desiccator prior to qBEI, while the Longitudinal specimens were not.

In this study, Wet E″ was greater than Dry E″, which is consistent with the idea that hydration is a key factor in the viscoelasticity of bone. Three studies were identified with comparable wet and dry data, given in terms of viscoelastic loss factor (tanδ). The data from these studies are shown in Table 29. Pathak et al. tested femora from 16 week old mice using dynamic nanoindentation in the frequency range 10-200 Hz [25]. Garner et al. tested human cortical tibia specimens in bending and torsion in the transverse and longitudinal directions from mHz to kHz frequencies [63]. Loss factor reached a minimum from 1 to 100 Hz. Lastly, Yamashita et al. tested human cortical femur specimens using DMA at 1 Hz [24]. As seen in Table 29, tanδ was always greater

Table 28: Bone nanoindentation E and H data from studies with both wet and dry tests

E (GPa)			H (GPa)			Section	Specimen Info	n	Ref
Wet	Dry	Ratio	Wet	Dry	Ratio				
14.1	17.1	**0.82**	0.40	0.51	**0.78**	Longitudinal	Human femora	26	This study
20.4	26.7	**0.76**	0.54	0.87	**0.62**	Transverse		25	
23.4	33.9	**0.69**	0.49	1.33	**0.37**	Transverse	Rat tibiae, age 24 months	9,10	
8.4	12.0	**0.70**				Longitudinal	Human vertebral trabeculae	104	[62]
11.2	14.2	**0.79**				Transverse			
19.3	23.7	**0.82**	0.59	0.93	**0.64**	Transverse	Human femora	4	[61]
11.5	20.1	**0.57**	0.23	0.74	**0.31**	Transverse	Mouse tibiae, age 9 weeks	4	[64]
13.4	27.0	**0.50**	0.49	1.16	**0.42**	Transverse	Canine femora	3	[65]
15.5	27.4	**0.57**	0.58	1.11	**0.52**	Longitudinal	Porcine femora	3,1	[66]
19.0	27.2	**0.69**	0.55	0.90	**0.61**	Transverse			
12.8	17.6	**0.73**	0.35	0.54	**0.65**	Longitudinal	Horse metacarpal	1	[67]
12.4	20.8	**0.60**	0.28	0.61	**0.46**	Transverse			
20.0	27.0	**0.74**				Longitudinal	Bovine femur	1	[68]
23.0	32.0	**0.72**				Transverse			
25.1	27.5	**0.91**	0.73	0.82	**0.89**	Transverse	Bovine femur	1	[69]
14.5	19.0	**0.76**	0.51	0.67	**0.76**	Longitudinal	Sheep tibia	1	[70]
22.8	27.5	**0.83**	0.60	1.01	**0.59**	Transverse			

Ratio = Wet/Dry
Bold indicates Wet < Dry
n = number of specimen donors, listed as “Wet, Dry” if not equal
Rows ordered by decreasing n, with human data listed before animal data
Note that the data listed in the E column from this study are E′
All long bone specimens were cortical and diaphyseal
Some values were estimated from plots

Table 29: Bone viscoelastic loss factor data from studies with both wet and dry tests

Wet	Dry	Ratio	Section	Specimen Info	n	Method	Ref
0.045	0.024	**1.9**	Longitudinal	Human femora	26	Indentation	This study
0.034	0.018	**1.9**	Transverse		25		
0.040	0.013	**3.1**	Transverse	Rat tibiae, age 24 months	9,10		
0.041	0.029	**1.4**	Transverse	Human femora	8	DMA	[24]
0.023	0.015	**1.5**	Longitudinal	Human tibiae	2	Torsion, Bending	[63]
0.021	0.016	**1.3**	Transverse				
0.130	0.020	**6.5**	Transverse	Mouse femora, age 16 weeks	4	Indentation	[25]

Ratio = Wet/Dry
Bold indicates Wet > Dry
n = number of specimen donors, listed as “Wet, Dry” if not equal
Rows ordered by decreasing n, with human data listed before animal data
Some values were estimated from plots, at approximately the 45 Hz frequency used in this study

when the bones were tested wet. The reference Wet/Dry tanδ ratios are in the range 1.3-1.5 for the human bone specimens, which is comparable to the ratio of 1.9 seen for both human femur sections in this study. The Wet/Dry tanδ ratios were greater for the rodent bones than the human bones. However, this may be at least partially attributable to the fact that the rodent bones were dehydrated and embedded in PMMA, while none of the human bone specimens were.

4.1.2 Anisotropy

Anisotropy was observed in the indentation data, as a result of the preferential orientation of the mineralized collagen fibrils in the direction of the bone long axis. Specifically, E′, E″, and H were all greater for the Transverse femur specimens than the Longitudinal specimens. Refer to Table 30 for a comparison of the anisotropy data from this study with similar published cortical bone nanoindentation data. Table 30 is limited to indentation E and H, since no other studies with bone viscoelasticity anisotropy data were found. The largest study with both longitudinal and transverse cortical bone nanoindentation data is that of Mirzaali et al., with hydrated nanoindentation data for femoral specimens from 39 human donors. Two other human studies involved multiple donors: Reisinger et al. [71] with 3 and Rho et al. [72] with 2. Finally, 4 studies included a single human donor. In these human studies, the E anisotropy ratios (Longitudinal/Transverse) were in the range 0.64-0.86. Both the Wet and Dry E′ anisotropy ratios in this study fell within this range.

The range of human H anisotropy ratios in Table 30 is 0.70-0.95, although a couple of the studies did not report H. The Wet H anisotropy ratio in this study falls within that range, while the Dry anisotropy ratio is lower. The lower Dry anisotropy ratio in this study can possibly be explained by the different treatments given to the Dry Longitudinal and Transverse specimens. Recall that the Dry Transverse specimens in this study were vacuum desiccated prior to qBEI, while the Longitudinal specimens were not. Also, note that Mirzaali et al. and the Wet data from this experiment have equivalent stiffness anisotropy ratios, but not hardness anisotropy ratios. In Mirzaali et al., the Longitudinal section H was 12% less than the Transverse section H, but the

Table 30: Cortical bone nanoindentation anisotropy data from this and other studies

E (GPa)			H (GPa)			Condition	Specimen Info	n	Ref
L	T	Ratio	L	T	Ratio				
14.1	20.4	**0.69**	0.40	0.54	**0.74**	Wet	Human femora	26	This
17.1	26.7	**0.64**	0.51	0.87	**0.59**	Dry		25	study
13.1	19.1	**0.69**	0.40	0.46	**0.88**	Wet	Human femora	39	[73]
20.5	27.6	**0.74**				Dry	Human femora	3	[71]
16.6	24.1	**0.69**	0.56	0.68	**0.82**	Dry	Human tibiae	2	[69]
16.6	26.1	**0.64**				Dry	Human tibia	1	[74]
22.9	26.6	**0.86**	0.80	0.84	**0.95**	Dry	Human femur	1	[75]
17.0	24.6	**0.69**	0.54	0.77	**0.70**	Dry	Human femur	1	[76]
16.6	23.5	**0.71**				Dry	Human femur	1	[77]
14.0	18.1	**0.77**	0.55	0.74	**0.74**	Dry	Bovine tibiae	6	[78]
13.5	19.0	**0.71**	0.60	0.69	**0.87**	Wet	Porcine femora	3	[66]
16.7	22.5	**0.74**	0.74	0.86	**0.86**	Dry	Bovine tibia	1	[79]
15.5	19.5	**0.79**				Dry	Bovine tibia	1	[80]
12.8	12.4	1.03	0.35	0.28	1.25	Wet	Horse metacarpal	1	[67]
17.6	20.8	**0.85**	0.54	0.61	**0.89**	Dry			
20.0	23.0	**0.87**				Dry	Bovine femur	1	[68]
27.0	32.0	**0.84**				Wet			
14.5	22.8	**0.64**	0.51	0.60	**0.85**	Wet	Sheep tibia	1	[70]
19.0	27.5	**0.69**	0.67	1.01	**0.66**	Dry			
15.8	25.9	**0.61**	0.55	0.82	**0.67**	Dry	Sheep femur	1	[76]
15.4	23.1	**0.67**				Dry	Bovine femur	1	[81]

L = Longitudinal, T = Transverse, Ratio = Longitudinal/Transverse
Bold indicates Longitudinal < Transverse
Rows ordered by decreasing number of donors (n), with human data listed before animal data
Note that the data listed in the E column from this study are E′
Some values were estimated from plots
In studies with both osteonal and interstitial data, their average was used

difference was not found to be statistically significant. In contrast, in this study the difference was 26% and was significant. The reason for this difference is unclear; however, note that for all of the studies reporting human H anisotropy data, the specimens were embedded in PMMA, while the specimens in this study were unembedded.

The remaining 9 studies listed in Table 30 used animal bones. Two of these studies involved multiple donors: Mullins et al. [78] with 6 and Feng et al. [66] with 3. In general, the anisotropy in the indentation data in the animal studies is similar to that in the human studies. The only study with a reported anisotropy ratio greater than 1 (Longitudinal > Transverse) was Faingold et al. [67] for hydrated indentation of horse metacarpal bone. However, note that pattern of loading of horse metacarpal bone is quite different from the predominately longitudinal loading experienced by human long bones such as the femur.

4.1.3 Location: Osteonal vs. Interstitial

Refer to Table 31 for a summary of bone nanoindentation studies with osteonal and interstitial data from multiple human donors. Note that all of the data in Table 31 are from transverse sections. Generally, interstitial areas were found to have higher E and H than osteonal areas, although the differences were not always statistically significant. In the 10 identified studies, the range of Osteonal/Interstitial E ratios was 0.82-1.00. The Wet and Dry E′ Osteonal/Interstitial ratios in this study were 0.97 and 0.98, respectively. These values fall within the upper range of those in Table 31. Interstitial tissue generally has higher indentation stiffness and hardness than osteonal tissue because it is older and consequently is more highly mineralized. Thus, the difference in properties between the two tissue types is a function of bone turnover rate. A low rate of turnover allows the osteonal areas sufficient time to approach the level of mineralization of the interstitial areas. The relatively small (2-3%) difference in E′ between the osteonal and interstitial regions in this study may be an indication that the bone turnover rate was low for the male femoral diaphysis specimens used in this study.

Table 31: Transverse section osteonal and interstitial nanoindentation data from studies with multiple human donors

E (GPa)			H (GPa)			Condition	Specimen Info	n	Ref
Ost	Int	Ratio	Ost	Int	Ratio				
20.0	20.7	0.97	0.51	0.56	**0.91**	Wet	Femora	25	This study
26.4	27.0	**0.98**	0.84	0.89	**0.94**	Dry			
18.1	20.1	**0.90**	0.41	0.50	**0.82**	Wet	Femora	39	[73]
16.5	20.2	**0.82**				Wet	Femora	20	[82]
15.1	16.1	**0.94**	0.51	0.55	**0.93**	Wet	Femoral neck	16	[83]
19.5	19.5	1.00	0.62	0.67	**0.93**	Wet	Femora	10	[84]
21.8	24.1	**0.90**				Dry	Femora	10	[85]
19.1	21.2	0.90				Wet	Femora	8	[86]
17.7	19.3	**0.92**	0.52	0.59	**0.88**	Wet	Femora	4	[61]
22.4	25.7	**0.87**	0.62	0.74	**0.84**	Dry	Tibiae	2	[72]
22.5	25.8	**0.87**	0.61	0.74	**0.82**	Dry	Tibiae	2	[87]
23.7	24.2	0.98				Dry	Femora	2	[88]

Ost = Osteonal, Int = interstitial
Ratio = Osteonal/Interstitial
Bold indicates a statistically significant Osteonal < Interstitial result
Note that the data listed in the E column from this study are E′
Some values were estimated from plots
Except for the femoral neck specimens, all specimens were diaphyseal

In this study, there was a greater Osteonal – Interstitial difference for H than for E′. For example, Osteonal H was 9% lower than Interstitial H for the Wet tests, while E was 3% lower. For the Dry tests the H and E′ differences were 6% and 2%, respectively. Also, the Osteonal – Interstitial difference was statistically significant for both the Wet and Dry tests for H but only for the Dry test for E′. Likewise, for the 6 other studies listed in Table 31, the relative difference in values between the osteonal and interstitial tissues was greater for H than for E. For the data of Hoffler et al., there was no E Osteonal – Interstitial difference, while for H there was a statistically significant difference [84]. In summary, the results from this study are in agreement with the literature consensus that osteonal tissue has generally lower indentation stiffness and hardness than interstitial tissue, and that the difference is seen to be larger for hardness than for stiffness.

4.1.4 Location: Periosteal vs. Mid-cortex

Indentation E′ and H were found to be lower for indents in the Periosteal region than the Mid-cortex region for the rat tibia specimens in this study. As with the difference in properties between osteonal and interstitial regions, the difference in properties between the periosteal and mid-cortex regions is largely due to tissue age differences. Specifically, the periosteal tissue is younger and less mineralized. Similar rodent indent nanoindentation studies with comparative data for both regions used rat femora [89-91], rat tibiae [92], rat humeri [93], and mouse femora [94, 95]. The studies by Busa et al. [92], Donnelly et al. [89, 93], and Kim et al. [90] used fluorescent labeling to identify tissue age. As would be expected, mineralization and stiffness increased with tissue age from the periosteal surface inwards. Similar work was done by Checa et al., who used scanning acoustic microscopy (SAM) to create stiffness maps of mice tibia cross-sections [96]. Like with the nanoindentation measurements, SAM stiffness was greatest in the mid-cortical region.

A variety of experimental techniques have been employed to study the compositional and structural differences between periosteal and mid-cortex regions of rodent bones. These techniques include Raman spectroscopy (RS) [25, 89, 90, 93, 94], qBEI [97], μCT [90], Fourier-transform infrared spectroscopy (FTIR) [98], synchrotron

infrared microspectroscopy (SIRMS) [92], 3D synchrotron microtomography [91], and x-ray scattering [99, 100]. In addition to the difference in the degree of mineralization, there are important structural differences between periosteal and mid-cortex tissues. First, the periosteal region has an organized lamellar structure in which the collagen fibers have a uniform orientation, while the mid-cortex region is less disorganized [91, 97, 99, 100]. This difference in structure allows the two regions to be readily differentiated under a microscope, as can be seen in Figure 4. Additionally, the mid-cortex tissue contains regions of highly mineralized cartilage. Bach-Gansmo et al. [97] and Shipov et al. [91] demonstrated that these cartilaginous regions were more highly mineralized and had greater nanoindentation stiffness and hardness than the surrounding tissue. Lastly, Turunen et al. reported that the mineral platelets in the mid-cortex were smaller than those in the periosteal region [99]. Thus, while the higher indentation stiffness and hardness of the mid-cortex region in comparison with the periosteal region can be explained by a higher degree of mineralization, other structural differences may contribute.

4.1.5 Age: Adult Human Bone

Indentation E′ and H were seen to increase with age for the adult male human femur specimens tested in this study. This is a novel result, as bone nanoindentation properties are typically described as being unchanged with age in adults [62, 73]. However, there are only a handful of other nanoindentation studies which have sought to measure changes with age for adult human cortical bone. Experimental details for these studies can be found in Table 32. On the other hand, E″ did not change significantly with age. There are no other studies with comparable data. The closest is that of Polly et al., on trabeculae from iliac biopsies from women taken before and after menopause [101]. No E″ difference was seen between the two groups.

Note that only a study with a large number of donors over a wide age range will be able to detect a modest change in properties with age. For example, in this study the change in E′ from 21 to 98 years of age for the Wet Transverse specimens was 2.8 GPa, a 15% increase. On a per decade basis this would be a change of 0.36 GPa, or

Table 32: Experimental details for nanoindentation studies of aging in human cortical bone

Specimen Info	n	Gender	Age Range (years)	Condition	Section	Ref
Femur	25-26	M	21-98	Wet, Dry	T, L	This study
Femur	39	20F 19M	F: 46, 64-99; M: 59-91	Wet	T, L	[73]
Iliac crest	32 (20, 12)	F	G1: 20-40; G2: 49-74	Dry	T	[102]
Femoral neck	27	16M 11F	M: 40-85; F: 27-93	Wet	T	[83]
Femur	9-10	M	35-90	Dry	T	[85, 103]
Humerus, tibia	5 (3, 2)	3M 2F	G1: 25-37; G2: 61-69	Dry	L	[36]
Femur	4 (2, 2)	F	G1: 43-47; G2: 80-83	Dry	T	[31]

n = total # of donors, if split into 2 age groups the # in each group added as (#, #)
F = female, M = male
G1 and G2 designate younger and older age groups, respectively
Section: L = longitudinal, T = transverse

1.9% of the youngest value. Also, note that due to the spatial variation in properties within a specimen, as well as individual differences between donors, bone nanoindentation studies inherently have a certain amount of data scatter. For example, the average standard deviation of E′ values for a given Transverse – Wet specimen in this study was 2.2 GPa. In other words, the per decade aging trend was a fraction of the intra-specimen data spread. Clearly, studies with a small number of donors or a limited age range would be expected to miss an aging trend of this magnitude.

In addition to the number of donors and the age range, there are a few other factors to consider when comparing results between the experiments shown in Table 32. First is the anatomical location of the specimens. Local bone properties adapt to satisfy habitual loading requirements, meaning that properties can vary between bones as well as within individual bones. For example, stiffness has been found to be greater in the femoral diaphysis than the femoral neck [84, 86, 104] and distal radius [84]. For the femoral shaft, the anterior quadrant has been reported to have higher stiffness than the posterior and medial quadrants [104]. Since bone properties vary between locations, it follows that aging trends may as well. Next is the gender composition of the donors. From the available literature, it is clear that male and female bones have comparable mechanical properties, as indentation studies commonly do not find a significant difference between them. However, there is a clear difference in skeletal aging between men and women, as men do not experience menopause and its associated bone loss. Thus, there may be gender-specific aging trends which have not been identified yet. Lastly is bone specimen preparation and hydration condition; specimens can be embedded or unembedded and tested wet or dry. As seen in this study and others, bound water decreases with age. By reducing this bound water difference, specimen dehydration could interfere with the identification of an aging trend. A potential example of this is the fact that the only Section – Condition combination for which E′ did not increase with age was Transverse – Dry, where the specimens had been vacuum desiccated prior to qBEI. Since the embedding process involves dehydration, it may be more difficult to measure an aging trend for embedded specimens when tested dry.

There is little nanoindentation data comparing embedded and unembedded specimens. However, note that Hoffler et al. reported no difference between wet embedded and wet unembedded specimens [61].

The work of Mirzaali et al. is the most similar to this study, and is the study of aging in human cortical bone with the largest number of donors, 39 [73]. Of the 39 donors, 20 were female and 19 were male. Note that the male age range was 59-91 years. The female age range was 64-99 years, plus one donor aged 46 years. The specimens were tested hydrated, and both longitudinal and transverse sections were tested. Indentation E and H were not found to change with age, with the exception of interstitial H for the transverse specimens, which decreased slightly with age. Longitudinal specimen H was 14% lower for the female specimens than for the male specimens. The E difference was 8%, but was not described as being statistically significant. Similarly, E and H were not found to be gender-dependent for the transverse specimens.

Because this study and that of Mirzaali et al. are the only nanoindentation studies of aging in femoral diaphyseal cortical bone with more than 10 donors, it is worthwhile to consider possible explanations for the differing results. First, the trend of increasing stiffness and hardness with age in this study could be a false positive. However, this seems unlikely since the same result of E' increasing with age was reached for the Longitudinal – Wet, Longitudinal – Dry, and Transverse – Wet experiments. Second, if male femoral cortical bone does generally tend to have an increase in E and H with age, then the result in Mirzaali et al. could be a false negative. In fact, given that the Mirzaali et al. male dataset consisted of 19 donors over a 33 year age range, it would be difficult to detect an aging trend of the magnitude identified in this study. Recall that the dataset in this study consisted of 26 male donors over a 78 year age range, a difference of 7 donors and 45 years spanned. The measured aging trend could be gender-specific. The result in Mirzaali et al. of 14% lower H for the female Longitudinal specimens hints at this possibility. Third, while both studies used cortical femoral specimens, the specimens were from different locations: proximal anterior-lateral in the case of Mirzaali

et al. and lateral mid-shaft in this study. Lastly, is the difference in specimen preparations: Mirzaali et al. used embedded specimens, while those in this study were unembedded.

As can be seen in Table 32, there are 2 other nanoindentation studies of aging trends in human cortical bone with more than 10 donors. Tjhia et al. tested iliac crest specimens from 32 female donors, split into 2 age groups [102]. The younger age group consisted of 20 donors aged 20-40 years, while the older age group had 12 donors aged 49-74 years. Indentation E and H were not seen to be significantly different between the two groups. Hoffler et al. used hydrated indentation to test femoral neck specimens from 27 donors. Data were collected for both cortical and trabecular locations. Sixteen of the donors were male and 11 were female. The respective age ranges were 40-85 years and 27-93 years. No trends with age or gender differences were seen. The difference in anatomical location and gender composition of the donors in these studies makes a direct comparison with the results of this study questionable. The femoral neck and iliac crest cortices are much thinner than that of the femoral diaphysis and are expected to have higher levels of bone turnover.

The work of Rho et al. is the second-most similar to the human femur portion of this study [103]. Rho et al. tested transverse sections of femoral cortical bone from 9 male donors aged 35-95 years. Note that the same indentation data in Rho et al. was also presented in an article by Zioupos, with the inclusion of one additional donor [85]. The specimens were from the anterior section of the femoral diaphysis and were dehydrated in alcohol before being epoxy embedded. Indents were performed dry and were split between osteonal and interstitial tissue types, as well as endosteal, middle, and periosteal regions. Six correlations with age were assessed; one for each tissue type – region combination. Of the six calculated correlations, the endosteal – interstitial correlation was negative, the periosteal – osteonal correlation was positive, and the remaining 4 were not statistically significant. Thus, no consistent trend with age was identified.

The remaining two studies listed in Table 32 are bone aging fracture toughness investigations which also featured nanoindentation data. The small sample sizes of the these studies preclude strong conclusions; however, they are worth mentioning in order to complete the discussion of the existing literature. Koester et al. indented longitudinal humerus and tibia specimens from 3 young donors and 2 aged donors. No significant difference was seen between the two age groups. Katsamenis et al. used AFM-based nanoindentation on femoral specimens from 4 female donors. Unfortunately, indentation E and H data were not given; the parameter used was “elastic inhomogeneity”, which was defined as the ratio of E between the lamellar and interlamellar areas within a given osteon. They reported that “elastic inhomogeneity” was lower for the specimens from the elderly donors. The difference in properties between the lamellar and interlamellar regions was proposed to act as a crack-stopping mechanism, and thus the observed decline in fracture toughness with age was partially attributed to the decline in osteonal elastic inhomogeneity.

Aging in male femoral cortical bone has also been investigated using scanning acoustic microscopy (SAM) by Malo et al. [104]. Femoral shaft and femoral neck specimens were tested from 21 men aged 17-82 years. Measurements were performed for both cortical and trabecular bone types. In all cases, stiffness was found to increase with age. Thus, in both Malo et al. and in this study, stiffness was seen to increase with age for the male femoral cortex. Note that these are the two studies of aging in male cortical bone with the most number of donors. Bone nanoindentation and SAM measurements are correlated [75]. The stiffness values in Malo et al. were larger than those in this study, but the magnitude of the trend was similar: ~10% increase over 66 years compared with 15% over 78 years.

Refer to Table 33 for a summary of the nanoindentation studies of aging in human trabecular bone. By far the largest such study is that of Wolfram et al., with vertebral specimens from 104 donors, 54 female and 50 male, aged 21-94 years [62]. Indentation modulus was not found to change with age. However, elastic energy and dissipated energy (calculated from the area under the load – displacement curve)

Table 33: Experimental details for nanoindentation studies of aging in human trabecular bone

Specimen Info	n	Gender	Age Range (years)	Condition	Ref
Vertebral	104	54F 50M	21-94	Wet, Dry	[62]
Iliac biopsies	30 (15, 15)	F	Pre, post menopause	Dry	[101]
Femoral neck	27	16M 11F	M: 40-85; F: 27-93	Wet	[83]
Femoral neck	21	M	17-82	Wet	[105]
Femoral neck	10 (5, 5)	F	G1: 65-66; G2: 85-95	Dry	[106]

n = total # of donors, if split into 2 age groups the # in each group added as (#, #)
F = female, M = male
G1 and G2 designate younger and older age groups, respectively

increased with age. This increase with age was attributed to an increase in maximum force. Unfortunately, H data were not given, although an increase in maximum force would likely translate to an increase in hardness. Aside from Gao et al. [106], the remaining studies in Table 33 found no changes with age for indentation E or H. The Gao et al. study reported an increase of E and H with age. However, this was the smallest study with only 5 female donors per age group. Thus, trabecular bone indentation values are generally found not to change with age, although the increase in elastic and dissipated energies with age in Wolfram et al. is interesting. Results from trabecular bone should not be expected to apply to cortical bone, due to the differences between the tissues. In particular, trabecular bone has a significantly higher surface area and rate of turnover.

4.1.6 Age: Rodent and Other Animal Bones

In this study, rat tibia E' and H increased with age from 6 months to 12 months and then did not change significantly from 12 to 24 months. This trend can be explained by a period of changing properties during adolescence and shortly thereafter, followed by a plateau after reaching skeletal maturity. Similar growth – plateau trends can be seen for rat femora [107, 108] and mouse tibiae [109]. Zhang et al. tested femora from 70 male Wistar rats, split between 7 age groups from 1 to 17 months of age. Indentation E and H increased from 1 to 7 months and were stable thereafter [108]. Isaza et al. used femora from 30 male Wistar rats, split between 5 age groups from 1 to 24 months [107]. Calculations were performed using an elastic-viscoelastic-plastic-viscoplastic mechanical model, which prevents a direct comparison with E and H calculated using the Oliver-Pharr method. The elastic stiffness term increased rapidly from 1-4 months, was unchanged 4-12 months, and decreased slightly between the 12 and 24 month groups. The plastic hardness term increased over a longer time span, with the last significant difference between the 12 and 24 month groups. The work of Miller et al. is the only other study of rodent bone aging to use hydrated indentation [109]. Tibiae from developing mice ages 1-40 days were compared with those from 450 day old mature mice. Elastic modulus was found to increase almost linearly from 1-40 days to 89% of

the mature value. Other nanoindentation studies of mouse cortical bone have demonstrated the increase of E and H during skeletal development [110-112].

The pattern of changing mechanical properties prior to skeletal maturity followed by slow or no change thereafter is universal. Burket et al. indented osteonal areas in femoral specimens from 12 female baboons aged 0.3-32.5 years [113]. Indentation E and H increased quickly through the maturity age of 5-6 years. For the specimens from adult donors, E increased slowly while no significant change was seen for H. Another study of aging in female baboon femora with 18 donors aged 6-27 years reported an increase in interstitial Vickers microhardness with age but no change for osteonal indentations [114]. Chittenden et al. indented porcine femora with age groups from 1-48 months [115]. Stiffness and hardness increased progressively from 1-30 months, and no difference was seen from 30-48 months. Changing cortical bone indentation properties during skeletal growth are also seen for other studies of porcine femora [66, 116], rabbit humeri [117], and porcine mandibular condyle [118].

No significant change with age was seen for E″ in this study. There are only a couple of other dynamic nanoindentation studies of aging in animal cortical bone, and in both the bone specimens were tested dry. Sakamoto et al. tested femora from 9 male Sprague-Dawley rats, with age groups of 6, 10, and 24 weeks of age [119]. No change in tanδ was seen over this time span. Isaksson et al. tested female rabbit humeri using age groups of newborn, 11 days, 4 weeks, 3 months, and 6 months [117]. Loss modulus increased progressively between the younger age groups, with the last significant difference between the 4 week and 3 month groups. Indentation E′ and H increased over the full 6 month age range. Thus, it seems that E″ increases with age during skeletal growth, but reaches a plateau earlier than E′ or H. Loss modulus reaching a plateau quickly can be explained by the process of bone creation and development. Recall that new bone begins as unmineralized osteoid. Subsequently, mineralization increases over time but the amount of collagen does not. Since the viscoelasticity of bone is due to its collagen component, while the stiffness and

hardness of bone are due to the mineral phase, it is expected that E′ and H will increase over a larger time frame than E″.

4.1.7 Tissue age and Bone Turnover

The effect of tissue age on indentation data is seen in the osteonal – interstitial and periosteal – mid-cortex differences, as discussed previously. Namely, the older interstitial and mid-cortex tissues are stiffer and harder than the younger osteonal and periosteal tissues. Similarly, for trabeculae the older inner region is stiffer than the younger surrounding region [62]. In a number of indentation studies, local tissue age was measured explicitly by fluorescent labeling. Bala et al. indented iliac biopsy specimens from ewes which had been administered fluorescent labels every 6 months for 2.5 years [43]. For both cortical and cancellous tissues, Vickers microhardness increased with the matched tissue age. Significant increases between successive time points were seen until 18 months. The 30 month values were the highest, meaning that hardness may have continued to increase slowly over the span of 18 months to 30 months, although no statistical test was calculated for this interval. Huja et al. used fluorescent labeling to identify younger osteons in mature canine femora [120]. These labeled young osteons had lower modulus and hardness than the older unlabeled osteons. Finally, fluorescent labeling was used in rat cortical bone to demonstrate the progression of tissue age inwards from the periosteal surface and the associated trend in indentation data [89, 90, 92, 93].

The average tissue age of a bone segment is a function of the rate of resorption of old bone and the creation of new bone. A decrease in bone turnover will result in an increase in average tissue age and thus increased stiffness and hardness. This can be seen experimentally. In a nanoindentation study of iliac trabeculae from 40 women, stiffness was negatively correlated with bone formation rate per bone surface (BFR/BS) [121]. In a similar study, Tjhia et al. used nanoindentation to compare iliac bone biopsy specimens from women in the following groups: (1) young normal , (2) age-matched normal, (3) osteoporotic with vertebral fracture, and (4) atypical fracture with severely suppressed bone turnover due to long-term alendronate usage [102]. The indentation

parameters used were E, H, and “plastic deformation resistance” (an alternative hardness parameter based off of a series elastic-plastic mechanical model, which is sometimes used for mineralized biological tissues because it is independent of E, unlike H [122]). For trabecular indents, all 3 parameters were greater for the suppressed turnover group than the other groups. The measured bone formation rate was negatively correlated with H, plastic deformation resistance, and nearly E. For cortical indents, plastic deformation resistance was greatest for the suppressed bone turnover group. Increased indentation E and H as a result of bisphosphonate usage has also been demonstrated in a canine vertebral model [123]. Conversely, increased bone turnover as a result of estrogen depletion due to ovariectomy has been shown to result in decreased indentation stiffness and hardness in sheep [124], rabbit [125], and rat [126] models.

4.2 Effect of Bone Composition on Mechanical Properties

4.2.1 Mineralization

For most two-component composites an increase in the volume fraction of the stiffer component will result in increased stiffness of the composite. For bone this means that stiffness and hardness would be expected to be correlated with mineral content. This expected result was seen in the positive correlation of E′ with TMD for both the human and rat experiments. Additionally, for the Transverse human femur specimens, E′ was positively correlated with the site-matched qBEI Ca wt.% data. Surprisingly, H was not correlated with TMD for the human femur specimens. It is unclear why this would be the case, especially given the high correlation between E′ and H values. Nevertheless, H was positively correlated with TMD in the rat experiment and with qBEI Ca wt.% for the Transverse human femur specimens.

There are numerous examples of the dependence of bone mechanical properties on mineral content. Interstitial areas are more highly mineralized than osteonal areas and consequently are stiffer and harder. The same is true for rodent mid-cortex –

periosteal lamellae comparisons, as well as cortical – trabecular comparisons. Much of the variation in the stiffness of osseous tissues across the animal kingdom is due to variations in mineral content, as seen in nanoindentation [127] and tensile [128] experiments. Cortical bone specimens from children have a lower compressive elastic modulus and ash density than those from adults [129]. Indentation E decreases with progressive demineralization [130]. Nanoindentation E or H have been seen to be positively correlated with mineral content as measured by μCT [82, 118, 131], qBEI [30, 132-135], Raman spectroscopy [95, 113, 136], and infrared spectroscopy [92, 93, 137]. However, nanoindentation data are sometimes not found to be correlated with the degree of mineralization [73, 88].

Loss modulus was uncorrelated with TMD for both the human and rat experiments and was also uncorrelated with site-matched qBEI Ca wt.% for the Transverse human femur specimens. Thus, in this study bone viscoelasticity was independent of the level of mineralization. Presumably, this is due to the fact that the mineral platelets are not viscoelastic, while the amount of the viscoelastic collagen in the bone matrix is relatively constant.

4.2.2 Collagen Crosslinking

Experimental evidence suggests that changes in collagen crosslinking concentration affect the post-yield properties of bone but not its elastic stiffness [138]. In studies where the formation of advanced glycation end-product (AGE) crosslinks was induced via in vitro glycation, elastic modulus was found to be unchanged relative to the control group in compression [139, 140], tension [141], and 3-point bending [142, 143] tests. Also, in compression of human vertebrae, stiffness was uncorrelated with pentosidine, pyridinoline, and deoxypyridinoline concentrations [144]. Willems et al. used nanoindentation to test in vitro glycated porcine trabeculae [145]. No significant effect on indentation stiffness was seen from in vitro glycation for either the intact or the demineralized specimens. However, note that the sample size was only 6 specimens per group, so a modest effect of AGE concentration on indentation measurements cannot be ruled out. Lastly, in vitro glycation was not seen to affect the Vickers

hardness of bovine cortical bone [142]. The data in this study also support a negligible effect of collagen crosslinking on the measured indentation parameters. Hardness and E″ saw no significant correlations with PE. The few significant E′ – PE correlations are presumably not causal. PE and E′ both increased with age, and the E′ - Age correlation is better explained by the correlation of E′ with TMD.

4.2.3 Bound Water

In order to discuss the effect of bound water on the indentation data, it is first necessary to consider the compositional and structural properties which affect the amount of bound water. First, bound water is inversely related to porosity, since less bone matrix means less matrix-bound water. Second, BoundWater is a function of a bone specimen's degree of mineralization. As the mineral platelets grow, water is displaced [146]. For this reason, bound water is expected to be negatively correlated with degree of mineralization measures such as TMD. In fact, in both of the experiments in this study, BoundWater and TMD were negatively correlated. This TMD – bound water correlation has also been demonstrated in mice [8]. Similarly, an inverse relation between water and mineral contents has been demonstrated for rat [147], rabbit [148], and porcine [115] cortical bones. Third, bound water content depends on factors related to the collagen phase. Nyman et al. reported that oxidative deproteination, thermal denaturation, and incubation in ribose each affected cortical bone bound water measurements, which are all treatments which affect collagen but not mineral [149]. The decrease in bound water as a result of incubation in ribose demonstrates the potential for accumulation of collagen crosslinks to reduce matrix hydration, although BoundWater and PE were not correlated for the human femur specimens.

An increase in bound water can be expected to result in softer, more ductile bone. Bound water is principally a measure of matrix water content, and the effect of hydration was clearly demonstrated in the difference in the Wet and Dry indentation data. Additionally, as just discussed, higher bound water often reflects a lower level of mineralization, which would also translate to lower indentation stiffness and hardness. However, since bound water depends on other properties which have little effect on the

indentation parameters (such as porosity), indentation – BoundWater correlations are unlikely to be very strong. For the human femur specimens, E′ was negatively correlated with BoundWater for the Longitudinal – Dry experiment and nearly ($p < 0.1$) for Longitudinal – Wet. In the rat experiment, BoundWater was negatively correlated with E′ and H. Taken together, these results are perhaps indicative of a weak negative correlation of BoundWater with indentation stiffness and hardness. There was no consistent correlation between E″ and BoundWater. Note that the likelihood of observing a significant correlation between E″ and BoundWater is reduced by the fact that E″ did not depend on mineralization, unlike E′ and H.

4.3 Dependence of Bone Fracture on Composition, Structure, and Indentation Data

4.3.1 Fracture: Changes with Age

As expected, fracture toughness was found to decrease with age. For the human femur specimens, crack initiation toughness (K_{init}) and overall resistance to crack propagation (J-integral) were negatively correlated with Age. Crack growth toughness (K_{grow}) was not correlated with Age. However, this was likely in part due to having 4 fewer data points than the other 2 fracture parameters, as the Young group average was 68% higher than that of the Aged group. For the rat femora, the energy to propagate the crack to failure (CrackingToughness) decreased with age. On the other hand, the resistance to initial crack propagation (K_c) increased with age. The purpose of this section is to discuss the effects of changes in the compositional, structural, and indentation data on fracture toughness towards the goal of understanding the causes of the observed changes in fracture toughness with age.

Before continuing there are a few points worth noting. First, because all of the parameters in the rat experiment were found to change with age, there will be many non-causal correlations. Second, interpretation of the rat femora fracture data is complicated by the relative changes in size of the mid-cortical and periosteal lamellar

areas. The periosteal lamellar region grows due to deposition of new bone on the periosteal surface, while the area of the mid-cortical region declines with age due to endocortical resorption. As discussed in Location: Periosteal vs. Mid-cortex, the two regions have different mechanical properties. Fracture of the rat femora reflects the combined effect of the these tissues and their relative quantities; however, it is unknown how they independently contribute to cracking initiation and crack growth.

4.3.2 Microdamage

Bone is damaged due to the wear and tear of everyday life in the form of linear microcracks, typically around 50-100 μm in length, and diffuse damage areas, which are dense clusters of much shorter cracks [150]. Microdamage can be beneficial to fracture resistance as an energy dissipation mechanism. However, over time microdamage accumulates in older tissues, leaving them less able to resist crack propagation. Microdamage accumulation is mitigated by the targeted removal of more highly damaged tissues in the bone turnover process. Still, in vivo microdamage has been seen to increase with age in human femora [85, 151, 152], tibiae [32, 153], and vertebrae [154].

Thus, microdamage represents a possible contributor to declining bone quality with age, which was not characterized in this study. Norman et al. reported a negative correlation between in vivo microdamage density and fracture toughness for human femur and tibia compact tension specimens [155]. Similarly, Zioupos reported a negative correlation between in vivo microcrack density and fracture toughness, as measured by notched 3-point bending, for male cortical femur specimens. Additionally, in vitro fatigue damage of bovine cortical bone reduces fracture resistance [156, 157]. In a canine model, bisphosphonate treatment has been demonstrated to result in increased in vivo microdamage, which was associated with reduced toughness [158, 159].

Diffuse damage may be characteristic of tougher, more ductile bone. In 4-point bending fatigue tests, the specimens from younger donors had a longer fatigue life and higher levels of diffuse damage than the specimens from the older donors, which had

more microcracking [160]. Higher levels of diffuse damage has also been associated with higher fracture toughness in mice [161]. Linear microcracks are formed preferentially in interstitial bone, while diffuse damage is higher in osteonal bone [32, 151, 162].

4.3.3 Porosity

Cortical porosity is detrimental to bone fracture resistance because voids within a material concentrate stress and provide a path for crack growth. Finite element models show that cortical porosity decreases crack initiation toughness and crack propagation toughness [163, 164]. For the human femur specimens, Porosity was negatively correlated with K_{init} but was uncorrelated with J-integral and K_{grow}. In a similar experiment on male femoral specimens from 10 donors, porosity was negatively correlated with K_c, J-integral, and work-to-fracture (W_f) [85]. Wang et al. performed 3-point bending fracture tests on femoral specimens from 30 donors and reported a negative correlation between porosity and W_f but not between porosity and K_{IC} [165]. Porosity has also been found to be detrimental to fracture toughness in compact tension and compact shear fracture tests [166].

Cortical porosity was also seen to be detrimental in the rat experiment, as Porosity was negatively correlated with CrackingToughness. Unexpectedly, Porosity was positively correlated with K_C. It doesn't make sense for increasing cortical porosity to cause greater resistance to initial crack propagation, so the Porosity – K_c correlation is the result of the two parameters independently increasing with age. Also, recall that PoreWater is another measure of porosity. In this study, PoreWater had the same correlations with the fracture parameters as Porosity, with the exception of PoreWater not being correlated with K_c in the rat experiment.

4.3.4 Mineralization

In the mechanics of materials there is typically a tradeoff between a material's strength and its toughness; increasing strength comes at the expense of decreased ductility. This strength – toughness tradeoff is seen in bone [167-169]. For example, the

bones of children are less mineralized than the bones of adults and fail in compression at a lower ultimate stress but higher ultimate strain [129]. Similarly, for tensile specimens made from 39 different bones from 22 different species, ultimate strain decreased with increasing mineralization [128]. Notably, antler has the lowest mineral content in the bone family, as well as the highest tensile strain to failure (~6 times that of human bone), and is one of the toughest known biological materials [170, 171]. In human bone, ash content has been found to be negatively correlated with work-to-fracture [39] and post-yield strain [172]. In mouse models, increased mineralization is associated with decreased post-yield deflection [136, 173] and fracture toughness [174]. However, the etiology of whole-bone fracture is complicated, and other factors such as total bone mass, porosity, etc. are important contributors. In fracture versus control group studies, the fracture group has been found to have increased [175-177], decreased [178, 179], and both increased and decreased mineralization levels [180].

In this study, TMD was negatively correlated with K_{init} and J-integral in the human femur experiment and CrackingToughness in the rat experiment. Therefore, increased mineralization was associated with reduced toughness, which is consistent with the tradeoff between material strength and toughness. On the other hand, TMD was positively correlated with K_c in the rat experiment. Again, it is difficult to say whether this relationship is causal, or simply the result of both parameters increasing independently with age.

4.3.5 Bound Water

Due to water's effect as a plasticizer of the collagen in bone, higher levels of matrix hydration should be beneficial to bone's fracture toughness. Rehydration of dry bone dramatically increases its toughness. The effect of increased bound water should be similar, just smaller. In fact, this is what was seen in a study using sequential drying, bound water measurement, and 3-point bending [181]. Also, recall that the measured bound water content is a function of porosity, mineralization, and (perhaps) collagen crosslinking content. To a certain extent, the effect of a change in bound water on fracture toughness can be inferred from the relationships of these parameters

themselves with fracture toughness. Higher bound water was indeed found to be associated with improved fracture toughness: BoundWater was positively correlated with K_{init} in the human femur experiment and CrackingToughness in the rat experiment. However, BoundWater was also negatively correlated with K_c for the rat specimens. Note that the BoundWater – fracture correlations are the opposite of the Porosity – fracture and TMD – fracture correlations (except for the TMD – J-integral correlation). Other studies on human cortical bone support the beneficial effect of bound water content on bone toughness or failure strain [42, 182, 183]. Additionally, treatments which resulted in increased bound water were associated with increased toughness or greater displacement at failure [184, 185].

4.3.6 Collagen Crosslinking

Because the concentration of advanced glycation end-products (AGEs) increases with age in bone, non-enzymatic crosslinks have been identified as a potential reason for the decline in bone quality with age. Elevated AGE content has also been associated with increased fracture risk in diabetics [186-188]. Non-enzymatic crosslinks are thought to embrittle bone by decreasing collagen ductility, manifested as decreased post-yield deformation and strain at failure. Conversely, mature enzymatic crosslinks such as pyridinoline and deoxypyridinoline may increase toughness by stabilizing the collagen matrix.

A number of other studies of aging in human cortical bone have reported negative correlations between pentosidine concentration and toughness. Wang et al. performed 3-point bending fracture tests on cadaveric femur specimens from 30 donors and found negative correlations between pentosidine concentration and K_{IC} and work-to-fracture [165]. In a similar test on cortical humerus specimens from 9 donors, Zimmerman et al. observed fracture toughness to decrease with age, while AGE content increased [189]. In tensile tests of cortical tibiae specimens from 17 donors, Nyman et al. found pentosidine concentration to be negatively correlated with toughness, as failure strain decreased with age [35].

Experiments on human cancellous bone have also negatively associated AGE concentration with toughness. Tensile tests of individual trabeculae revealed a weak negative correlation between pentosidine concentration and ultimate strain [190]. For compression of tibial plateau trabecular bone cores from 42 donors, Karim et al. reported toughness to be negatively correlated with total fluorescent AGEs, while enzymatic crosslinking content (pyridinoline/deoxypyridinoline ratio) had a positive correlation [191]. In compression of vertebrae from 19 donors, Viguet-Carin et al. found no correlation between pentosidine, pyridinoline, and deoxypyridinoline concentrations with work-to-fracture [144]. However, in a regression model of work-to-fracture, pentosidine content was a significant factor in combination with mean areal bone mineral density.

To investigate the effects of AGEs on bone mechanics independent of other changes with age, in vitro glycation can be used. Incubation of bovine cortical bone specimens in ribose resulted in lower failure strain and toughness in 3-point bending [143] and increased yield stress in tension [141]. In compression of human femoral cancellous bone cores, in vitro glycation was seen to decrease post-yield strain energy [139]. In a similar study involving compression of tibial cancellous bone cores, in vitro glycation decreased post-yield energy dissipation and resulted in increased microcracking [140]. Thus, the in vitro glycation studies demonstrate that AGE crosslinking accumulation can decrease bone's capacity for post-yield deformation; however, the AGE concentrations reached are often much greater than typically seen in vivo.

Increased non-enzymatic crosslinking may also reduce fracture resistance indirectly, through impairment of the bone turnover process. In in vitro cultivation studies, increased AGE content has been found to inhibit osteoclasts in the resorption of old bone [192] and osteoblasts in the deposition of new bone [193]. In human cortical bone, resorption pit area was found to decrease with AGE content, independent of age [153]. Also, in human femora, pentosidine concentration has been reported to be

negatively correlated with the area per osteon [165]. Finally, AGE concentration has been seen to affect trabecular architecture and microdamage morphology [191, 194].

In the human femur portion of this study, PE was uncorrelated with each of the 3 fracture toughness parameters. For the rat bones, PE was negatively correlated with CrackingToughness and was uncorrelated with K_c. However, the PE correlation with CrackingToughness was weaker than the correlations seen for the other compositional and structural parameters. In summary, despite the detrimental effects of increasing AGE concentration seen in other studies, pentosidine concentration was seen to be a poor predictor of fracture toughness.

4.3.7 Osteonal Area Fraction

The surface area of the human femur specimens consists of osteonal, interstitial, and porosity regions. A decline in the osteonal area fraction is equivalent to a relative increase in the proportion of interstitial and porosity areas. The detrimental effect of increased cortical porosity has already been discussed. As a consequence of their greater age, interstitial tissues have greater mineralization [177, 195, 196], accumulated microdamage [32, 151, 162], and non-enzymatic crosslinking content [197-199] than osteonal tissues. Again, as already discussed, each of these changes is disadvantageous to fracture toughness. Consequently, interstitial areas can be expected to be less tough than osteonal areas. In support of an osteonal – interstitial fracture toughness difference is the fact that indentation crack lengths (cube corner indenter) are longer in interstitial areas [200]. Thus, an increase in the relative proportion of interstitial areas would be unfavorable. The positive correlations of OstAr with K_{init} and J-integral for the human femur specimens support a beneficial role of osteons towards fracture resistance.

Osteons are also beneficial for fracture toughness because they are effective at halting crack growth or forcing crack deflection. Specifically, cracks propagating in interstitial tissue can get trapped at the osteonal-interstitial interface (cement line) [32, 201]. Larger osteons are preferable because they cause more crack deflection. For cadaveric femur specimens from 30 donors, Wang et al. found the average area per

osteon to decrease with age and to be positively correlated with energy-to-failure in 3-point bending fracture [165]. Other researchers have also reported the average area of an osteon decreasing [202] or remaining unchanged [73] with age. Increasing osteonal density has also been identified as a source of declining fracture resistance with age, as it results in decreased crack bridging [36, 41, 189].

4.3.8 Indentation Data

Table 19 presents the correlations between the fracture and indentation data for the human femur experiments. In summary, E′ and H were found to be negatively correlated with fracture toughness, while E″ was not. The negative correlations of indentation stiffness and hardness with the fracture toughness parameters are another example of the strength – toughness tradeoff seen already with mineralization and bound water. In fact, these correlations tell the same story, since the nanoindentation measurements are reflective of local matrix composition. In other words, changes in bone composition which are seen to increase indentation stiffness or hardness will also result in lowered fracture toughness. There are few studies which compare bone indentation and fracture toughness data. However, for skeletally mature baboons, interstitial Vickers microhardness has been seen to be negatively correlated with K_{IC} in one study [203] and uncorrelated in another [114].

The indentation – fracture correlations for the rat specimens were similar to those for the human femur specimens (see Table 20). Namely, significant correlations were seen for E′ and H but not for E″. The negative correlations of E′ and H with CrackingToughness in the Dry condition reflect the strength – toughness tradeoff, as was also seen for the human femur specimens. The correlation for the Wet condition was not statistically significant. On the other hand, E′ and H were positively correlated with cracking initiation toughness, K_c, for which there are two possible explanations. First, the stiffer matrix may increase the stress necessary for cracking initiation. Second, the increase in K_c with age could be primarily due to the change in the relative areas of the mid-cortex and periosteal lamellae regions, in which case the correlations are non-causal.

4.4 Compositional and Structural Changes with Age

4.4.1 Porosity

Intracortical porosity increases with age for both men and women, although the spatial distribution and pattern of change can vary anatomically and by gender [204-206]. Similar studies using bone specimens from the male femoral diaphysis have observed increasing cortical porosity with age [73, 85, 104]. Nevertheless, in this study cortical porosity (Porosity, PoreWater) was not found to change significantly with age for the human femur specimens. There was considerable spread in the data (Porosity coefficient of variation = 0.51). In a microradiography study of intracortical porosity in the femoral diaphysis with specimens from 86 female and 77 male donors, Bousson et al. found that “age explained 52% of the porosity variance in females and 13.5% in males” [204]. Thus for the human femur specimens in this study, the variance in porosity between individuals outweighed the well-known trend towards increasing intracortical porosity with age.

For the rat femur specimens, porosity was seen to increase progressively with age. Most of the porosity was located near the endosteal surface and was greatest on the posterior side [56]. This trend with age for male Fisher F344 rat femora is consistent with that seen in Zhang et al. for male Wistar rat femora [108]. Zhang et al. found cortical porosity to decrease from 1 to 7 months of age (approximate age of skeletal maturity) and then to increase from 9 months to 17 months of age, which was the oldest age group in the study.

4.4.2 Mineralization

It is clear that the level of bone mineralization increases with age until skeletal maturity. However, the available data are limited and inconclusive with respect to mineralization changes during adulthood. The largest study of mineralization changes with age for the human femoral diaphysis is that of Bergot et al., using microradiography with anterior midfemoral cortical specimens from 193 donors [195]. The 99 female and

94 male specimens were divided into 7 10-year age groups. For males, interstitial mineralization was positively correlated with age (r = 0.212), while osteonal mineralization was uncorrelated with age. For females, both osteonal and interstitial mineralization decreased with age (r = -0.249 and r = -0.222, respectively). Until 50 years of age mineralization was higher in females, but in the elderly groups mineralization was higher in males. The diverging aging trends seen for men and women highlights the necessity of treating male and female data separately; when the data were pooled no significant correlations with age were seen. Also, the relatively low correlation coefficients indicate that the mineralization trends with age were relatively modest and would likely be missed in studies with small sample sizes.

For the 29 human femur specimens in this study, TMD was positively correlated with Age. For a least squares fit to the data, TMD increased from 956 mgHA/cm^3 at 21 years to 1003 mgHA/cm^3 at 98 years, a change of 5%. Such a change is consistent with the modest increase in male interstitial mineralization with age seen in Bergot et al. Another study in which mineralization was found to increase with age in the male femoral cortex is that of Yerramshetty et al., for 16 donors aged 52-85 years [207]. As measured by Raman spectroscopy, average mineralization increased when pooled over all 4 quadrants, with the greatest increase in the medial quadrant. Using a density fractionization technique with femoral midshaft specimens from 15 male donors, Simmons et al. reported the proportion of bone in the highest density fraction group to increase with age [208]. In contrast, Goldman et al. reported decreasing mineralization with age for 20 male femoral midshaft specimens, using qBEI (halogenated dimethacrylate standard) [209]. Mirzaali et al. found no change in mineralization over the age range 59-91 years for specimens from 19 male donors, as measured by Raman spectroscopy [73].

Much of the difficulty in identifying aging trends in adult human bone stems from the amount of variation between individuals of the same age. One important source of variation is bone morphology. Long bone robustness, defined as cross-sectional area divided by length (Tt.Ar/Le), is a heritable trait which is established by 2 years of age

[210]. Bone robustness is found to be negatively correlated with degree of mineralization [172, 211]. Bone robustness can also explain mineralization differences between different mice strains [173]. Slender bones being more highly mineralized than robust bones is thought to be a compensation for having a lower moment of inertia. All else being equal, the bending stiffness of robust bones would be greater. By increasing the stiffness of the matrix through increased mineralization, slender bones can achieve the same bending stiffness as robust bones, despite having a lower moment of inertia.

For the rat femora in this study, TMD increased progressively with age. Analysis of aging trends in rodent bone is simpler than in human bone, due to the absence of Haversian remodeling; new bone deposition occurs at the periosteal surface but not intracortically. The increase in average TMD from 6-12 months and again from 12-24 months is therefore explained by a decreasing proportion of younger bone with age and the time course of secondary mineralization over months-years. A couple other studies have mineralization data for rats up to 24 months of age. Vanleene et al. used male Wistar rats ages 1, 4, 9, 12, 18, and 24 months with 6 rats per age group [212]. Degree of mineralization of the femoral diaphysis, as measured by FTIR (PO_4/Amide I), decreased from 1-12 months and was stable from 12-24 months. Akkus et al. tested femoral diaphysis specimens from female Sprague-Dawley rats ages 3, 8, and 24 months, with 4-5 donors per age group [213]. Using Raman spectroscopy, degree of mineralization was found to be greater for the 24 month group than the 3 and 8 month groups. Additionally, Zhang et al. tested femora from 70 male Wistar rats with 10 age groups from 1-17 months of age and 7 rats per age group [108]. Degree of mineralization (Ca and P concentrations, as determined by quantitative chemical analyses using inductively coupled plasma optical emission spectroscopy (ICP)) was found to increase from 1 to ~9-11 months and was stable thereafter.

4.4.3 Collagen Crosslinking

The concentration of advanced glycation end-product (AGE) crosslinking in bone increases with age, as demonstrated in experiments on human [35, 165, 189, 197, 199, 214, 215] and rat [188, 216, 217] bones. Pentosidine concentration increased with age

in both the human and rat experiments in this study. For the human femur specimens, PE was the parameter most strongly correlated with age.

4.4.4 Bound Water

BoundWater decreased with age in the human and rat femora, which is consistent with the observed trends of increased mineralization, porosity (rat femora only), and collagen crosslinking with age. Bound water in femoral cortical bone has been similarly found to decrease with age in earlier studies by Nyman et al. [19, 42]. Additionally, the weight percentage of water in porcine femora decreases with age, at least over the range of 1-48 months [115, 116].

4.4.5 Bone Turnover

For the human femur specimens in this study, degree of mineralization and indentation stiffness and hardness were found to increase with age. In the existing literature, however, comparable data are limited and often inconsistent. On the other hand, because of the relative ease in collecting serum and urinary samples, there are several large studies of age-related changes in biochemical bone turnover markers (BTMs) in men [218-221]. For example, Chaitou et al. collected BTM data for 1149 men aged 19-85 years [218]. Since average tissue age is a function of the rate of bone resorption and bone formation, BTM data provide insight into the likely aging trends of compositional and indentation data. These studies show that for men bone turnover is highest at 20-30 years of age and declines to a minimum around 50-60 years. With advancing age after 60 years, bone resorption increases slightly while bone formation remains stable or declines slightly [52, 218]. Histomorphometric data also demonstrate decreased bone turnover with age in men [222]. The changes with age for the human femur specimens in this study are consistent with the trend of decreased bone turnover with age seen in the BTM studies. Specifically, decreased bone turnover leads to an increase in average tissue age, which means a higher degree of average mineralization, which in turn means higher indentation stiffness and hardness.

Note that the general aging trends of bone turnover are different for men and women. Bone turnover in women increases during menopause as a result of decreased estrogen levels and remains elevated thereafter [48, 223, 224]. Recall that the largest study of mineralization changes with age of the human femoral cortex, by Bergot et al., found a slight decline in mineralization with age for females and a slight increase in interstitial mineralization with age for males [195]. These diverging trends match with the theoretical expectations from the bone turnover studies. Namely, a decline in bone turnover with age in men, resulting in slightly increased mineralization with age, and an increase in bone turnover in women, resulting in slightly decreased mineralization with age. This also means that studies of aging in bone should be cautious about pooling male and female data. The increase in indentation stiffness and hardness with age for the human femur specimens in this study is consistent with the expected effects of the decline in bone turnover with age seen in males.

CHAPTER 5
CONCLUSIONS

5.1 Primary Conclusions

1) Indentation loss modulus (E″) is not a useful measure of bone quality.

One of the motivating hypotheses of this study is the idea that bone viscoelasticity may decrease with age and be indicative of declining fracture resistance. However, the data do not support this hypothesis. In both the human and rat experiments, E″ was unchanged with age and was uncorrelated with the fracture parameters.

2) The dependence of storage modulus (E′), loss modulus, and hardness (H) on Section, Condition, Location, and Age

The experimental variables in the human femur nanoindentation experiments were Condition: Wet vs. Dry, Section: Longitudinal vs. Transverse, Location: Osteonal vs. Interstitial, and Age: 21-98 years. The dependencies of E′, E″, and H were found to be:

$$\mathrm{E}' = f(\mathrm{Section}, \mathrm{Condition}, \mathrm{Age})$$

$$\mathrm{E}'' = f(\mathrm{Section}, \mathrm{Condition})$$

$$\mathrm{H} = f(\mathrm{Section}, \mathrm{Condition}, \mathrm{Age}, \mathrm{Location})$$

Specifically: Longitudinal < Transverse for all 3 parameters, Wet < Dry for E′ and H, Wet > Dry for E″, E′ and H increased with age, and Osteonal < Interstitial for H.

The experimental variables in the rat tibia nanoindentation experiment were Condition: Wet vs. Dry, Location: Periosteal vs. Mid-cortex, and Age: 6, 12, and 24 months. The rat tibia Wet vs. Dry comparisons were the same as for the human femur experiment. For E′ and H: Periosteal < Mid-cortex, 6 months < 12 months, and there was no significant difference between 12 and 24 months.

3) Increasing indentation stiffness and hardness with age is a novel result for adult male cortical bone.

For the Wet specimens, E′ increased ~15% from 21 to 98 years of age. At ~12-13%, the increase for H was slightly less than for E′. This is the first study with a sample

size greater than 10 to report an increase in indentation stiffness or hardness with age in adult male cortical bone. In the handful of comparable studies, typically no changes with age were observed. However, studies with small samples sizes or limited age ranges would be expected to miss an aging trend of the magnitude observed in this study, which had indentation data for 26 male donors over a 78 year age range (21-98 years). The most comparable indentation study had a dataset of 19 male donors over a 33 year age range (59-91 years) [73]. Using surface acoustic microscopy, Malo et al. found stiffness to increase with age in the femoral shaft and neck for a dataset of 21 male donors aged 17-82 years [104]. Thus, increasing matrix stiffness with age in the male femoral diaphysis has now been demonstrated using two different experimental techniques.

4) Increased indentation stiffness and hardness is associated with decreased fracture toughness.

Typically there is a tradeoff between material strength and toughness. Therefore, increased stiffness and hardness would be expected to be detrimental to fracture resistance. The results from this study are consistent with this expectation. In the human femur experiment, E′ and H were found to be negatively correlated with the 3 fracture toughness parameters. Either E′ or H were included in each of the regression models of fracture. In the rat bone experiment, E′ and H were negatively correlated with CrackingToughness, a measure of the energy required to propagate the crack till failure.

5) The trend of increasing indentation stiffness and hardness with age is primarily attributable to an increase in mineralization with age.

As the mineral phase is responsible for the stiffness of bone, increased mineral content can be expected to result in increased stiffness. Because the mineral platelets displace water, increased mineralization also leads to increased stiffness by decreasing matrix hydration. In both the human and the rat experiments E′ was positively correlated with TMD, and H was positively correlated with TMD for the rat bones. Additionally, E′ and H were positively correlated with the site-matched qBEI Ca wt.% data for the

Transverse human femur specimens. In the rat experiment, TMD increased from 6 to 12 months and from 12 to 24 months. While the 12-24 month difference was not statistically significant for E′ and H, the values were highest in the 24 month group. In the human femur experiment TMD increased slightly with age, increasing ~5% from 21 to 98 years. The literature on mineralization trends with age in male cortical bone is limited and often contradictory. However, the modest TMD increase seen in this study is consistent with the work of Bergot et al., which with 99 female and 94 male femoral diaphysis specimens is the largest such study [195]. In Bergot et al., male interstitial mineralization was positively correlated with age (r = 0.212), while male osteonal mineralization was not significantly correlated with age. In contrast to the limited data on mineralization trends with age, there are a number of large studies on aging trends in biochemical markers of bone turnover in men [218-221]. These studies demonstrate that in adult males bone turnover is highest at 20-30 years of age and declines to a minimum around 50-60 years of age. Thereafter, the rate of bone formation remains low. Because it takes months-years for newly formed bone to become fully mineralized, a decline in the rate of turnover leads to an increase in the average degree of mineralization [45]. Therefore, the bone turnover studies indicate a tendency towards increased mineralization with age in male cortical bone, which is what was observed in this study, as well as in Bergot et al.

6) Fracture resistance is multifactorial.

Given its complex hierarchical structure, bone fracture can be expected to be complex as well, and features at all length scales of the structural hierarchy have been identified which contribute to the fracture resistance of bone. In this study, the multifactorial nature of cortical bone fracture toughness was reflected in the regression models of fracture for the human femur specimens:

$$\mathrm{K_{init}} = f\left(\mathrm{E'_{L,Wet}}, \mathrm{BoundWater}, \mathrm{PoreWater}, \mathrm{OstAr}\right)$$

$$\text{J-integral} = f(\mathrm{OstAr}, \mathrm{H_{L,Wet}}, \mathrm{H_{T,Wet}})$$

$$\mathrm{K_{grow}} = f(\mathrm{E'_{L,Wet}})$$

It was found that K_{init} and J-integral were best predicted by a combination of indentation (E′, H), compositional (BoundWater), and structural (PoreWater, OstAr) parameters. A key takeaway from this study is that the fracture toughness of male cortical bone was found to decrease with age, due to increased stiffness and hardness. However, the multifactorial nature of bone fracture means that increased matrix stiffness and hardness was not the sole cause of the decreased fracture toughness.

The same can be said for the fracture resistance of the rat femora. However, for the rat femora an important factor which was not characterized in this study is the area fraction of the mid-cortical and periosteal lamellae regions. These tissues are different in composition and structure and likely differ in terms of fracture toughness, which complicates the interpretation of the correlations between the rat indentation and fracture data.

5.2 Closing Remarks

This study provides an improved understanding of the decline in bone quality with age in male cortical bone. Specifically, an increase in stiffness and hardness with age was found to result in lower fracture toughness. Viscoelastic loss modulus was unchanged with age and was not associated with fracture toughness. A limitation of this study is that fact that the femoral diaphysis is not a typical fracture site, such as the femoral neck or distal radius. These common fracture sites have thinner cortices than the femoral shaft and consequently may be remodeled more frequently. However, while there may be some anatomical variation, because the rate of bone turnover is largely hormonally driven, aging trends in cortical bone are expected to be systemic. Note that Malo et al. found stiffness to increase with age in males at both the femoral shaft and the femoral neck [104]. Men and women have different aging trends in the rate of bone turnover. Consequently, researchers looking at compositional or mechanical property changes with age should assess gender-specific trends first and exercise caution prior to pooling data.

The results from this study have implications for the use of bisphosphonates in the prevention of osteoporotic fractures. Bisphosphonates act by reducing bone turnover, which helps preserve bone mass in cases of elevated turnover, as is typical of postmenopausal osteoporosis. However, bisphosphonate use is associated with fractures at “atypical” sites such as the femoral diaphysis [225]. This is because, as previously discussed, unremodeled tissue progressively becomes less tough over time due to increased mineralization, microdamage accumulation, decreased bound water, etc. In men, however, turnover is not elevated in old age, and this study demonstrates that male cortical bone becomes less tough with age, due in part to changes associated with increased tissue age. By further depressing the remodeling rate, the use of bisphosphonates could make things worse.

In conclusion, bone is a remarkably complex material, and there is a good deal left to learn about its mechanics. In particular, data on changes with age in compositional and mechanical properties are insufficient. The aging trends in male cortical bone identified in this study will hopefully prove useful towards an improved understanding of age-related fragility fractures and aid in their prevention.

5.3 Proposed Future Work

With respect to understanding the age-related decline in bone fracture toughness, future research could include:

- Establishing a relationship between bone turnover and storage modulus.
- Identifying other determinants of indentation storage modulus, such as collagen fibril orientation or mature collagen crosslinking concentration.
- Using a larger number of indents per specimen to characterize the distribution of local mechanical properties and the effect of heterogeneity on fracture toughness.
- Developing empirical relations between mineralization, indentation, and fracture toughness data for improved modeling.
- Performing a similar study of aging in female cortical bone.

REFERENCES

1. Schuit, S.C.E., et al., *Fracture incidence and association with bone mineral density in elderly men and women: the Rotterdam Study.* Bone, 2004. **34**(1): p. 195-202.
2. Kanis, J., et al., *Ten year probabilities of osteoporotic fractures according to BMD and diagnostic thresholds.* Osteoporosis International, 2001. **12**(12): p. 989-995.
3. Hui, S.L., C.W. Slemenda, and C.C. Johnston Jr, *Age and bone mass as predictors of fracture in a prospective study.* Journal of clinical investigation, 1988. **81**(6): p. 1804.
4. Brauer, C.A., et al., *Incidence and mortality of hip fractures in the United States.* Jama, 2009. **302**(14): p. 1573-1579.
5. Weinkamer, R. and P. Fratzl, *Mechanical adaptation of biological materials — The examples of bone and wood.* Materials Science and Engineering: C, 2011. **31**(6): p. 1164-1173.
6. Mellon, S.J. and K.E. Tanner, *Bone and its adaptation to mechanical loading: a review.* International Materials Reviews, 2012. **57**(5): p. 235-255.
7. Gao, H., *Application of Fracture Mechanics Concepts to Hierarchical Biomechanics of Bone and Bone-like Materials.* International Journal of Fracture, 2006. **138**(1-4): p. 101-137.
8. Granke, M., M.D. Does, and J.S. Nyman, *The Role of Water Compartments in the Material Properties of Cortical Bone.* Calcified Tissue International, 2015. **97**(3): p. 292-307.
9. Weiner, S. and H.D. Wagner, *THE MATERIAL BONE: Structure-Mechanical Function Relations.* Annual Review of Materials Science, 1998. **28**(1): p. 271-298.
10. Launey, M.E., M.J. Buehler, and R.O. Ritchie, *On the Mechanistic Origins of Toughness in Bone*, in *Annual Review of Materials Research, Vol 40*, D.R. Clarke, M. Ruhle, and F. Zok, Editors. 2010, Annual Reviews: Palo Alto. p. 25-53.
11. Varga, P., et al., *Investigation of the three-dimensional orientation of mineralized collagen fibrils in human lamellar bone using synchrotron X-ray phase nano-tomography.* Acta Biomaterialia, 2013. **9**(9): p. 8118-8127.
12. Zebaze, R.M.D., et al., *Intracortical remodelling and porosity in the distal radius and post-mortem femurs of women: a cross-sectional study.* The Lancet, 2010. **375**(9727): p. 1729-1736.
13. Riggs, B.L., et al., *A population-based assessment of rates of bone loss at multiple skeletal sites: evidence for substantial trabecular bone loss in young adult women and men.* Journal of Bone and Mineral Research, 2008. **23**(2): p. 205-214.
14. Holzer, G., et al., *Hip Fractures and the Contribution of Cortical Versus Trabecular Bone to Femoral Neck Strength.* Journal of Bone and Mineral Research, 2009. **24**(3): p. 468-474.
15. Barth, H.D., et al., *On the effect of X-ray irradiation on the deformation and fracture behavior of human cortical bone.* Bone, 2010. **46**(6): p. 1475-1485.

16. Wang, X., et al., *The role of collagen in determining bone mechanical properties.* Journal of orthopaedic research, 2001. **19**(6): p. 1021-1026.
17. Yan, J., et al., *Fracture toughness and work of fracture of hydrated, dehydrated, and ashed bovine bone.* Journal of Biomechanics, 2008. **41**(9): p. 1929-1936.
18. Rai, R.K. and N. Sinha, *Dehydration-Induced Structural Changes in the Collagen–Hydroxyapatite Interface in Bone by High-Resolution Solid-State NMR Spectroscopy.* The Journal of Physical Chemistry C, 2011. **115**(29): p. 14219-14227.
19. Nyman, J.S., et al., *Partial removal of pore and loosely bound water by low-energy drying decreases cortical bone toughness in young and old donors.* Journal of the Mechanical Behavior of Biomedical Materials, 2013. **22**(0): p. 136-145.
20. Nyman, J.S., et al., *The influence of water removal on the strength and toughness of cortical bone.* Journal of Biomechanics, 2006. **39**(5): p. 931-938.
21. Lucksanasombool, P., et al., *Fracture toughness of bovine bone: influence of orientation and storage media.* Biomaterials, 2001. **22**(23): p. 3127-3132.
22. Nalla, R.K., et al., *Effects of polar solvents on the fracture resistance of dentin: role of water hydration.* Acta Biomaterialia, 2005. **1**(1): p. 31-43.
23. Samuel, J., et al., *Water residing in small ultrastructural spaces plays a critical role in the mechanical behavior of bone.* Bone, 2014. **59**: p. 199-206.
24. Yamashita, J., et al., *The use of dynamic mechanical analysis to assess the viscoelastic properties of human cortical bone.* Journal of Biomedical Materials Research, 2001. **58**(1): p. 47-53.
25. Pathak, S., et al., *Measuring the dynamic mechanical response of hydrated mouse bone by nanoindentation.* Journal of the Mechanical Behavior of Biomedical Materials, 2011. **4**(1): p. 34-43.
26. Koester, K.J., J.W. Ager, and R.O. Ritchie, *The true toughness of human cortical bone measured with realistically short cracks.* Nature Materials, 2008. **7**(8): p. 672-677.
27. Peterlik, H., et al., *From brittle to ductile fracture of bone.* Nature Materials, 2006. **5**(1): p. 52-55.
28. Yan, J., J.J. Mecholsky Jr, and K.B. Clifton, *How tough is bone? Application of elastic–plastic fracture mechanics to bone.* Bone, 2007. **40**(2): p. 479-484.
29. Nalla, R.K., J.H. Kinney, and R.O. Ritchie, *Mechanistic fracture criteria for the failure of human cortical bone.* Nature Materials, 2003. **2**(3): p. 164-168.
30. Gupta, H.S., et al., *Mechanical modulation at the lamellar level in osteonal bone.* Journal of Materials Research, 2006. **21**(08): p. 1913-1921.
31. Katsamenis, O.L., T. Jenkins, and P.J. Thurner, *Toughness and damage susceptibility in human cortical bone is proportional to mechanical inhomogeneity at the osteonal-level.* Bone, 2015. **76**(0): p. 158-168.
32. Diab, T. and D. Vashishth, *Morphology, localization and accumulation of in vivo microdamage in human cortical bone.* Bone, 2007. **40**(3): p. 612-618.
33. Ritchie, R.O., M.J. Buehler, and P. Hansma, *Plasticity and toughness in bone.* Physics Today, 2009. **62**(6): p. 41-47.

34. Nyman, J.S., et al., *Mechanical behavior of human cortical bone in cycles of advancing tensile strain for two age groups.* Journal of Biomedical Materials Research Part A, 2009. **89A**(2): p. 521-529.
35. Nyman, J.S., et al., *Age-related factors affecting the postyield energy dissipation of human cortical bone.* Journal of Orthopaedic Research, 2007. **25**(5): p. 646-655.
36. Koester, K., H. Barth, and R. Ritchie, *Effect of aging on the transverse toughness of human cortical bone: evaluation by R-curves.* Journal of the mechanical behavior of biomedical materials, 2011. **4**(7): p. 1504-1513.
37. Chan, K.S., C.K. Chan, and D.P. Nicolella, *Relating crack-tip deformation to mineralization and fracture resistance in human femur cortical bone.* Bone, 2009. **45**(3): p. 427-434.
38. Abraham, A.C., et al., *Multiscale predictors of femoral neck in situ strength in aging women: contributions of BMD, cortical porosity, reference point indentation, and nonenzymatic glycation.* Journal of Bone and Mineral Research, 2015. **30**(12): p. 2207-2214.
39. Currey, J.D., K. Brear, and P. Zioupos, *The effects of ageing and changes in mineral content in degrading the toughness of human femora.* Journal of Biomechanics, 1996. **29**(2): p. 257-260.
40. Wang, X., et al., *Age-related changes in the collagen network and toughness of bone.* Bone, 2002. **31**(1): p. 1-7.
41. Nalla, R.K., et al., *Role of microstructure in the aging-related deterioration of the toughness of human cortical bone.* Materials Science and Engineering: C, 2006. **26**(8): p. 1251-1260.
42. Nyman, J.S., et al., *Measurements of mobile and bound water by nuclear magnetic resonance correlate with mechanical properties of bone.* Bone, 2008. **42**(1): p. 193-199.
43. Bala, Y., et al., *Time sequence of secondary mineralization and microhardness in cortical and cancellous bone from ewes.* Bone, 2010. **46**(4): p. 1204-1212.
44. Fuchs, R.K., et al., *In situ examination of the time-course for secondary mineralization of Haversian bone using synchrotron Fourier transform infrared microspectroscopy.* Matrix Biology, 2008. **27**(1): p. 34-41.
45. Ruffoni, D., et al., *The bone mineralization density distribution as a fingerprint of the mineralization process.* Bone, 2007. **40**(5): p. 1308-1319.
46. Ruffoni, D., et al., *Effect of temporal changes in bone turnover on the bone mineralization density distribution: a computer simulation study.* Journal of Bone and Mineral Research, 2008. **23**(12): p. 1905-1914.
47. Roschger, P., et al., *Bone mineralization density distribution in health and disease.* Bone, 2008. **42**(3): p. 456-466.
48. Feng, X. and J.M. McDonald, *Disorders of bone remodeling.* Annual Review of Pathology: Mechanisms of Disease, 2011. **6**: p. 121-145.
49. Roschger, P., et al., *Alendronate increases degree and uniformity of mineralization in cancellous bone and decreases the porosity in cortical bone of osteoporotic women.* Bone, 2001. **29**(2): p. 185-191.

50. Zoehrer, R., et al., *Effects of 3-and 5-Year Treatment With Risedronate on Bone Mineralization Density Distribution in Triple Biopsies of the Iliac Crest in Postmenopausal Women.* Journal of Bone and Mineral Research, 2006. **21**(7): p. 1106-1112.
51. Misof, B.M., et al., *Effects of intermittent parathyroid hormone administration on bone mineralization density in iliac crest biopsies from patients with osteoporosis: a paired study before and after treatment.* The Journal of Clinical Endocrinology & Metabolism, 2003. **88**(3): p. 1150-1156.
52. Meier, C., et al., *Endocrine regulation of bone turnover in men.* Clinical endocrinology, 2005. **63**(6): p. 603-616.
53. Delp, M.D., M.V. Evans, and C. Duan, *Effects of aging on cardiac output, regional blood flow, and body composition in Fischer-344 rats.* Journal of Applied Physiology, 1998. **85**(5): p. 1813-1822.
54. Granke, M., et al., *Identifying novel clinical surrogates to assess human bone fracture toughness.* Journal of Bone and Mineral Research, 2015. **30**(7): p. 1290-1300.
55. Granke, M., et al., *Prevalent role of porosity and osteonal area over mineralization heterogeneity in the fracture toughness of human cortical bone.* Journal of Biomechanics, 2016.
56. Uppuganti, S., et al., *Age-related changes in the fracture resistance of male Fischer F344 rat bone.* Bone, 2016. **83**: p. 220-232.
57. Oliver, W.C. and G.M. Pharr, *An improved technique for determining hardness and elastic modulus using load and displacement sensing indentation experiments.* Journal of materials research, 1992. **7**(06): p. 1564-1583.
58. Nyman, J.S., et al., *Measuring Differences in Compositional Properties of Bone Tissue by Confocal Raman Spectroscopy.* Calcified Tissue International, 2011. **89**(2): p. 111-122.
59. Ritchie, R.O., et al., *Measurement of the toughness of bone: A tutorial with special reference to small animal studies.* Bone, 2008. **43**(5): p. 798-812.
60. Roschger, P., et al., *Validation of quantitative backscattered electron imaging for the measurement of mineral density distribution in human bone biopsies.* Bone, 1998. **23**(4): p. 319-326.
61. Hoffler, C.E., et al., *An application of nanoindentation technique to measure bone tissue lamellae properties.* Journal of Biomechanical Engineering-Transactions of the Asme, 2005. **127**(7): p. 1046-1053.
62. Wolfram, U., H.-J. Wilke, and P.K. Zysset, *Rehydration of vertebral trabecular bone: Influences on its anisotropy, its stiffness and the indentation work with a view to age, gender and vertebral level.* Bone, 2010. **46**(2): p. 348-354.
63. Garner, E., et al., *Viscoelastic dissipation in compact bone: Implications for stress-induced fluid flow in bone.* Journal of Biomechanical Engineering-Transactions of the Asme, 2000. **122**(2): p. 166-172.
64. Rodriguez-Florez, N., M.L. Oyen, and S.J. Shefelbine, *Insight into differences in nanoindentation properties of bone.* Journal of the Mechanical Behavior of Biomedical Materials, 2013. **18**: p. 90-99.

65. Lee, K.-L., et al., *The effects of loading conditions and specimen environment on the nanomechanical response of canine cortical bone.* Materials Science and Engineering: C, 2013. **33**(8): p. 4582-4586.
66. Feng, L., et al., *Mechanical properties of porcine femoral cortical bone measured by nanoindentation.* Journal of Biomechanics, 2012. **45**(10): p. 1775-1782.
67. Faingold, A., et al., *The effect of hydration on mechanical anisotropy, topography and fibril organization of the osteonal lamellae.* Journal of Biomechanics, 2014. **47**(2): p. 367-372.
68. Guidoni, G., M. Swain, and I. Jäger, *Nanoindentation of wet and dry compact bone: Influence of environment and indenter tip geometry on the indentation modulus.* Philosophical Magazine, 2010. **90**(5): p. 553-565.
69. Rho, J.-Y. and G.M. Pharr, *Effects of drying on the mechanical properties of bovine femur measured by nanoindentation.* Journal of Materials Science: Materials in Medicine, 1999. **10**(8): p. 485-488.
70. Schwiedrzik, J., et al., *In situ micropillar compression reveals superior strength and ductility but an absence of damage in lamellar bone.* Nat Mater, 2014. **13**(7): p. 740-747.
71. Reisinger, A.G., D.H. Pahr, and P.K. Zysset, *Principal stiffness orientation and degree of anisotropy of human osteons based on nanoindentation in three distinct planes.* Journal of the Mechanical Behavior of Biomedical Materials, 2011. **4**(8): p. 2113-2127.
72. Rho, J.-Y., et al., *Elastic properties of microstructural components of human bone tissue as measured by nanoindentation.* Journal of Biomedical Materials Research, 1999. **45**(1): p. 48-54.
73. Mirzaali, M.J., et al., *Mechanical properties of cortical bone and their relationships with age, gender, composition and microindentation properties in the elderly.* Bone, 2015.
74. Fan, Z., et al., *Anisotropic properties of human tibial cortical bone as measured by nanoindentation.* Journal of Orthopaedic Research, 2002. **20**(4): p. 806-810.
75. Hofmann, T., et al., *Assessment of composition and anisotropic elastic properties of secondary osteon lamellae.* Journal of Biomechanics, 2006. **39**(12): p. 2282-2294.
76. Schwiedrzik, J.J. and P.K. Zysset, *Quantitative analysis of imprint shape and its relation to mechanical properties measured by microindentation in bone.* Journal of Biomechanics, 2015. **48**(2): p. 210-216.
77. Turner, C.H., et al., *The elastic properties of trabecular and cortical bone tissues are similar: results from two microscopic measurement techniques.* Journal of biomechanics, 1999. **32**(4): p. 437-441.
78. Mullins, L., et al., *Differences in the crack resistance of interstitial, osteonal and trabecular bone tissue.* Annals of Biomedical Engineering, 2009. **37**(12): p. 2574-2582.
79. Carnelli, D., et al., *Nanoindentation testing and finite element simulations of cortical bone allowing for anisotropic elastic and inelastic mechanical response.* Journal of Biomechanics, 2011. **44**(10): p. 1852-1858.

80. Carnelli, D., et al., *Orientation and size-dependent mechanical modulation within individual secondary osteons in cortical bone tissue.* Journal of the Royal Society Interface, 2013. **10**(81).
81. Seto, J., et al., *Tough lessons from bone: Extreme mechanical anisotropy at the mesoscale.* Advanced Functional Materials, 2008. **18**(13): p. 1905-1911.
82. Wu, Z., T.C. Ovaert, and G.L. Niebur, *Viscoelastic properties of human cortical bone tissue depend on gender and elastic modulus.* Journal of Orthopaedic Research, 2012. **30**(5): p. 693-699.
83. Hoffler, C.E., et al., *Age, gender, and bone lamellae elastic moduli.* Journal of Orthopaedic Research, 2000. **18**(3): p. 432-437.
84. Hoffler, C.E., et al., *Heterogeneity of bone lamellar-level elastic moduli.* Bone, 2000. **26**(6): p. 603-609.
85. Zioupos, P., *Ageing Human Bone: Factors Affecting its Biomechanical Properties and the Role of Collagen.* Journal of Biomaterials Applications, 2001. **15**(3): p. 187-229.
86. Zysset, P.K., et al., *Elastic modulus and hardness of cortical and trabecular bone lamellae measured by nanoindentation in the human femur.* Journal of Biomechanics, 1999. **32**(10): p. 1005-1012.
87. Rho, J.-Y., T.Y. Tsui, and G.M. Pharr, *Elastic properties of human cortical and trabecular lamellar bone measured by nanoindentation.* Biomaterials, 1997. **18**(20): p. 1325-1330.
88. Spiesz, E.M., et al., *Computational and experimental methodology for site-matched investigations of the influence of mineral mass fraction and collagen orientation on the axial indentation modulus of lamellar bone.* Journal of the Mechanical Behavior of Biomedical Materials, 2013. **28**: p. 195-205.
89. Donnelly, E., et al., *Effects of tissue age on bone tissue material composition and nanomechanical properties in the rat cortex.* Journal of Biomedical Materials Research Part A, 2010. **92A**(3): p. 1048-1056.
90. Kim, G., et al., *Improved prediction of rat cortical bone mechanical behavior using composite beam theory to integrate tissue level properties.* Journal of Biomechanics, 2012. **45**(16): p. 2784-2790.
91. Shipov, A., et al., *Unremodeled endochondral bone is a major architectural component of the cortical bone of the rat (Rattus norvegicus).* Journal of structural biology, 2013. **183**(2): p. 132-140.
92. Busa, B., et al., *Rapid establishment of chemical and mechanical properties during lamellar bone formation.* Calcified Tissue International, 2005. **77**(6): p. 386-394.
93. Donnelly, E., et al., *Contribution of Mineral to Bone Structural Behavior and Tissue Mechanical Properties.* Calcified Tissue International, 2010. **87**(5): p. 450-460.
94. Kavukcuoglu, N., et al., *Nanomechanics and Raman spectroscopy of fibrillin 2 knock-out mouse bones.* Journal of Materials Science, 2007. **42**(21): p. 8788-8794.

95. Pathak, S., et al., *Assessment of lamellar level properties in mouse bone utilizing a novel spherical nanoindentation data analysis method.* Journal of the mechanical behavior of biomedical materials, 2012. **13**: p. 102-117.
96. Checa, S., et al., *Skeletal maturation substantially affects elastic tissue properties in the endosteal and periosteal regions of loaded mice tibiae.* Acta Biomaterialia, 2015. **21**: p. 154-164.
97. Bach-Gansmo, F.L., et al., *Calcified Cartilage Islands in Rat Cortical Bone.* Calcified Tissue International, 2013. **92**(4): p. 330-338.
98. Aido, M., et al., *Effect of in vivo loading on bone composition varies with animal age.* Experimental Gerontology, 2015. **63**: p. 48-58.
99. Turunen, M.J., et al., *Bone mineral crystal size and organization vary across mature rat bone cortex.* Journal of Structural Biology, 2016. **195**(3): p. 337-344.
100. Bünger, M.H., et al., *Strontium and bone nanostructure in normal and ovariectomized rats investigated by scanning small-angle X-ray scattering.* Calcified tissue international, 2010. **86**(4): p. 294-306.
101. Polly, B.J., et al., *Intrinsic Material Properties of Trabecular Bone by Nanoindentation Testing of Biopsies Taken from Healthy Women Before and After Menopause.* Calcified Tissue International, 2012. **90**(4): p. 286-293.
102. Tjhia, C.K., et al., *Mechanical property and tissue mineral density differences among severely suppressed bone turnover (SSBT) patients, osteoporotic patients, and normal subjects.* Bone, 2011. **49**(6): p. 1279-1289.
103. Rho, J.Y., et al., *Microstructural elasticity and regional heterogeneity in human femoral bone of various ages examined by nano-indentation.* Journal of Biomechanics, 2002. **35**(2): p. 189-198.
104. Malo, M.K.H., et al., *Longitudinal elastic properties and porosity of cortical bone tissue vary with age in human proximal femur.* Bone, 2013. **53**(2): p. 451-458.
105. Ojanen, X., et al., *Relationships between tissue composition and viscoelastic properties in human trabecular bone.* Journal of Biomechanics, 2015. **48**(2): p. 269-275.
106. Gao, J., et al., *Age-related regional deterioration patterns and changes in nanoscale characterizations of trabeculae in the femoral head.* Experimental Gerontology, 2015. **62**: p. 63-72.
107. Jaramillo Isaza, S., et al., *Time-dependent mechanical properties of rat femoral cortical bone by nanoindentation: An age-related study.* Journal of Materials Research, 2014. **29**(10): p. 1135-1143.
108. Zhang, R., et al., *Multi-level femoral morphology and mechanical properties of rats of different ages.* Bone, 2015. **76**: p. 76-87.
109. Miller, L.M., et al., *Accretion of Bone Quantity and Quality in the Developing Mouse Skeleton.* Journal of Bone and Mineral Research, 2007. **22**(7): p. 1037-1045.
110. Makowski, A.J., et al., *The loss of activating transcription factor 4 (ATF4) reduces bone toughness and fracture toughness.* Bone, 2014. **62**: p. 1-9.

111. Nyman, J.S., et al., *Increasing duration of type 1 diabetes perturbs the strength–structure relationship and increases brittleness of bone.* Bone, 2011. **48**(4): p. 733-740.
112. Silva, M.J., et al., *Nanoindentation and whole-bone bending estimates of material properties in bones from the senescence accelerated mouse SAMP6.* Journal of Biomechanics, 2004. **37**(11): p. 1639-1646.
113. Burket, J., et al., *Microstructure and nanomechanical properties in osteons relate to tissue and animal age.* Journal of Biomechanics, 2011. **44**(2): p. 277-284.
114. Phelps, J.B., et al., *Microstructural heterogeneity and the fracture toughness of bone.* Journal of Biomedical Materials Research, 2000. **51**(4): p. 735-741.
115. Chittenden, M., et al., *Nanoindentation and ash content study of age dependent changes in porcine cortical bone.* Journal of Mechanics in Medicine and Biology, 2015. **15**(05): p. 1550074.
116. Feng, L. and I. Jasiuk, *Multi-scale characterization of swine femoral cortical bone.* Journal of Biomechanics, 2011. **44**(2): p. 313-320.
117. Isaksson, H., et al., *Rabbit cortical bone tissue increases its elastic stiffness but becomes less viscoelastic with age.* Bone, 2010. **47**(6): p. 1030-1038.
118. Willems, N.B.K., et al., *The correlation between mineralization degree and bone tissue stiffness in the porcine mandibular condyle.* Journal of Bone and Mineral Metabolism, 2014. **32**(1): p. 29-37.
119. Sakamoto, M. and K. Kobayashi, *Viscoelastic Properties of Microstructural Components of Rat Cortical Bone Tissue as Measured by Dynamic Nanoindentation.* Journal of the Japanese Society for Experimental Mechanics, 2009. **9**(Special_Issue): p. s151-s155.
120. Huja, S.S., F.M. Beck, and D.T. Thurman, *Indentation Properties of Young and Old Osteons.* Calcified Tissue International, 2006. **78**(6): p. 392-397.
121. Wang, X., et al., *Human iliac crest cancellous bone elastic modulus and hardness differ with bone formation rate per bone surface but not by existence of prevalent vertebral fracture.* Journal of Biomedical Materials Research Part B: Applied Biomaterials, 2008. **85B**(1): p. 68-77.
122. Oyen, M.L., *Nanoindentation hardness of mineralized tissues.* Journal of Biomechanics, 2006. **39**(14): p. 2699-2702.
123. Wang, X., et al., *Identification of material parameters based on Mohr–Coulomb failure criterion for bisphosphonate treated canine vertebral cancellous bone.* Bone, 2008. **43**(4): p. 775-780.
124. Brennan, M., et al., *Effects of ageing, prolonged estrogen deficiency and zoledronate on bone tissue mineral distribution.* journal of the mechanical behavior of biomedical materials, 2014. **29**: p. 161-170.
125. Wen, X.-X., et al., *Time related changes of mineral and collagen and their roles in cortical bone mechanics of ovariectomized rabbits.* PloS one, 2015. **10**(6).
126. Yang, X., et al., *Positive alterations of viscoelastic and geometric properties in ovariectomized rat femurs with concurrent administration of ibandronate and PTH.* Bone, 2013. **52**(1): p. 308-317.

127. Oyen, M.L., et al., *Composite bounds on the elastic modulus of bone.* Journal of biomechanics, 2008. **41**(11): p. 2585-2588.
128. Currey, J.D., *Tensile yield in compact bone is determined by strain, post-yield behaviour by mineral content.* Journal of Biomechanics, 2004. **37**(4): p. 549-556.
129. Öhman, C., et al., *Compressive behaviour of child and adult cortical bone.* Bone, 2011. **49**(4): p. 769-776.
130. Tai, K.S., H.J. Qi, and C. Ortiz, *Effect of mineral content on the nanoindentation properties and nanoscale deformation mechanisms of bovine tibial cortical bone.* Journal of Materials Science-Materials in Medicine, 2005. **16**(10): p. 947-959.
131. Mulder, L., et al., *Intratrabecular distribution of tissue stiffness and mineralization in developing trabecular bone.* Bone, 2007. **41**(2): p. 256-265.
132. Ferguson, V.L., A.J. Bushby, and A. Boyde, *Nanomechanical properties and mineral concentration in articular calcified cartilage and subchondral bone.* Journal of Anatomy, 2003. **203**(2): p. 191-202.
133. Gupta, H., et al., *Two different correlations between nanoindentation modulus and mineral content in the bone–cartilage interface.* Journal of structural biology, 2005. **149**(2): p. 138-148.
134. Hoc, T., et al., *Effect of microstructure on the mechanical properties of Haversian cortical bone.* Bone, 2006. **38**(4): p. 466-474.
135. Smith, L.J., J.P. Schirer, and N.L. Fazzalari, *The role of mineral content in determining the micromechanical properties of discrete trabecular bone remodeling packets.* Journal of Biomechanics, 2010. **43**(16): p. 3144-3149.
136. Bi, X., et al., *Raman and mechanical properties correlate at whole bone- and tissue-levels in a genetic mouse model.* Journal of Biomechanics, 2011. **44**(2): p. 297-303.
137. Gourion-Arsiquaud, S., et al., *Spatial Variation in Osteonal Bone Properties Relative to Tissue and Animal Age.* Journal of Bone and Mineral Research, 2009. **24**(7): p. 1271-1281.
138. Vashishth, D., *Advanced glycation end-products and bone fractures.* IBMS BoneKEy, 2009. **6**(8): p. 268-278.
139. Tang, S.Y., U. Zeenath, and D. Vashishth, *Effects of non-enzymatic glycation on cancellous bone fragility.* Bone, 2007. **40**(4): p. 1144-1151.
140. Tang, S. and D. Vashishth, *Non-enzymatic glycation alters microdamage formation in human cancellous bone.* Bone, 2010. **46**(1): p. 148-154.
141. Vashishth, D., et al., *Influence of nonenzymatic glycation on biomechanical properties of cortical bone.* Bone, 2001. **28**(2): p. 195-201.
142. Viguet-Carrin, S., et al., *An in vitro model to test the contribution of advanced glycation end products to bone biomechanical properties.* Bone, 2008. **42**(1): p. 139-149.
143. Willett, T.L., et al., *In vitro non-enzymatic ribation reduces post-yield strain accommodation in cortical bone.* Bone, 2013. **52**(2): p. 611-622.
144. Viguet-Carrin, S., et al., *Contribution of the advanced glycation end product pentosidine and of maturation of type I collagen to compressive biomechanical properties of human lumbar vertebrae.* Bone, 2006. **39**(5): p. 1073-1079.

145. Willems, N.M., et al., *Higher number of pentosidine cross-links induced by ribose does not alter tissue stiffness of cancellous bone.* Materials Science and Engineering: C, 2014. **42**: p. 15-21.
146. Bala, Y., D. Farlay, and G. Boivin, *Bone mineralization: from tissue to crystal in normal and pathological contexts.* Osteoporosis International, 2013. **24**(8): p. 2153-2166.
147. Fernández-Seara, M.A., et al., *Water Content Measured by Proton-Deuteron Exchange NMR Predicts Bone Mineral Density and Mechanical Properties.* Journal of Bone and Mineral Research, 2004. **19**(2): p. 289-296.
148. Anumula, S., et al., *Ultra-short echo-time MRI detects changes in bone mineralization and water content in OVX rat bone in response to alendronate treatment.* Bone, 2010. **46**(5): p. 1391-1399.
149. Nyman, J.S., et al., *Manipulating the Amount and Structure of the Organic Matrix Affects the Water Compartments of Human Cortical Bone.* JBMR Plus, 2019.
150. Seref-Ferlengez, Z., O.D. Kennedy, and M.B. Schaffler, *Bone microdamage, remodeling and bone fragility: how much damage is too much damage[quest].* BoneKEy Rep, 2015. **4**.
151. Schaffler, M., K. Choi, and C. Milgrom, *Aging and matrix microdamage accumulation in human compact bone.* Bone, 1995. **17**(6): p. 521-525.
152. Norman, T.L., T.M. Little, and Y.N. Yeni, *Age-related changes in porosity and mineralization and in-service damage accumulation.* Journal of Biomechanics, 2008. **41**(13): p. 2868-2873.
153. Ural, A., et al., *Association between non-enzymatic glycation, resorption, and microdamage in human tibial cortices.* Osteoporosis International, 2015. **26**(3): p. 865-873.
154. Follet, H., et al., *Effects of preexisting microdamage, collagen cross-links, degree of mineralization, age, and architecture on compressive mechanical properties of elderly human vertebral trabecular bone.* Journal of Orthopaedic Research, 2011. **29**(4): p. 481-488.
155. Norman, T.L., et al., *Influence of microdamage on fracture toughness of the human femur and tibia.* Bone, 1998. **23**(3): p. 303-306.
156. Yeni, Y.N. and D.P. Fyhrie, *Fatigue damage-fracture mechanics interaction in cortical bone.* Bone, 2002. **30**(3): p. 509-514.
157. Reilly, G.C. and J.D. Currey, *The effects of damage and microcracking on the impact strength of bone.* Journal of Biomechanics, 2000. **33**(3): p. 337-343.
158. Mashiba, T., et al., *Suppressed bone turnover by bisphosphonates increases microdamage accumulation and reduces some biomechanical properties in dog rib.* Journal of Bone and Mineral Research, 2000. **15**(4): p. 613-620.
159. Komatsubara, S., et al., *Long-term treatment of incadronate disodium accumulates microdamage but improves the trabecular bone microarchitecture in dog vertebra.* Journal of Bone and Mineral Research, 2003. **18**(3): p. 512-520.
160. Diab, T., et al., *Age-related change in the damage morphology of human cortical bone and its role in bone fragility.* Bone, 2006. **38**(3): p. 427-431.

161. Poundarik, A.A., et al., *Dilatational band formation in bone.* Proceedings of the National Academy of Sciences, 2012. **109**(47): p. 19178-19183.
162. O'Brien, F.J., D. Taylor, and T.C. Lee, *Microcrack accumulation at different intervals during fatigue testing of compact bone.* Journal of Biomechanics, 2003. **36**(7): p. 973-980.
163. Ural, A. and D. Vashishth, *Effects of Intracortical Porosity on Fracture Toughness in Aging Human Bone: A μCT-Based Cohesive Finite Element Study.* Journal of Biomechanical Engineering, 2007. **129**(5): p. 625-631.
164. Besdo, S. and D. Vashishth, *Extended Finite Element models of introcortical porosity and heterogeneity in cortical bone.* Computational Materials Science, 2012. **64**(0): p. 301-305.
165. Wang, X., et al., *Age-related changes of noncalcified collagen in human cortical bone.* Annals of biomedical engineering, 2003. **31**(11): p. 1365-1371.
166. Yeni, Y.N., C.U. Brown, and T.L. Norman, *Influence of Bone Composition and Apparent Density on Fracture Toughness of the Human Femur and Tibia.* Bone, 1998. **22**(1): p. 79-84.
167. Currey, J., *Incompatible mechanical properties in compact bone.* Journal of Theoretical Biology, 2004. **231**(4): p. 569-580.
168. Les, C.M., et al., *Determinants of ovine compact bone viscoelastic properties: effects of architecture, mineralization, and remodeling.* Bone, 2004. **35**(3): p. 729-738.
169. Ritchie, R.O., *The conflicts between strength and toughness.* Nature Materials, 2011. **10**(11): p. 817-822.
170. Launey, M.E., et al., *Mechanistic aspects of the fracture toughness of elk antler bone.* Acta Biomaterialia, 2010. **6**(4): p. 1505-1514.
171. Chen, P.Y., A.G. Stokes, and J. McKittrick, *Comparison of the structure and mechanical properties of bovine femur bone and antler of the North American elk (Cervus elaphus canadensis).* Acta Biomaterialia, 2009. **5**(2): p. 693-706.
172. Tommasini, S.M., et al., *Biological Co-Adaptation of Morphological and Composition Traits Contributes to Mechanical Functionality and Skeletal Fragility.* Journal of Bone and Mineral Research, 2008. **23**(2): p. 236-246.
173. Jepsen, K.J., et al., *Bone brittleness varies with genetic background in A/J and C57BL/6J inbred mice.* Journal of bone and mineral research, 2001. **16**(10): p. 1854-1862.
174. Inzana, J.A., et al., *Bone fragility beyond strength and mineral density: Raman spectroscopy predicts femoral fracture toughness in a murine model of rheumatoid arthritis.* Journal of Biomechanics, 2013. **46**(4): p. 723-730.
175. Gourion-Arsiquaud, S., et al., *Use of FTIR Spectroscopic Imaging to Identify Parameters Associated With Fragility Fracture.* Journal of Bone and Mineral Research, 2009. **24**(9): p. 1565-1571.
176. Milovanovic, P., et al., *Nano-structural, compositional and micro-architectural signs of cortical bone fragility at the superolateral femoral neck in elderly hip fracture patients vs. healthy aged controls.* Experimental Gerontology, 2014. **55**(0): p. 19-28.

177. Wu, Y., et al., *Cortical bone mineralization differences between hip-fractured females and controls. A microradiographic study.* Bone, 2009. **45**(2): p. 207-212.
178. Gourion-Arsiquaud, S., et al., *Fourier transform infrared imaging of femoral neck bone: Reduced heterogeneity of mineral-to-matrix and carbonate-to-phosphate and more variable crystallinity in treatment-naive fracture cases compared with fracture-free controls.* Journal of Bone and Mineral Research, 2013. **28**(1): p. 150-161.
179. Sutton-Smith, P., H. Beard, and N. Fazzalari, *Quantitative backscattered electron imaging of bone in proximal femur fragility fracture and medical illness.* Journal of microscopy, 2008. **229**(1): p. 60-66.
180. Ciarelli, T.E., D.P. Fyhrie, and A.M. Parfitt, *Effects of vertebral bone fragility and bone formation rate on the mineralization levels of cancellous bone from white females.* Bone, 2003. **32**(3): p. 311-315.
181. Unal, M. and O. Akkus, *Raman spectral classification of mineral- and collagen-bound water's associations to elastic and post-yield mechanical properties of cortical bone.* Bone, 2015. **81**: p. 315-326.
182. Bae, W.C., et al., *Quantitative ultrashort echo time (UTE) MRI of human cortical bone: correlation with porosity and biomechanical properties.* Journal of Bone and Mineral Research, 2012. **27**(4): p. 848-857.
183. Manhard, M.K., et al., *MRI-derived bound and pore water concentrations as predictors of fracture resistance.* Bone, 2016. **87**: p. 1-10.
184. Gallant, M.A., et al., *Bone cell-independent benefits of raloxifene on the skeleton: A novel mechanism for improving bone material properties.* Bone, 2014. **61**: p. 191-200.
185. Silva, M.J. and S.R. Ulrich, *In vitro sodium fluoride exposure decreases torsional and bending strength and increases ductility of mouse femora.* Journal of biomechanics, 2000. **33**(2): p. 231-234.
186. Nyman, J.S., *Effect of diabetes on the fracture resistance of bone.* Clinical Reviews in Bone and Mineral Metabolism, 2013. **11**(1): p. 38-48.
187. Silva, M.J., et al., *Type 1 Diabetes in Young Rats Leads to Progressive Trabecular Bone Loss, Cessation of Cortical Bone Growth, and Diminished Whole Bone Strength and Fatigue Life.* Journal of Bone and Mineral Research, 2009. **24**(9): p. 1618-1627.
188. Saito, M., et al., *Role of collagen enzymatic and glycation induced cross-links as a determinant of bone quality in spontaneously diabetic WBN/Kob rats.* Osteoporosis international, 2006. **17**(10): p. 1514-1523.
189. Zimmermann, E.A., et al., *Age-related changes in the plasticity and toughness of human cortical bone at multiple length scales.* Proceedings of the National Academy of Sciences of the United States of America, 2011. **108**(35): p. 14416-14421.
190. Hernandez, C.J., et al., *Trabecular microfracture and the influence of pyridinium and non-enzymatic glycation-mediated collagen cross-links.* Bone, 2005. **37**(6): p. 825-832.

191. Karim, L. and D. Vashishth, *Heterogeneous glycation of cancellous bone and its association with bone quality and fragility.* PLoS One, 2012. **7**(4): p. e35047.
192. Valcourt, U., et al., *Non-enzymatic glycation of bone collagen modifies osteoclastic activity and differentiation.* Journal of Biological Chemistry, 2007. **282**(8): p. 5691-5703.
193. Sanguineti, R., et al., *Pentosidine Effects on Human Osteoblastsin Vitro.* Annals of the New York Academy of Sciences, 2008. **1126**(1): p. 166-172.
194. Viguet-Carrin, S., et al., *Association between collagen cross-links and trabecular microarchitecture properties of human vertebral bone.* Bone, 2010. **46**(2): p. 342-347.
195. Bergot, C., et al., *The degree and distribution of cortical bone mineralization in the human femoral shaft change with age and sex in a microradiographic study.* Bone, 2009. **45**(3): p. 435-442.
196. Raum, K., et al., *Site-matched assessment of structural and tissue properties of cortical bone using scanning acoustic microscopy and synchrotron radiation μCT.* Physics in medicine and biology, 2006. **51**(3): p. 733.
197. Nyman, J.S., et al., *Age-related effect on the concentration of collagen crosslinks in human osteonal and interstitial bone tissue.* Bone, 2006. **39**(6): p. 1210-1217.
198. Sroga, G.E., et al., *Biochemical characterization of major bone-matrix proteins using nanoscale-size bone samples and proteomics methodology.* Molecular & Cellular Proteomics, 2011. **10**(9): p. M110. 006718.
199. Dong, X.N., et al., *In situ accumulation of advanced glycation endproducts (AGES) in bone matrix and its correlation with osteoclastic bone resorption.* Bone, 2011. **49**(2): p. 174-183.
200. Mullins, L.P., M.S. Bruzzi, and P.E. McHugh, *Measurement of the microstructural fracture toughness of cortical bone using indentation fracture.* Journal of Biomechanics, 2007. **40**(14): p. 3285-3288.
201. O'Brien, F.J., D. Taylor, and T.C. Lee, *The effect of bone microstructure on the initiation and growth of microcracks.* Journal of Orthopaedic Research, 2005. **23**(2): p. 475-480.
202. Ural, A. and D. Vashishth, *Interactions between microstructural and geometrical adaptation in human cortical bone.* Journal of Orthopaedic Research, 2006. **24**(7): p. 1489-1498.
203. Wang, X.D., et al., *Changes in the fracture toughness of bone may not be reflected in its mineral density, porosity, and tensile properties.* Bone, 1998. **23**(1): p. 67-72.
204. Bousson, V., et al., *Distribution of intracortical porosity in human midfemoral cortex by age and gender.* Journal of bone and mineral research, 2001. **16**(7): p. 1308-1317.
205. Kazakia, G.J., et al., *Age- and gender-related differences in cortical geometry and microstructure: Improved sensitivity by regional analysis.* Bone, 2013. **52**(2): p. 623-631.
206. Nirody, J.A., et al., *Spatial distribution of intracortical porosity varies across age and sex.* Bone, 2015. **75**(0): p. 88-95.

207. Yerramshetty, J.S., C. Lind, and O. Akkus, *The compositional and physicochemical homogeneity of male femoral cortex increases after the sixth decade.* Bone, 2006. **39**(6): p. 1236-1243.
208. Simmons, E.D., K.P.H. Pritzker, and M.D. Grynpas, *Age-related changes in the human femoral cortex.* Journal of Orthopaedic Research, 1991. **9**(2): p. 155-167.
209. Goldman, H., et al., *Intrapopulation variability in mineralization density at the human femoral mid-shaft.* Journal of anatomy, 2003. **203**(2): p. 243-255.
210. Jepsen, K.J., *Functional Interactions Among Morphologic and Tissue Quality Traits Define Bone Quality.* Clinical Orthopaedics and Related Research, 2011. **469**(8): p. 2150-2159.
211. Schlecht, S.H. and K.J. Jepsen, *Functional integration of skeletal traits: An intraskeletal assessment of bone size, mineralization, and volume covariance.* Bone, 2013. **56**(1): p. 127-138.
212. Vanleene, M., C. Rey, and M.-C.H.B. Tho, *Relationships between density and Young's modulus with microporosity and physico-chemical properties of Wistar rat cortical bone from growth to senescence.* Medical engineering & physics, 2008. **30**(8): p. 1049-1056.
213. Akkus, O., F. Adar, and M.B. Schaffler, *Age-related changes in physicochemical properties of mineral crystals are related to impaired mechanical function of cortical bone.* Bone, 2004. **34**(3): p. 443-453.
214. Odetti, P., et al., *Advanced glycation end products and bone loss during aging.* Annals of the New York Academy of Sciences, 2005. **1043**(1): p. 710-717.
215. Saito, M., et al., *Single-column high-performance liquid chromatographic–fluorescence detection of immature, mature, and senescent cross-links of collagen.* Analytical biochemistry, 1997. **253**(1): p. 26-32.
216. Katayama, Y., et al., *Role of nonenzymatic glycosylation of type I collagen in diabetic osteopenia.* Journal of Bone and Mineral Research, 1996. **11**(7): p. 931-937.
217. Tomasek, J.J., et al., *Diabetic and age-related enhancement of collagen-linked fluorescence in cortical bones of rats.* Life Sciences, 1994. **55**(11): p. 855-861.
218. Chaitou, A., et al., *Association between bone turnover rate and bone microarchitecture in men: The STRAMBO study.* Journal of Bone and Mineral Research, 2010. **25**(11): p. 2313-2323.
219. Szulc, P., et al., *Cross-Sectional Evaluation of Bone Metabolism in Men*.* Journal of Bone and Mineral Research, 2001. **16**(9): p. 1642-1650.
220. Khosla, S., et al., *Relationship of serum sex steroid levels and bone turnover markers with bone mineral density in men and women: a key role for bioavailable estrogen 1.* The Journal of Clinical Endocrinology & Metabolism, 1998. **83**(7): p. 2266-2274.
221. Fatayerji, D. and R. Eastell, *Age-Related Changes in Bone Turnover in Men.* Journal of Bone and Mineral Research, 1999. **14**(7): p. 1203-1210.
222. Clarke, B.L., et al., *Changes in quantitative bone histomorphometry in aging healthy men.* The Journal of Clinical Endocrinology & Metabolism, 1996. **81**(6): p. 2264-2270.

223. Garnero, P., et al., *Increased bone turnover in late postmenopausal women is a major determinant of osteoporosis.* Journal of Bone and Mineral Research, 1996. **11**(3): p. 337-349.
224. Recker, R., et al., *Bone remodeling increases substantially in the years after menopause and remains increased in older osteoporosis patients.* Journal of Bone and Mineral Research, 2004. **19**(10): p. 1628-1633.
225. Geissler, J.R., D. Bajaj, and J.C. Fritton, *American Society of Biomechanics Journal of Biomechanics Award 2013: Cortical bone tissue mechanical quality and biological mechanisms possibly underlying atypical fractures.* Journal of Biomechanics, 2015. **48**(6): p. 883-894.

APPENDIX

A.1 Defined Indent Exclusion Criteria

Following is a list of the 13 exclusion criteria. Listed first for each criterion is the step in the indentation method (described in the Indentation Method section) for which the criterion was checked, followed after a colon by the criterion. Note that P = load, h = displacement, dP/dh = measured stiffness, and Δ = change between data points (5 Hz data acquisition rate during the hold segments). Thus, Δh = displacement rate (with respect to data point index, not time) and Δ^2h = change in the displacement rate. Exclusion criteria and bulleted commentary:

1) Preliminary: Missing data index marker
2) Preliminary: Incorrect marker order
3) Approach: dP/dh never < 0 N/m
    - Interpretation: Stiffness too high at start of approach. This could be due to a false surface find or the indenter being in contact with the sample at the start of the approach segment.
4) Approach: Displacement at first contact > 300 nm from surface displacement
    - Interpretation: Stiffness did not increase as rapidly as should be expected, given contact with the sample.
    - A slow increase in stiffness could be due to tip fouling or a surface void.
    - First contact is defined as the first point after dP/dh < 0 N/m for the last time.
    - Surface displacement is defined as first point dP/dh > 200 N/m.
5) Approach: Total approach distance < 250 nm
    - A sufficient approach is necessary to check instrument behavior.
6) Approach: |dP/dh| > 45 N/m from approach start to first contact
    - For a good approach dP/dh ≈ 0 N/m. High |dP/dh| values meant the indenter was not traveling smoothly.
7) Loading: Any Δh < -2 nm during the loading segment.

- Displacement is expected to increase monotonically during the loading segment.

8) Loading: Load at end of loading too low (< 1 mN human exp., < 0.5 mN rat exp.)
    - Due to false surface finds or hitting voids.
9) Initial Hold/CSM start segment: Any $\Delta^2 h > 2.5$ nm
    - During this segment displacement should increase at a decreasing rate. This is due to 1) viscoelastic creep, and 2) increasing harmonic load.
    - Tag indents which exhibit a sudden change in displacement rate.
10) Hold: Hold time < 2 min
11) Hold: h_{max}-$h_{hold\ stop} > 1$ nm
    - Due to viscoelastic creep, h is expected to increase.
12) Hold: Any $|\Delta(\Delta h/\Delta t)| > 0.35$ nm/s
    - Due to viscoelastic creep, h is expected to increase at a decreasing rate.
    - Calculate h_{mean}=mean(h) in 2 second intervals for the segment between hold start and hold stop (2 minutes).
    - Repeat above tagging procedure using time bins offset 1 second from 1st calculation (since each h_{mean} depends how the data were binned for averaging).
13) Unload: Load spike (P_{max} - $P_{unload\ start} > 0.025$ mN).
    - Occasionally a load spike was seen prior to unloading, despite not being prescribed in the method.

VITA

Robert Singleton was born in West Point, NY on September 12, 1988. He lived in Kansas and North Carolina as a young boy before moving to Oak Ridge, TN in time for the 5th grade. Robert graduated from ORHS in 2007 and subsequently enrolled in the University of Tennessee, Knoxville. He received the Bachelor of Science in Mechanical Engineering degree in 2011. For graduate study Robert remained at UT, but switched to the Department of Materials Science and Engineering.